CR–137782

FLIGHT DATA ANALYSIS AND FURTHER DEVELOPMENT OF VARIABLE-CONDUCTANCE HEAT PIPES

RESEARCH REPORT NO. 1

February 1976

Prepared for
AMES RESEARCH CENTER
NATIONAL AERONAUTICS AND SPACE ADMINISTRATION
Moffett Field, California 94035

TRW

ONE SPACE PARK · REDONDO BEACH · CALIFORNIA 90278

CR 137782

26263-6021-RU-00

FLIGHT DATA ANALYSIS AND FURTHER DEVELOPMENT OF VARIABLE-CONDUCTANCE HEAT PIPES

Research Report No. 1

February 1976

Prepared by

J. E. Eninger
E. E. Luedke
D. J. Wanous

Contract No. NAS 2-8310

Prepared for

AMES RESEARCH CENTER
NATIONAL AERONAUTICS AND SPACE ADMINISTRATION
Moffett Field, California 94035

TRW SYSTEMS GROUP
ONE SPACE PARK · REDONDO BEACH · CALIFORNIA 90278

TABLE OF CONTENTS

TABLE OF CONTENTS (CONTINUED)

LIST OF FIGURES

LIST OF FIGURES (CONTINUED)

LIST OF FIGURES (CONTINUED)

LIST OF TABLES

1.0 INTRODUCTION

Heat pipes are at a stage of development where they are often indispensable elements in the optimum thermal design of spacecraft. Large gains in heat-pipe performance, however, are still to be had in control, as well as reliability and capacity. This report is on continuing efforts in these areas by TRW Systems Group under contract NAS 2-8310 with Ames Research Center. In addition, we are reporting the results from data analysis of two successful zero-gravity flight experiments that were developed on a previous contract NAS 2-5503.

In Section 2, we report the results of the Ames Heat Pipe Experiment (AHPE), which is a variable-conductance heat-pipe/radiator system launched aboard the OAO-3 spacecraft in August 1972. All available flight data were reviewed, and those from selected orbits were correlated with predictions of an analytical model of the system. The principal conclusion is that gas-controlled variable-conductance heat pipes can perform reliably for long periods in space and effectively provide temperature stabilization for spacecraft electronics. Furthermore, the performance of such systems can be adequately predicted using existing design tools.

Arterial heat pipes offer high heat-transport capacity, however even a trace impurity of noncondensable gas can be trapped in an arterial bubble during priming and cause the artery to fail under load. This critical problem has in the past ruled out arteries for gas-loaded variable-conductance heat pipes. The second zero-gravity experiment, reported in Section 4, studied a solution that allows the gas to vent through the arterial wall. Zero-gravity was achieved for six minutes on board a sounding rocket. Two heat pipes had instrumentation inside the arteries to detect the state of prime. The principal conclusion is that the solution works effectively in zero gravity as well as on earth, and the experiment provided confidence that gas-loaded arterial heat pipes of the type tested will function reliably on spacecraft.

In conjunction with the analysis of arterial priming on the sounding-rocket experiment, a glass-walled heat pipe was used to visually investigate the priming mechanism in the laboratory. This investigation, which is reported in Section 5, uncovered the source of a discrepancy between the actual fluid charge required for the arteries to prime and the predicted charge, which was low by over 30%. A solution was found that allows the arteries to prime at a much lower fluid charge.

Although arterial heat pipes have a high heat-transport capacity, they also have stringent leveling requirements for priming, and they are generally complex to fabricate. In addition, nonarterial heat pipes are inherently more reliable. Under the task reported in Section 6, a high-capacity nonarterial heat pipe was developed. A combined theoretical and experimental effort was first undertaken to construct a mathematical model of capillary flow through a fibrous wick. The key to high capacity is to use the model to vary the wick's porosity along its length. The computer program GRADE was written to calculate optimum porosity variations. A half-inch-diameter all-aluminum heat pipe with ammonia as the working fluid was designed and tested. Its demonstrated capacity of 226 watt-m at 21 C is far superior to any existing half-inch-diameter nonarterial ammonia heat pipe, and the mathematical model predicts an additional 50% increase is possible by a refinement of the wick's porosity variation.

As part of the effort to develop a high-capacity nonarterial heat pipe, a task was undertaken, which is still in progress, to experimentally study the pressure variation of the vapor flow since it can directly affect the optimum porosity variation of the wick. The results of this study are deferred to the next research report where we plan to present them with the results of a theoretical study.

Our task in the area of heat-pipe control, which is reported in Section 3, was to develop a flight prototype variable-conductance heat pipe based on modulating the vapor flow. In the course of the task, we discovered a new control mechanism that circumvents some of the limitations of the existing vapor-modulated mechanism. Two heat pipes were fabricated. The first pointed to several needed design changes, which were incorporated into the second. The result is a heat pipe with high capacity (in excess of 200 watt-m) and close temperature control of the heat source (less than 0.04C rise in temperature per watt), independent of large variations in sink temperature.

2.0 A VARIABLE-CONDUCTANCE HEAT-PIPE FLIGHT EXPERIMENT: PERFORMANCE IN SPACE

The Ames Heat Pipe Experiment (AHPE) is a variable-conductance heat pipe which was launched aboard the OAO-3 spacecraft by NASA in August of 1972. AHPE is being utilized to control the temperature of the spacecraft's On-Board Processor (OBP). Variable conductance is achieved by a noncondensable gas loading contained in a "hot", non-wicked reservoir.

AHPE was developed and fabricated by TRW under a previous contract. On the current contract, the flight temperature data were analyzed and compared to analytical predictions (see Reference 2.6). With a view of achieving maximum utilization of the flight data as an aid in future applications of variable-conductance heat pipes, it was established that the following questions should be answered during the study:

(1) Does operation of the experiment correspond to established theory, and can it be predicted with existing analytical tools?

(2) How effective is the heat pipe in providing temperature stability for the OBP, i.e., what temperature would be expected without the heat pipe?

An analytical model of the heat-pipe system was first generated. To establish confidence in the model, it was then used to correlate ground-test data where heat inputs and environmental conditions were well known, and a large number of temperature measurements were available. Flight data were then collected, examined and several orbits selected for correlation. Primary criteria for selection were that the data were for a full orbit and showed orbital stability, i.e., temperatures at the beginning and end of the orbit were approximately equal. This allowed correlation of data for an individual orbit without having data from previous orbits. Environmental conditions for these orbits were input to the analytical model, and the predicted heat-pipe performance was compared with the flight data. Finally, the model was modified to simulate a failed heat pipe, and the performance of this system compared with the existing AHPE design to give a measure of the heat-pipe effectiveness in providing temperature control.

2.1 AHPE DESIGN DESCRIPTION

A complete discussion of the system design and a detailed description of the AHPE hardware can be found in References 2.1 and 2.2. A summary of the important design features is given below.

Working fluid: methanol

Control gas: helium (1.16×10^{-3} g-mole)

Pipe material: stainless steel

Reservoir: Hot, non-wicked (216.3 cm^3)

Wick system: Hybrid; homogeneous and filled artery

Maximum heat load (design spec.): 22 watts

Radiator sink temperature (design values)*: -19C (max), -52C (min)

Control range: 14 to 20C

Radiator: Alzak-coated aluminum (α/ε = 0.17/0.75)

Reservoir/condenser volume ratio: 10:1

*Includes heat input to back of radiator.

Figure 2-1 shows the AHPE as integrated into the Orbiting Astronomical Observatory (OAO-3). OAO-3 has 926 km , circular orbit. The spacecraft is in sunlight from 65 to 81 percent of the time, corresponding to orbit planes between 0° and 55° to the ecliptic. Heat generated by the OBP electronics is rejected to space by an Alzak-coated radiator mounted on an external face of the spacecraft. The spacecraft is oriented such that the panel surface on which the AHPE radiator is mounted is always parallel to the sun-earth line. Therefore, the radiator gets no direct solar energy but receives earth emission and albedo plus infrared energy emitted from the solar array. This solar array IR flux is the dominant external heating source as can be seen from Table 2.1.

Transfer of heat from the OBP platform to the radiator is by two parallel paths. The first is direct radiation and the second is through the AHPE variable-conductance heat pipe. An experiment constraint was that, for an AHPE failure, the OBP platform would not exceed 60C. This required the radiative heat-transfer path in parallel with the heat pipe.

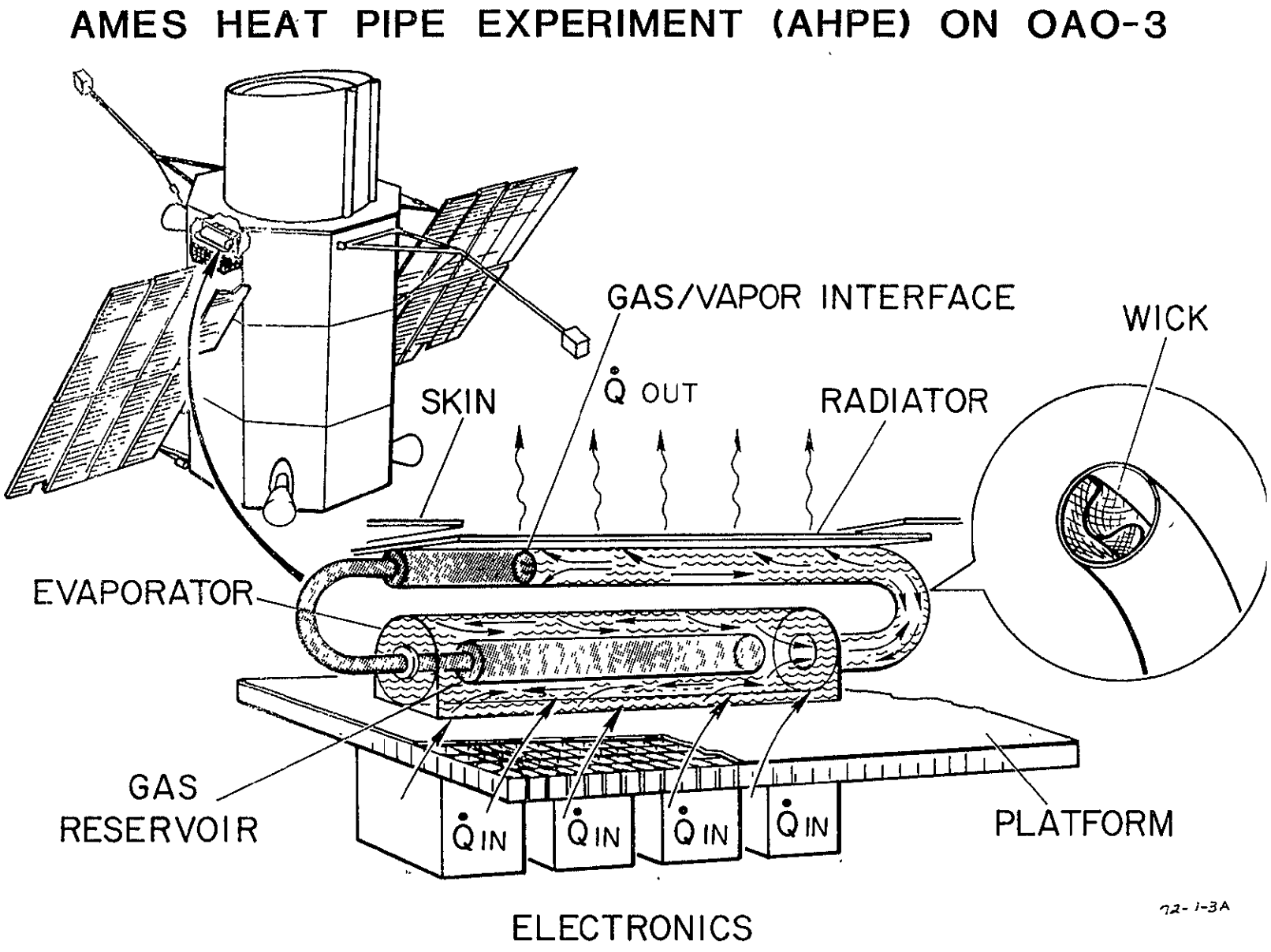

Figure 2-1. Ames Heat Pipe Experiment (AHPE) on OAO-3.

Table 2.1. Incident External Heat Fluxes on AHPE Radiator+

	Solar	Infrared	
	Albedo	Earth	Solar Array
Max	49.29	57.43	159.36
Min	19.74	34.85	42.45

+Watts/m^2, Orbital Average.

The AHPE design is shown in Figure 2-2. Methanol was chosen as the working fluid because of its superior properties for control. The control gas is He to maximize diffusion rates. It is stored in the unwicked reservoir that is located inside the evaporator. Stainless steel is used for the heat-pipe walls and wicks because of its low thermal conductivity, which is beneficial to control performance, and it is compatible with methanol.

The saddle for mounting the heat pipe to the OBP platform is of aluminum for light weight and high conductance. As discussed in Reference 2.1, the optimum characteristics for the radiator are high conductance perpendicular to the condenser tube, to yield high radiator effectiveness, but a low conductance in the axial direction to minimize the control temperature range. This leads to the segmented radiator shown in Figure 2-2. Low-conductivity fiberglass spacers are fitted between high-conductivity aluminum fins. The region of the radiator nearest the reservoir entrance has finer segments to locally give an even smaller axial conductance. Low conductance in this region is important to achieve maximum utilization of the radiator surface.

The back of the main section of the radiator is painted black to provide a heat-transfer path in parallel with the heat pipe as a back-up in case of heat-pipe failure. If the heat pipe should fail, OBP dissipation would be rejected totally by this path with an increased temperature resulting. The back of the cold-trap region is insulated with aluminized mylar to lower its effective sink temperature and thus minimize the partial pressure of methanol in the gas reservoir.

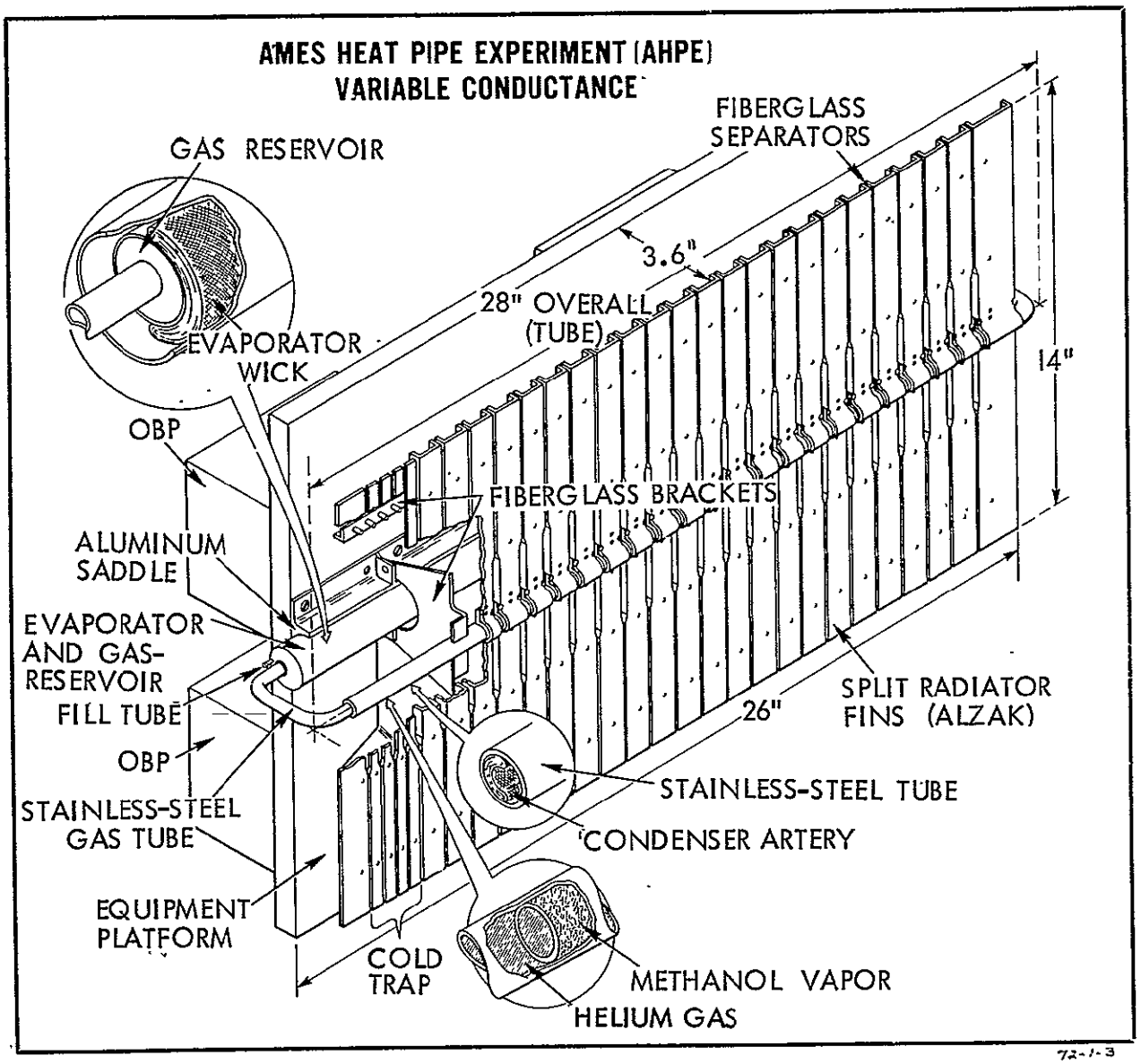

Figure 2-2. AHPE Hardware Configuration.

2.2 THERMAL MODEL

An analytical representation of the configuration was developed that has two major elements: 1) a standard nodal-network representation and 2) a subroutine which calculates the variable-conductance heat-pipe performance. The model is solved on the Systems Improved Numerical Differencing Analyzer (SINDA) Program, Reference 2.3.

The nodal model of the AHPE is shown in Figure 2-3. It consists of 53 nodes to represent the radiator, heat pipe, platform, OBP and boundary conditions. Two models were generated: 1) a steady-state representation to correlate ground test data and 2) a transient model to correlate flight data. A subroutine to the SINDA program was written to calculate performance of the variable-conductance heat pipe using the same basic formulation described in Reference 2.4. This formulation was modified to include the effect of diffusion, which is necessary in this application because sink conditions undergo a large change each orbit with a corresponding variation in methanol partial pressure in the cold trap at the entrance to the reservoir.. The partial pressure of methanol in the reservoir will attempt to equilibrate with the cold-trap partial pressure by diffusion and convection. Under steady-state conditions, the reservoir methanol partial pressure would become equal to the cold-trap methanol partial pressure. However, under the orbital transients of AHPE this assumption would not be valid and diffusion dynamics must be included in the analytical model.

Figure 2-4 shows the manner in which the heat pipe is modeled and gives a block diagram indicating the method of solution for a transient problem. The heat pipe is divided into a number of nodes with all condenser and evaporator nodes connected to a single vapor node. Initial temperatures for all nodes are input to start the calculation procedure. Time is then advanced, boundary temperatures are updated and the nodal network solved for the new conditions. Reservoir and heat-pipe wall temperatures calculated are input to the VCHP subroutine, which then calculates a new heat-pipe vapor temperature. Flow of vapor into or out of the reservoir due to diffusion and convection during the time step are next calculated, as

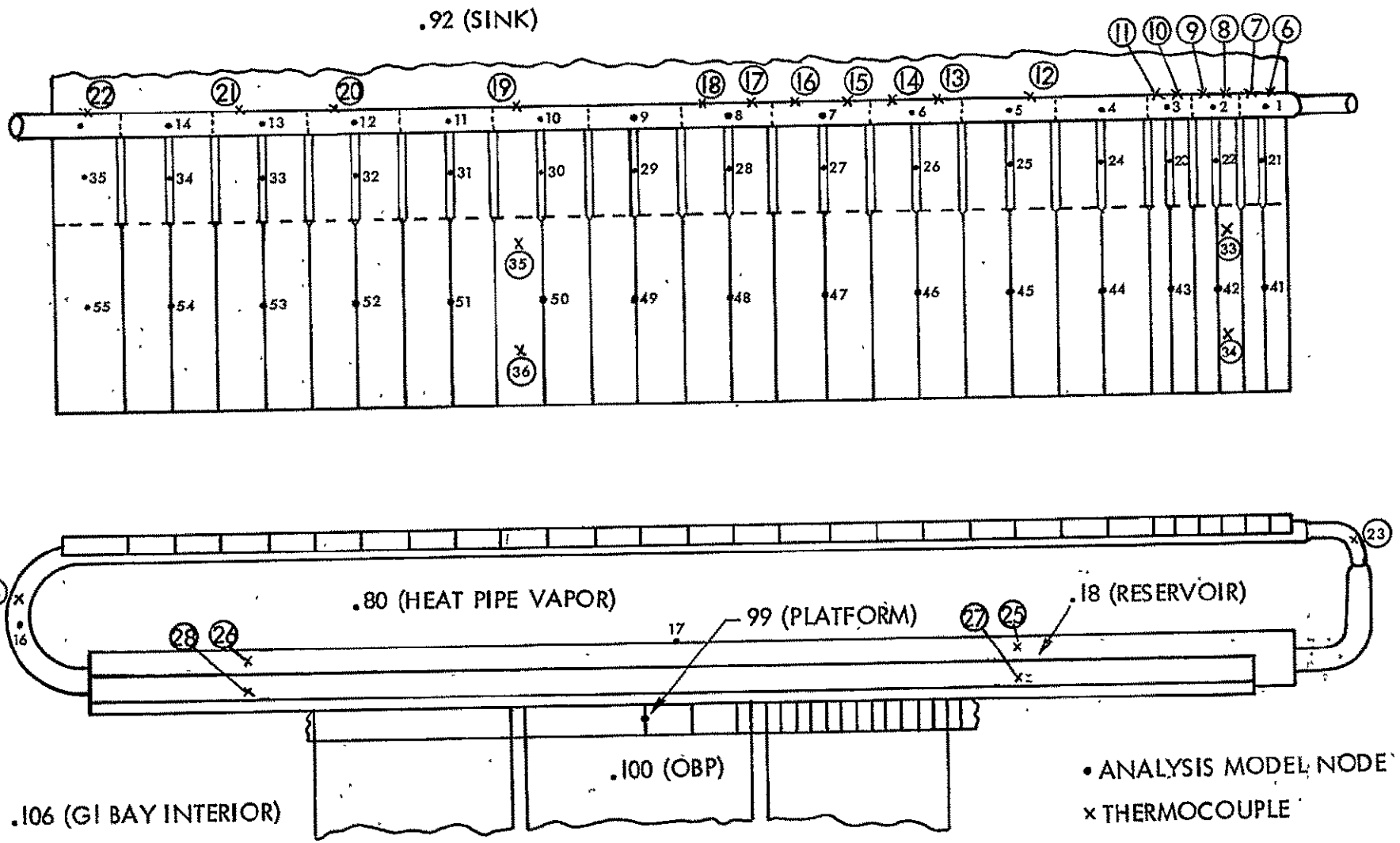

Figure 2-3. AHPE Analysis Model Node Locations.

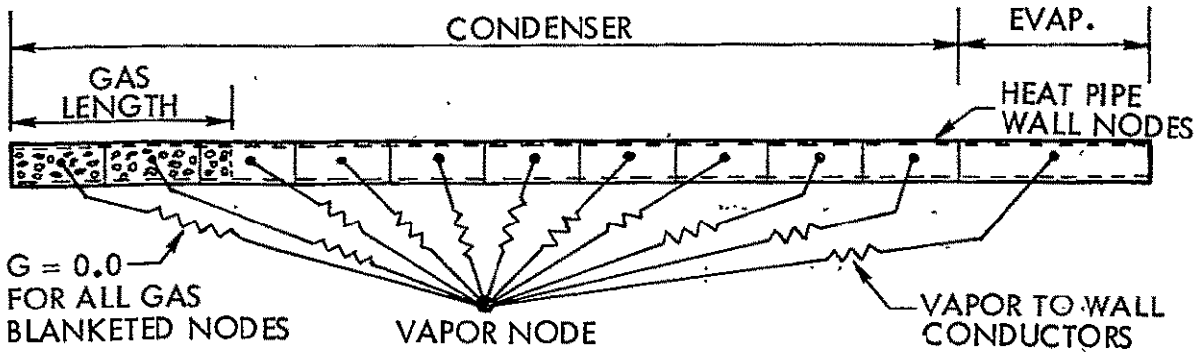

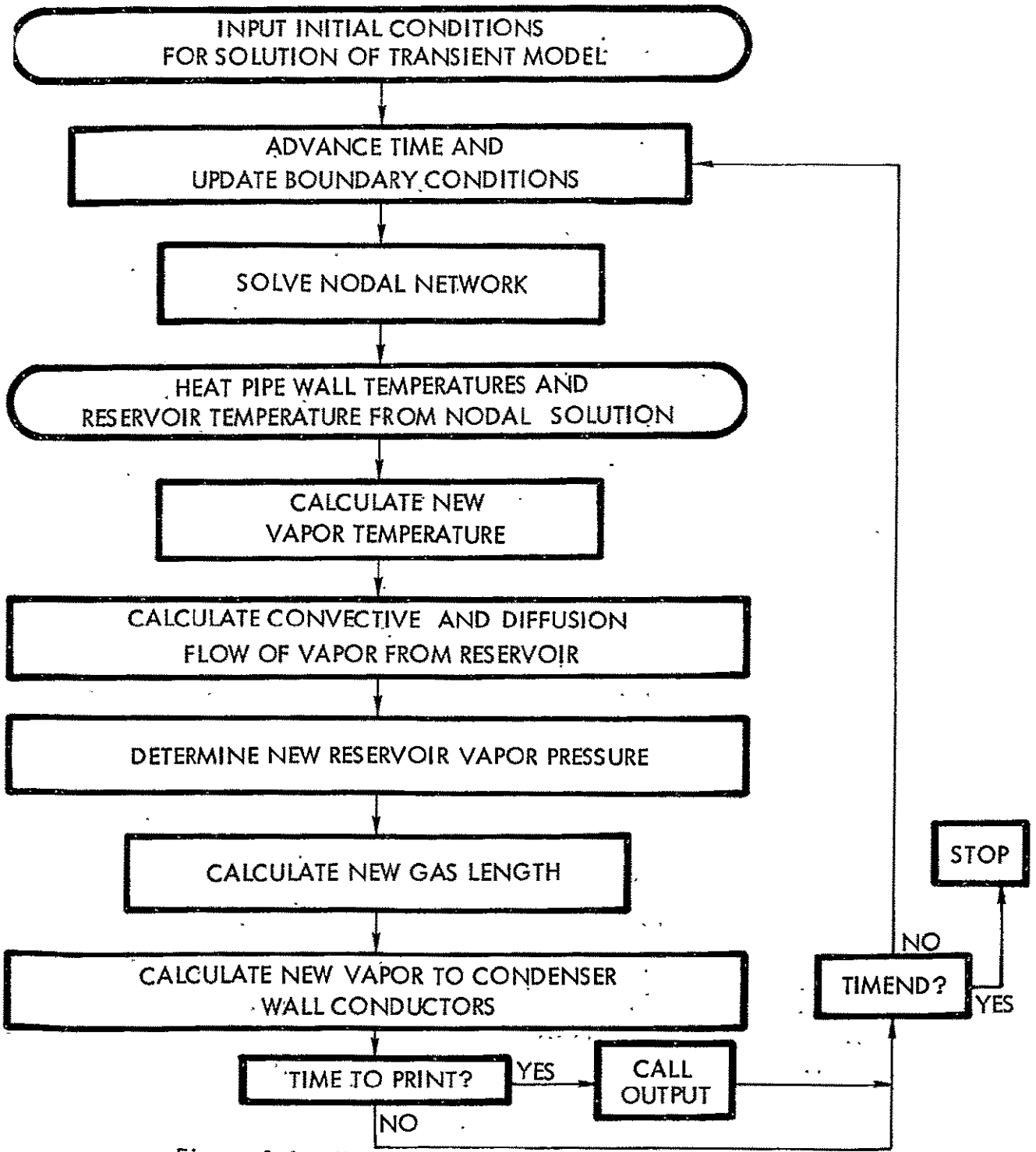

Figure 2-4. VCHP Analysis Model.

75-30A

well as the new reservoir vapor pressure (see Appendix A for details of these calculations). A new gas length in the condenser is next calculated and condenser-to-evaporator conductor values updated. If a condenser node is completely blanketed by gas, its conductance to the vapor node is set to zero. If the gas front is located somewhere within the boundary of a particular node, the conductor value is calculated from the fraction of the node which is not blanketed by gas. The evaporator temperature and conductor values thus calculated are then input to the nodal-network solution routine and used during the next time step.

2.3 CORRELATION OF GROUND PERFORMANCE TESTS

Thermal-performance tests were conducted to verify the predicted performance of the AHPE for the fluctuations in power dissipation and external boundary conditions anticipated during flight. Of particular interest were the control range and axial temperature profiles, the minimum and maximum pipe conductances and the maximum heat-load capacity. Although these tests simulated the thermal energy incident on the radiator during flight, their purpose was to determine the performance of the AHPE itself with well-defined thermal boundary conditions, rather than attempting to simulate the complex interactions within the OAO-3/G-1 bay. Thus, these tests were ideal for verification of the thermal model and VCHP simulation subroutine.

The test set-up is shown in Figure 2-5. The AHPE was mounted on the vertical supports so that the centerline of the evaporator was approximately 0.64 cm above the centerline of the condenser. Teflon washers were used to conductively insulate the AHPE from the support structures, and guard heaters were used to minimize heat losses through the thermocouple leads and from the back of the evaporator. All but the outboard surface of the radiator was insulated with approximately 20 layers of crinkled aluminized mylar. The albedo (S) and infrared energy (IR) incident on the radiator during flight were simulated by a shroud completely encompassing the radiator's field of view and heated to an effective space temperature (T_S) defined by the equation

$$\sigma\varepsilon T_S^4 = \alpha S + \varepsilon IR$$

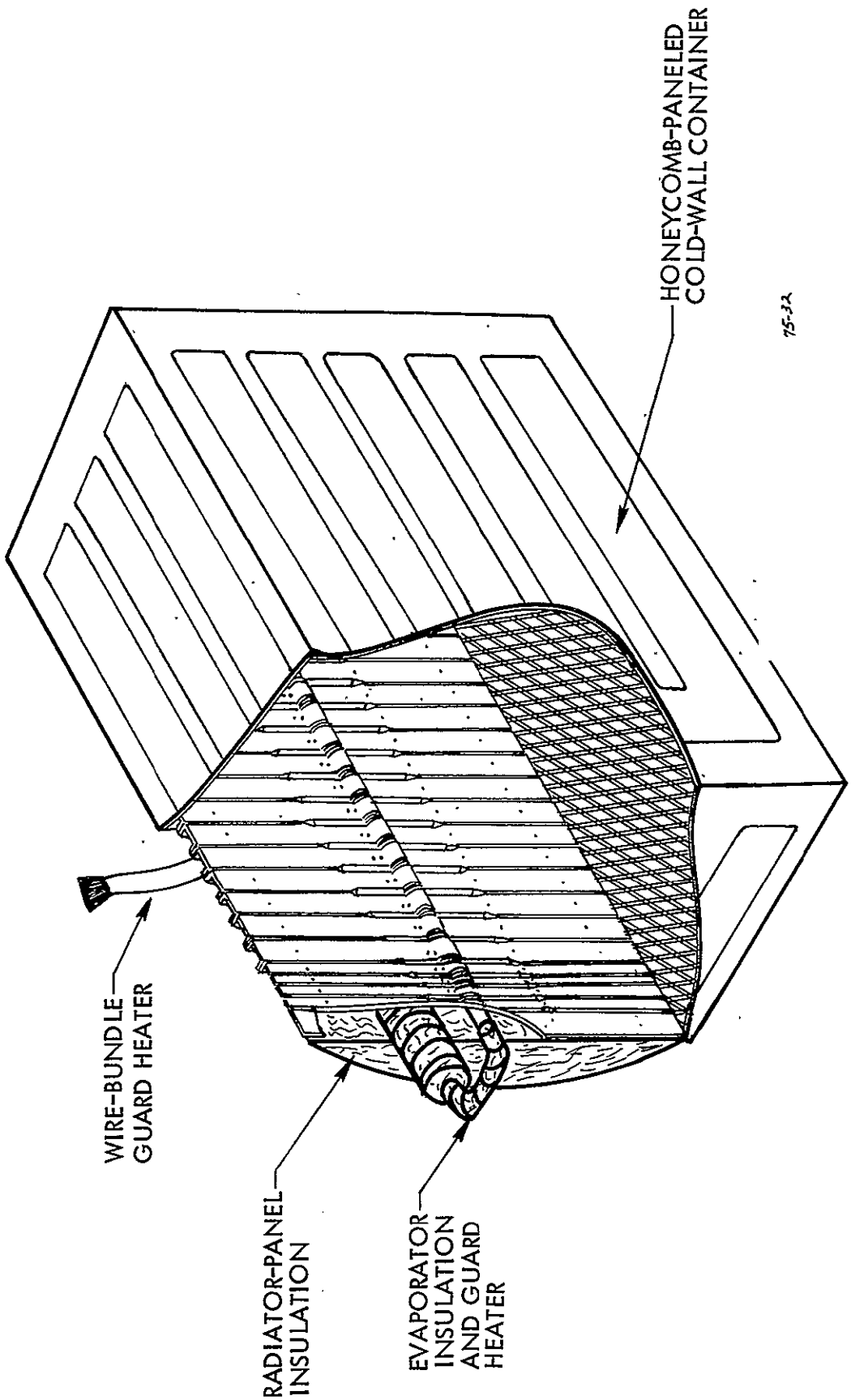

Figure 2-5. Thermal Performance Test Set-Up.

where α and ε are the solar absorptance and infrared emittance of the Alzak radiator. The heated shroud was lined with open-cell honeycomb and painted with Cat-a-lac black to yield a shroud emittance of nearly unity. Power to the evaporator was supplied by four flight-type foil heaters bonded to the sides of the evaporator saddle.

The test conditions were specified to map the heat pipe's performance under maximum and minimum external flux conditions. In the flight configuration the inward-facing surface of the cold trap has a low-emittance coating while the inward side of the main radiator is painted black. This results, as indicated in Section 2.4, in an effective sink temperature variation between -19C and -52C for the main radiator. The effective sink temperature for the cold trap is lower because its low emittance coating on the inward-facing surface results in a reduced heat load from the OBP platform. Calculated sink-temperature range for the cold trap is -28C to -77C. During ground test for the low-sink condition, the cold-trap sink temperature was approximately the same as the main-radiator temperature, i.e., -51C. Since the difference in methanol vapor pressure between the specified sink temperatures of -77C and -52C is very small, it was judged unnecessary to simulate the lower-temperature cold-trap sink. However, for the maximum sink conditions the shroud temperature profile was controlled to give effective sink temperatures approximating -19C and -28C for the main radiator and cold trap respectively.

Figure 2-6 shows comparisons between test data and analytical predictions of the heat-pipe control characteristics. Good correlation is achieved except at very low power levels where small heat leaks which are difficult to accurately predict are dominant. Figure 2-7 shows a representative comparison of analysis and test data for the condenser temperature profile. Again, reasonably good agreement is in evidence.

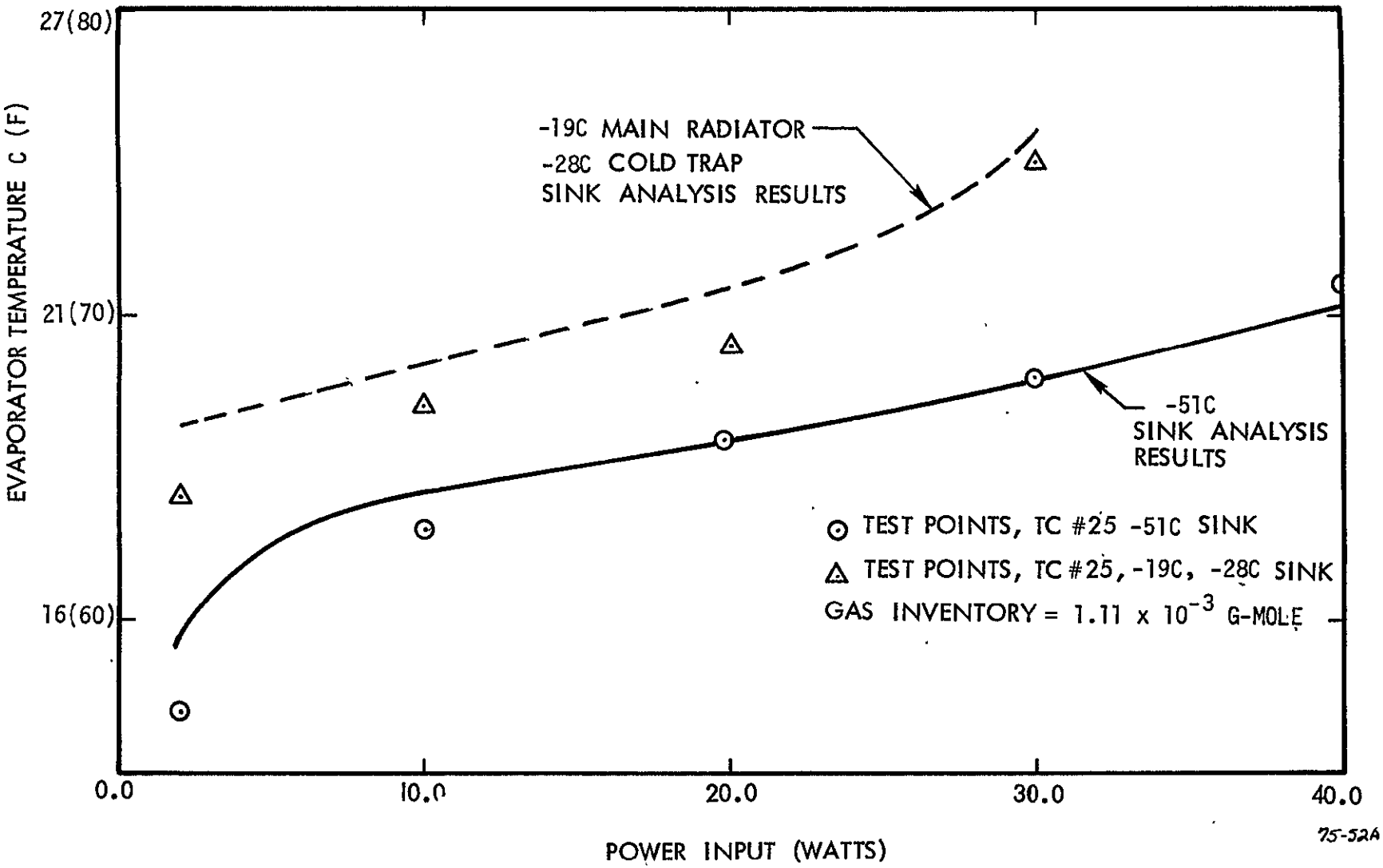

Figure 2-6. Comparison of Evaporator Temperatures.

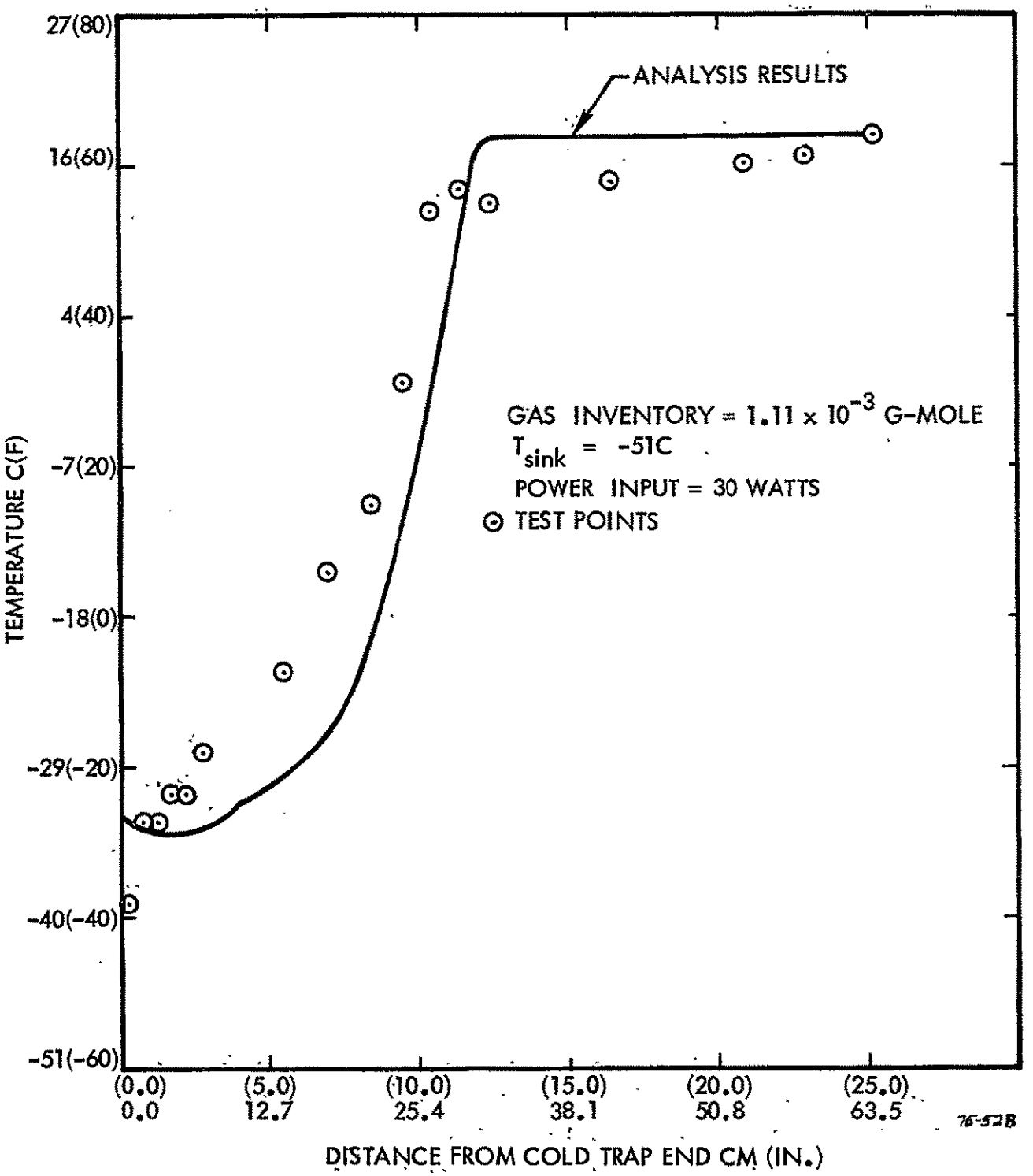

Figure 2-7. Comparison of Condenser Temperature Profile.

2.4 FLIGHT DATA ANALYSIS, NORMAL OPERATION

A great deal of flight data has been accumulated over the two plus years the spacecraft has been in orbit. All available data was reviewed and a summary of OBP platform temperatures is shown in Table 2.2.

Table 2.2. Summary of AHPE Orbital Data

Orbit No.	% Time In Sun	Orbital Average OBP Platform Temperature (°C)	β^*(Deg.)
420	66	19	62
426	66	19	26
967	66	21	30
1592	69	21	26
3360	66	19	+
4225	81	22	30
5716	67	24	51
5801	68	21	93
9852	79	23	27
17336	77	21	29

*β = Spacecraft pitch angle.
+ = Not available.

The data shown in Table 2.2, representing over three years in orbit, show some evidence of possible minor degradation in heat-pipe performance. For example, orbits 4225 and 9852, which are approximately 400 days apart, have about the same environmental conditions but the latter orbit shows a 1°C higher OBP platform temperature. The last data point, however, after about three years is near the orbit 4225 data. Comparing temperature with early data is not readily accomplished due to different orbital conditions, but any changes in heat pipe operation appear to be minor.

All data discussed in this section are for the nominal OBP power dissipation of about 15 watts. Some data supplied by NASA indicated higher power levels: however, those were for only short time periods or for conditions not sufficiently specified to warrant presentation. Data for higher powers using the flight heaters was obtained. This data is discussed in the next section. From the data, a few orbits

representing a broad range in environmental conditions were selected for correlation with the analytical model. Environmental conditions for these orbits were input to the analytical model and the predicted heat-pipe performance compared with the measured flight data.

Figures 2-8, 2-9, and 2-10 show comparisons between analytical predictions and flight data. Flight instrumentation of the radiator consisted of two thermistors, one on the heat pipe at the cold trap and one at the beginning of the condenser. This latter thermistor thus indicates turn-on and turn-off of the heat pipe. Turn-on of the heat pipe is defined as when the gas front location reaches the beginning of the condenser. This condition is indicated by an increase in the reading of condenser thermistor. Turn-off is defined as when the gas front location recedes into the adiabatic section or evaporator and results in a decrease in the condenser thermistor reading. Additionally, there were two thermistors on the evaporator and one on the OBP platform.

All results shown are for one complete orbit where orbital stability was achieved, i.e., temperatures at the beginning and end of orbit are approximately equal. The comparisons indicate that the zero-g performance of the heat pipe is indeed in accord with theory. There is a fairly large discrepancy between analysis and data for the cold trap, the most probable explanation for which is a faulty cold-trap thermistor. Study of all flight data has shown that readings from this thermistor were inconsistent and, in some cases, appeared to be physically impossible. For example, in some cases the cold-trap thermistor has a higher reading than the condenser thermistor which is unrealistic.

A number of other possibilities were explored in an attempt to analytically match the flight data before it was judged highly probable that the cold-trap thermistor was giving faulty readings. Assuming the cold-trap thermistor readings were correct and inputting these values into the analytical model, we then determined under what conditions flight performance of the heat pipe could be reproduced. It was found that flight performance could be fairly well matched by either assuming the evaporator thermistors were reading about 2°C too low or that there was approximately 10 percent less noncondensable gas in the heat pipe than the

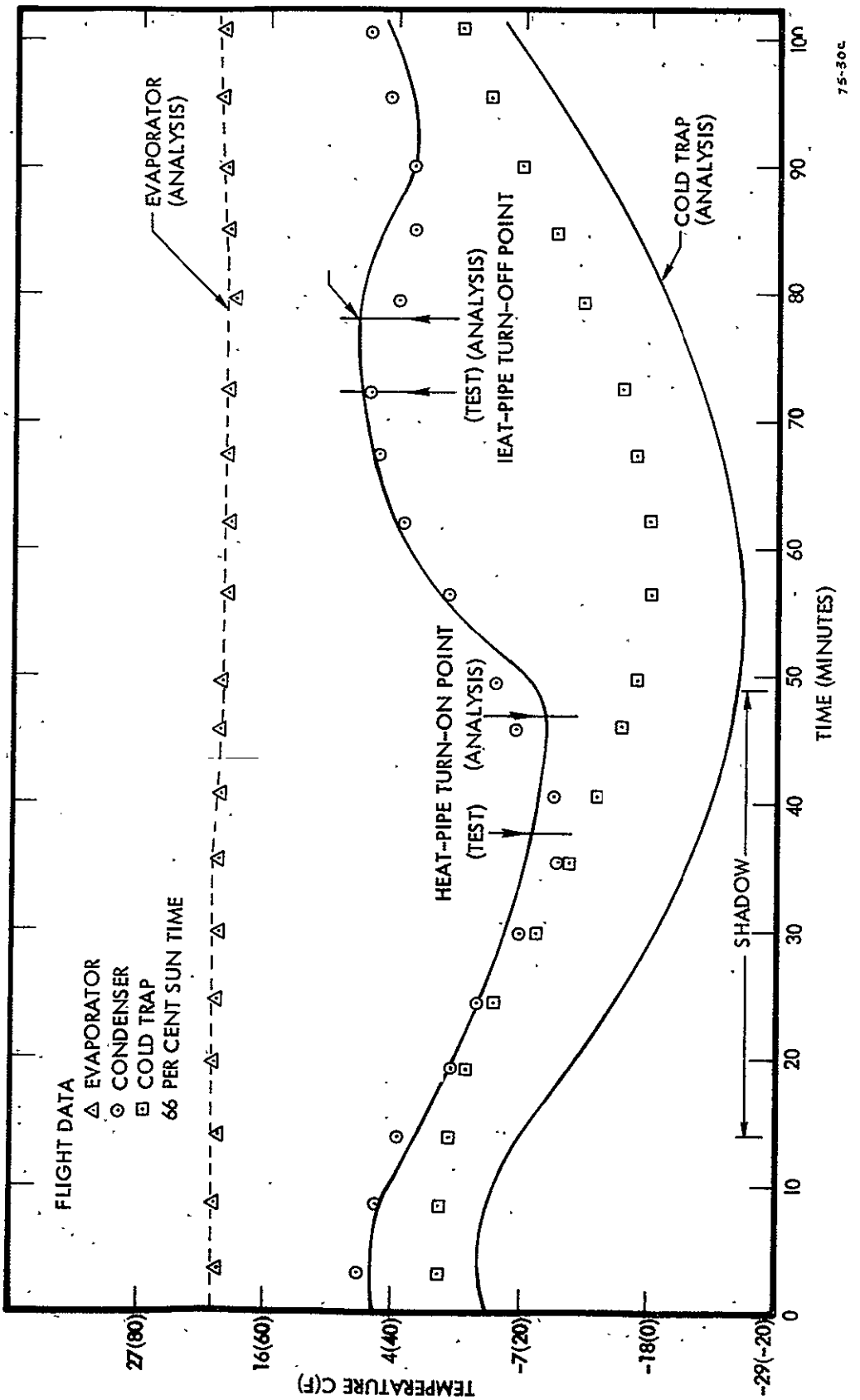

Figure 2-8. Correlation of Flight and Analysis Data, Orbit 420.

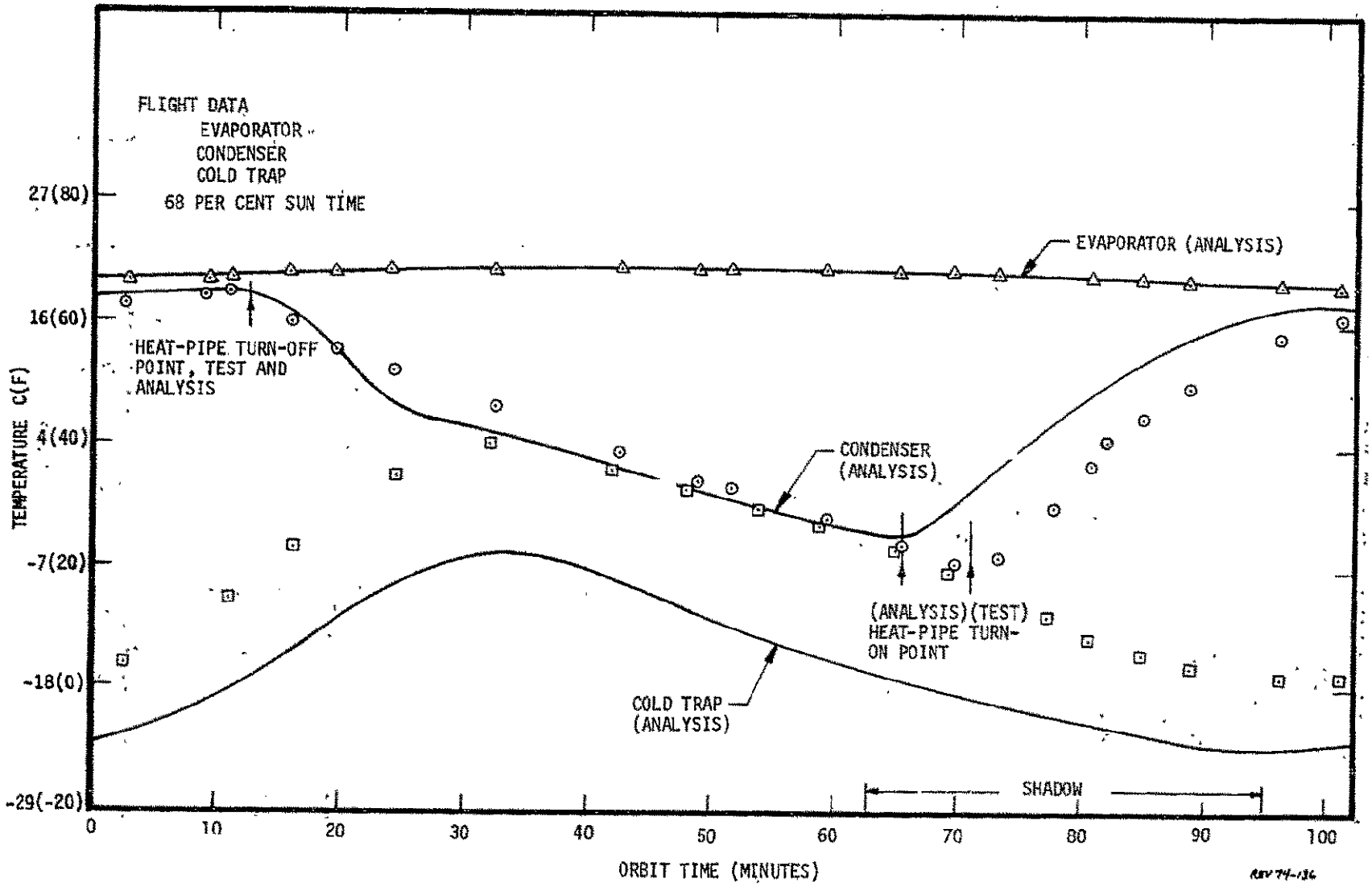

Figure 2-9. Correlation of Flight and Analysis Data, Orbit 1592.

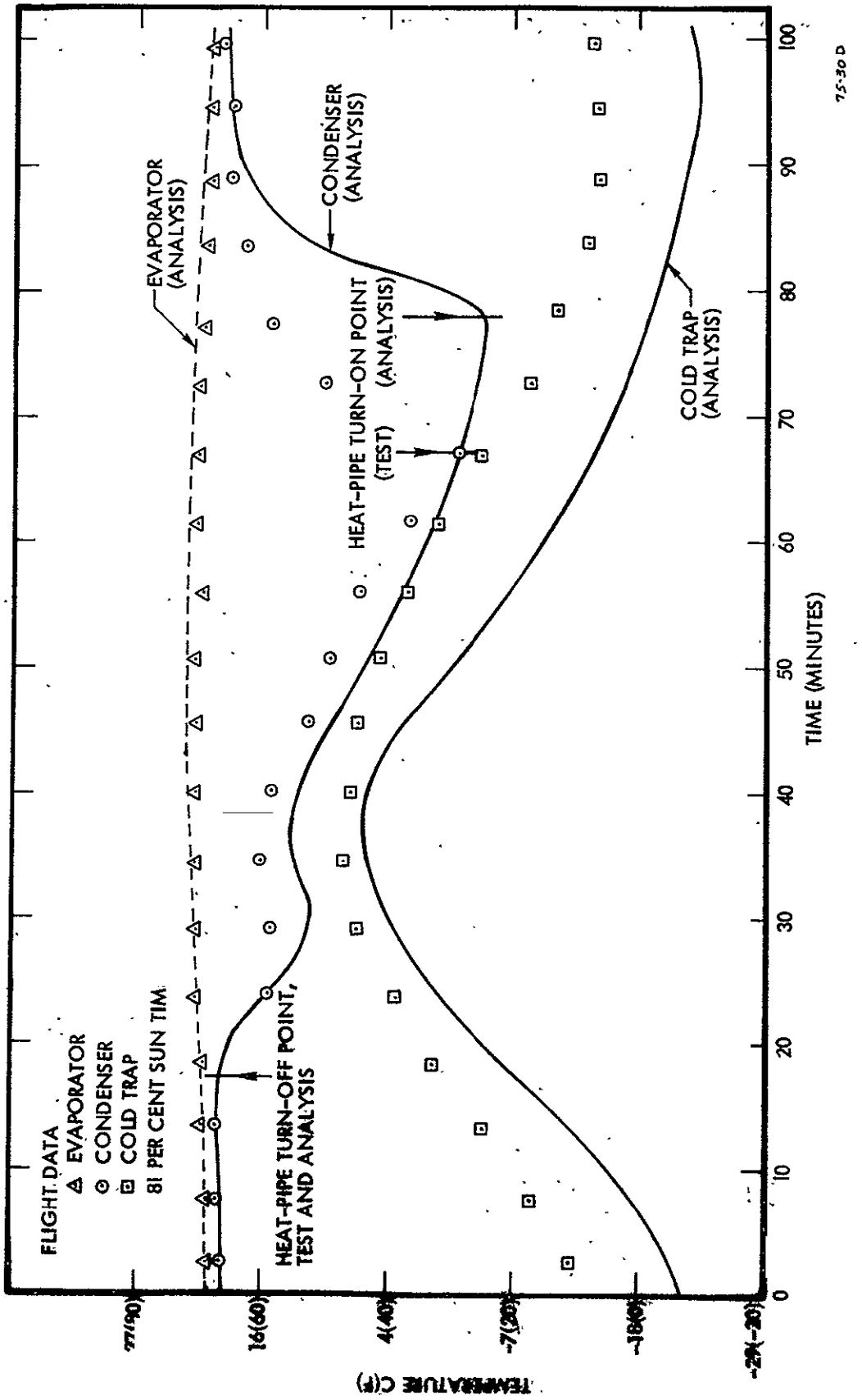

Figure 2-10. Correlation of Flight and Analysis Data, Orbit 4225.

nominal initial charge. Both of these possibilities are unlikely. There are two evaporator thermistors giving consistent readings which are also in accord with the OBP platform thermistor. On the other hand, the 10 percent reduction in noncondensable gas loading is well beyond the gas loading tolerance of approximately $\pm 2\%$ and a gas leak is inconsistent with the rise in operating temperature with time discussed previously. In addition, to match the cold-trap thermistor data, a significantly higher external heat input would be required for the cold trap than for the main radiator. However, calculated external heating is nearly uniform over the entire radiator cold-trap surface.

The heat pipe, in all three orbits, has a somewhat unusual turn-on and turn-off performance as shown by the flight data and also reproduced analytically, Figures 2-8, 2-9 and 2-10. The heat pipe undergoes a turn-on turn-off cycle every orbit as indicated by the condenser temperature profile which corresponds to a thermistor located at the beginning of the condenser section. It is interesting to note that the turn-off of the heat pipe does not coincide with a decreasing evaporator temperature nor does the turn-on occur with a rising evaporator temperature as one might expect of a gas-controlled heat pipe. A closer look at the results, however, shows that the heat pipe's control function was not responding to variations in OBP power dissipation (which was nearly constant throughout the orbit), but to variations in radiator sink conditions as reflected by the cold-trap temperature profile. The heat pipe turn-off coincides with an increasing cold-trap temperature which results in an increase in methanol partial pressure within the gas reservoir. This, in turn, displaces a quantity of noncondensable gas into the condenser which shuts the pipe off. Conversely, the turn-on occurs while the sink conditions (cold-trap temperature) are falling. The corresponding decrease in methanol partial pressure in the gas reservoir causes noncondensable gas to flow from the condenser into the reservoir, thus turning the heat pipe on.

Turn-on turn-off characteristics of the VCHP are very sensitive to the noncondensable gas loading. This is, in part, due to the fact that under nominal OBP power ($\approx$15 watts) the heat pipe carries very little load

(most is by direct radiation between platform and radiator), and hence the gas front is very near the evaporator end of the condenser. Active lengths of the condenser are short and a small increase in gas inventory would turn the pipe completely off. For example, a one percent change in gas inventory corresponds to a gas-front movement of approximately five cm. In correlating the flight data it was found that a better match to experimental data was achieved if a reduction of 2 percent in gas loading from the nominal value was assumed. This tolerance is within the accuracy to which the pipe was filled and thus is not felt to be a discrepancy between analysis and flight data. When the nominal value of gas loading was used in the analytical model the results indicated that the pipe would never turn on.

Because a hot, non-wicked reservoir is utilized in this design, the partial pressure of vapor in the reservoir is established by diffusion of vapor through the gas tube between the reservoir and cold trap section of the condenser. The ramifications of this phenomenon were studied in detail and reported in an earlier publication, Reference 2.5. Reservoir working-fluid partial pressure has a significant effect on heat-pipe control characteristics since any vapor in the reservoir displaces control gas into the condenser. Under steady-state conditions, the partial pressure of vapor in the reservoir would become equal to the partial pressure at the end of the wicked portion of the condenser, the cold-trap region in this case. However, during the OAO-3 flight, the sink temperature is changing throughout the orbit and steady-state conditions are not realized.

Figure 2-11 shows analytical predictions of cold-trap and reservoir partial pressures for a typical full orbit. The effect of the diffusion is to damp fluctuations in the reservoir vapor pressure and to cause a time delay between cold-trap and reservoir vapor-pressure peaks. The 13-minute time delay shown in Figure 2-11 reflects this diffusion phenomenon as well as variations in total heat-pipe pressure due to evaporator temperature changes. Clearly, diffusion dynamics must be considered to accurately predict transient performance of hot-reservoir heat pipes.

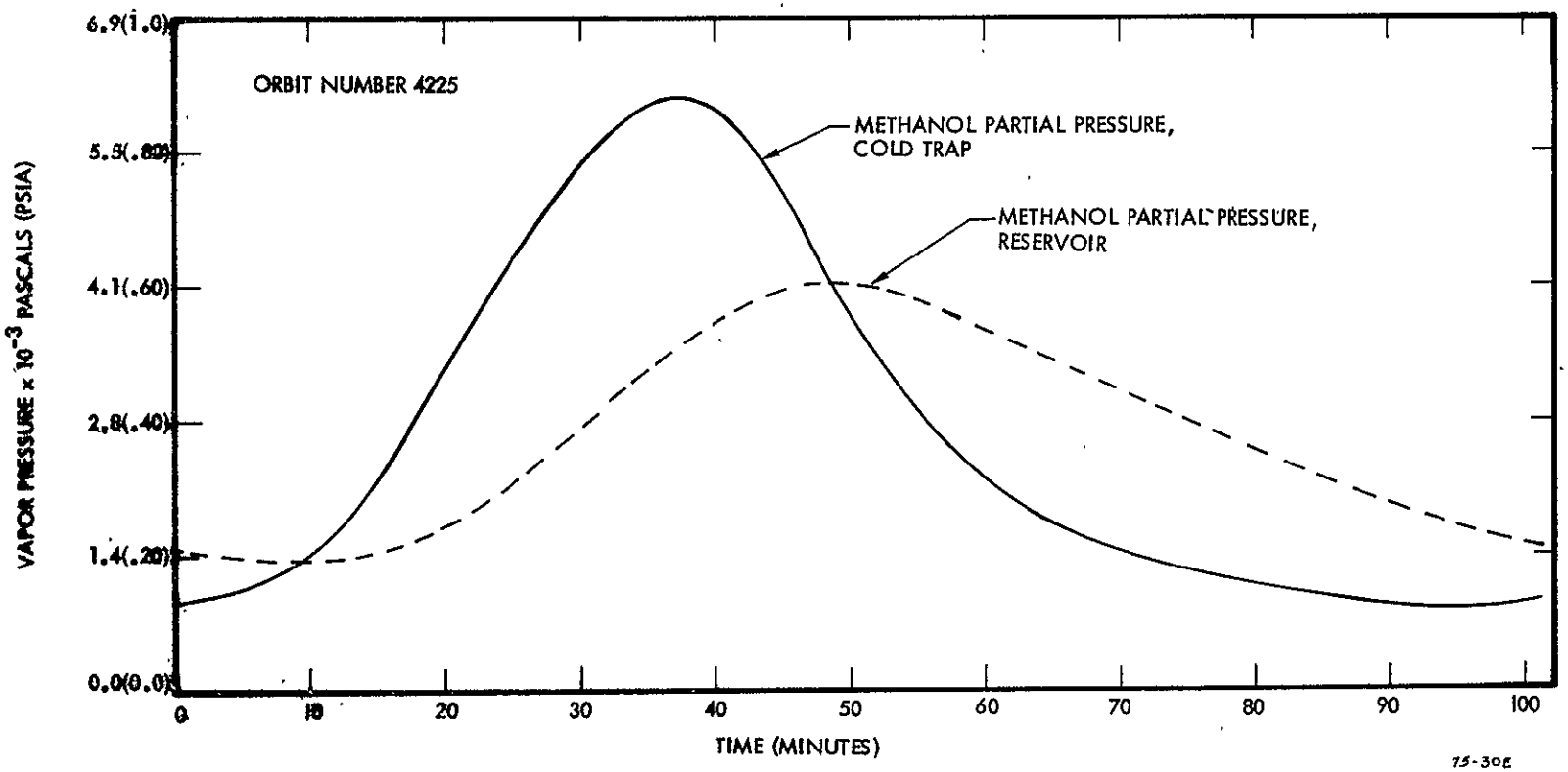

Figure 2-11. Methanol Vapor Partial Pressure Profile.

2.5 PREDICTED PERFORMANCE WITHOUT HEAT PIPE AND AT HIGHER POWER LEVELS

The analytical model was next modified to eliminate the heat-pipe function, and comparisons were made with the system having an operating heat pipe. Table 2.3 shows OBP platform orbital-average-temperature data compared with analytical predictions with a non-operating heat pipe (all conductors between vapor and condenser wall set equal to zero).

Table 2.3. Comparison of Results With And Without Heat Pipe

Orbit Number	% Sun Time	OBP Platform Average Temperature	
		Heat Pipe (°C) Operative	Heat Pipe (°C) Non-Operative
420	65.0	20	22
1592	69.0	21	23
4225	81.0	22	26
17350	79.0	25	44
17370	79.0	31	58 (Est.)
17387	78.0	41	71 (Est.)

Differences in OBP heat-sink temperatures with and without the heat pipe are quite small

of the heat is transferred by the radiation path with very little energy being carried by the heat pipe. The effect of the heat pipe is to reduce fluctuations in temperature due to changing sink conditions by about 2°C.

At higher power levels the effect of the heat pipe in stabilizing OBP platform temperatures is more dramatic. Figure 2-12 shows calculated control characteristics for OBP dissipations between 10 and 30 watts. The heat pipe reduces the predicted temperature variation of the OBP platform from a value of 18°C to 4°C for the same 20-watt dissipation range.

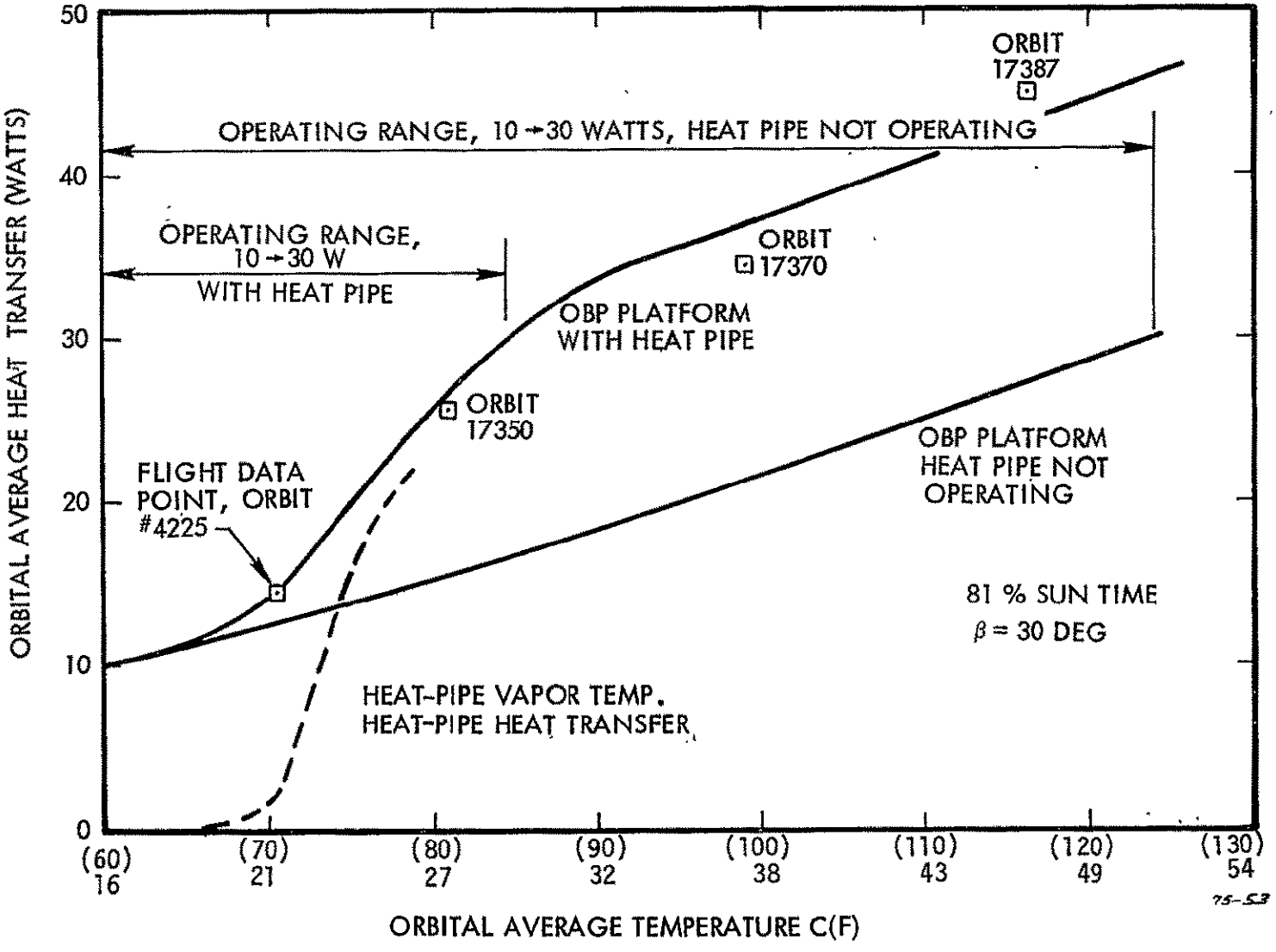

Figure 2-12. Analytical Predictions of AHPE Control Characteristics.

Design goal for the heat-pipe evaporator was 17 ± 3C for heat pipe energy rates between 2 and 20 watts for the predicted radiator sink range of -52C to -19C. Of this 6°C temperature range, 3°C is due to the variation in sink conditions. Therefore, for a given sink condition, the variation in evaporator temperature for heat rates between 2 and 22 watts should be 3°C with a maximum temperature of 20C at 22 watts and a -19C sink condition. The predictions shown in Figure 2-12 are for orbital conditions near the maximum sink conditions and should thus result in an evaporator temperature range of about 17C to 20C for a 2- to 22-watt heat-pipe power variation. However, the actual predicted range is 21C to 26C, which can be explained as follows.

This discrepancy is believed to be primarily due to sink-temperature effects. First, the actual orbital-average sink temperature for this condition as derived from flight data is approximately 9C as compared to the design maximum value of -19C. This can be expected to cause an increase in operating temperature since more of the heat-pipe condenser must be active for a given amount of heat rejection. This requires a higher evaporator temperature. Also, the higher sink temperature results in a higher gas temperature and vapor pressure in the reservoir, further increasing the required operating temperature for a given heat rate. It is estimated that the effect of increasing the average sink temperature to 9C is to raise the evaporator operating temperature to about 23C at 22 watts which would only account for one-half the discrepancy.

Sink temperatures specified for design of the heat pipe were based on orbital-average heat rates. Using an orbital average would also be expected to result in an increased operating temperature when the system operates under actual orbital fluctuations. This is because the variation of vapor pressure with temperature is extremely non-linear. Thus, orbital-average reservoir vapor pressure will corespond to a higher temperature than the orbital-average sink temperature based on environmental heating. The net result will be for a higher heat-pipe evaporator temperature being required when the system is exposed to the actual fluctuating sink conditions. Effect of the actual variable sink conditions as compared with an average value of -9C is estimated to raise the evaporator operating temperature an additional 2 to 3C.

2.6 FLIGHT TEST USING ON-BOARD HEATERS

Between orbits 14462 and 14482 on-board heaters were exercised in an attempt to obtain flight data at higher powers to correlate the analytical data in Figure 2-12. Results are shown in Figure 2-13. At orbit number 14462 the 10 watt flight heater was turned on. Up until this time, without the heater, the OBP platform temperature was about 19C which correlates well with the 65%-sun-time prediction of 19.7C.

The 10-watt increase in dissipation caused an increase in OBP platform temperature of about 6°C to 25C. Steady-state conditions appeared to have occurred after orbit number 14468. Referring to Figure 2-12, it can be seen that the analytical prediction for a power increase of 10 watts is a 5°C rise in OBP platform temperature. Until orbit number 14473, it could be concluded that the AHPE was operating in close agreement with prediction. However, at orbit 14474 the platform and heat-pipe temperatures started to rise. These temperatures were still increasing when the 20-watt heater was turned on at orbit 14480 and when the test was terminated at orbit 14482. When the heaters were turned off, the system recovered such that platform temperatures of approximately 21C were reached after about 30 orbits.

The cause of the increase in temperatures between orbits 14473 and 14480 has not been explained. It does not appear to be a heat pipe failure since the difference between evaporator and condenser temperatures remains fairly small. The on-board heater tests were repeated between orbits 17338 and 17400. Results are shown in Figure 2-14. The data show that no high-temperature anomaly occurred as in the previous test. The system was able to reject a total of approximately 44 watts (30 watts heater and 14 watts OBP) and the OBP temperatures correspond closely to those predicted in Figure 2-12. After the heater shutoff, the OBP temperature came down to its normal operating temperature in about 22 hours.

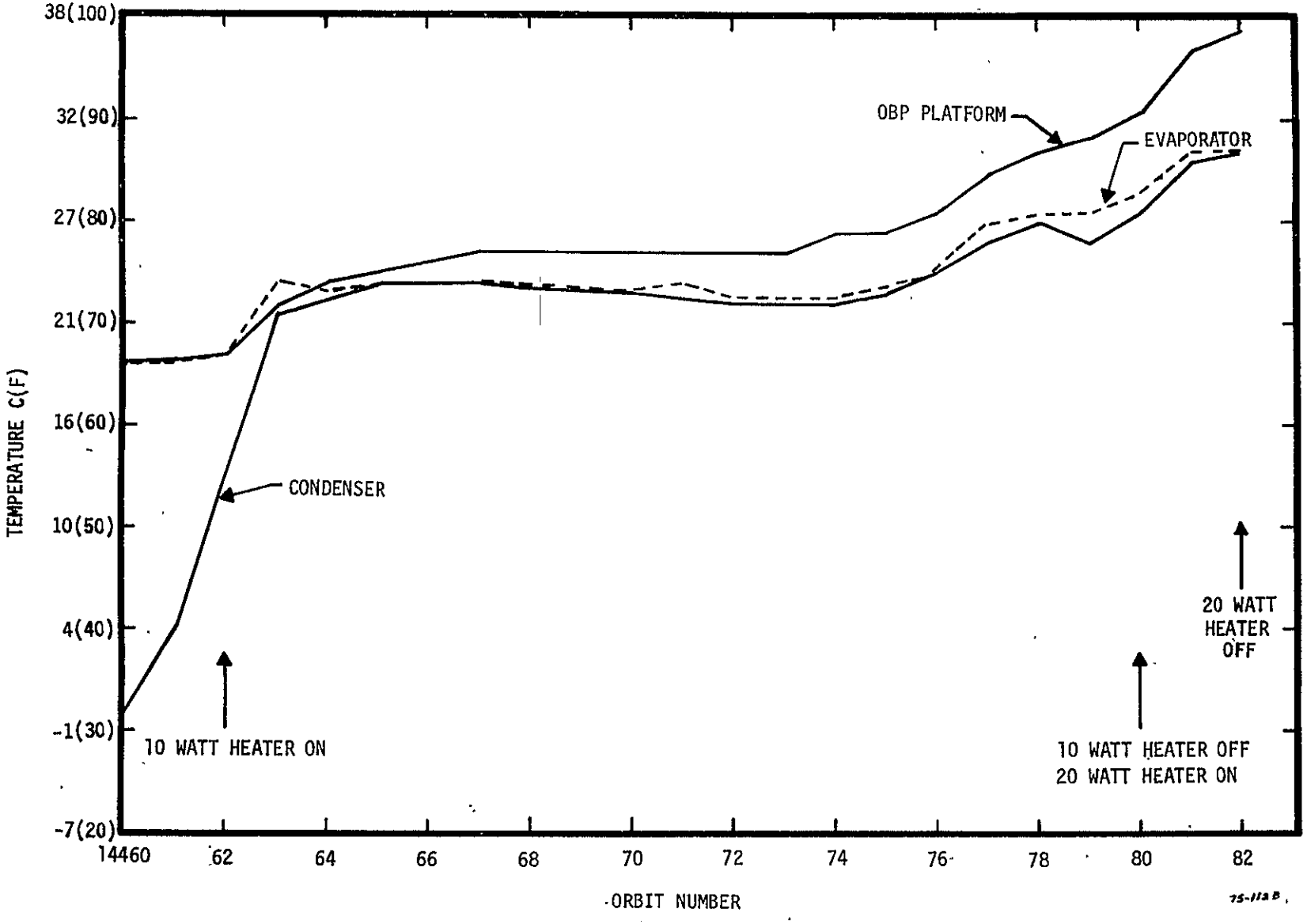

Figure 2-13. AHPE Flight Test Results.

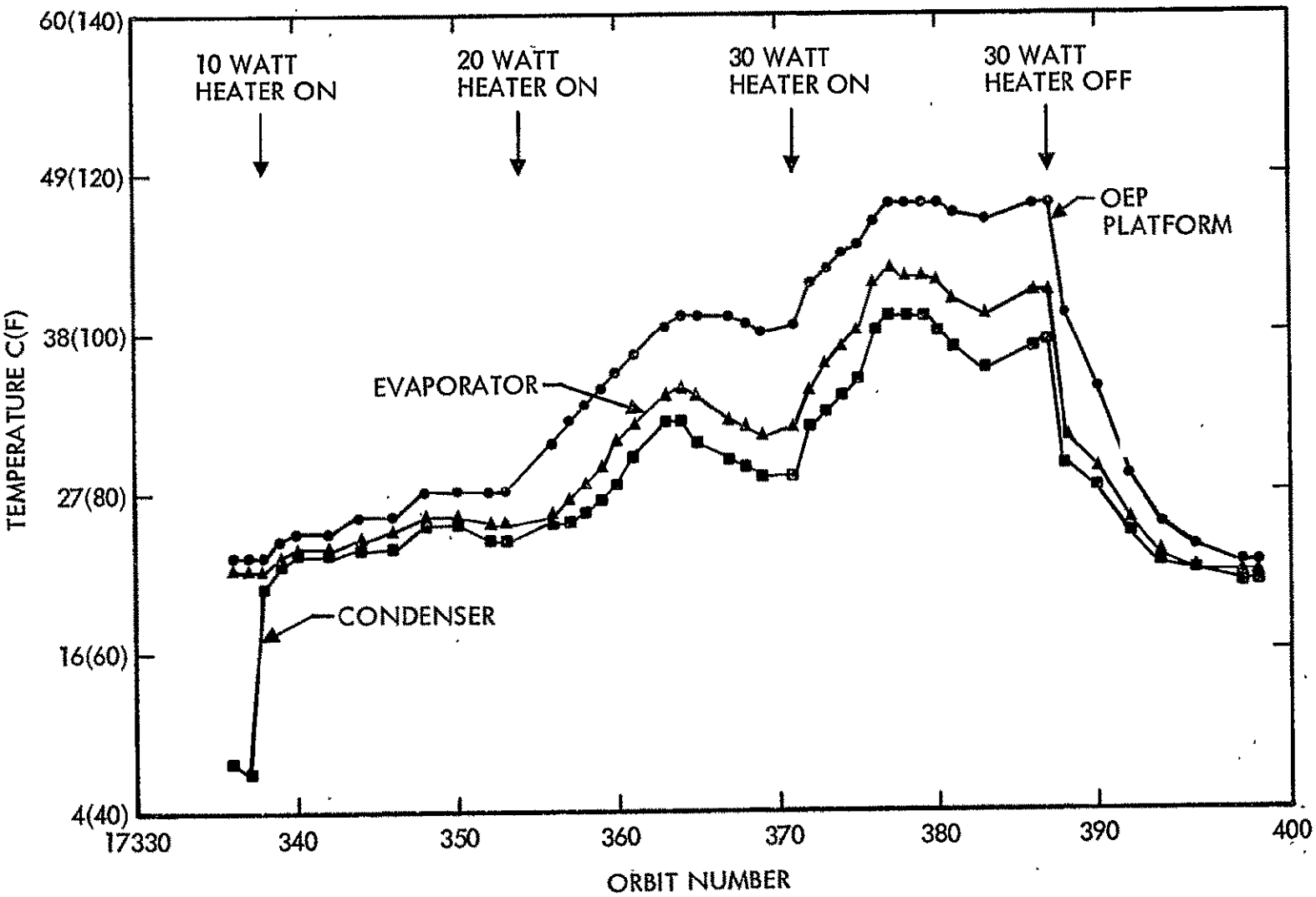

Figure 2-14. AHPE Flight Test Results

2.7 DISCUSSION AND CONCLUSIONS

The principal conclusions of this study are that gas-controlled, variable-conductance heat pipes can perform reliably in the space environment for long periods of time (3-1/2 years to-date) and can effectively provide temperature stabilization for spacecraft electronics which have wide variations in power dissipations and/or thermal boundary conditions. Very little (if any) degradation in performance of the system was detected during the more than two-year period for which data were evaluated. Effect of the VCHP is to reduce a potential temperature variation of 36°C due to a heat-dissipation range of 20 watts down to13°C. Variation in the OBP temperature due to environmental changes was only about 2°C in this application.

Performance of the VCHP system can be accurately predicted by an analytical model consisting of a nodalized network coupled with a subroutine to calculate location of gas front in the condenser. Diffusion-dynamic effects must be considered when calculating the gas-front location in this case where a hot gas reservoir is utilized and boundary conditions are changing.

Under normal OBP-power dissipation, the heat pipe turn-on turn-off characteristics are determined by the variations in sink conditions over the orbit. Turn-on of the pipe coincides with a decrease in cold-trap temperature and hence a decrease in reservoir methanol vapor pressure (lagging somewhat because of diffusion effects) and turn-off occurs when the cold-trap temperature rises. The analytical model was able to predict this phenomenon.

2.8 REFERENCES

2.1 Kirkpatrick, J. P., and Marcus, B. D., "A Variable-Conductance Heat Pipe Flight Experiment," AIAA Paper 71-411, April 1971.

2.2 Marcus, B. D., "Ames Heat-Pipe Experiment (AHPE) Experiment Description Document," NASA Contract No. NAS2-5503, January 1972.

2.3 Smith, J. P., "SINDA User's Manual," NASA Contract No. 9-10435, April 1971.

2.4 Fleischman, G. L., and Wanous, D. J., "Active Control Heat Pipe Performance for Long Life Battery Cooling," ASME Paper 72-WA/HT-43, November 1972.

2.5 Marcus, B. D., and Fleischman, G. L., "Steady State and Transient Performance of Hot Reservoir Gas-Controlled Heat Pipes," ASME Paper 70-HT/SPT-11, March 1970.

2.6 Wanous, D. J., Marcus, B. D., and Kirkpatrick, J. P., "A Variable Conductance Heat Pipe Flight Experiment: Performance in Space, "AIAA Paper No. 75-725.

3.0 DEVELOPMENT OF VAPOR MODULATION AS A CONTROL MECHANISM

Of the various mechanisms for achieving variable conductance of a heat pipe, the one currently in widest use is blockage of the condenser with noncondensable gas. This mechanism, however, has drawbacks under certain conditions often encountered in spacecraft applications. For example, with a passive heat pipe, that is, without the use of a feedback-controlled reservoir heater, close temperature control of the heat source is impossible when the sink temperature varies not far below the source temperature. When close control is required, active feedback control must be used. In some applications, however, electrical power for the reservoir heaters is unavailable. Two alternative conductance-control mechanisms based on modulating the vapor flow overcome these drawbacks. Although their principles of operation are basically different, both mechanisms utilize a vapor-flow throttling valve activated by liquid expansion in a sensor volume that is in thermal contact with the heat source. Thus close feedback control is achieved without electrical power. In addition, the vapor-modulated control mechanisms are inherently insensitive to sink temperature variations even when the sink temperature approaches that of the source. Other advantages are that no bulky gas reservoirs are needed and no special design of the heat sink is required to minimize axial conduction as is often the case with gas-controlled heat pipes.

The present contract calls for development of flight-type prototype vapor-modulated heat pipes, first for a moderate-heat-load requirement of approximately 20 watts, then for a high-heat-load requirement of 100 watts. The following sections describe these efforts.

3.1 VARIABLE CONDUCTANCE BY CONTROL OF THE VAPOR FLOW RATE

The first of the two mechanisms for achieving variable conductance by vapor-flow modulation is illustrated in Figure 3-1. In this configuration the sensor volume is inside the evaporator and controls the temperature of the vapor. A configuration with an external sensor volume that controls the heat-source temperature is also possible. The pressure difference

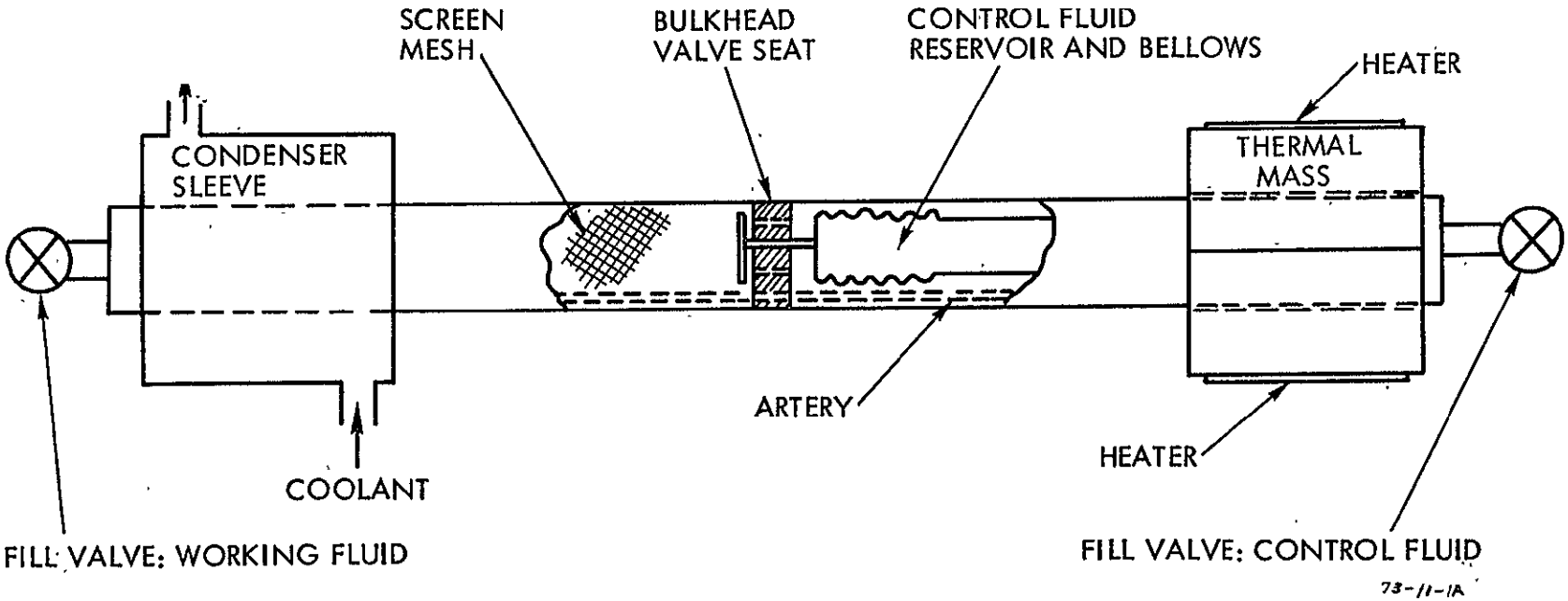

Figure 3-1. Vapor-Modulated Heat Pipe With Control Achieved by Vapor-Flow-Rate Control.

that drives the flow through the valve is provided by the difference in saturation pressures in the evaporator and condenser regions. The valve is actuated by expansion of liquid in the sensor volume in such a way that the valve's opening is proportional to the deviation of the heat-source temperature from the set-point temperature. Thus, the source seeks a temperature close to the set point such that the latent-heat transport through the valve exactly matches the rate of heat from the source. If, for example, the source heating rate suddenly increases, at first the latent-heat transport is insufficient to prevent the source from rising in temperature. As it does so, the valve opens until the latent-heat transport again matches the source heating rate,and the source temperature stabilizes at a slightly higher level. As another example, consider the effect of a sudden decrease in the sink temperature. If the flow through the valve is choked, which occurs if the ratio of condenser to evaporator saturation pressures is below the critical value, the decrease will not affect the source temperature. If, on the other hand, the flow is not choked, then the decrease in sink temperature temporarily increases the latent-heat transport above the source heating rate. The result is a slight drop in source temperature, and the valve closes until the latent-heat transport again matches the source rate. A water/monel heat pipe of the type describedwas developed on a previous contract, Reference 3.1. It demonstrated good control characteristics with control range of 2.2°C for large variations in sink temperature and heat load.

The primary limitation of vapor-flow-rate control is that the maximum temperature difference that can be sustained between the source and the sink is set by the capillary-pressure limit of the wick. The vapor-liquid pressure difference that the wick structure must sustain includes the pressure drop across the valve in addition to the usual liquid-flow pressure drop in the wick. Once the wick's limit is exceeded, vapor "blows thru" where the wick penetrates the valve bulkhead. Table 3.1 gives the pore size of the wick required to prevent blow-thru when the condenser side is 220 K and the evaporator side is 294 K. With the exception of water, the fluid/wick combinations listed have low transport capacities. Unfortunately, water must be ruled out for the often occurring applications where the condenser side falls below 273 K because the water

Table 3.1. Fluid-Wick Combinations for Vapor-Flow Control

FLUID	VAPOR PRESSURE AT 294K	WICK PORE DIAMETER TO PREVENT BLOW-THRU*	HEAT PIPE FIG. OF MERIT	FREEZING TEMP.
Ammonia	6720 torr	1.44×10^{-5} cm	70×10^{9} w/m^2	195K
Methanol	100.8	0.00067	37×10^{9}	175
Water	18.97	0.01146	180×10^{9}	273
Isopropyl Alcohol	32.88	0.00198	5.26×10^{9}	187
Isobutyl Alcohol	9.28	0.00688	3.03×10^{9}	165
Isoamyl Alcohol	2.509	0.0279	2.85×10^{9}	156
Octane	10.71	0.00609	10.15×10^{9}	216
Nonane	3.46	0.0177	7.47×10^{9}	219

*Evaporator Temperature = 294K, Condenser Temperature = 220K.

would freeze in the condenser and be unavailable for return to the evaporator.

Two approaches can be taken to increase capacity. First, as illustrated in Figure 3-1, an artery can be used. However, entrappment of an arterial bubble of residual noncondensable gas during priming is a problem. Priming foils (Reference 3.2) offer a practical solution only for pore sizes down to approximately 0.013 cm. For smaller pores, the foil must be impractically thin. A second approach to increase capacity is to make the vapor-modulated heat pipe as short as possible and use it as a variable-conductance coupler between two conventional heat pipes. An increased overall temperature drop in the full-on condition is incurred, however, because of the additional evaporation and condensation processes.

3.2 VARIABLE CONDUCTANCE BY INDUCED WICK/GROOVE DRY-OUT

An alternative mechanism for achieving variable conductance by vapor modulation is not limited by vapor blow-thru. Consider the double heat-pipe configuration illustrated in Figure 3-2(a). If the source temperature falls slightly below the set point due to either a decrease in heat load or a drop in sink temperature, the valve closes and the increased pressure drop is imposed on the groove/wick structure, which then begins to empty. Regions of the evaporative interface between the two pipes dry out and the overall thermal resistance of the system increases. Conversely, if the source temperature rises slightly above the set point, the valve opens which relieves the pressure and allows the dried-out regions to rewet. Thus, this induced dry-out mechanism establishes a temperature drop across the interface that accounts for the temperature difference between the set point and the sink.

Other mechanisms that have been proposed for achieving dry-out control are throttling the liquid return or interrupting the wick. The vapor-modulated induced-dry-out mechanism, however, has a crucial advantage. When the valve closes and the pressure builds up, the wick structure empties by the liquid flowing out of it to the other side of the bulkhead. This occurs rapidly. On the other hand, when dry-out is achieved by throttling the liquid return or interrupting the wick, the wick structure

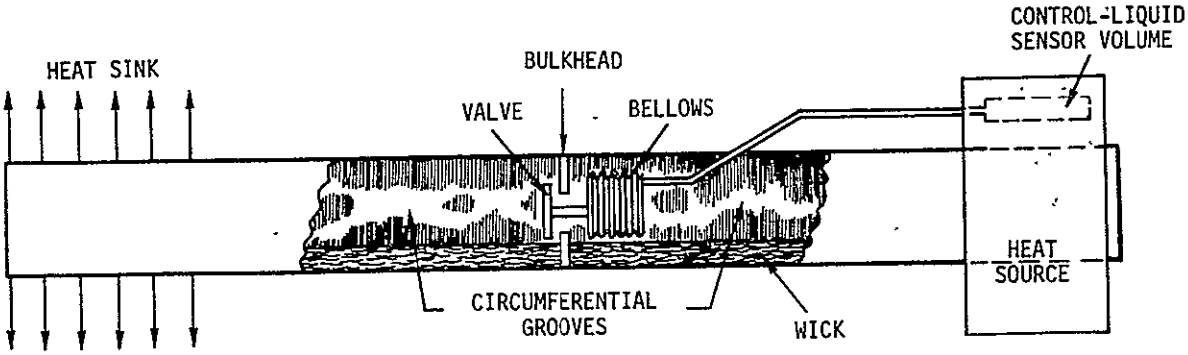

(a) SINGLE-HEAT-PIPE CONFIGURATION.

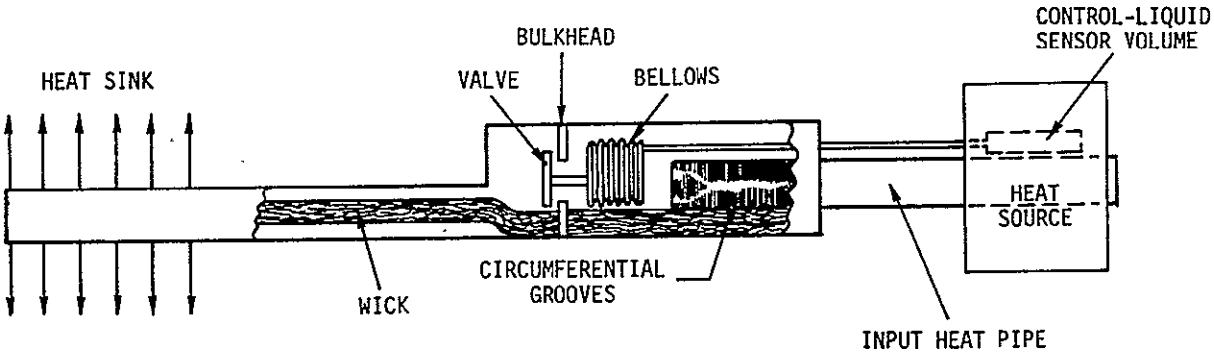

(b) DOUBLE-HEAT-PIPE CONFIGURATION.

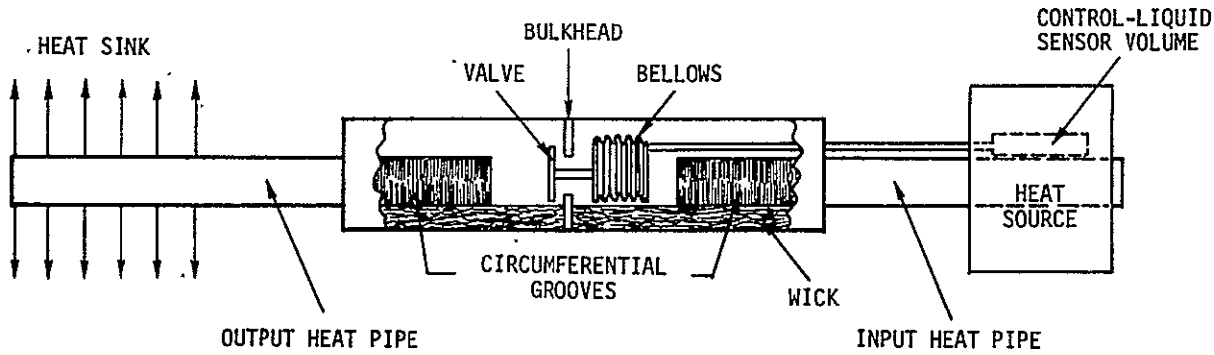

(c) TRIPLE-HEAT-PIPE CONFIGURATION.

Figure 3-2. Vapor Modulated Heat Pipe Based on Induced Wick/Groove Dry Out

empties by evaporation. This takes a long time especially when the source is turned down to a very low heat-rejection rate and large temperature undershoots can be expected.

3.2.1 Design Features of the Induced-Dry-Out Mechanism

Although a double-heat-pipe configuration is shown in Figure 3-2(b), single- and triple-pipe configurations are also possible [Figure 3-2(a) and (c)]. With the single heat pipe, the valve induces partial dry-out in the evaporator which can result in a severely nonuniform temperature distribution. On the other hand, it has the lowest overall thermal resistance with the valve fully open and hence, the single-pipe configuration can maintain temperature control of the source for a higher sink temperature than the other configurations. The multi-heat-pipe configurations have the advantage of maintaining a uniform temperature distribution of the source. Also, there is generally less wick to reprime after the valve opens and, hence, the response is faster with less overshoot. For each configuration, the heat-transport capacity is limited by the wick's ability to reprime under load when the valve is fully open. The three-heat-pipe configuration, which consists of two conventional heat pipes coupled by a short vapor-modulated variable-conductance heat pipe, has the highest capacity, although also the highest open-valve thermal resistance.

To ensure that the grooves and wick completely dry out when the valve is closed, the wick is separated where it penetrates the valve bulkhead by a short segment of porous material of a much smaller effective pore size than the wick or grooves. Once blow-thru has occurred and before the pressure difference across the bulkhead has reduced sufficiently for the grooves and wick to reprime, the capillary barrier will re-establish itself.

3.2.2 Advantages of the Induced-Dry-Out Mechanism

The primary advantage of the induced-dry-out over vapor-flow control is that blow-thru is not a limitation and therefore there is no restriction to very-low-pressure fluids. Ammonia and methanol, which both have good heat-transport capabilities and low freezing points, can be used. Another advantage is high thermal resistance in shut-down operation. With the groove/wick structure completely dried out, the heat-leak path is down

the tube wall that surrounds the dried out region. The vapor-flow control mechanism, on the other hand, leaks heat directly across the valve bulkhead. Therefore, with the dry-out mechanism, control of the source temperature can be maintained for much lower source heating rates.

3.3 DEVELOPMENT OF A MODERATE-CAPACITY PROTOTYPE VAPOR-MODULATED HEAT PIPE

The first development was a prototype heat pipe for a typical spacecraft application with heat loads up to 20 watts, a set-point temperature of 294 K, and a sink that varies from 220 K to nearly as high as the set point. The first design considered was based on vapor-flow control. Although it was eventually abandoned, we briefly discuss it here because it led to the induced dry-out mechanism. The design began with a search for the best working fluid. The properties sought were:

- Freezing point below 220 K
- Practical wick pore size (>0.01 cm) that will prevent blow-thru in the cold-sink conditions
- Highest possible figure of merit.

Referring to Table 3.1, we see that nonane is the best candidate. Its figure of merit is low, though, so a three-heat-pipe system was selected. Nonane would be used only in a 20-cm-long vapor-modulated coupling section. X-13 felt metal was selected as the wick, and its capacity with nonane predicted to be 7.47 watt-m (294 watt-in) per square cm of wick area. To attain a capacity of 20 watts with an adequate safety margin, the cross-sectional area was taken as 0.90 cm^2. Some increase in performance is attained by shunting the wick on the condenser side of the bulkhead with open-ended screen tubes.

The capacity prediction for X-13 metal felt and nonane was verified with the test of a simple circumferentially grooved, slab-wick heat pipe. Although the measured axial transport of the wick agreed with theory, the circumferential grooves (40/cm) dried out. Clearly, the capillary limit of the grooves was far lower than the wick. Much finer grooves could be fabricated for the actual heat pipe, and predictions showed the performance of the finer grooves would be marginal with the valve fully open. With the

valve partially closed, however, the grooves would not function because of the increased capillary load imposed by the pressure drop across the valve. This was of concern until we realized that the temperature drop associated with groove failure reduces the difference in saturation pressure across either side of the valve and hence contributes to the reduction of latent-heat transfer through it. Thus, groove dry-out enhances the control. It was then realized that vapor-flow control was not needed at all if one designed for both groove and wick dry-out when the valve closed. Because of nonane's marginal open-valve groove perfor mance, it was decided to switch to a methanol heat pipe with the new control mechanism.

The design of the heat pipe that was fabricated and tested is shown in SK740903 (pg.136) in Appendix B. The most important features of the design, the bellows/valve subassembly and the wick feed-through, are discussed below.

3.3.1 The Bellows/Valve Subassembly

The bellows/valve subassembly is shown in SK740907 (pg.142) and also in the photograph of Figure 3-3. The bellows is welded into a can, thus the control fluid is on the outside of the bellows and compresses it upon expansion. The can is held in place by three posts that also serve as valve guides. The valve is held in place by the conical return spring. The valve stem is not connected to the bellows so in the closed position the spring causes automatic alignment.

The sensor volume is shown in SK750310E (pg.153). A bellows is welded into the end of it, and the extension of the bellows is adjusted with a screw to provide convenient set-point adjustment. The sensor volume contains 2.2 cm^3 of control liquid. Perfluoropentane was selected because of its high coefficient of thermal expansion ($2.06 \times 10^{-3}/°C$). The displacement ΔX of the valve for a temperature change ΔT of the control liquid in the reservoir of volume V_ℓ is given by

$$\Delta X/\Delta T = \beta/(A/V_\ell + \alpha K/A) = 0.141 \text{ mm/°C}$$

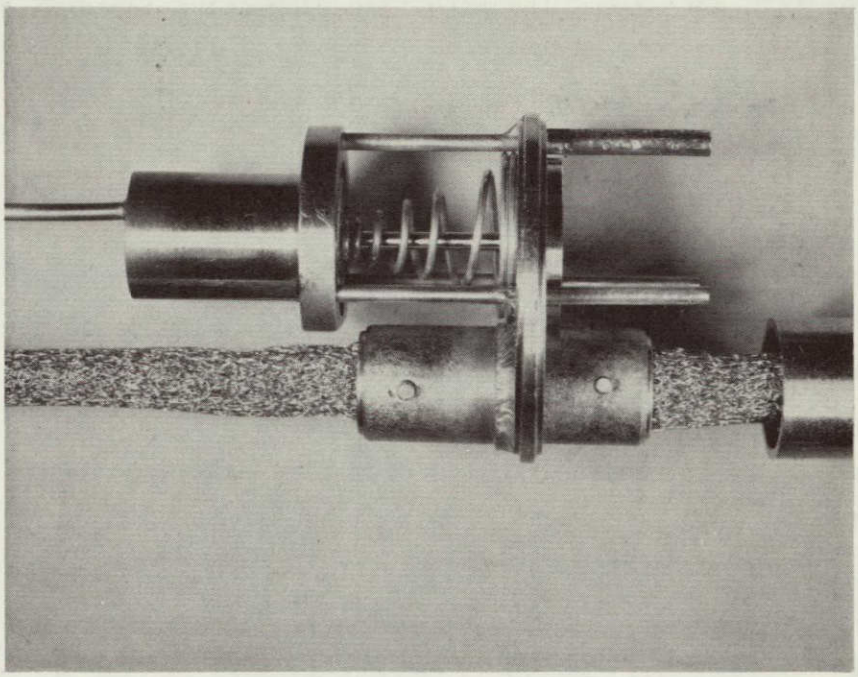

Figure 3-3. Bellows/Valve Subassembly and the Wick Feed-Thru for the Moderate Capacity Heat Pipe.

where

β = 2.06×10^{-3}/°C at 25°C is the thermal expansion coefficient

A = 0.316 cm^2 is the effective area of the bellows

K = 23.3 N/cm is the spring constant of the system and

α = 3.24×10^{-5} cm^2/N is the compressibility at 25°C.

The pressure drop ΔP across the valve is derived from the model depicted in Figure 3-4. The resulting expression in terms of the heat transfer rate $\dot{Q}$, latent heat h_{fg}, vapor density ρ, valve diameter D, valve opening ΔX and contraction coefficient C_c is

$$\Delta P = \frac{1}{2\rho} \left[\frac{\dot{Q}}{h_{fg}\pi D \Delta X C_c}\right]^2 \qquad [3.1]$$

For methanol at 294 K and for a heat-transfer rate of 50 watts, we find that the pressure drop is approximately 1 mm of methanol for a valve opening of 0.75 mm. We take this as the fully open displacement, since 1 mm of methanol is small compared to the capillary pressure generated by the wick and grooves. The valve goes from completely closed to fully open when the sensor-volume temperature increases 5.3°C. This temperature excursion is then the approximate control range of the heat pipe. The bellows is protected from damage due to liquid expansion for temperatures above the set point. For example, the valve opening at 30°C above the set point is 4.23 mm, at which point the bellows is still not bottomed out.

3.3.2 The Wick Feed-Thru

The wick feed-thru is shown in the subassembly drawing SK740910 (pg. 145) and also the photograph of Figure 3-3. The capillary barrier consists of two layers of 250-mesh stainless-steel screen, which is sintered between two tubes. This sintered assembly is welded into a hole in the bulkhead. The two ends of the wick are formed into a round cross-section and pinned into the two wick clamps. The wick is cut square, pressed against the capillary screen and pinned in place. A disc of X-7 stainless-steel felt metal 0.254-mm thick was placed inside the wick tunnel on each side of the screen when cracks in the screen were found after the wick tunnel was welded into the bulkhead.

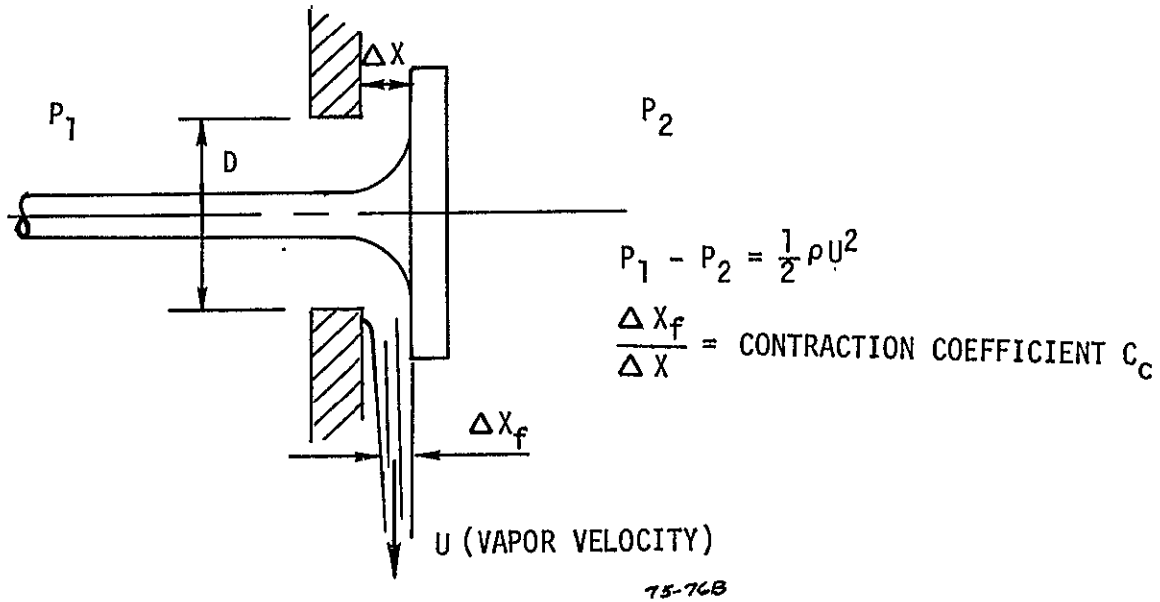

Figure 3-4. Model for Calculating Pressure Drop Across Valve.

3.3.3 Test Results

The heat pipe was instrumented with thermocouples as shown in SK750324E (pg.135). The condenser was clamped to a cold plate with saddle blocks. The evaporator and sensor volume were clamped between two aluminum blocks having double saddles. Strip heaters were used on the outside of these blocks. To simulate a thermal resistance between a heat pipe and the equipment whose temperature is being controlled, 0.15 mm of Teflon were used between the heat pipe and the heater blocks. The sensor volume, on the other hand, was thermally close-coupled to the heater blocks with RTV.

The test demonstrated the functioning of the induced-dry-out mechanism, however, the overall performance fell short of the goals. The development of this heat pipe was nevertheless essential for pointing out design features that must be incorporated into a high-performance version.

The steady-state performance is displayed in Figure 3-5 where the temperature distribution along the heat pipe is shown with a 10-watt load and three different sink temperatures. In curve (a), the sink is above the set point and the valve is fully open. The overall open-valve temperature drop between the vapor temperature of the input and output heat pipes corresponds to an average heat-transfer coefficient of 6800 watt/m^2-°C (1200 BTU/hr-ft^2-F) for condensation and evaporation at the interface, which is an exceptionally good value for methanol and stainless steel. The heat pipe was practically free of noncondensable gas when the data for curve (a) were taken.

Curves (b) and (c) show temperature distributions with the sink below the set point. The valve has partially closed and the induced dry out maintains the source temperature relatively stable. A portion of the overall temperature drop is due to noncondensable gas blockage of the condenser. Gas generation is attributed to the fact that the heat pipe was not vacuum-fired at a high temperature (980C), which is part of our normal cleaning procedure for methanol/stainless-steel heat pipes. The vacuum firing was eliminated so the bellows and valve-return spring would not anneal. Subsequent to testing, the heat pipe was run continuously at 38C, generation went to completion, and the gas was vented from the pipe.

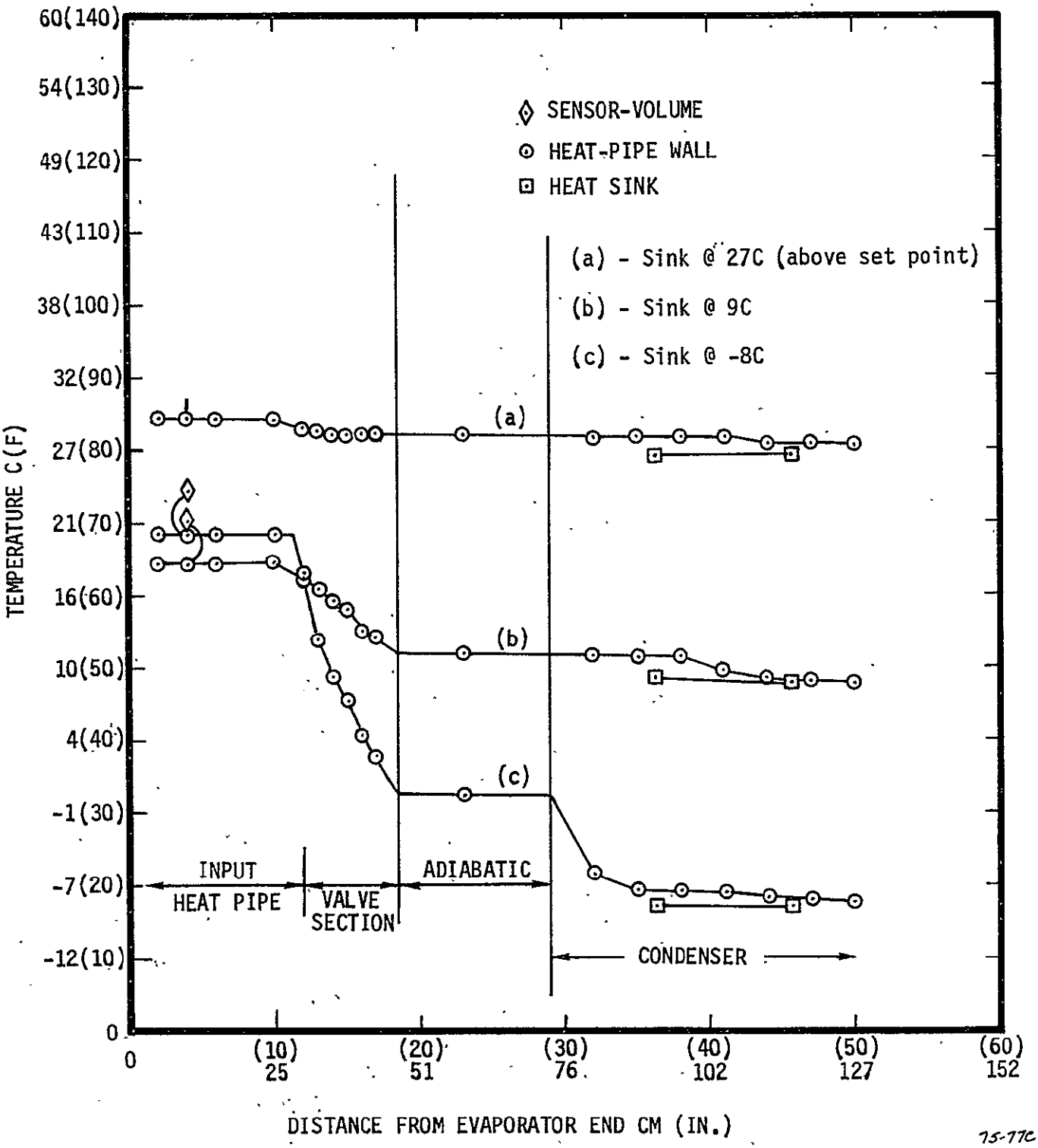

75-77C

Figure 3-5. Temperature Distribution Along Heat Pipe.

A peculiar control characteristic of this heat pipe is that the source temperature increases with decreasing sink temperature. Figure 3-6 displays this dependence. There are three contributing factors. The primary factor is that when the valve shuts down, the bellows temperature is set by conduction to approximately the vapor temperature in the output heat pipe. The volume of control liquid surrounding the bellows is significant (approximately 0.56 cm^3). Its contraction as the sink temperature falls must be compensated for by expansion of control fluid in the sensor volume. The required source temperature increase is approximately 0.28 C per °C drop in sink temperature, which is shown by the dashed line in Figure 3-6. The second factor is that as the sink temperature is lowered, the figure of merit for methanol degrades which results in a contribution to dry-out from the increased liquid-flow pressure drop in the wick. The third factor is that for a fixed heat-transport rate, a decrease in the vapor temperature, and hence vapor density of the output heat pipe results in an increased pressure drop across the valve. This increased drop is relieved by the source rising in temperature and opening the valve.

The dependence of source temperature on heat-transport rate is displayed in Figure 3-7. The increase in source temperature is greatly in excess of what one would expect solely from the induced-dry-out control mechanism. The liquid pressure drop in the wick, which increases proportionally to the heat-transport rate, is the other contributing factor. The fact that the effect is so large is because the output heat pipe is operating close to the repriming limit of the wick.

To find the open-valve capacity of the output heat pipe, the temperature of the source was maintained at 38C by adjusting the sink, which assures that the valve remains open. As shown in Figure 3-8, the heat input was increased in 5-watt increments until the temperature difference between the vapor in the input and output heat pipes increased markedly which defines failure of the saturated wick. The heat input was then decreased in 5-watt increments until the heat pipe recovered, which did not occur until the power was reduced to 10 watts. This result is in line with the hysteresis behavior of fibrous wicks, that is, the capillary-pressure

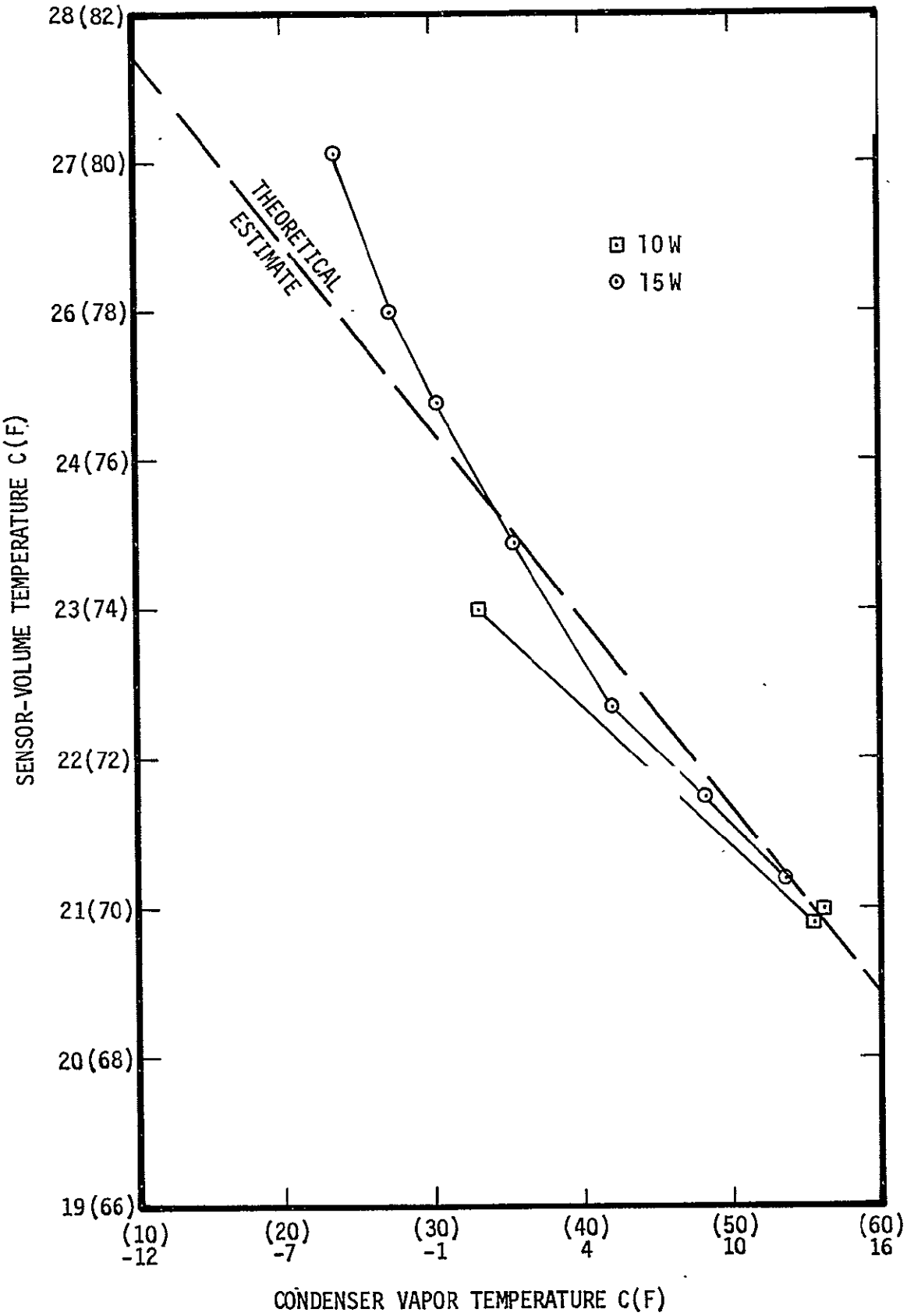

Figure 3-6. Effect of Condenser Heat-Pipe Vapor Temperature on Set Point.

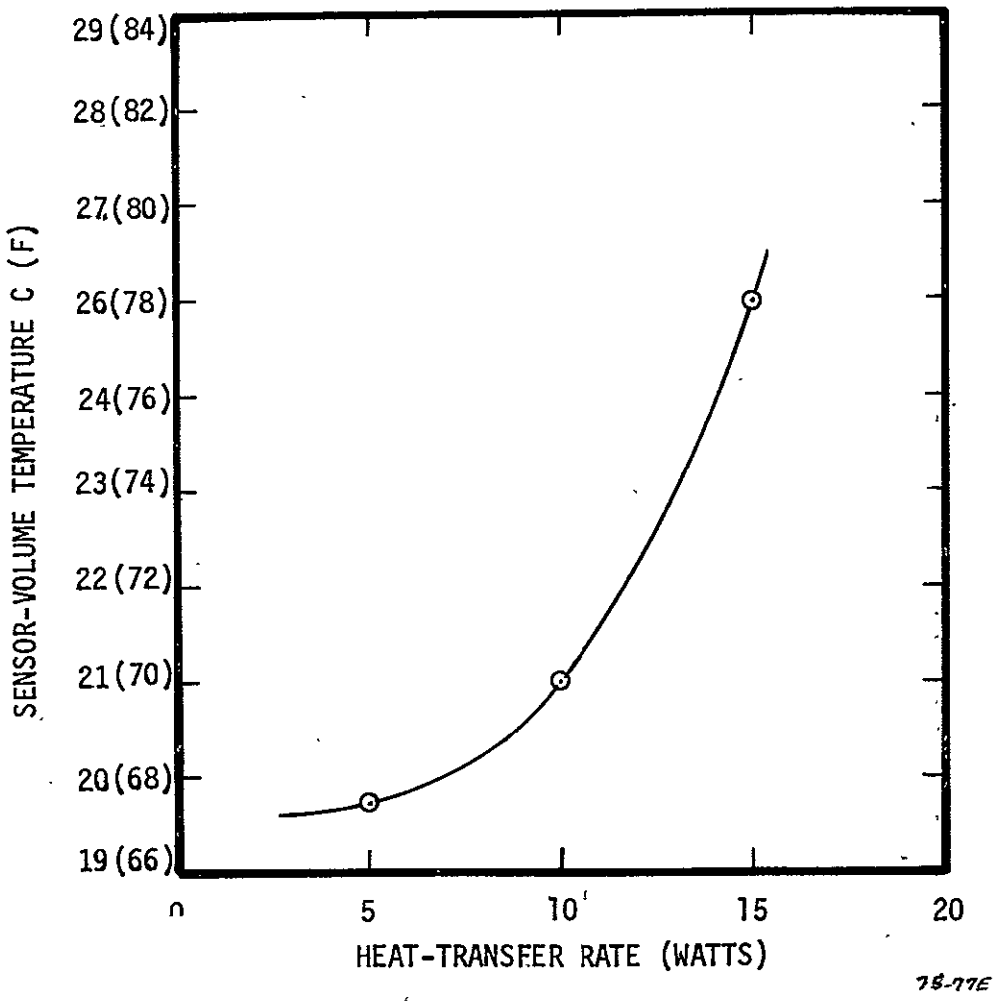

Figure 3-7. Set Point as Function of Load for 4C Sink.

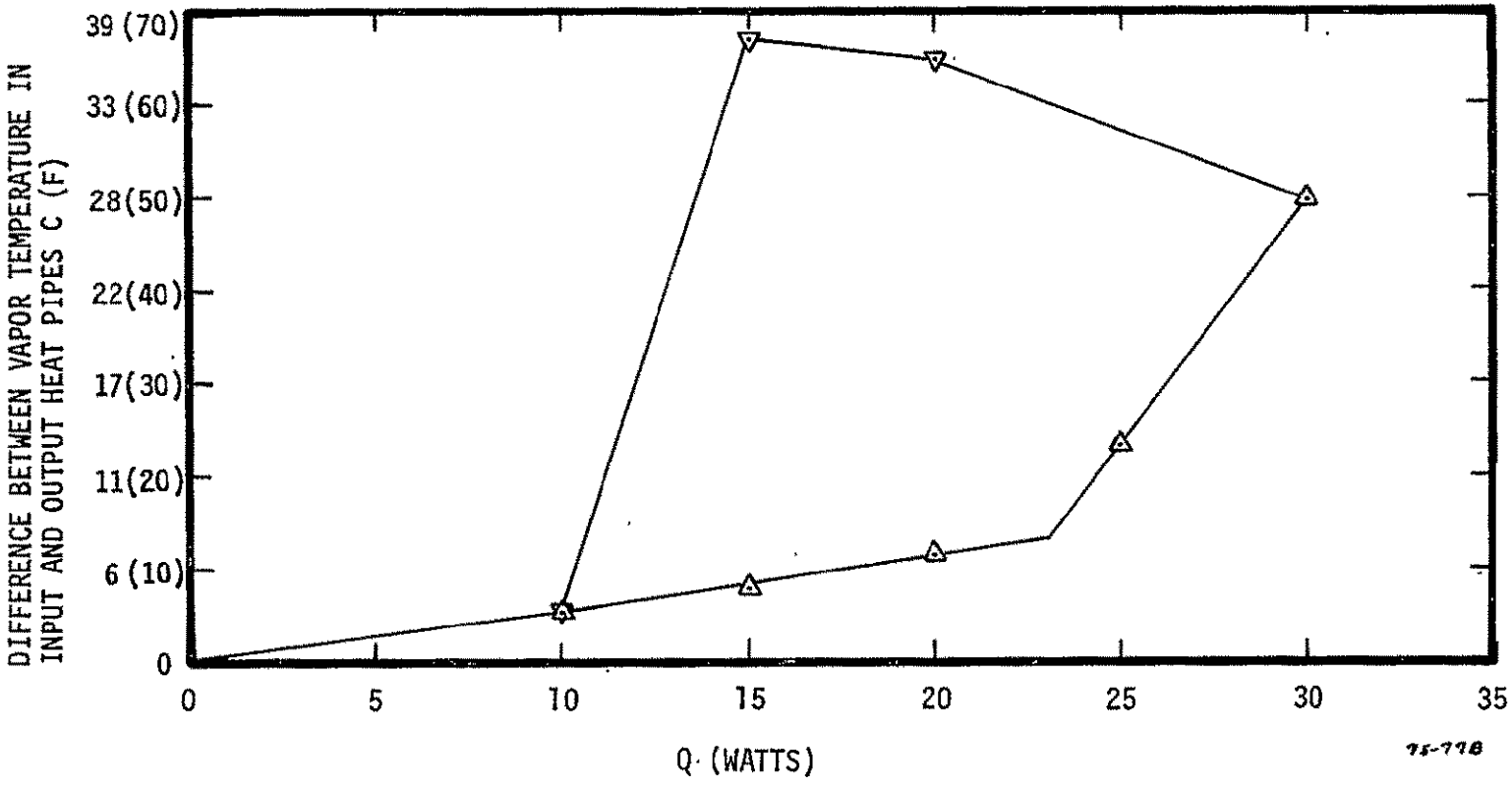

Figure 3-8. Vapor-Modulated Heat Pipe Capacity Tests With an Evaporator Elevation of 2.54 mm and the Source Temperature Maintained at 38 C.

limit for a wick on the verge of emptying is twice that for a wick that is priming. The predicted open-valve capacity was 50 watts for the saturated wick and thus 25 watts for repriming under load. The fact that the measured capacities were 50% lower is attributed to the liquid flow resistance of the feed-thru, which was neglected in the prediction.

The heat pipe was generally well behaved in its transient response except for a steady-state temperature oscillation that occurred only at a 5-watt heat load. This is displayed in Figure 3-9 where the oscillatory behavior at 5 watts and the steady behavior at 10 watts are seen. The oscillations result from the thermal time lag between a change in the source temperature and the response of the valve as well as the time it takes for the dried-out wick to reprime. For example, as the source increases in temperature, the valve opens, which in turn allows the wick to reprime and finally the source-temperature drops. By the time the sensor volume detects the drop and closes the valve, the source has cooled below the set point. The valve remains closed until the source again increases in temperature, and the cycle begins again. Evidently, the parameters governing oscillatory behavior allowed it only at the 5-watt level.

The set-point control mechanism was demonstrated to be particularly effective. A set point changed 4C per turn of the screw, which approximates the preliminary design calculation of 5C per turn.

3.3.4 Conclusions and Recommendations for the Moderate-Capacity Prototype Vapor-Modulated Heat Pipe

The principal conclusions from the effort to develop a moderate capacity prototype vapor-modulated heat pipe are:

- The heat pipe that was fabricated and tested demonstrated the principle of operation of the new induced-dry-out control mechanism.
- The new mechanism provides a means of avoiding the restrictions of the blow-thru limit of the conventional vapor-modulation mechanism and provides a much higher shut-down thermal resistance.

The development uncovered some secondary elements that adversely affected performance. These are:

- Low capacity especially at low vapor temperatures of the condenser heat pipe
- Gas generation
- Set-point dependence on heat load and sink conditions
- Steady-state oscillations in some cases

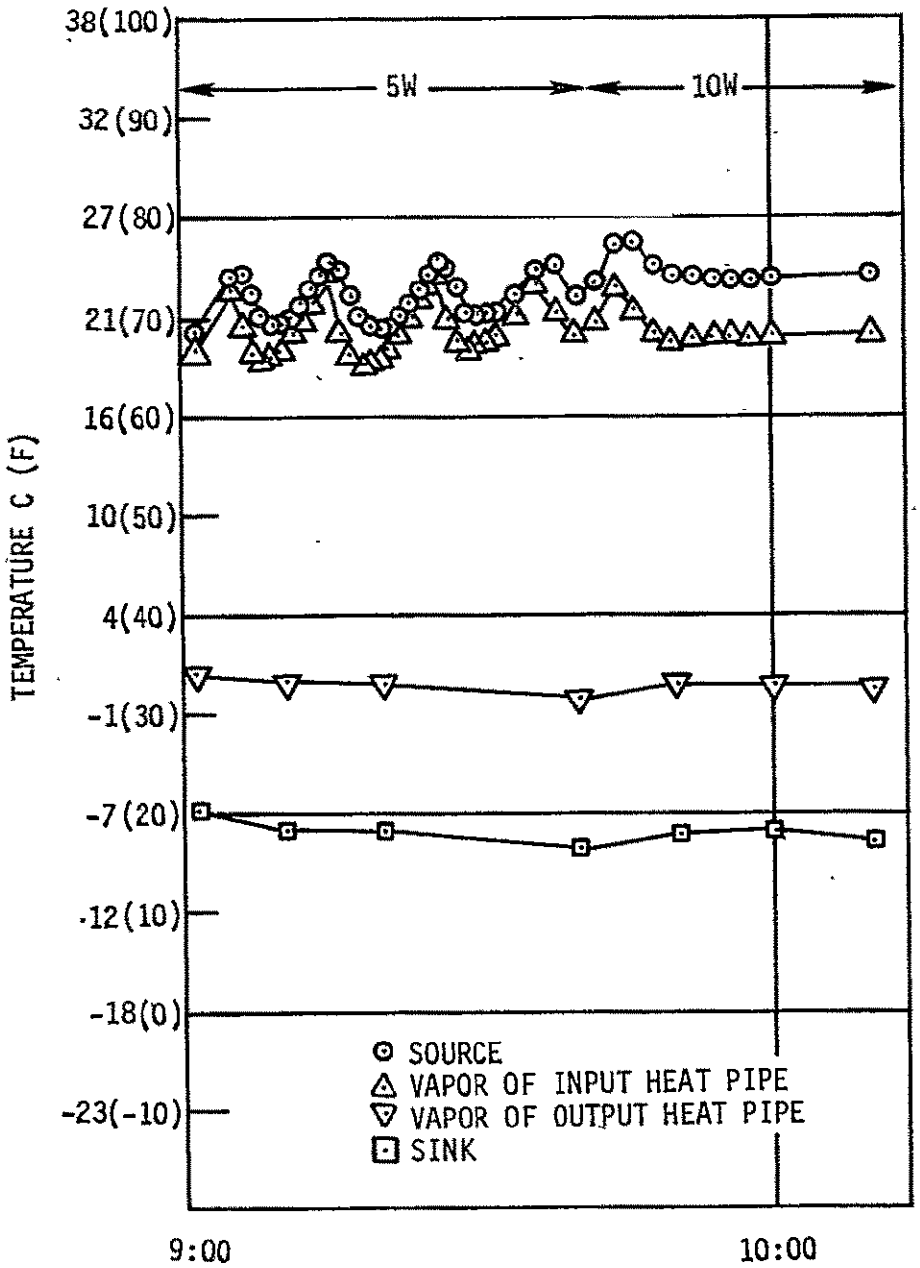

Figure 3-9. Temperature as a Function of Time for 5- and 10-Watt Heat-Transport Rates.

Design modifications to solve these problems include the use of a three-heat-pipe system. The vapor-modulated coupling heat pipe should have an optimized hydrodynamic design that includes a larger wick cross-section and a redesigned low-flow-resistance wick feed-thru and capillary barrier. The increase in capacity should allow the short vapor-modulated coupling section to operate well below its hydrodynamic limit. In this way, the liquid-flow pressure drop will not contribute significantly to groove and wick dry-out, and the set point will be relatively independent of heat load. To eliminate the set-point dependence on sink temperature, the bellows container should be thermally coupled to the input heat pipe and isolated from the bulkhead. The liquid around the bellows would then be stabilized at a relatively constant temperature. Thermal oscillations would be minimized by shortening the thermal lag of the sensor volume, which can be accomplished by providing internal fins or reducing its diameter, and optimizing the wick hydrodynamics to shorten its repriming time. These refinements as well as the switch to ammonia as the working fluid are incorporated in the development of the second prototype for a high-capacity application.

3.4 DESIGN OF A HIGH-CAPACITY PROTOTYPE VAPOR-MODULATED HEAT PIPE

The high-capacity design, shown in SK75044 (pg.156) in Appendix C, uses a short vapor-modulated heat pipe to couple two conventional heat pipes. Several factors contribute to increase its capacity over the previous methanol prototype. For example, the effective length of the vapor-modulated section is 4.4 times shorter, and the cross-sectional area of the wick is 2.8 times larger. In addition, a two-step gradation in porosity is used, that is, on the condenser side of the bulkhead the porosity is 86% which provides low flow resistance and on the evaporator side it is 76% which provides the necessary capillary pressure. The switch to ammonia provides a capacity increase at 294 K of 1.84 over methanol because of its higher figure of merit. This factor is considerably higher at low sink conditions because ammonia's figure of merit increases and methanol's decreases as the temperature falls.

Other design features include the use of aluminum for the relatively long output heat pipe to demonstrate weight-saving potential for an actual application. A stainless-steel/aluminum transition joint is used just outside the vapor-modulated coupler section. The use of aluminum saves

160 grams. Aluminum could similarly be used as the material for the input heat pipe. This would leave only the variable-conductance coupler heat pipe of stainless steel, which is desirable for a low shut-down heat leak.

For good transient response it is crucial to minimize the thermal time lag of the sensor volume. This was done by designing one with a small diameter (0.635 cm compared with 1.27 cm for the methanol prototype). The set-point-control feature of the previous pipe was abandoned, thus in an actual application final adjustment of the set point would be made at the time of the functional test, and the feed tube to the sensor volume would then be sealed.

Since ammonia has a much higher vapor density than methanol, a smaller diameter valve can be used, which allows a more compact design. The various components were carefully arranged to fit inside a 2.54-cm-diameter tube (compared to 2.18 cm for the moderate-capacity methanol heat pipe). The wall thickness of the coupler heat pipe was reduced from 0.71 mm to 0.51, which, along with its smaller diameter and a longer length (15.2 cm compared to 11.2 cm), reduces the shut-down conductance along the tube by a factor of 0.418.

3.4.1 Bellows/Valve Design

As recommended after the test of the first prototype, the bellows can has been placed on the end of the input heat pipe where its temperature remains relatively stable. The valve return spring has been moved to the low pressure side of the valve, which, along with the use of a shorter bellows than before, allows the distance between the input and output heat pipes to be minimum. Since ammonia pressure is on the inside of the bellows, a strong spring is not required to overcome the bellows spring constant. As the control liquid in the sensor volume contracts, the extension of the bellows is primarily due to the ammonia pressure; the return spring which exerts a force of approximately 0.3 kg, is required only to seat the valve after the bellows has displaced away from the valve stem. In addition, the ammonia pressure is impressed on the control fluid which ensures that it remains subcooled and does not vaporize. (The boiling point of perfluoropentane is only 29.3C). For the methanol heat pipe, the stronger 1.8 kg spring was needed to prevent vaporization.

A bellows/valve test assembly was fabricated to test all aspects of the design from fabricability to performance. The test assembly, which is shown before assembly in Figure 3-10 and after assembly in Figure 3-11, is identical to the final design except that the output heat pipe and half of the coupler heat pipe were deleted, and a plain tube was substituted for the input heat pipe. No fabrication problems occurred. The valve displacement was measured as a function of pressure difference across the bellows. The results showed .00214 mm/torr and a slight pressure difference of 67 torr was required to close the valve. When a bubble-point test of the wick feed-thru was carried out, which is discussed in the next section, the valve seal was found to be unsatisfactory. In fact, unless the valve seat was wet with acetone, it would not sustain a pressure difference. Examination of the valve with a microscope showed that the problem was particulate contamination between the valve and the seat. For the assembly of the actual heat pipe, a high level of cleanliness was maintained to prevent this problem. In addition, the bulkhead was laser welded to the tube to prevent the valve seat from warping from the high heat that would have resulted from a TIG weld.

3.4.2 The Wick Feed-Thru

The wick on either side of the bulkhead is separated at the bulkhead by two layers of 250-mesh screen, which forms the capillary barrier. The screen is seam-welded to the bulkhead which ensures no leak path past it. The wicks are inserted into the wick holders, pinned in place, trimmed flush and pressed against the capillary barrier. The wick holder is spot-welded on its flanges to the bulkhead.

The effective pore size of the capillary barrier in the test assembly was found by a bubble-point test. The high-pressure side of the bulkhead was pressurized with the valve closed and the wick was saturated with acetone. The pressure continued to rise until the capillary barrier failed and bubbles were observed emerging from the wick. The pressure at failure corresponds to an effective capillary pore size of 0.076 mm. The pressure then fell until the capillary barrier re-established itself.

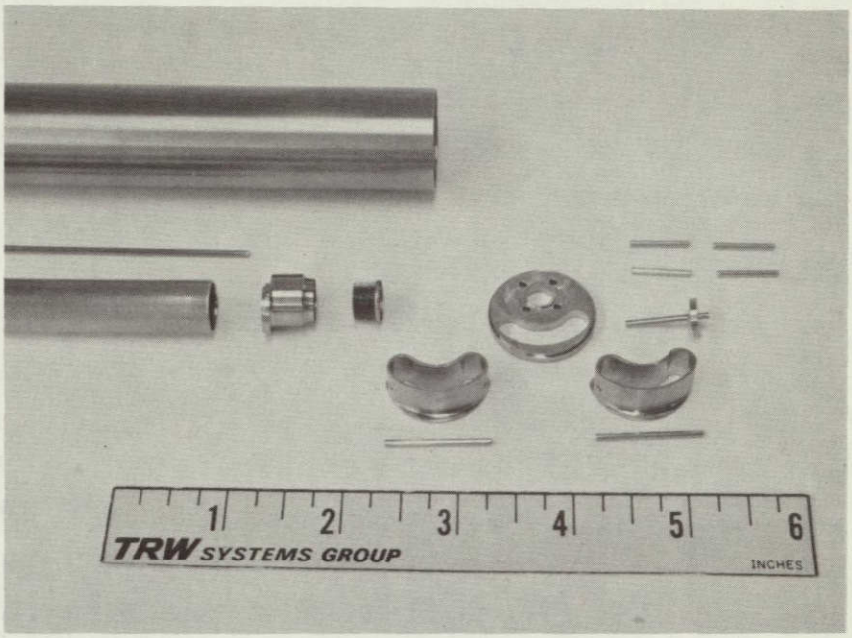

Figure 3-10. Test Subassembly of the Ammonia Vapor-Modulated Heat Pipe Before Assembly.

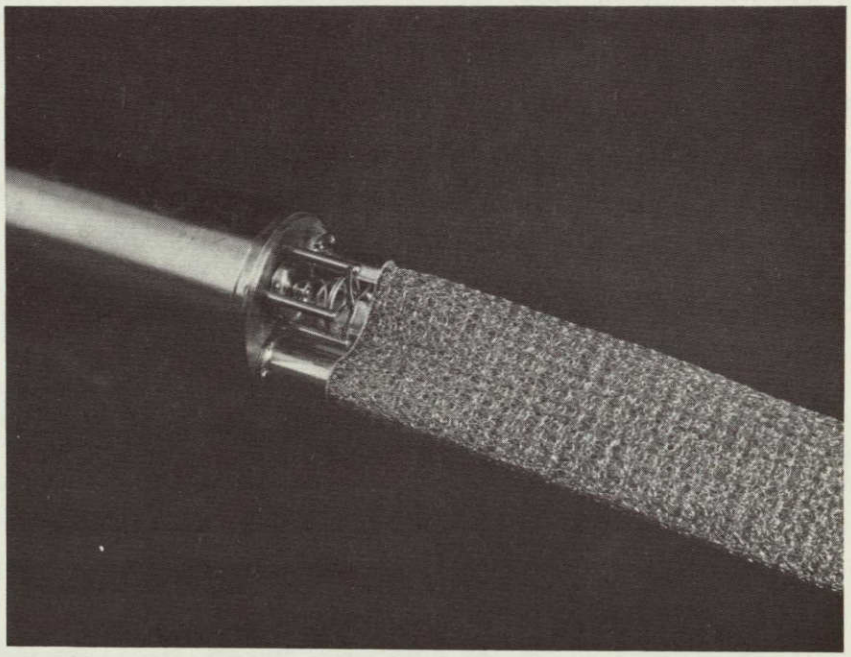

Figure 3-11. Test Subassembly of the Ammonia Vapor-Modulated Heat Pipe After Assembly.

A pore size of 0.165 mm corresponds to this pressure. Both pore sizes for capillary-barrier failure and re-establishment are sufficiently small to ensure that the evaporator side of the bulkhead will dry out when the valve closes and remain dry.

3.4.3 Test

Before the heat pipe was charged with ammonia, the sensor volume and bellows can was filled with control fluid. The fluid was then pressurized to 1.10×10^3 torr, which was previously found to be the pressure at which the valve just began to open when the pressure on the other side of the bellows was atmospheric. Thus, the set point of the heat pipe should be the temperature of the sensor volume at the time the valve to it was closed, which was 22 C. The actual set point found during test, however, was 31 C. A possible reason for this discrepancy is that a small bubble of noncondensable gas was trapped in the sensor volume or bellows can. When the coupler heat pipe was charged with ammonia, the high pressure impressed on the control fluid compressed the bubble and it diffused into the liquid. In any case, since the set point was selected arbitrarily, no attempt was made to change it.

After the heat pipe was charged with ammonia, it was instrumented according to SK75061. To simulate the thermal mass of typical electrical equipment, a 1.4 kg aluminum block with tape heaters on it was used for the heat source. The sensor volume was inserted into a hole drilled into it.

3.4.3.1 Steady-State Performance

The steady-state performance is summarized in Figures 3-12, 3-13 and 3-14. Heat-transport rates of 4, 10, 50, 100, 150, and 200 watts were run at sink temperatures of -54 C, -9 C and 10 C. The performance in general is excellent. Figure 3-12 shows that the source temperature is practically independent of sink temperature and from the low load of 4 watts at the lowest sink of -54 C to the maximum design load of 100 watts at the high sink of 10 C, the temperature range of the source is 4.2 C. Figures 3-13 and 3-14 show where the temperature drops between the source and sink occur. The temperature drops of primary interest are between

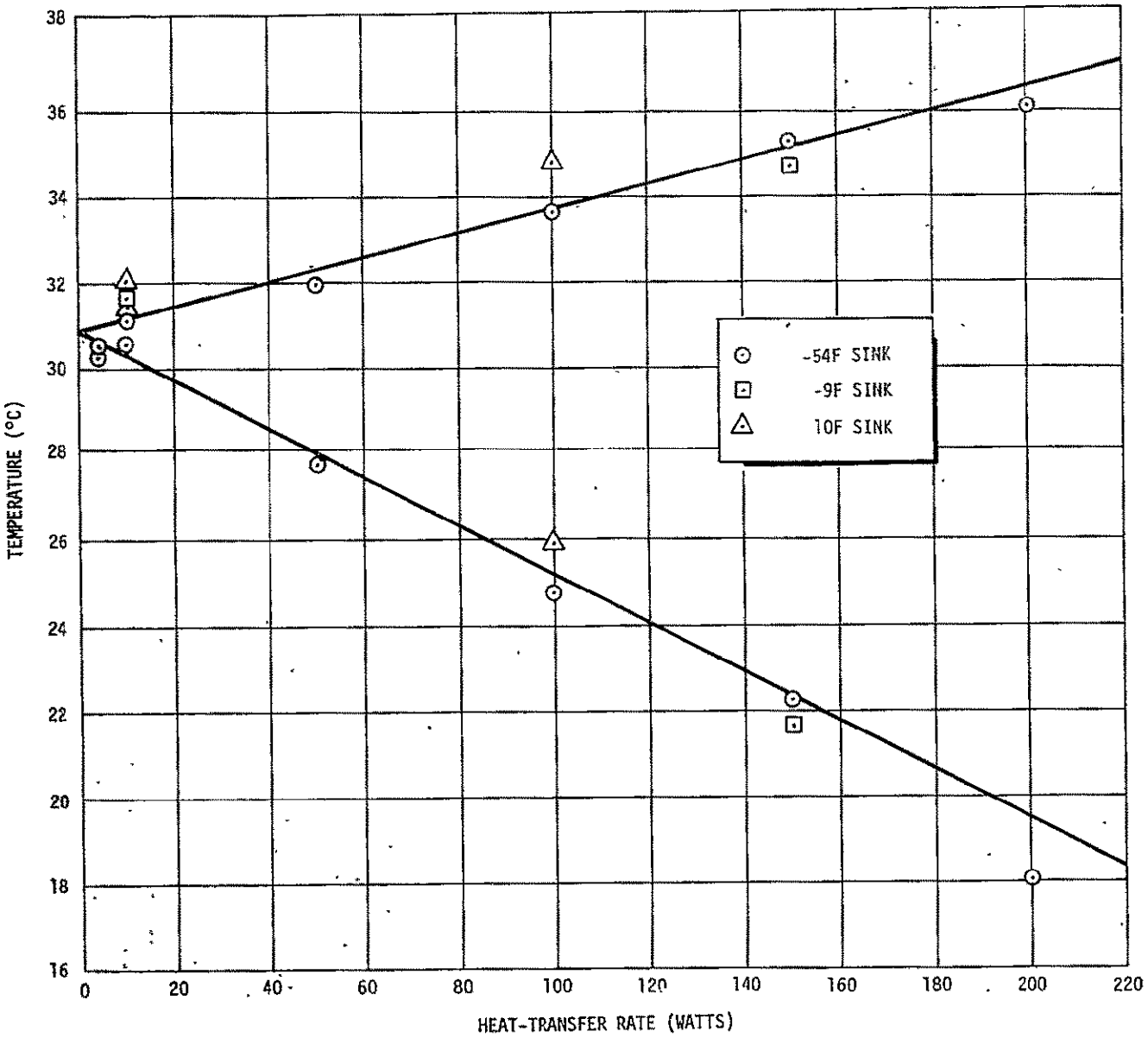

Figure 3-12. Steady-State Control Characteristics of the Induced-Dry-Out Heat Pipe.

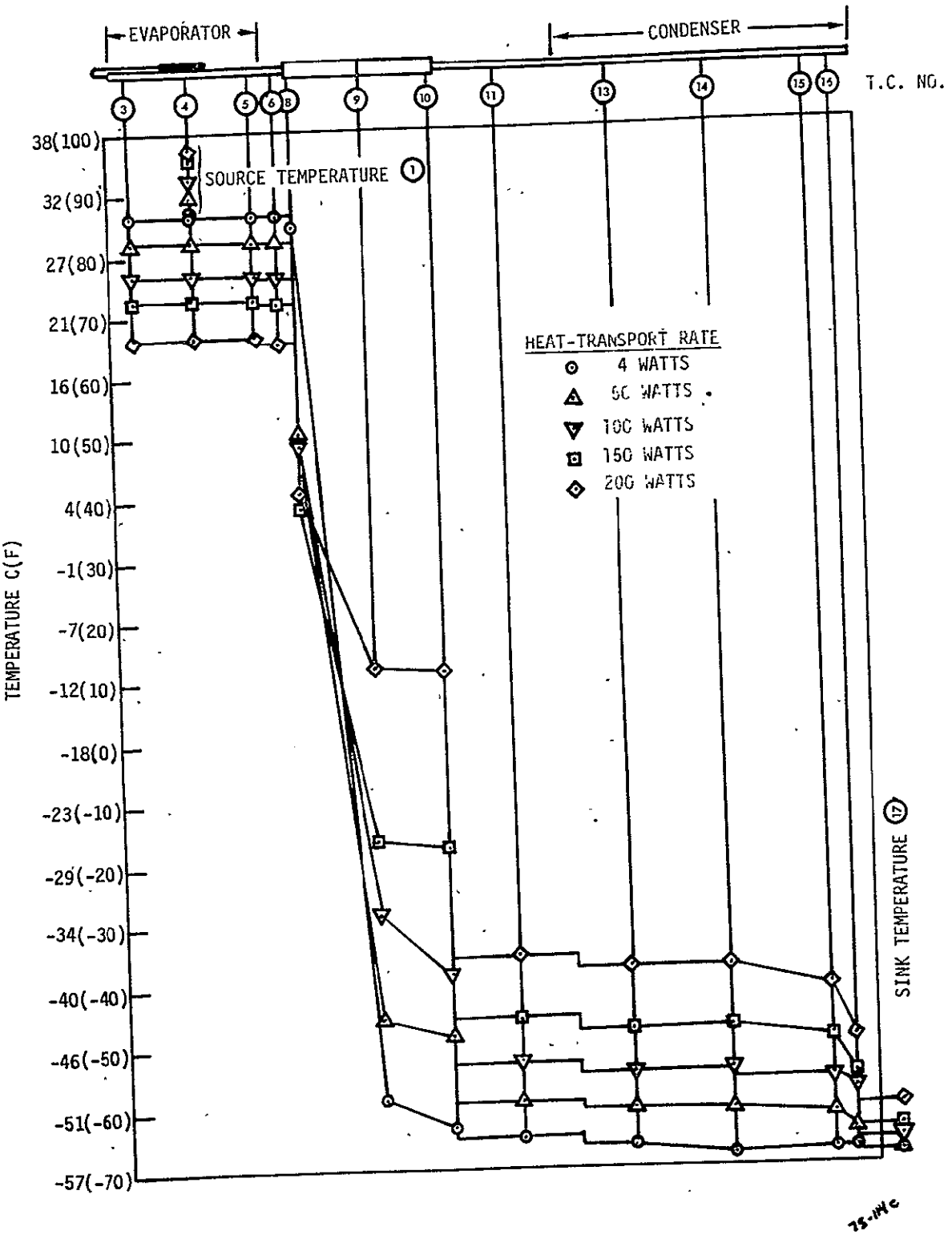

Figure 3-13. Steady-State Temperature Distribution Along the Ammonia VMHP as a Function of Heat-Transport Rate.

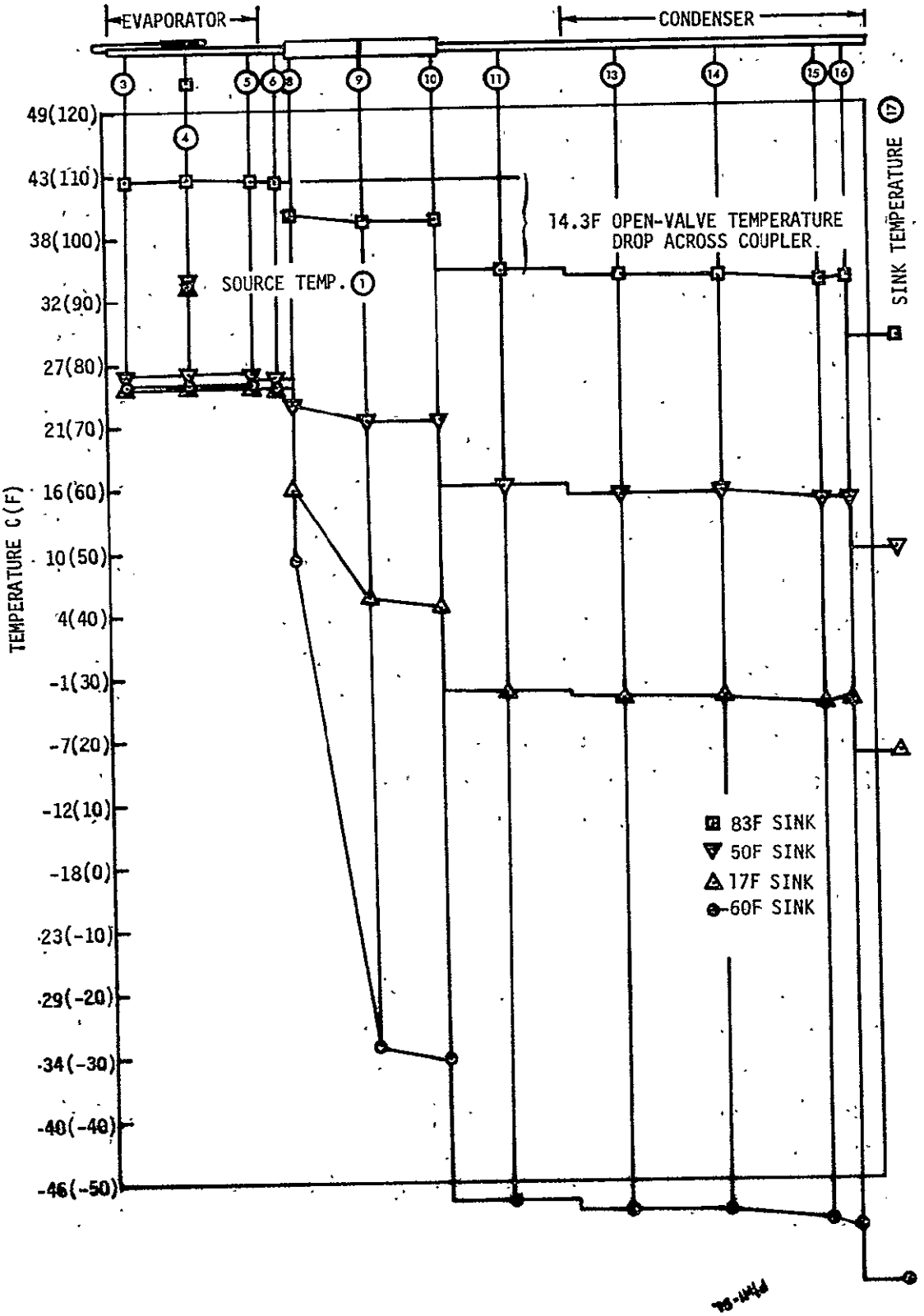

igure 3-14. Steady-State Temperature Distribution Along Ammonia VMHP as a Function of Sink Temperature. Heat transfer rate is 100 watts in each case.

the vapor temperature of the input heat pipe (T.C.6) and the output heat pipe (T.C 7) since these drops are solely due to the variable conductance coupling section. The other temperature drops are the usual ones that occur with ordinary heat pipes. The vapor temperature on the low pressure side of the bulkhead is given approximately by T.C.9 and 10, however, these sometimes run higher than the vapor because the thermal couples are on the coupler-heat-pipe wall which is not wicked or grooved on the inside. The temperature drop $T_6 - T_{10}$ between the vapor in the input and coupler heat pipes is feedback controlled by induced dry-out to stabilize the source temperature. The temperature drop $T_{10} - T_{11}$ between the vapor of the coupler and output heat pipes also contributes to control. For example, as the valve closes and induces wick dry out on the high-pressure side of the bulkhead, the liquid leaving the wick flows to the other side and increases the condensation temperature drop due to increased flooding of the grooves. This is seen in Figure 3-14 where at 100 watts, $T_6 - T_{10}$ increases with decreasing sink temperature.

As the sink rises in temperature, the valve opens and the overall temperature drop across the coupler heat pipe decreases. The drop with the valve fully open is of particular importance because it directly affects the highest temperature of the sink for which the source temperature is still controlled. The measured open-valve drop of 7.9 C with a 100 watts load corresponds to an average heat-transfer coefficient of 12000 watts/M^2-°C for the two condensations and two evaporations that take place within the coupler.

The minimum conductance for the low power case was measured by setting the sink at the lowest temperature of -55.6C and adjusting the heat load to the lowest setting that maintained the source above the set point. Three watts were insufficient and four were required. This is an upper bound for the heat leak because the source was running approximately 7°C above ambient and the leak through the insulation was estimated to be 2.4 watts. A precise heat-leak measurement would require a thermal vacuum test.

3.4.3.2 Transient Performance

The transient response to step changes in power and rapidly varying sink conditions is excellent with small overshoots and no steady-state oscillations. Figure 3-15 shows a typical run where initially there was no heat load and the sink was at -51 C. At 15:06 a step increase in heat load to 150 watts was applied. Since initially the source was below the set point and the valve was closed, both the source and the input heat pipe rapidly increased in temperature. When the valve opens, the vapor in the input heat pipe suddenly drops in temperature which prevents the source from rising further. The response is similar for the other step increases in load except the initial spike in the vapor pressure of the input pipe is missing because the source is not below the set point when the load is applied and hence the valve response is more rapid.

For a step decrease in load such as the reduction from 200 to 100 watts at 15:27 or from 100 to 10 watts at 15:48, the source is cooled below the set point where the valve closes. The source then increases in temperature until it reaches the operating state, which takes longer at low loads than at high loads.

The high degree of independence of source temperature on sink temperature is seen where the sink was increased from -51 C to -9.4 C as rapidly as possible. The source temperature was hardly affected.

3.4.4 Conclusions

The task to develop a spacecraft prototype vapor-modulated heat pipe was an example of how a new mechanism was conceived and how the practical problems of its implementation were discovered and solved. The motivation for the new induced-dry-out mechanisms was the blow-thru limit of the conventional vapor-flow-control mechanism, which restricts the choice of fluids to ones with unacceptably low transport capacities or water with its high freezing point. Although the first prototype based on the induced-dry-out mechanism failed to meet its design goal of close temperature control for sink temperatures as low as 220 K and heat loads up to 20 watts, it did demonstrate the new mechanism and point to design changes to overcome its deficiencies. All of these changes were incorporated into

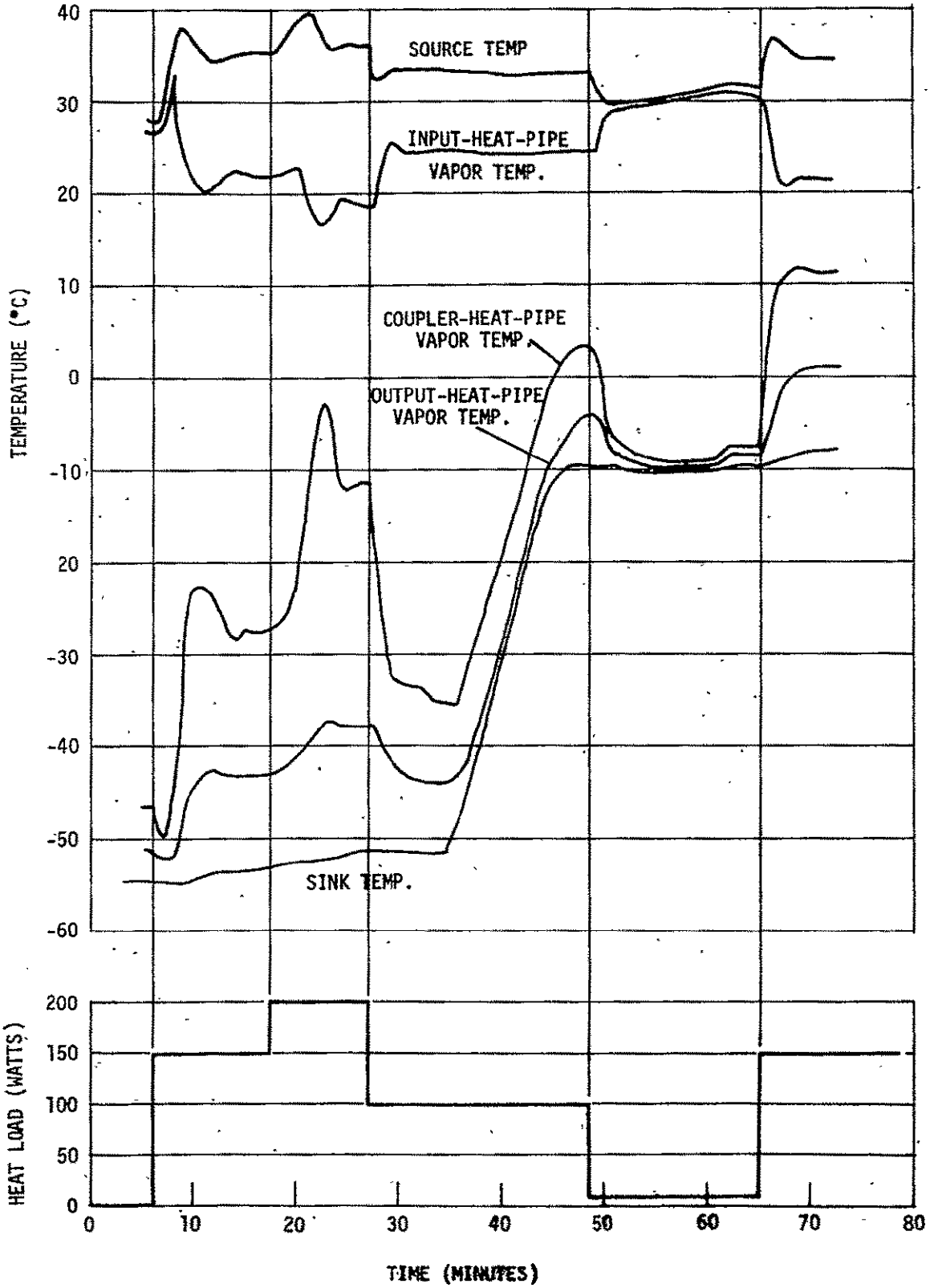

Figure 3-15. Transient Response of Induced-Dry-Out Heat Pipe.

the high-performance prototype and the result was successful. The heat pipe operated at twice the 100-watt design heat load, which corresponds to a capacity in excess of 213 watt-inches. The source temperature was practically independent of sink conditions and increased with load at a rate of only 0.03 °C per watt. The full-on conductance is 13 watts/°C, and the full-off conductance, while it could not be accurately measured, was less than 0.018 watts/°C.

There is the potential for further improvement. For example, a larger sensor volume will result in even tighter source temperature control. A longer coupler heat pipe with optimized grooves at the heat-pipe interfaces will result in higher full-on conductance. The heat pipe is inherently insensitive to noncondensable gas and the off heat leak could be greatly reduced if enough gas were added to block off the condenser in low sink conditions. This would also allow the heat pipe to operate with extremely low sink temperatures below the fluid's freezing point. Since the primary temperature control is from vapor-modulation, only a small amount of gas and probably no reservoir would be required. In its present state of development, the vapor-modulated heat pipe is ready for a spacecraft application when a passive feedback-controlled heat pipe is required.

3.5 REFERENCES

3.1 Marcus, B. D., Edwards, D. K., and Anderson, W. T., "Variable-Conductance Heat Pipe Technology - Research Report No. 4," NASA CR-114686, December 1973.

3.2 Eninger, J. E., "Menisci Coalescence as a Mechanism for Venting Noncondensable Gas From Heat-Pipe Arteries," AIAA Paper No. 74-748 July 1974.

4.0 SOUNDING-ROCKET HEAT-PIPE EXPERIMENT

Ames Research Center provided two of the seventeen heat pipes for the October 4, 1974 sounding-rocket launch of the International Heat-Pipe Experiment. The payload reached an altitude of 140 miles, and accelerations less than 200 micro g's were attained for almost six minutes. The two ARC heat pipes, which were fabricated by TRW Systems Group, are of the same type that will be used on the Communications Technology Satellite and on a TRW spacecraft. These heat pipes utilize arteries to attain high heat-transfer capacity and noncondensable gas to attain variable conductance. The priming of arteries without trapping a noncondensable gas bubble has remained a crucial problem of heat-pipe technology, and the flight experiment provided the first opportunity of a zero-gravity test of a solution to this problem. The details of design, fabrication and ground test of the experimental heat pipes can be found in the final research report of the previous contract, Reference 4.1. The task on the current contract is for analysis of the flight data. A brief description of the experiment is given here, however, the emphasis is on the flight results.

To prevent the entrapment of a bubble, noncondensable gas is vented from the artery through a priming foil (Reference 4.2), which is a thin foil-walled section of artery at the evaporator end with a pattern of capillary-sized venting holes. The flight-experiment test of this scheme was especially challenging because of the short time available in zero gravity for priming and then applying a heat load to verify that a primed state was achieved. In addition, there were uncertainties as to whether the so-called "pogo effect" would interfere with priming. If, at the instant of rocket-engine shut-down, a surge of excess liquid arrives at the evaporator before the artery primes, the evaporator end of the artery may fill with liquid and prevent venting. Our task was not only to test whether or not the heat pipe primes, but also to obtain some crucial information on the internal conditions of the heat pipe during the experiment. Each heat pipe has one of two otherwise identical arteries instrumented at the evaporator end with a miniature thermistor. The thermistor, which is

electrically self-heated, is markedly cooler when submerged in liquid than when in vapor. Thus, it detects the presence or absence of liquid in the priming foil. The research heat pipes, therefore, partially overcome a nagging difficulty of arterial heat pipes, that of diagnosing the cause of unsuccessful priming.

Priming failure can have several causes; however, they generally fal into one of two categories listed below.

1. Evaporator stress* too high for priming due to:
   - insufficient fluid in the heat pipe,
   - too large a residual heat load during priming,
   - too large of a hydrostatic load due to adverse orientation in an acceleration field.
2. Entrapment of noncondensable gas bubble due to:
   - failure to vent the gas through the priming foil,
   - a gas bubble at some location in the artery other than the evaporator end.

If during the priming period liquid <u>is not</u> detected in the evaporator end of the artery, then priming failure is attributed to the first category, excessive evaporator stress. If, on the other hand, liquid <u>is</u> detected, the stress was low enough for priming to take place, and a subsequent failure of the uninstrumented functional artery is attributed to the second category, entrapment of noncondensable gas.

The thermistor instrumentation also provides a means of verifying that a sufficient heat load is applied to test for the primed state of the functional artery. If the thermistor detects that liquid recedes (which it should, due to a large hole cut in the instrumented artery), then the heat load is sufficient to empty the functional artery if priming is unsuccessful. If subsequently a burnout does not occur, then the primed state of the functional artery is verified.

*We define stress as the vapor-liquid pressure difference that is sustained by surface tension.

The diagnostic logic is summarized in Figure 4-1, where the heavy line represents successful priming and verification of such.

4.1 DESCRIPTION OF THE HEAT PIPES

As shown in Figure 4-2, the heat pipes are of an arterial slab-wick configuration. The two heat pipes used in the flight experiment differ only in the details of their priming foils. For the heat pipes designated X-2, the active length of the priming foil is 1.5 inches, the holes are in spiral rows, and the end on the functional artery is crimped closed, whereas for the heat pipe designated X-1, the active length is 0.375 inches, the holes are in straight rows and the end is closed with a plug. The X-2 configuration priming foil is a design similar to that used on the Communication Technology Satellite program. X-1 configuration priming foil is an experimental design that represents an attempt to improve the ruggedness and minimize the chance of trapping a gas bubble in the last instant of priming the foil itself.

The instrumentation consists of a bead-type thermistor that is held at the apex of the conical end of a cylindrical teflon plug, which in turn fits into the end of one of the priming foils. The platinum leads from the bead pass through two holes that run the length of the plug. The plug is held in the end of the priming foil by a band of heat-shrink tubing. The thermistor leads are connected to the prongs of an electrical feed-through in the heat-pipe end cap. The electronic circuit for the thermistor is particularly simple; it consists of a 3000-ohm resistor and a 28-volt power supply in series with the thermistor. The circuit output is the voltage across the thermistor. The output voltage is approximately 3.7 volts when the arteries are primed and 1.2 volts when deprimed. Sometimes, however, in the primed state boiling occurs at the bead, in which case the output oscillates rapidly about some mean voltage greater than 3.5 volts. In the deprimed state, discrete intermediate output voltages occur that are attributed to partial cooling of the thermistor bead by small liquid fillets around it. With sufficient evaporator stress these fillets are not replenished from neighboring liquid and they evaporate, which results in the low 1.2-volt output.

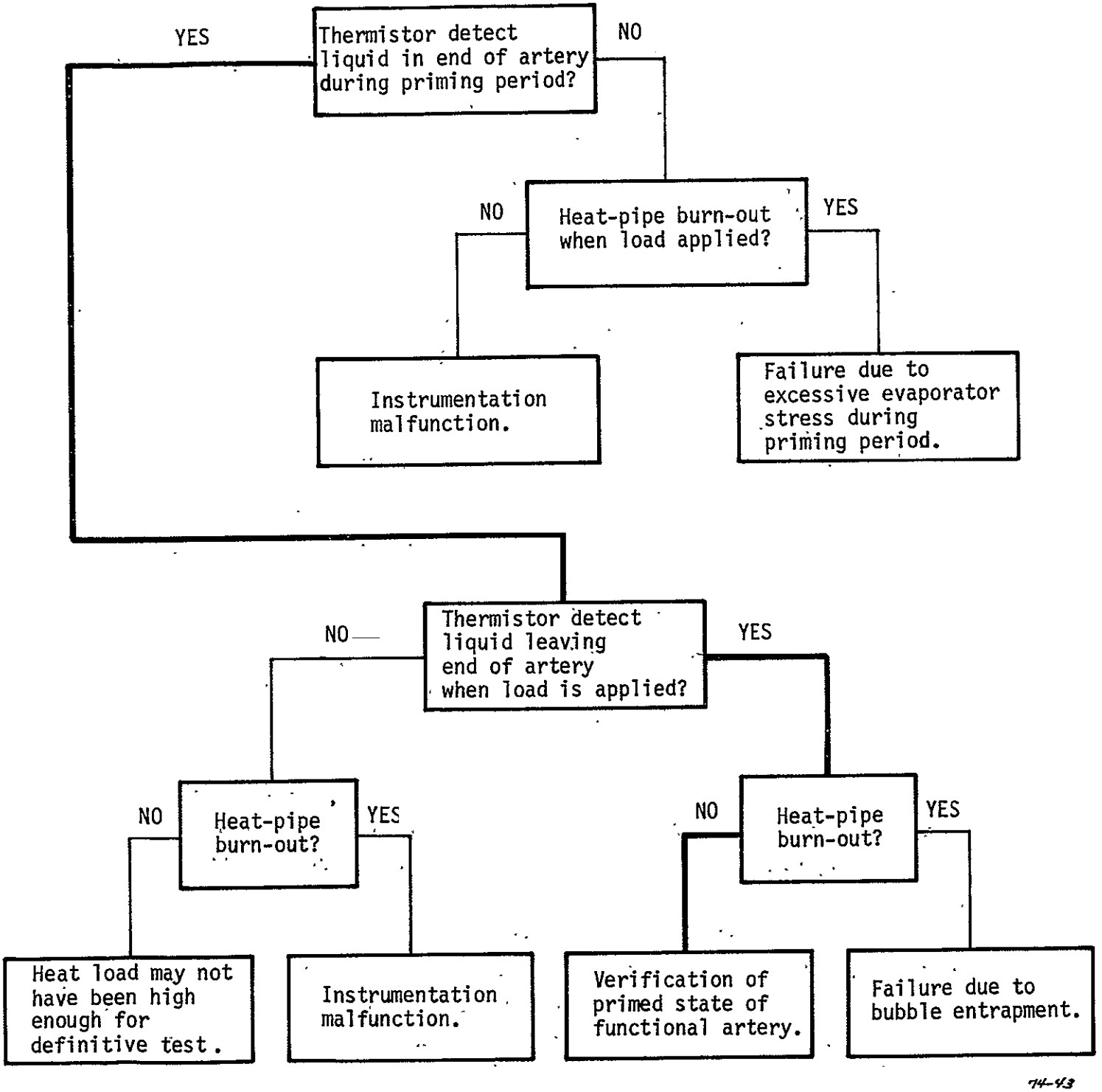

Figure 4-1. Summary of Diagnostic Logic for the Flight Experiment.

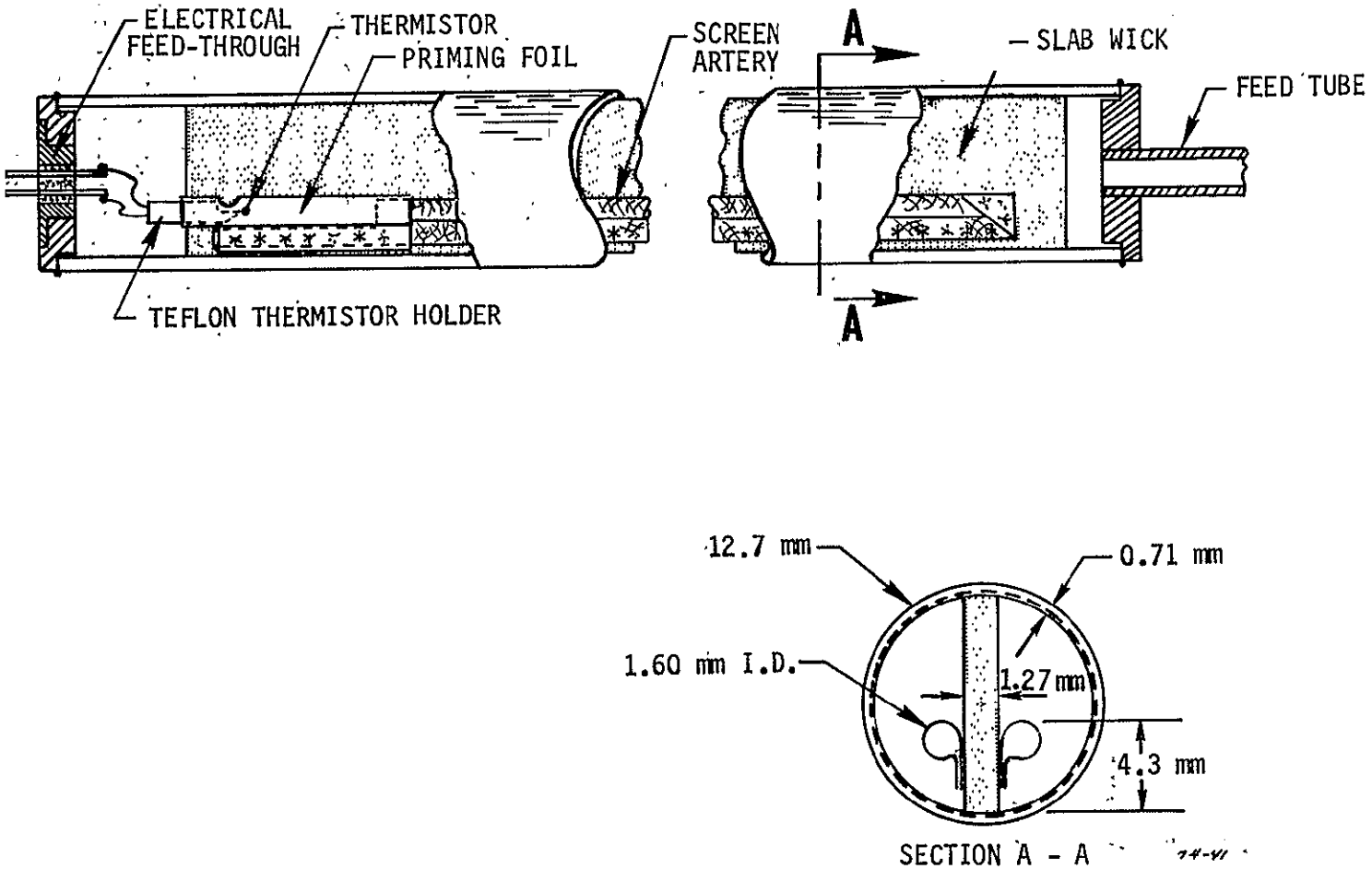

Figure 4-2. Configuration of the Flight Heat Pipe (X-2 configuration).

4.2 FLIGHT RESULTS

The power profile used in the experiment is shown in Figure 4-3 below:

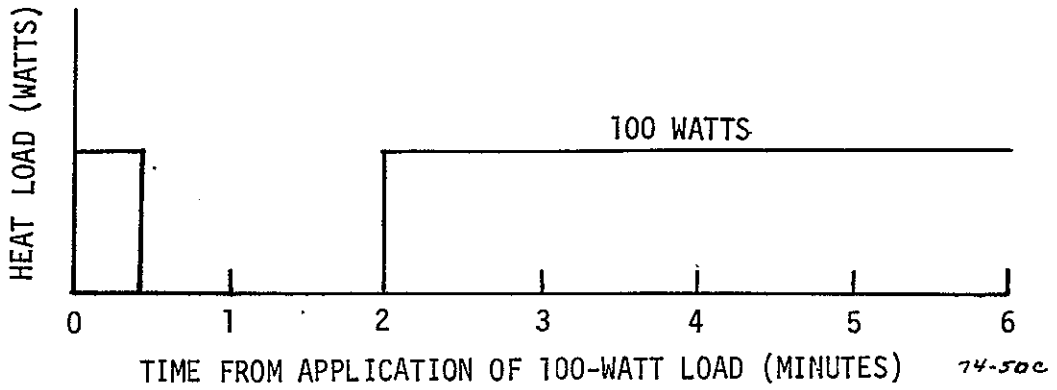

Figure 4-3. Power Profile for the Flight Experiment.

During the first half minute, 100 watts were applied to move excess liquid to the condenser end of the heat pipe. This amount of heat is sufficient to transfer 12% of the total amount of methanol. The zero-power period from $t = 0.5$ minutes to $t = 2$ minutes was for priming. During the remainder of the zero-gravity period, 100 watts were again applied.

The data from the flight are displayed in Figures 4-4, 4-5, 4-6 and 4-7. In both heat pipes, the artery thermistor indicated that liquid filled the evaporator end of the dummy artery just after rocket-engine shut-down. Both heat pipes isothermalized after the initial 100-watt load, and the final 100-watt load was successfully transported without a burnout. No real-time commands were called for.

The artery thermistor voltage did not suddenly drop and thus indicate liquid leaving the evaporator end of the instrumented artery during the final 100-watt load. The gradual voltage reduction after $t = 200$ sec. is due to the overall temperature rise. In the absence of direct indication of a heat load high enough to verify a primed state of the functional artery, we must rely on theoretical computer predictions. When primed, the instrumented artery generates a capillary pressure set by the relatively large hole cut

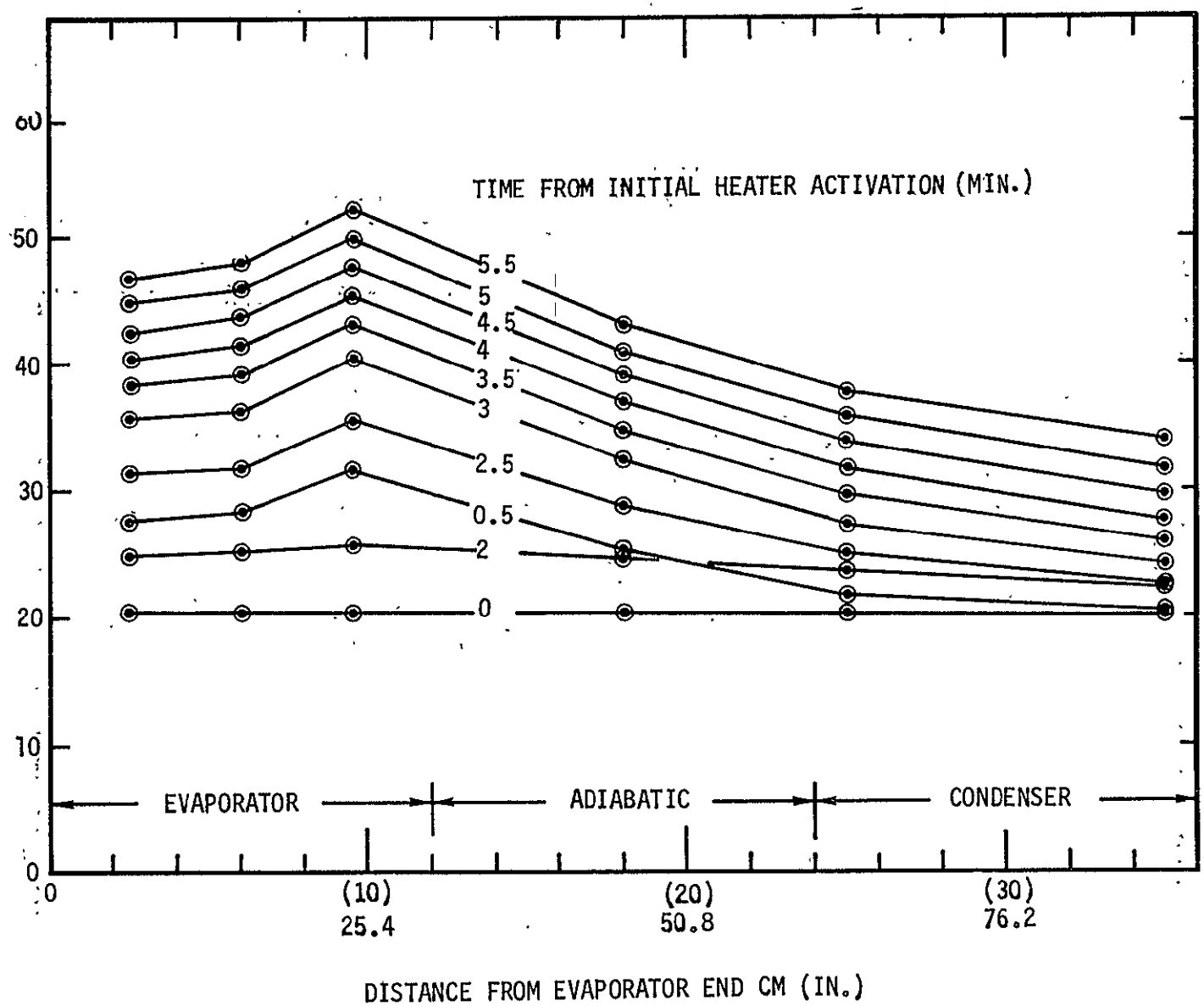

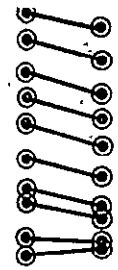

HEAT SINK

14-43A

Figure 4-4. Temperature Distribution Along Ames Slab Wick X-1 During Rocket Flight.

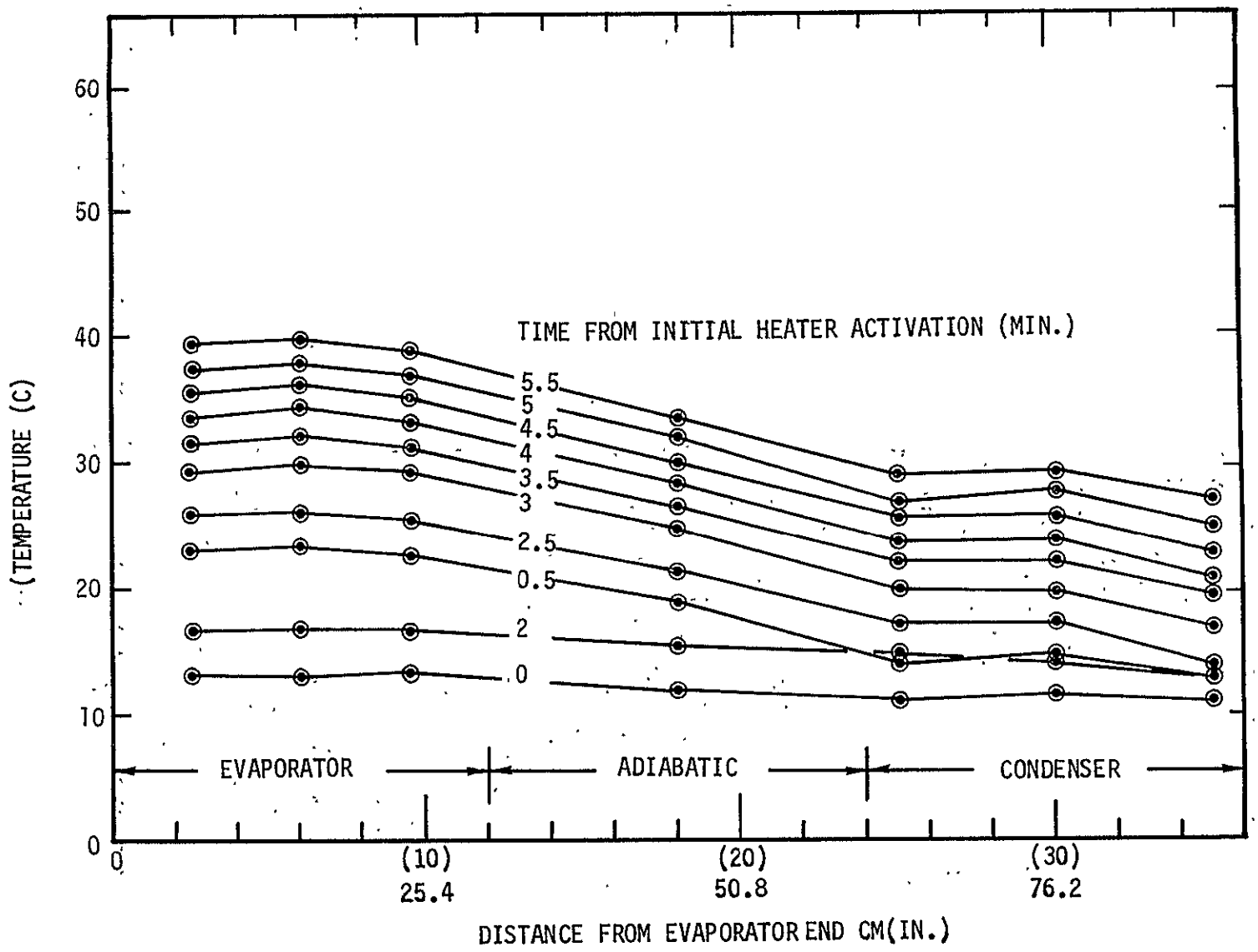

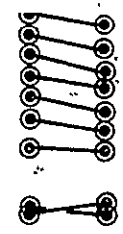

74-163B

Figure 4-5. Temperature Distribution Along Ames Slab Wick X-2 During Rocket Flight.

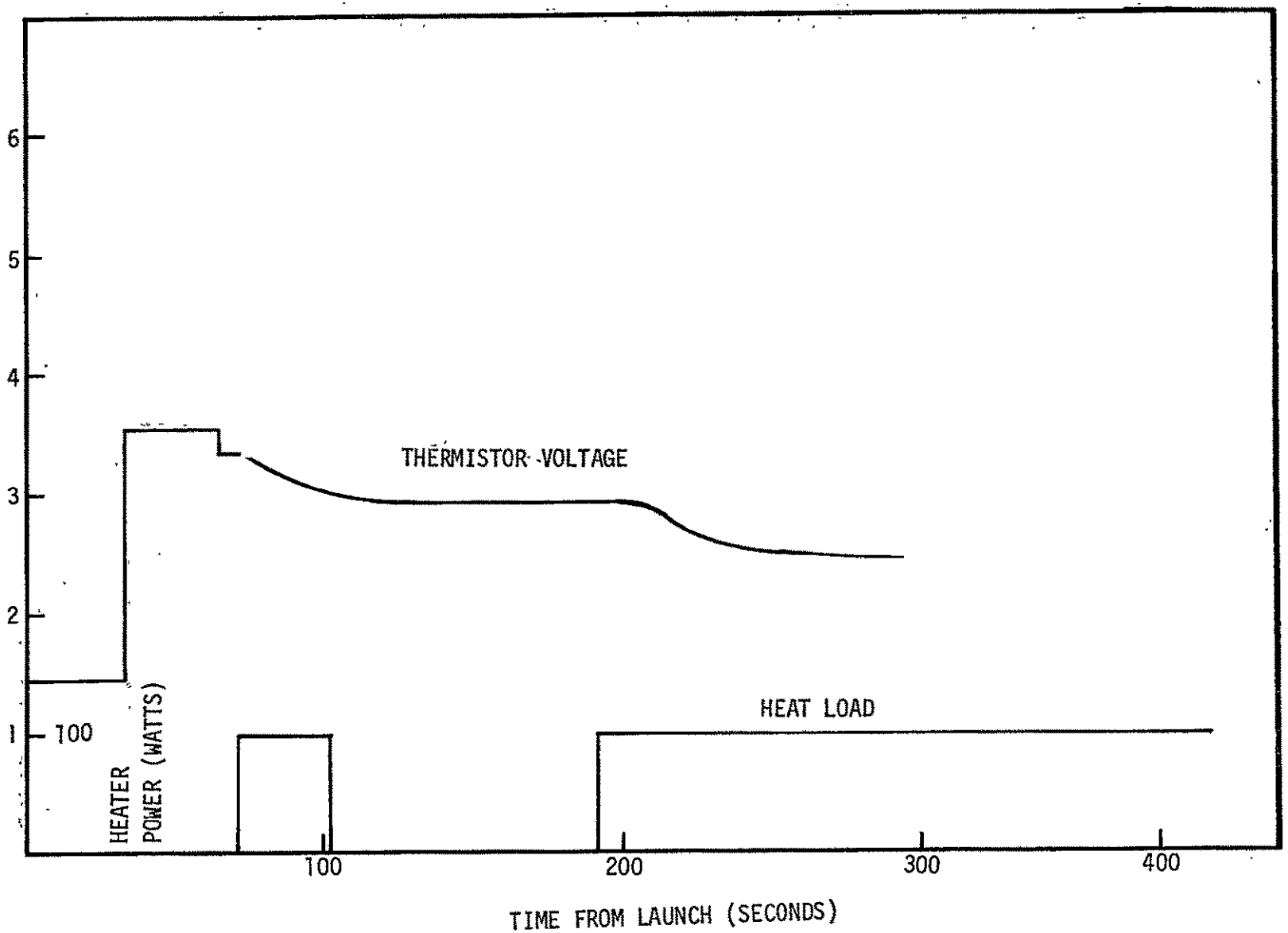

Figure 4-6. Artery Thermistor Voltage and Power Profile for Ames Slab Wick X-1 During Rocket Flight.

74-165e.

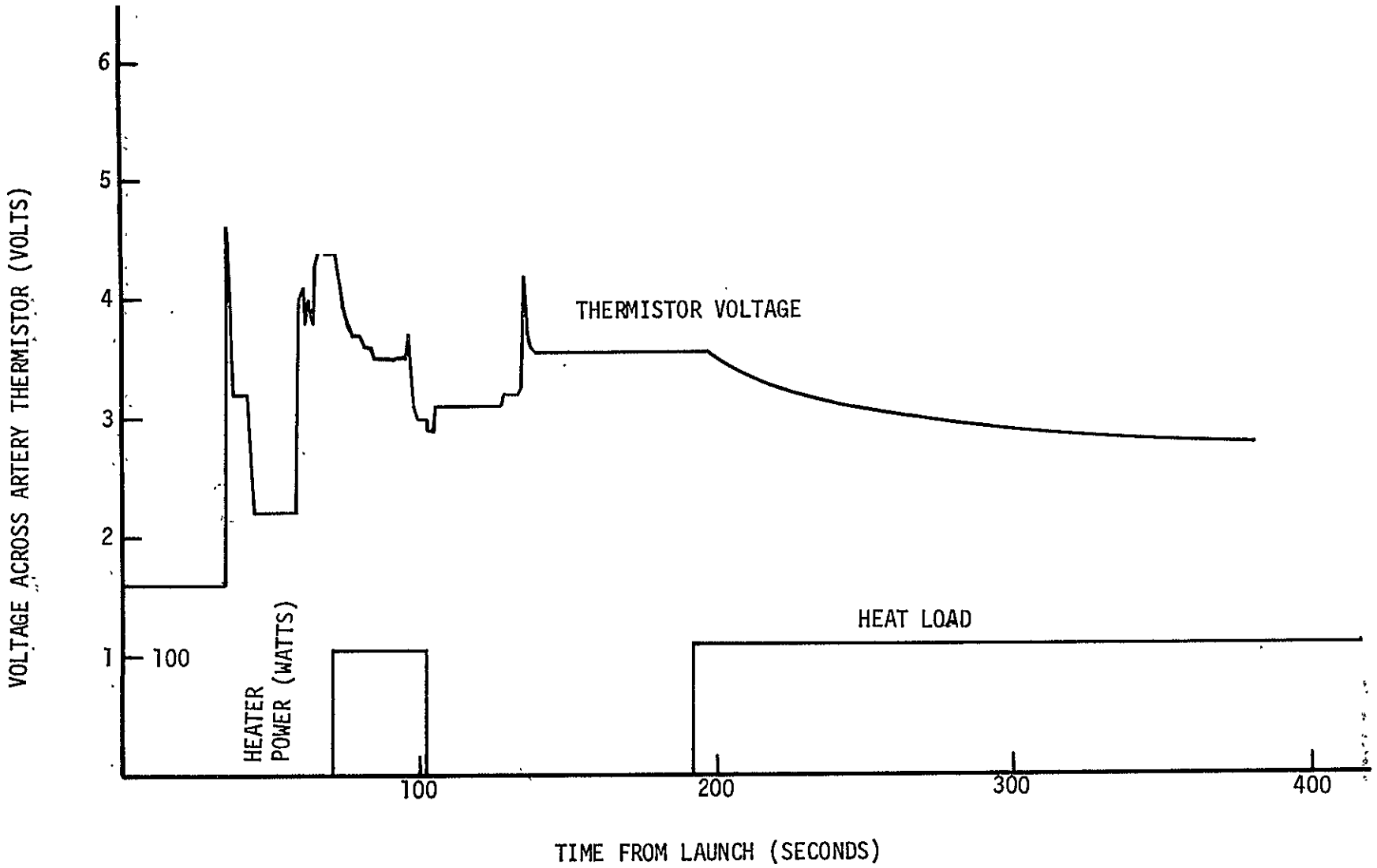

Figure 4-7. Artery Thermistor Voltage and Power Profile for Ames Slab Wick X-2 During Rocket Flight.

in the priming foil. As shown in Figure 4-2, the teflon plug is cut away under the hole, but it still blocks half of the artery. The effective capillary pore diameter, therefore, is taken as half the artery diameter. Figure 4-8 shows predicted zero-gravity capacity both with and without the functional artery and instrumented artery primed. Curve 2 of the figure, for example, gives the predicted heat load for the liquid in the instrumented artery to recede provided the functional artery has primed, while Curve 3 gives that load provided the functional artery has not primed. The fact that the thermistor did not indicate liquid recession is attributed to the functional artery being primed and the actual 100-watt load not being sufficiently in excess of Curve 2. The actual load is considerably greater than Curves 3 and 4, thus a burnout would have occurred if the functional artery had not primed. Note from Figure 4-8 that as the heat load is increased, the instrumented artery fails (Curve 2) due to its large pore, but the functional artery remains primed until it fails at a much higher load (Curve 1). This explains the paradox of Curve 2 with two primed arteries lying below Curve 1 with one primed artery.

Two features of the temperature profiles of Figures 4-4 and 4-5 merit discussion. First, the thermistor instrumentation indicated a temperature difference of approximately 5°C develops between the evaporator and adiabatic regions. The temperature difference measured with thermocouples in ground test, however, was approximately 1.1°C, corresponding to a heat-transfer coefficient of 7380 watts/m^2-°C, which is in line with previous experience with methanol and grooved stainless-steel tubes. The large evaporator-adiabatic temperature difference during the flight may be due to poor thermal contact of the thermistors with the heat-pipe wall. That the large temperature difference is not a zero-gravity effect can be ruled out because the same difference was measured with the flight instrumentation in ground tests.

The second feature of temperature distributions is the low condenser-end temperature. The MULTIWICK computer program predicts that additional fluid required for priming results in a liquid slug in the vapor spaces at the condenser end. The noncondensable gas added to the pipe causes a further blockage. The low condenser-end temperature was apparent in ground tests as well as during the flight.

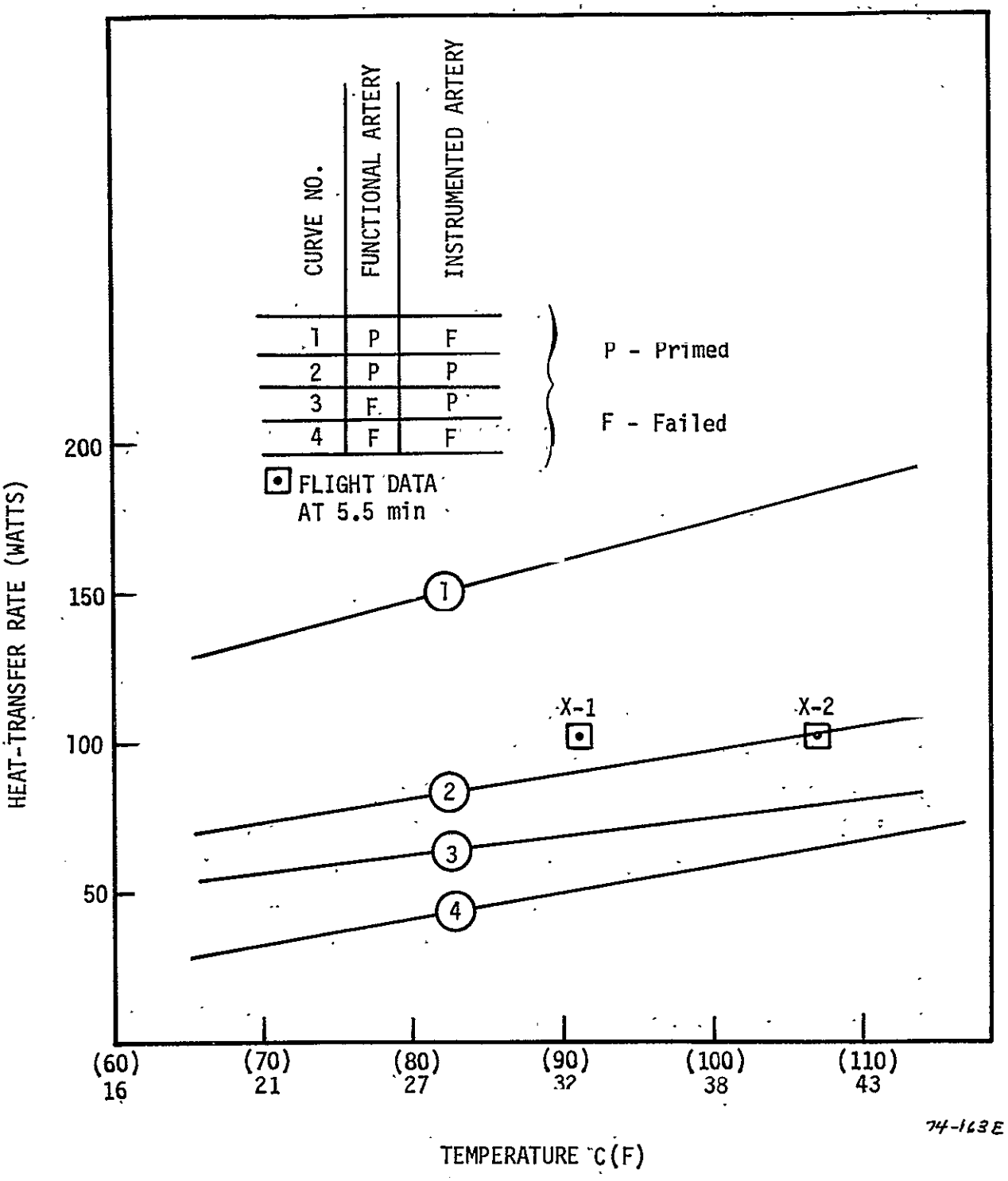

Figure 4-8. Zero-Gravity Capacity Predictions for all Combinations of Primed or Failed Artery States.

In summary, both Ames heat pipes primed and transported 100 watts during the flight. The experiment was the first zero-gravity test of arterial heat pipes that had noncondensable gas intentionally added to them. The special thermistor at the evaporator end of the artery indicated that priming occurred just after rocket-engine shut-down. Although the thermistor did not indicate liquid receding from the instrumented artery, the MULTIWICK program showed that the 100-watt load was considerably in excess of the heat-pipe capacity if the functional artery had not primed.

4.3 REFERENCES

4.1 Anderson, W. T., Edwards, D. K., Eninger, J. E. and Marcus, B. D., "Variable-Conductance Heat-Pipe Technology - Final Research Report," NASA CR-114750, March 1974.

4.2 Eninger, J. E., "Menisci Coalescence as a Mechanism for Venting Noncondensable Gas From Heat-Pipe Arteries," AIAA Paper No. 74-748, July 1974.

5.0 ARTERIAL PRIMING RESEARCH WITH A GLASS HEAT PIPE

The purpose of the glass-heat-pipe research was to answer some crucial questions regarding a method of priming heat-pipe arteries in the presence of noncondensable gas. As discussed in Section 4.0, this method was successfully tested for the first time in zero gravity by the two research heat pipes provided by Ames Research Center for the sounding-rocket launch of the International Heat Pipe Experiment. Priming is accomplished by venting the noncondensable gas, which would otherwise form an arterial bubble, through capillary-sized holes in a foil-walled section of the artery at the evaporator end.

Several questions on the priming method required visual observation for answers. The most important unanswered question was why the computer-predicted fluid charge is insufficient for the arteries to prime. The glass heat pipe was used to uncover the source of the problem and to test a solution. Other questions were:

- Is a heat load sufficiently low for priming still high enough to convect an arterial bubble along the artery and into the priming foil where it would vent?
- Can excess liquid in the vapor space arrive at the priming foil, submerge it and thus prevent gas venting before the artery has primed?
- If a bubble is prevented from venting because the foil is submerged, will application of a heat load result in recession of the excess liquid and venting of the bubble?

5.1 DESIGN AND FABRICATION OF APPARATUS

The glass heat pipe to be used in the experimental study was designed and fabricated on the previous contract and it is described in Reference 5.1. The main component of the apparatus is a 1.9-cm-O.D. (0.752-inch-I.D.) 1.3-cm-I.D. (0.515-inch-I.D.) glass tube, 109 cm (43 inches) long, with machined stainless-steel end fittings. Research in the present program was limited to methanol which is the working fluid in the heat pipes currently being built by TRW for spacecraft VCHP applications.

The cross section of the heat pipe is shown in Figure 5-1. The heat pipe is designed to closely model the two-artery/slab-wick heat pipes used on the experimental sounding-rocket heat pipes. The artery is spot welded to one side of the felt-metal slab wick and a sheathed rod heater is inserted into a double layer screen casing that is spot-welded to the other side of the wick. The unheated end of the heater passes through and is brazed into the evaporator end cap. In the condenser region, a stainless-steel cooling loop extends along the opposite side of the wick as the artery. It passes through and is brazed into the condenser end cap. A sheathed thermocouple extends into the adiabatic section so the vapor temperature can be monitored.

5.2 EXPERIMENTAL RESULTS

The experimental effort was first aimed at uncovering the cause of the discrepancy between computer predicted fluid charges and the larger charges actually required for the heat pipes to prime. As shown in Figure 5-2(a), the foil-walled evaporator end of the artery (which we call a priming foil) has spiral rows of 0.0254-cm-diameter (0.010-inch-diameter) holes. The foil thickness is 0.00127-cm (0.0005 inches).

Priming tests consisted of first elevating the evaporator end of the glass heat pipe sufficiently so that the artery empties. A low heat load was applied. Then the evaporator end was lowered until the screen walled portion of the artery had filled with liquid. The elevation of the evaporator end relative to the condenser end was measured with a cathetometer. The evaporator end was lowered further until the foil-walled portion filled, and the evaporator elevation was measured again. Figure 5-3 shows the results at several heat loads. The crucial finding is that the evaporator end must be depressed 0.25-cm to fill the priming foil after the screen-walled portion has primed. Previous computer predictions of required fluid inventories for priming, however, were based on the assumption that the screen-walled and foil-walled portion of artery have the same capillary pressure for priming, which is given by 4 x (surface tension)/(artery diameter). While the actual inside diameter of the foil region is 0.1854 cm (0.073 in.), the region behaves, as far as priming is concerned, as if its inside diameter were 0.244 cm (0.096 in.).

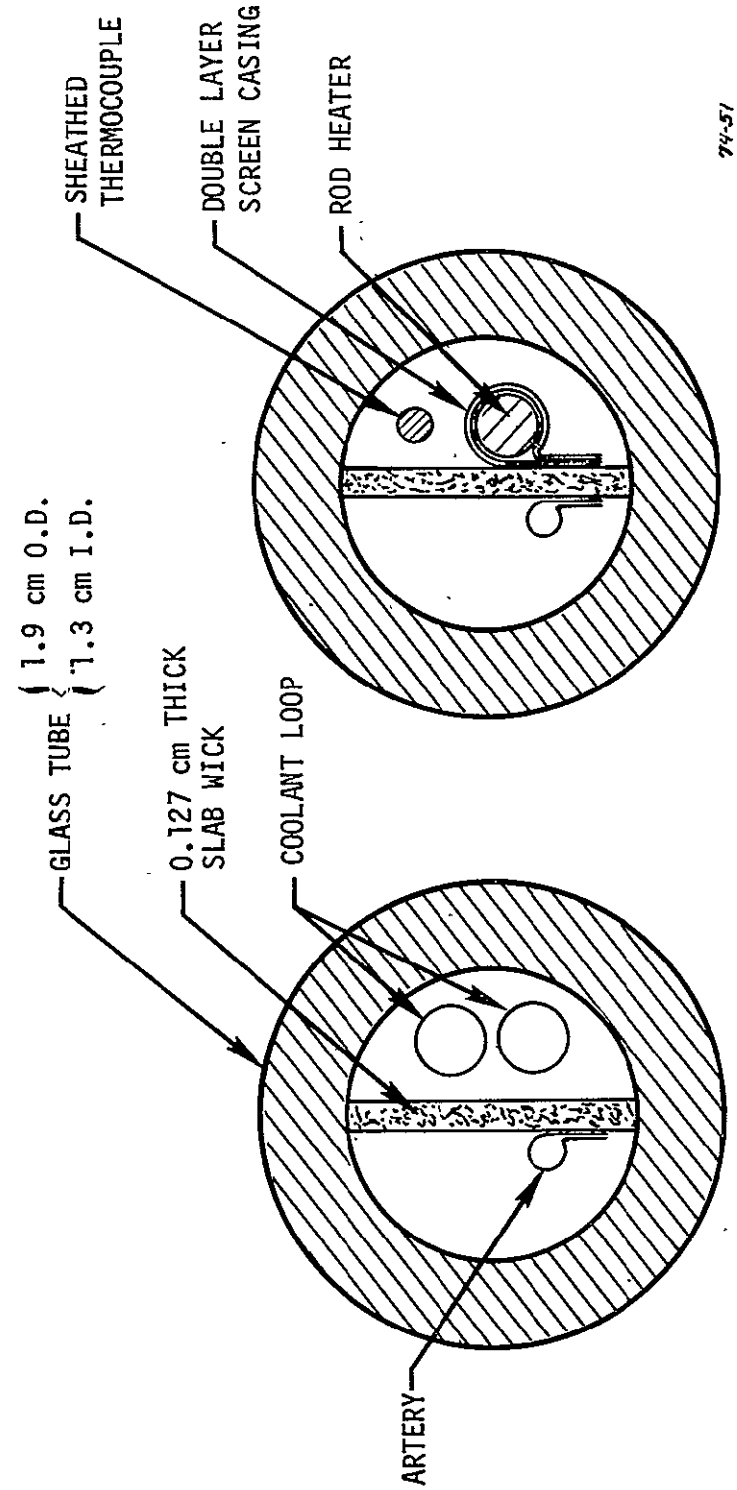

Figure 5-1. Cross Section of the Glass Heat Pipe in the Condenser and Evaporator Regions.

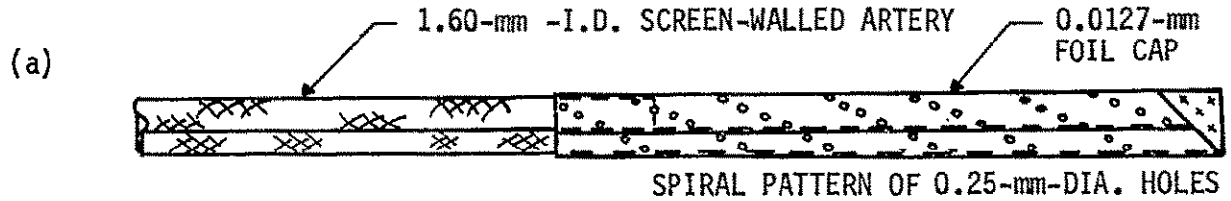

CTS PRIMING-FOIL DESIGN

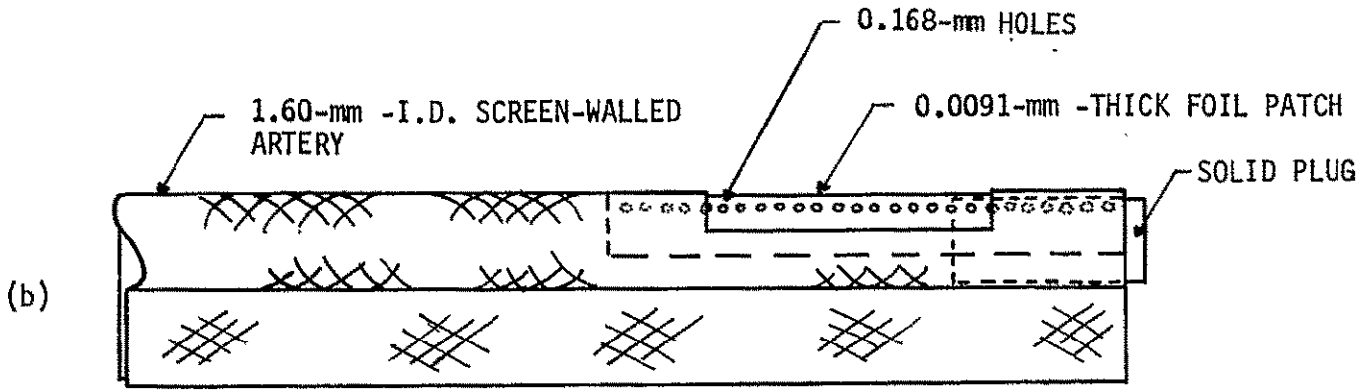

PATCH-OVER-WINDOW PRIMING FOIL

74-181-a

Figure 5-2. Priming Foil Designs.

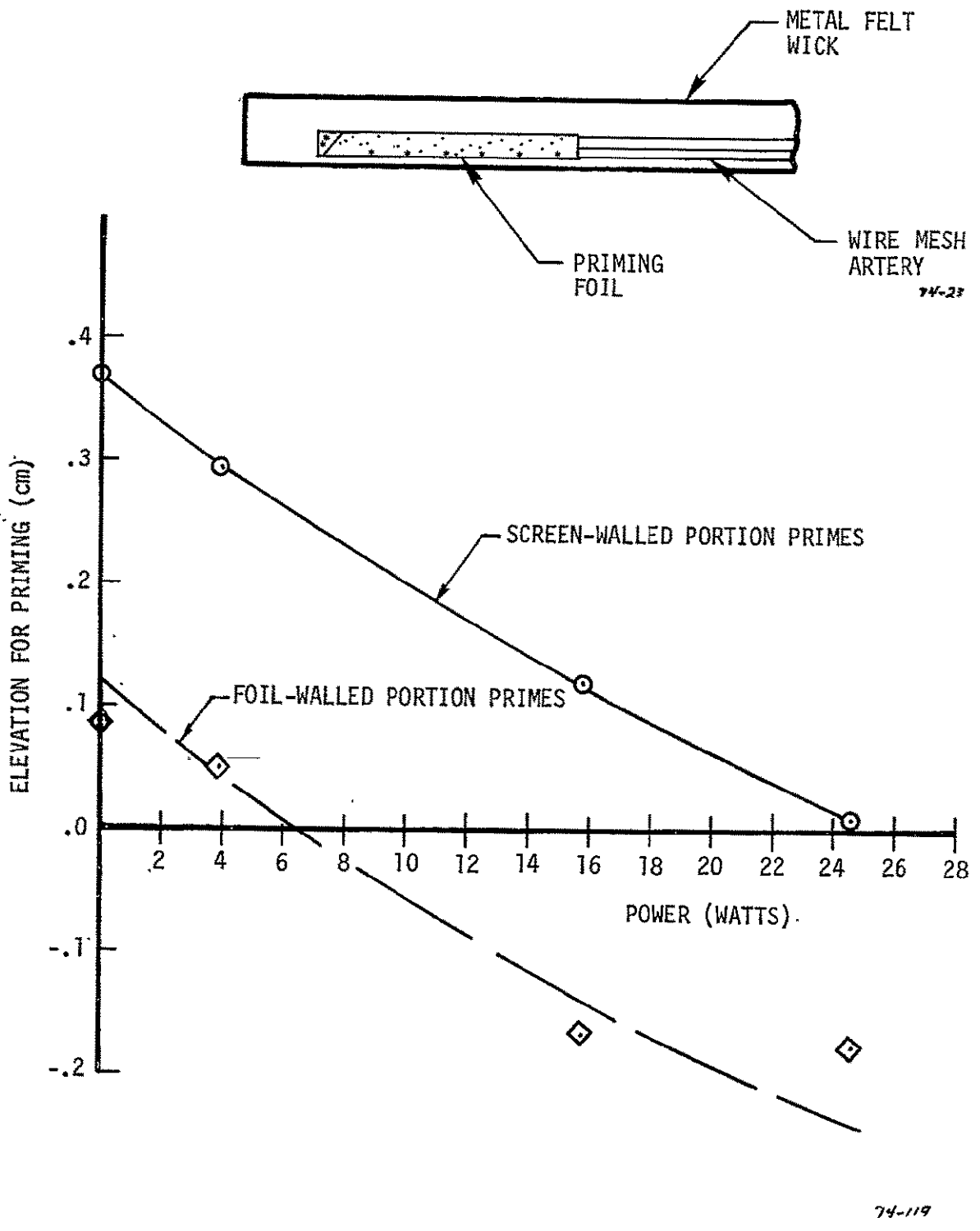

Figure 5-3. Priming Characteristics of Artery With Priming Foil.

The reason for MULTIWICK underpredicting the fluid charges for priming is now clear. For example, the previously predicted minimum charge for the sounding-rocket heat pipes to prime was 17.9 cm^3 of methanol, which was based on priming the 0.160 cm (0.063-in.) - I.D. artery. MULTIWICK now predicts a minimum charge of 26.9 cm^3 based on an effective inside diameter of 0.244 cm (0.096 in.) for the priming foil. The actual original charge of the heat pipes of 22.4 cm^3 was, in fact, found to be insufficient for priming. When the charge was increased above the predicted minimum to 27.9 cm^3, the heat pipes primed reliably.

It was suspected that the reluctance of the priming foil to fill might be due to a finite non-zero wetting angle between the methanol and the foil. Oxidization is known to improve wetting especially with water. As an attempt to improve the priming performance, the wick and artery were removed from the glass heat pipe and oxidized by firing in air. As shown in Figure 5-4, however, oxidization did not improve the performance.

It is now thought that the reluctance of the priming foil to fill is due to its slightly larger inside diameter of (0.073-in.) compared to the 0.160-cm-I.D. (0.063-in.-I.D.) of the main screen-walled portion and, more importantly, to the empty priming-foil holes pulling back by surface tension on the advancing meniscus as it crosses them. A new priming foil, shown in Figure 5-2(b), was designed to partially overcome these problems. The priming foil consists of a foil patch with a single row of holes, spot-welded inside the screen-walled artery over a small window. The inside diameter of this design is essentially the same as that of the artery, and there is at most only one hole at any axial location along the priming foil to impede the advancing meniscus. Results of priming tests of this configuration, as displayed in Figure 5-4, show that a hydrostatic head reduction necessary to fill the priming foil is 0.09 cm. This small reluctance to prime is desirable to ensure that the priming foil remains empty to vent gas until the entire screen-walled artery has primed. Although the actual inside diameter of the priming foil is that of the artery (0.160 cm or 0.063 in.), its effective inside diameter for priming is 0.183 cm (0.072 in.).

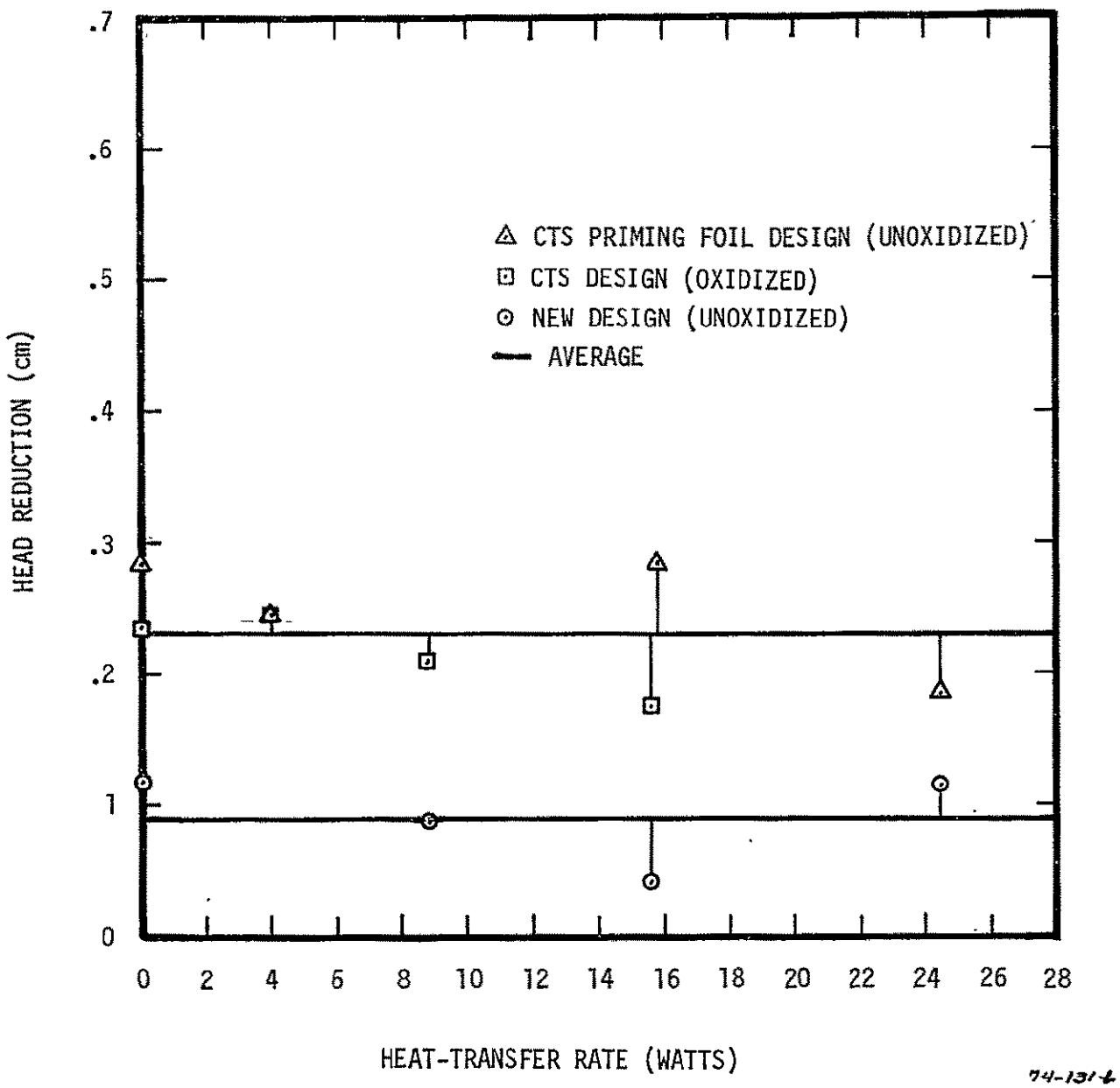

Figure 5-4. Required Hydrostatic Head Reduction to Prime Foiled-Walled Region.

In addition to having improved priming performance, the new priming foil was constructed of thinner foil (0.000914 cm or 0.00036 in.) that allows a smaller capillary hole size (0.0152 cm or 0.0066 in.). In comparison, the foils used for the sounding-rocket heat pipes were 0.00127 cm (0.0005 in.) thick with a capillary hole size of 0.0254 cm (0.010 in.). The small holes in the new design result in a 52% increase in heat-pipe capacity.

The next question investigated concerned convection of arterial bubbles. A bubble was trapped in the artery by raising the condenser end of the heat pipe high enough to empty the artery, and then leveling. The condenser end of the artery does not have a priming foil, and hence a bubble was trapped there.

A heat load was applied in attempt to convect the bubble to the evaporator end. Several runs were made for various heat loads and initial bubble sizes and locations. The results indicate that bubble convection was impossible at heat loads and evaporator elevations low enough for priming.

Bubbles were observed to convect at heat loads greater than for priming; however, when the bubbles entered the priming foil and vented, the artery would empty of liquid.

As a consequence of these results, for actual heat-pipe operation any arterial bubble that might exist would have to be cleared by applying a heat load in excess of the critical priming load, but below the maximum open-artery load. Then the load is reduced sufficient for priming. Another approach is to purposely ignore the existence of any arterial bubble. If a bubble did exist, a burnout would result the first time the heat load was increased above the open-artery capacity. Powering down below the critical priming load would result in successful priming because any bubbles would be convected to the evaporator end.

The next question investigated was concerned with the possibility of excess liquid in the vapor space flooding the venting holes of the priming foil. The evaporator end of the deprimed heat pipe was quickly dropped to level or even below level in attempt to trap a bubble by excess liquid submerging the priming foil. In every attempt, however, the artery completely primed before the venting holes were flooded. Failure to prime due to venting-hole flooding does not appear to be a problem.

5.3 CONCLUSIONS

The glass heat pipe has furthered our understanding of priming. The current research effort for a methanol, slab-wick, priming-foil/artery heat pipe has shown that:

- The priming-foil design used for the sounding-rocket experiment (and CTS) primes as if its I.D. were 0.244 cm (0.096 in.) instead of its actual I.D. of 0.185 cm (0.073 in.).
- The larger effective I.D. explains the required fluid charge for priming being significantly larger than previously predicted.
- The large effective I.D. is due to holes in the priming foil imposing a surface-tension retarding force on the advancing meniscus.
- By placing the priming foil with a single row of holes inside a "window" in the artery, the priming foil effective I.D. is reduced to 0.183 cm (0.072 in.), which is only slightly larger than the artery I.D.
- To clear an arterial bubble that has somehow been trapped somewhere along the artery other than in the priming foil, a heat load in excess of the critical priming load is required.
- Excess liquid could not block the priming-foil holes to prevent venting - venting always occurred before the holes were flooded.

5.4 REFERENCES

5.1 Eninger, J.E., "Sounding-Rocket Heat-Pipe Experiment," TRW Report No. 26263-6008-RU-00, December 30, 1974.

6.0 DEVELOPMENT OF HIGH-CAPACITY NON-ARTERIAL HEAT PIPES

High capacity in ambient-temperature heat pipes can be attained with the use of arteries, which simultaneously provide high capillary pressure and low flow resistance for the condensed liquid. Arterial heat pipes, however, have several disadvantages, especially if they are also gas-loaded variable-conductance heat pipes. In fact, arteries will not function at all for ammonia VCHP's evidently because of pressure fluctuations that occur as a result of instability of the gas front, Reference 6.1. With fluids such as methanol that can be used, priming foils are required to vent the noncondensable gas and rigid leveling requirements are necessary during test to prime the arteries.

Conventional, non-arterial heat pipes are in general more reliable and easier to test than arterial heat pipes; however, they have a far lower capacity. A task on the current contract calls for development of a high-capacity non-arterial heat pipe by optimally varying the porosity of the wick along its length. The limited capacity of the conventional non-arterial heat pipe is due to the fact that the two factors governing wick performance, the capillary-pressure limit and the permeability, are related inversely. Thus, a decrease in the porosity of the wick will increase the capillary-pressure limit but decrease the permeability. A conventional wick whose porosity is uniform along its length has an unnecessarily high capillary-pressure limit and hence an unnecessarily low permeability everywhere except at the evaporator end where the limit is reached at the maximum heat load. By varying the porosity, the capillary-pressure limit is only as high as required to sustain the local vapor-liquid pressure difference and, thus, the permeability is as high as possible everywhere along the length of the wick. The potential increase in capacity depends on the particular application, but it is typically greater than a factor of two. A particular goal is the development of a half-inch diameter all-aluminum heat pipe for use with ammonia that has a heat-transport capacity in excess of 250 watt-m. Such a heat pipe was fabricated and although its measured capacity of 226 watt-m fell short of the goal, the computer model predicts that with a refined porosity variation more than 330 watt-m will be achieved.

A parallel theoretical and experimental study of flow through fibrous wicks was first carried out that provided the basis of the computer program GRADE (Reference 6.2) for the design and analysis of graded-porosity wicks. Two aluminum/ammonia heat pipes were fabricated and tested; one of which had a graded-porosity wick and the other, for purposes of comparison, had a uniform-porosity or homogeneous wick. In addition, two half-inch-diameter stainless-steel cryogenic heat pipes for use with ethane or methane were designed and fabricated. These are for processing and testing by ARC.

6.1 THEORETICAL AND EXPERIMENTAL STUDY OF CAPILLARY FLOW THROUGH A FIBROUS WICK

In this section we present the results of the research on capillary flow through fibrous materials such as metal felt, compressed metal fibers, layers of screen mesh, etc. The theoretical model was originated on another program sponsored by the Naval Air Systems Command, Contract 00019-72-C0340, Reference 6.3. However, it was extensively corrected and expanded both theoretically and experimentally on the present program, so the complete work is presented here (also see Reference 6.4).

In addition to developing expressions for the capillary-pressure limit and permeability for a saturated wick, hysteresis in emptying and filling and flow through a partially-saturated wick is also included. A partial-saturation model is needed to predict heat-pipe performance when there is an insufficient volume of liquid to completely fill the wick, which can occur, for example, as the result of liquid contraction in a heat pipe operating below its design temperature. In addition, wicks operating near their capillary-pressure limit become partially saturatec before failure. Not only is the permeability lowered in the partially saturated region, but also the liquid given up can contribute to vapor-space slugging and flooding of the condenser. A model of hysteresis in the wick's capillary behavior for filling and emptying is needed to predic the maximum heat-transfer rate under which a burned-out heat pipe will recover, as well as to design wicks that can prime in a gravitational field.

It was apparent that existing models of saturated wicks were inadequate for extension to a theory of partial saturation. For example, the generally used expression given by Tien and Sun (Reference 6.5) for the wick's capillary-pressure limit in terms of the fiber diameter δ, surface tension σ, permeability K and porosity ε is

$$P_C = \frac{4\sigma}{\delta + \sqrt{32K/\varepsilon}} \qquad [6.1]$$

The radical in this expression represents the "pore size" of the wick; however, microscopic examination reveals nothing in a fibrous material that even resembles a pore. For the permeability, the generally used expression is that given by Schmidt (Reference 6.6):

$$K = \frac{\delta^2}{122} \frac{\varepsilon^3}{(1-\varepsilon)^2} \qquad [6.2]$$

This expression is based on Kozeny hydraulic-diameter theory that assumes a porous material resembles tortuous channels. Although this applies in the low-porosity limit, for high porosities the situation is rather that of flow over an aggregate of randomly distributed cylinders. Although the above expressions (6.1) and (6.2) have been useful for correlating experimental data, the assumptions on which they are based do not reflect the actual geometry of fibrous materials.

In the present theory, the wick is idealized as a random distribution of cylindrical fibers. Capillary pressure is generated by surface tension acting on the individual fibers where they penetrate a vapor-liquid interface, and flow resistance is generated by the drag on the fibers. Hysteresis in capillary pressure is accounted for by a factor H that is unity if the wick is filling and an empirically found value greater than unity if emptying. To model partial saturation, the wick is envisioned as consisting of local regions each having uniform porosity. The porosities of these regions, however, are assumed to have a statistical distribution with a standard deviation σ_d. The theoretical expressions developed for a saturated wick are applied to the local regions.

Four experiments were conducted to test the theoretical results. By dimensional analysis one can show that the capillary-pressure limit of a saturated wick is proportional to σ/δ and the permeability to δ^2. The crucial question, though, is how well the theory predicts the dependence on porosity. To answer this question, the first two experiments measure the capillary-pressure limit and permeability of a set of aluminum-fiber wicks that were identical except for their porosities, which varied from 0.6 to 0.9 . The capillary-pressure experiment employed a novel technique that provides a simple method of measuring the empirical hysteresis constant H and porosity standard deviation σ_d from curves of the wick's weight vs its depth of submersion in liquid. The third experiment* used β-ray absorption to directly measure the liquid fill vs vapor-liquid pressure difference of a partially saturated metal-felt wick. The same wick was instrumented with close-spaced pressure taps in the fourth experiment* to provide the data required to measure permeability in the partially-saturated state.

Besides providing a quantitative test for the theory, the experimental results indicate that the hysteresis factor H is independent of fiber diameter and porosity, and that its value is 1.96. In other words, fibrous wicks generally have approximately twice the capillary-pressure limit for emptying than for filling. Further, the porosity standard deviation σ_d appears to be independent of fiber diameter, but proportional to one minus the porosity.

The theoretical expressions for a saturated wick were used to optimize the wick with respect to its porosity and fiber diameter. The results show that for a specified capillary-pressure limit, a porosity of 0.79 gives the highest permeability. The corresponding fiber diameter is set such that the expression for the capillary-pressure limit gives the specified value. Wicks previously used in heat pipes were often far from optimum.

* These experiments were carried out on the Navy-sponsored program.

6.1.1 Capillary Pressure

The class of materials we are considering is idealized as consisting of long fibers with circular cross sections of diameter δ. Each fiber is divided into segments of length ℓ. The centerpoints of these segments are assumed to be randomly distributed in space with a number density n. The orientation of each segment is specified by spherical coordinates (ϕ,θ) as shown in Figure 6-1. Two types of orientation distributions are considered. For a two-dimensional distribution, which we specify by $J=2$, all fibers lie parallel to the same plane, such as the x-z plane, so we take $\theta=0$ for each segment. The distribution of ϕ, however, is random. An example of such a material is a fibrous mat that is fabricated by alternately laying down and pressing fibers in layers. For a three dimensional distribution, which we specify by $J=3$, both ϕ and θ are random.

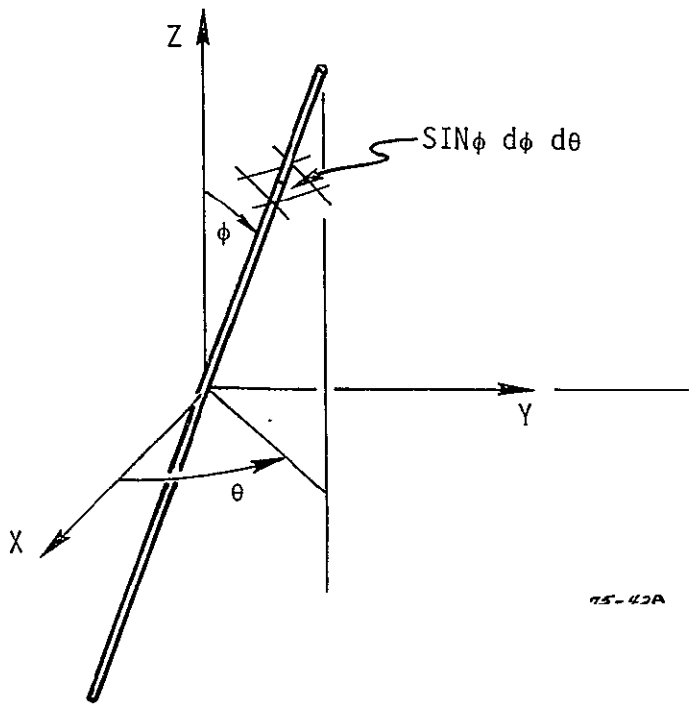

Figure 6-1. A Fiber Segment With Orientation (ϕ,θ) Penetrating an Elemental Area of a Unit-Radius Hemisphere.

Presently, we will need an expression for the probability that the orientation of a fiber segment is between ϕ and $\phi + d\phi$. For a two-dimensional distribution, the probability is uniform and it is simply $d\phi/(\pi/2)$. For a three-dimensional distribution, consider that the probability a segment is oriented such that it penetrates the elemental area of a unit-radius hemisphere is the ratio of the elemental area to the total area of the hemisphere, that is, $(\sin\phi \; d\phi \; d\theta)/2\pi$. To obtain the probability that a fiber segment is oriented between ϕ and $\phi + d\phi$ irrespective of θ, we integrate from $\theta=0$ to 2π and obtain $\sin\phi \; d\phi$ The two-and three-dimensional results for the probability of orientation between ϕ and $\phi + d\phi$ are combined in the following expression:

$$[(3-J)\; 2/\pi + \; (J-2) \; \sin\phi] \; d\phi \qquad [6.3]$$

We begin the calculation of the capillary-pressure limit by estimating the surface-tension force acting on a single fiber that penetrates the vapor-liquid interface. As shown in Figure 6-2, the z axis is normal to the interface and the wetting angle is assumed to be zero.

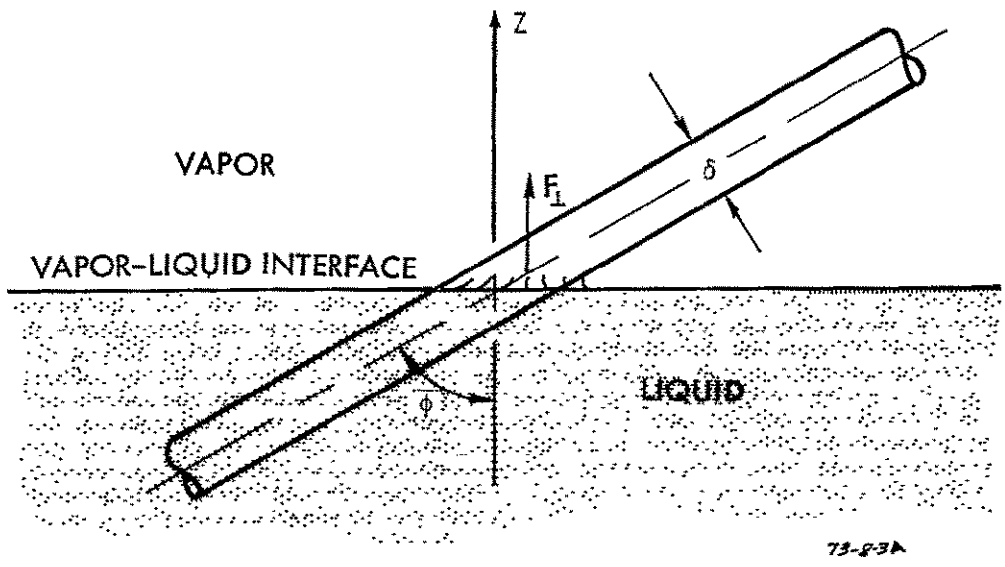

Figure 6-2. Fiber Penetrating a Liquid-Vapor Interface at Orientation ϕ.

The component force $F_\perp$ in the z direction is taken as the product of the surface tension σ and the circumference of the ellipse formed by the intersection of the fiber and the plane, which is given approximately by

$$F_\perp = \frac{\pi\sigma\delta}{\cos\phi}\sqrt{(1 + \cos^2\phi)/2} \qquad [6.4]$$

We must now find the number of fibers that penetrate an area of the interface with an orientation between ϕ and $\phi + d\phi$. Consider, as shown in Figure 6-3, a large area A of the interface with a volume element A dz located at a distance z from it. The number of segments whose centerpoints lie within the volume is n A dz. Not all of these will penetrate the area, only those for which $\phi < \cos^{-1} 2|z|/\ell$. Consider that the number of segments (1) whose centerpoints lie within the volume A dz, (2) that penetrate the interface, and (3) whose orientation is from ϕ to $\phi + d\phi$ [expression (3)] is

$$d^2N_A = n\,A\,dz\,U(\phi^*-\phi)[(3-J)2/\pi + (J-2)\sin\phi]\,d\phi \qquad [6.5]$$

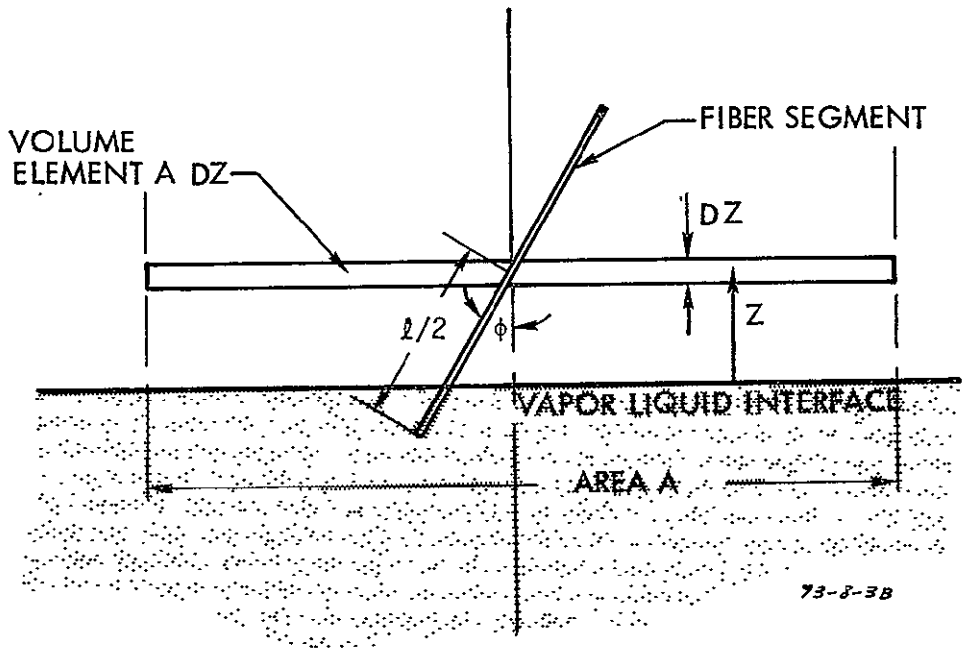

Figure 6-3. Volume Element Above a Vapor-Liquid Interface.

where $\phi^* = \cos^{-1} 2|z|/\ell$, and $U(\text{arg}) = 0$ if $\text{arg} < 0$ and $+1$ if $\text{arg} \geq 0$. The number of fibers penetrating a unit area with orientations between ϕ and $\phi + d\phi$ is obtained by integrating Equation 6.4 from $z = -\ell/2$ to $\ell/2$ and then dividing the result by A , which gives

$$dN = [(3-J)2/\pi + (J-2)\sin\phi]\, n\ell \cos\phi \, d\phi \qquad [6.6]$$

The combination $n\ell$ is eliminated from Equation 6.6 in favor of the porosity ε and the fiber diameter δ by equating the total volume taken up by fibers in a unit volume to $1-\varepsilon$, which leads to

$$n\ell = 4(1-\varepsilon)/(\pi\delta^2) \qquad [6.7]$$

With this result Equation 6.6 becomes

$$dN = [(3-J)2/\pi + (J-2)\sin\phi] \frac{4(1-\varepsilon)}{\pi\delta^2} \cos\phi \, d\phi \qquad [6.8]$$

The sum of the forces on those fibers penetrating a unit area of interface with orientations between ϕ and $\phi + d\phi$ is $dF = F_\perp \, dN$, where $F_\perp$ and dN are given respectively by Equations 6.5 and 6.8. The capillary-pressure limit P_C generated by the wick is obtained by integrating dF from $\phi = 0$ to $\phi = \pi/2$, and then dividing by the liquid area per unit area of interface, which is easily shown to be ε . The resulting expression is

$$P_C = \{(3-J)\frac{8}{\pi} E(\sqrt{2}/2, \pi/2) + (J-2)[2+\sqrt{2}\ \ln\ (1+\sqrt{2})]\} \times \left[\frac{(1-\varepsilon)}{\varepsilon} \frac{\sigma}{\delta}\right] \qquad [6.9]$$

where $E(k, \pi/2)$ is the complete elliptic integral of the second kind, and its value is 1.3506 for $k = \sqrt{2}/2$.

The above expression is appropriate for liquid filling a wick. For liquid emptying a wick a greater capillary pressure is generated, because the interface has the chance to recede to a favorable configuration among the fibers. We account for hysteresis by introducing an empirical factor H that is unity if the wick is filling and an experimentally found value greater than unity if emptying, which gives Equation 6.9 after the expression in braces is numerically evaluated

$$P_c = [3.4393(3-J) + 3.2465(J-2)] \; H \frac{(1-\varepsilon)}{\varepsilon} \frac{\sigma}{\delta} . \qquad [6.10]$$

In the preceding discussion we assumed that the wick is either empty or full depending on whether the pressure difference across the vapor-liquid interface, which hereafter we will call capillary stress, is greater or less than the wick's capillary-pressure limit. In fact, the fractional fill of a wick, or saturation fraction S, varies continuously over a range of stress. To model partial saturation, we assume that a wick has a statistical distribution of local porosity, and that those local regions with a relatively low porosity have greater tendency to fill with or hold liquid than ones with a relatively high porosity. A conceptual procedure to find the porosity distribution is to sample the porosity of a wick with a small control volume. The fraction of samples having porosities between ε and $\varepsilon + d\varepsilon$ is $f(\varepsilon)\, d\varepsilon$. The mean value of the probability distribution $f(\varepsilon)$ is independent of the control-volume size and is equal to the overall porosity ε_0 of the wick. The standard deviation σ_d, however, is dependent on the control-volume size, and because of our lack of knowledge of the correct value for its size, the standard deviation will be an experimentally found parameter in the theory.

For a given value of capillary stress P, a local region is filled with liquid if the porosity is low enough that the capillary-pressure limit P_c given by Equation 6.10 is greater than P. A critical value ε^* that just allows a region to be filled is obtained by solving Equation 6.10 for ε and replacing P_c by P, which results in

$$\varepsilon^* = \left\{ 1 + \frac{P\delta/\sigma}{[3.4393(3-J) + 3.2465(J-2)]H} \right\}^{-1} \qquad [6.11]$$

The fraction of a unit volume of wick having a porosity between ε and $\varepsilon + d\varepsilon$ is $f(\varepsilon)\, d\varepsilon$, and this fraction is filled with liquid only if $\varepsilon<\varepsilon^*$. The amount of liquid held in this fraction is $\varepsilon\, f(\varepsilon)\, d\varepsilon$. We obtain the total amount of liquid held in the unit volume by integrating this expression from $\varepsilon = 0$ to ε^*. The saturation fraction $S(P)$ is the ratio of the actual amount of liquid held in the unit volume at a stress P to the amount ε_o when it is completely filled, hence it is given by

$$S(P) = \frac{1}{\varepsilon_o} \int_0^{\varepsilon^*} \varepsilon\, f(\varepsilon)\, d\varepsilon \qquad [6.12]$$

A normal distribution is assumed for the porosity, which allows us to characterize f by two parameters, the overall porosity ε_o and the standard deviation σ_d. Thus, we write

$$f(\varepsilon) = \frac{1}{\sqrt{2\pi}\sigma_d} e^{-(\varepsilon-\varepsilon_o)^2/2\sigma_d^2} \qquad [6.13]$$

In terms of the standardized normal distribution

$$f(z) = \frac{1}{\sqrt{2\pi}} e^{-z^2/2} \qquad [6.14]$$

and the standardized cumulative distribution

$$F(z) = \frac{1}{\sqrt{2\pi}} \int_{-\infty}^{z} e^{-t^2/2}\, dt \qquad [6.15]$$

the saturation fraction $S(P)$ given by Equation 6.12 can be written as

$$S(P) = F[(\varepsilon^*-\varepsilon_o)/\sigma_d] - \frac{\sigma_d}{\varepsilon_o} f\,[(\varepsilon^*-\varepsilon_o)/\sigma_d] \qquad [6.16]$$

where ε^* is given in terms of P by Equation 6.11. The curve of S vs P has two branches depending on whether P is increasing and the wick is emptying or P is decreasing and the wick is filling. In the former case, the hysteresis constant H in Equation 6.11 is taken as the experimentally found value greater than unity, and in the latter H is unity.

6.1.2 Capillary-Pressure Experiments

The apparatus for the experimental study of partial saturation is depicted schematically in Figure 6-4. β-rays emitted from a strontium-90 source penetrate the wick and are counted by a detector. The rate at which they are absorbed by liquid in the wick is a direct measure of the saturation fraction. The capillary stress is controlled hydrostatically by raising or lowering the liquid level in the glass cylinder. The liquid used was methanol. The test wick was a 1.27-mm slab of metal felt with a porosity of 0.835 , and an average fiber diameter of 0.0216 mm. Microphotographs show that the fibers are in a three-dimensional random distribution (J=3).

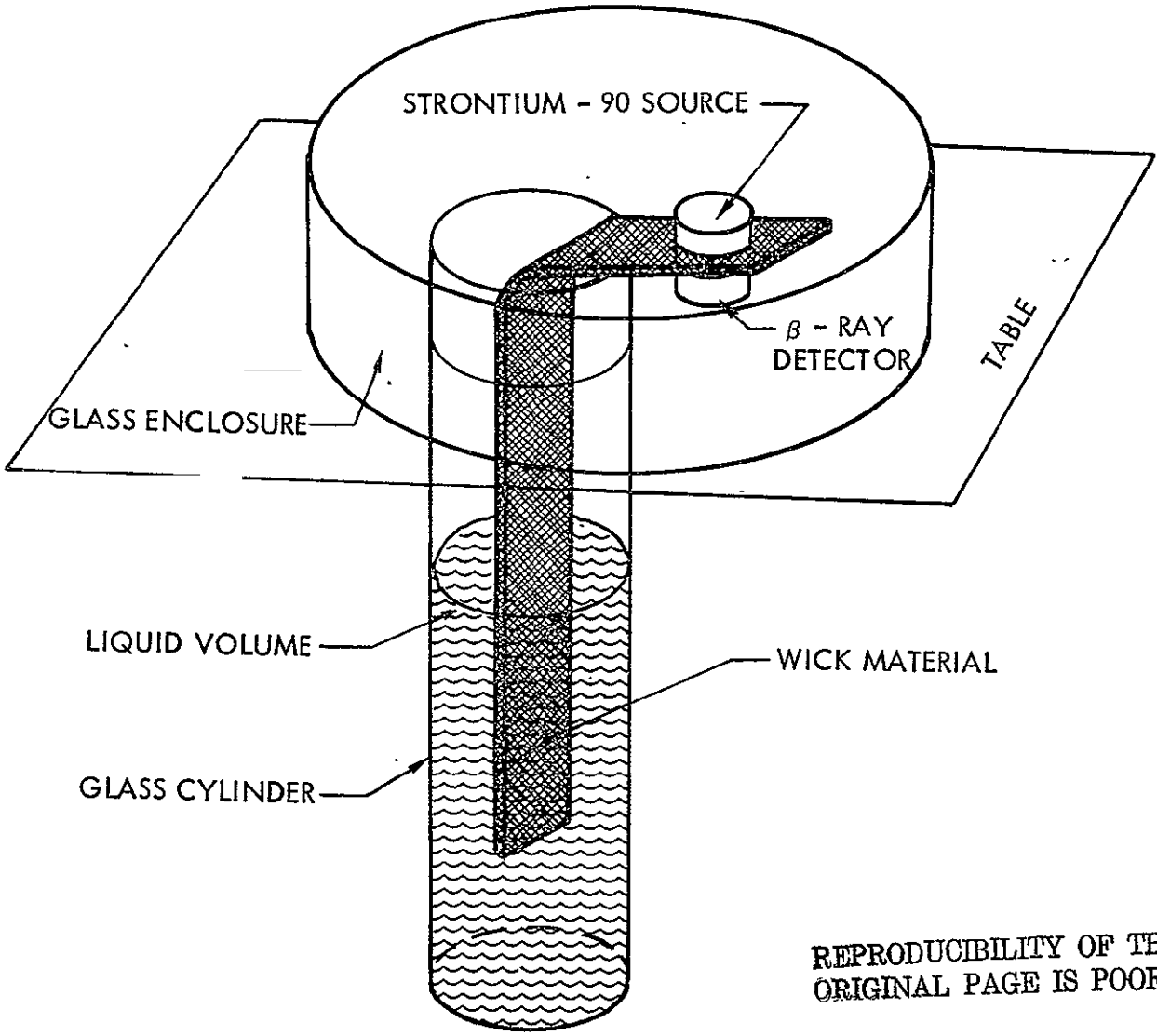

Figure 6-4. β-Ray Absorption Experiment for Measuring the Saturation Fraction as a Function of Capillary Stress. 73-8-4

The data displayed in Figure 6-5 give the measured saturation fraction S vs dimensionless stress $\overline{P} = P\delta/\sigma$ for both increasing and decreasing stress. The solid curves are from the theory (Equation 6.16). The empirical hysteresis constant H was taken as 1.955 to match the point on the increasing-stress curve where S is 0.5, and the standard deviation σ_d was taken as 0.0301 to match the slope of the curve at that point.

Another experiment was designed to test the theory over a wide range of porosity and to provide a simple procedure to find the empirical constants H and σ_d for a particular wick. A long strip of wick is suspended inside a glass cylinder from the weighing hook of a precision balance. As shown in Figure 6-6, the wick is weighed as a function of the height of its top edge above the liquid level in the cylinder. Two curves are generated depending on whether the level is rising or falling. For a wick of cross-sectional area A, perimeter p, length L, and fiber density ρ_f in a liquid of density ρ_ℓ, the expression for the weight with a length x of the wick above the liquid level is

$$W(x) = \rho_f g(1-\varepsilon_o)LA - \rho_\ell g(1-\varepsilon_o)(L-x)A + \rho_\ell g\varepsilon_o A \int_0^x S(\rho_\ell g\tilde{x})d\tilde{x} + p\sigma \ , \qquad [6.17]$$

where g is the gravatitional acceleration. The physical interpretation of the four terms to the right of the equal sign are, respectively, the total weight of the fibers, the bouyancy of those fibers below the liquid level, the weight of the liquid wicked up by capillary pressure, and the surface tension acting around the wick's perimeter. The slope of the curve W vs x is given by

$$W'(x) = \rho_\ell gA[1-\varepsilon_o + \varepsilon_o S(\rho_\ell gx)]. \qquad [6.18]$$

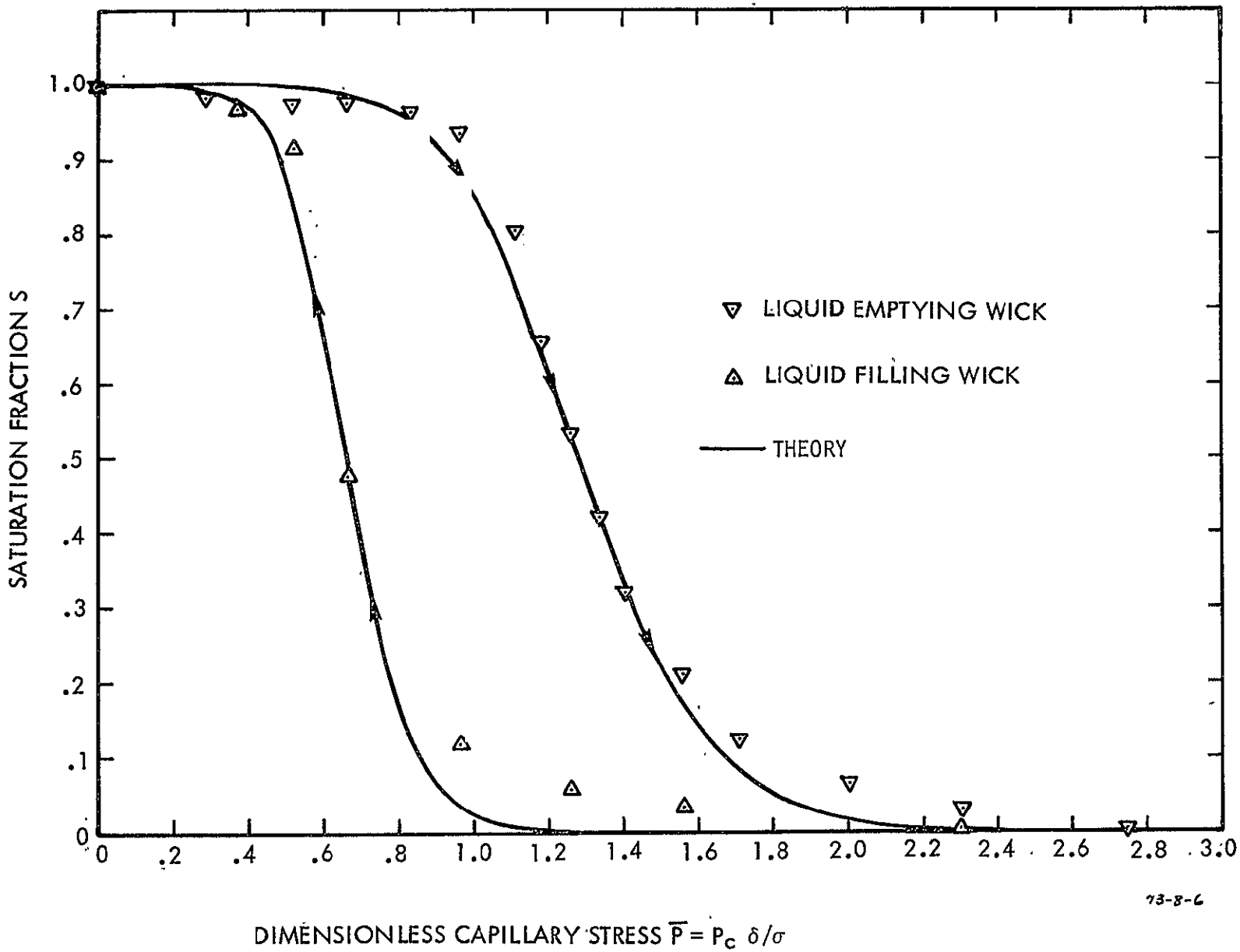

Figure 6-5. Theoretical and Experimental Results for Saturation Fraction as a Function of Capillary Stress.

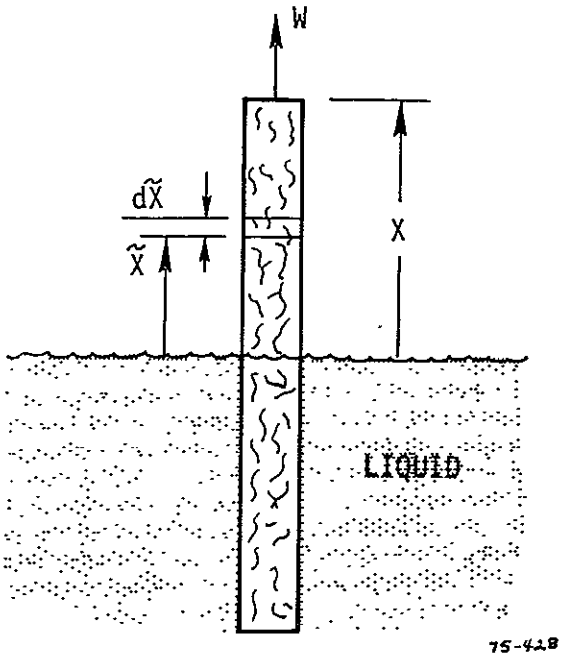

Figure 6-6. Wick-Weighing Experiment for Measurement of the Capillary-Pressure Limit.

The saturation fraction S approaches unity as the stress approaches zero, and S approaches zero as the stress becomes large. We expect from Equation 6.18, therefore, the data for W vs x to approach straight line asymptotes for $x \to 0$ and $x \to \infty$ with slopes given by $W'(x \to 0) = \rho_\ell g A$ and $W'(x \to \infty) = \rho_\ell g A(1-\varepsilon_o)$. This asymptotic behavior is apparent in Figure 6-7 which shows typical data for a wick with a porosity of 0.712 with acetone as the liquid. Of particular interest is the stress in terms of hydrostatic head at which the saturation fraction is 50%. This point occurs on the curve W vs x where the slope is half-way between the slope of the asymptotes, and it is found geometrically as shown in Figure 6-8. If we neglect the second term of Equation 6.16 on the basis that $\sigma_d/\varepsilon_o << 1$, then the stress corresponding to a 50% saturation fraction is also given theoretically by Equation 6.10 with ε equal to the wick's overall porosity ε_o

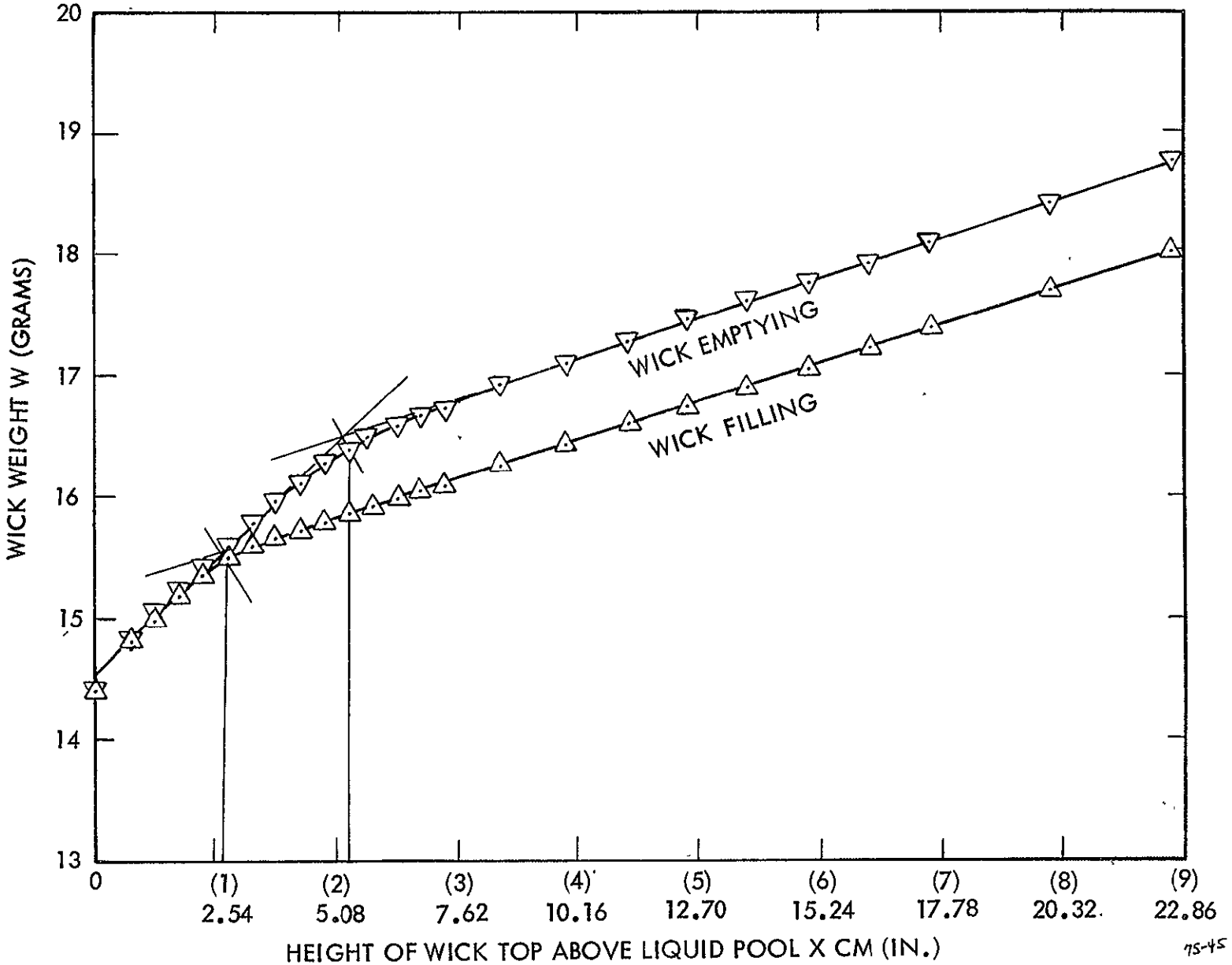

Figure 6-7. Typical Data From Wick-Weighing Apparatus.

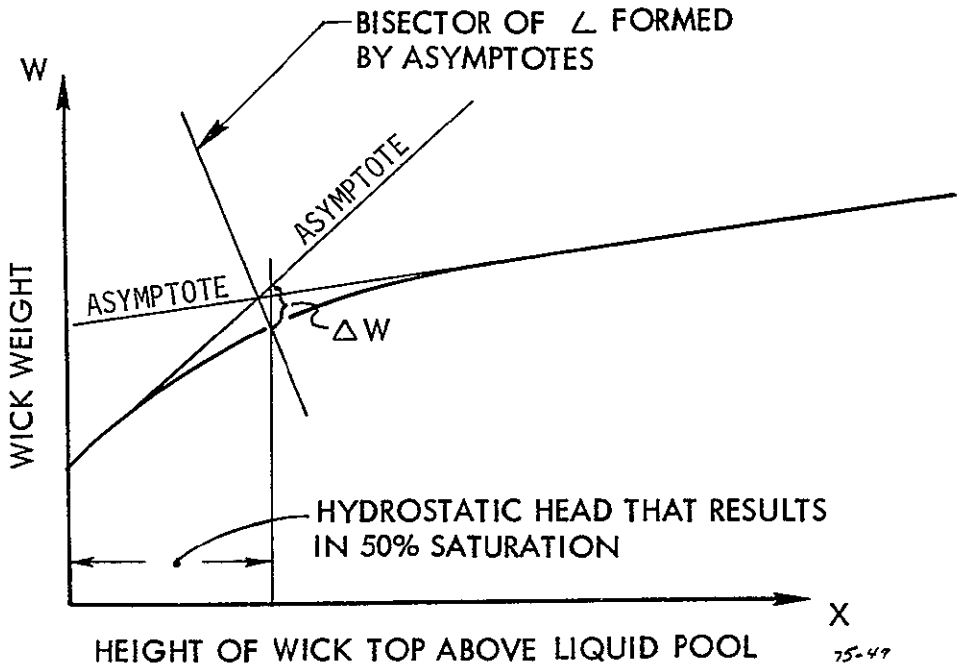

Figure 6-8. Geometrical Construction for Finding the Capillary Stress that Gives 50% Saturation and the Parameter ΔW that is a Measure of σ_d .

Experimental results for a set of aluminum-fiber wicks (0.127 mm fiber diameter) that vary only in porosity are compared to theory in Figure 6-9. The hysteresis constant H used is that found in the β-ray absorption experiment with metal felt. The agreement with data for the aluminum-fiber wicks indicates that the value for H of 1.955 is generally applicable to fibrous wicks independent of their porosity and fiber diameter. The theoretical curve of Tien and Sun (Reference 6.5) based on Equations 6.1 and 6.2 is also presented in Figure 6-9.

The extent to which the curve W vs x deviates from its asymptotes is a measure of the standard deviation σ_d. The theoretical expression for the deviation ΔW as defined geometrically in Figure 6-8 is given by

$$\Delta W = \rho_\ell g \varepsilon_o A \int_0^{x_o} [1-S(\rho_\ell g \tilde{x})] d\tilde{x} \qquad [6.19]$$

If in Equation 6.16 for S we neglect the second term to the right of the equal sign on the basis $\sigma_d/\varepsilon_o << 1$, then the following dimensionless expression for ΔW is obtained:

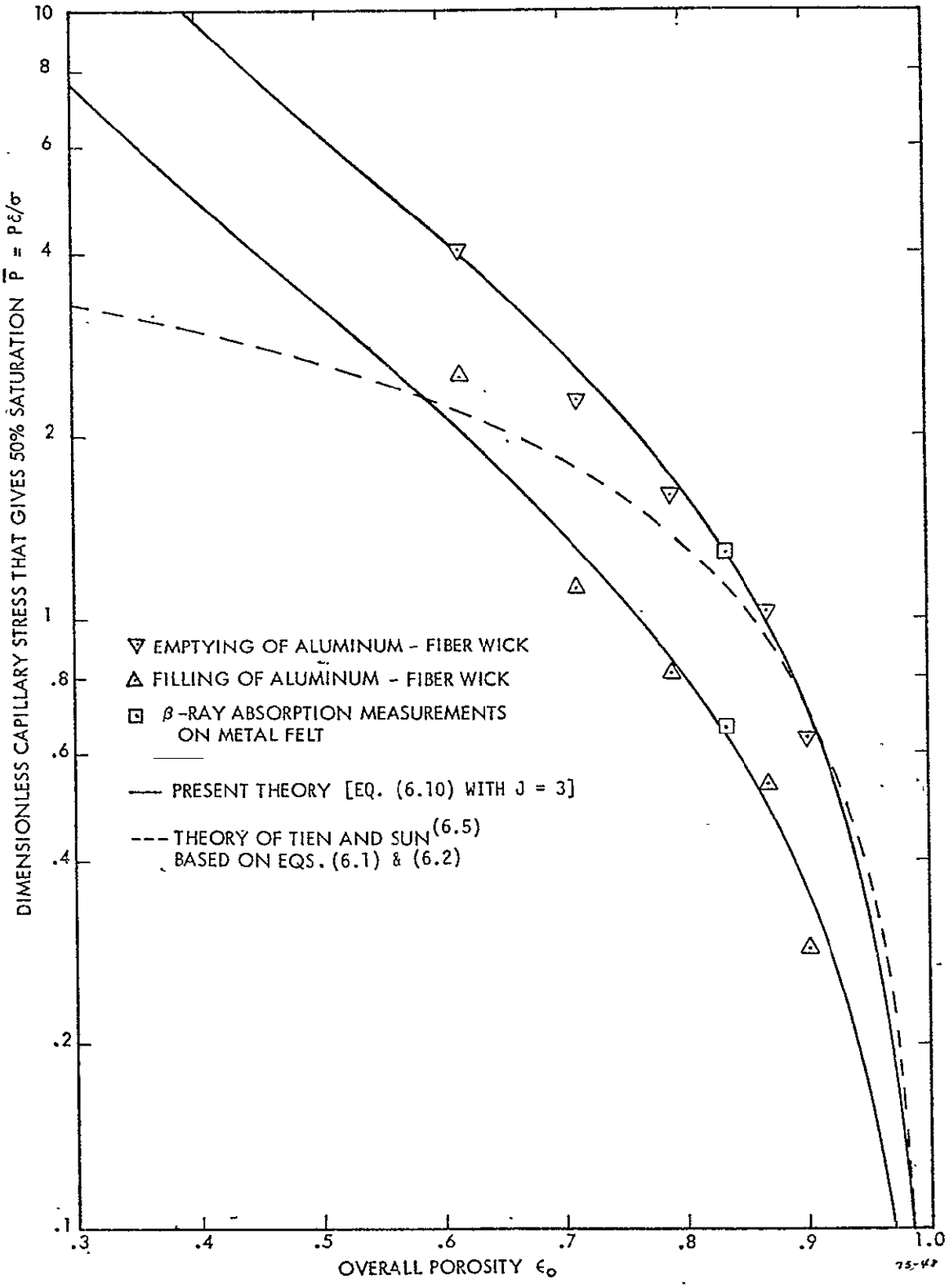

Figure 6-9. Experimental and Theoretical Results for the Capillary-Pressure Limit.

$$\Delta\overline{W} = \Delta W/(3.246H\sigma\varepsilon_o A/\delta) =$$

$$\frac{1}{2\varepsilon_o} - \frac{1}{\sqrt{2\pi}} \int \frac{1-\varepsilon_o}{\sigma_d} \frac{e^{-z^2/2}}{\varepsilon_o + \sigma_d z} dz \qquad [6.20]$$

The integral was evaluated numerically and the results, displayed in Figure 6-10, are used to find σ_d from the measured value of ΔW. Figure 6-11 displays σ_d vs ε_o for the wicks tested by both weighing and β-ray absorption. The standard deviation is seen to be independent of the fiber diameter and it correlates with the overall porosity by the formula

$$\sigma_d = 0.22(1-\varepsilon_o) \qquad [6.21]$$

The fact that both σ_d and H were found experimentally to be independent of fiber diameter gives credibility to the theoretical model. Since both constants are dimensionless, then by dimensional analysis they should be independent of the single dimensional parameter that characterizes the wick in our model, the fiber diameter.

6.1.3 Permeability

Our approach to permeability, which follows that of Happel, (Reference 6.7), is to calculate the drag on a single segment of fiber and then sum the drags on all segments in a unit volume. In relating the drags to the pressure gradient, however, we differ from Happel and obtain a modified expression for the permeability. Consider, as shown in Figure 6-12, a fiber segment inclined at an angle ϕ to the flow direction. Beavers and Sparrow (Reference 6.8) have shown that the non-linear inertial effects on flow through a fibrous media are negligible if the Reynolds number based on the square root of the permeability is less than unity. This is typically the case for heat-pipe operation, and therefore the flow is governed by the linear Stokes equation.

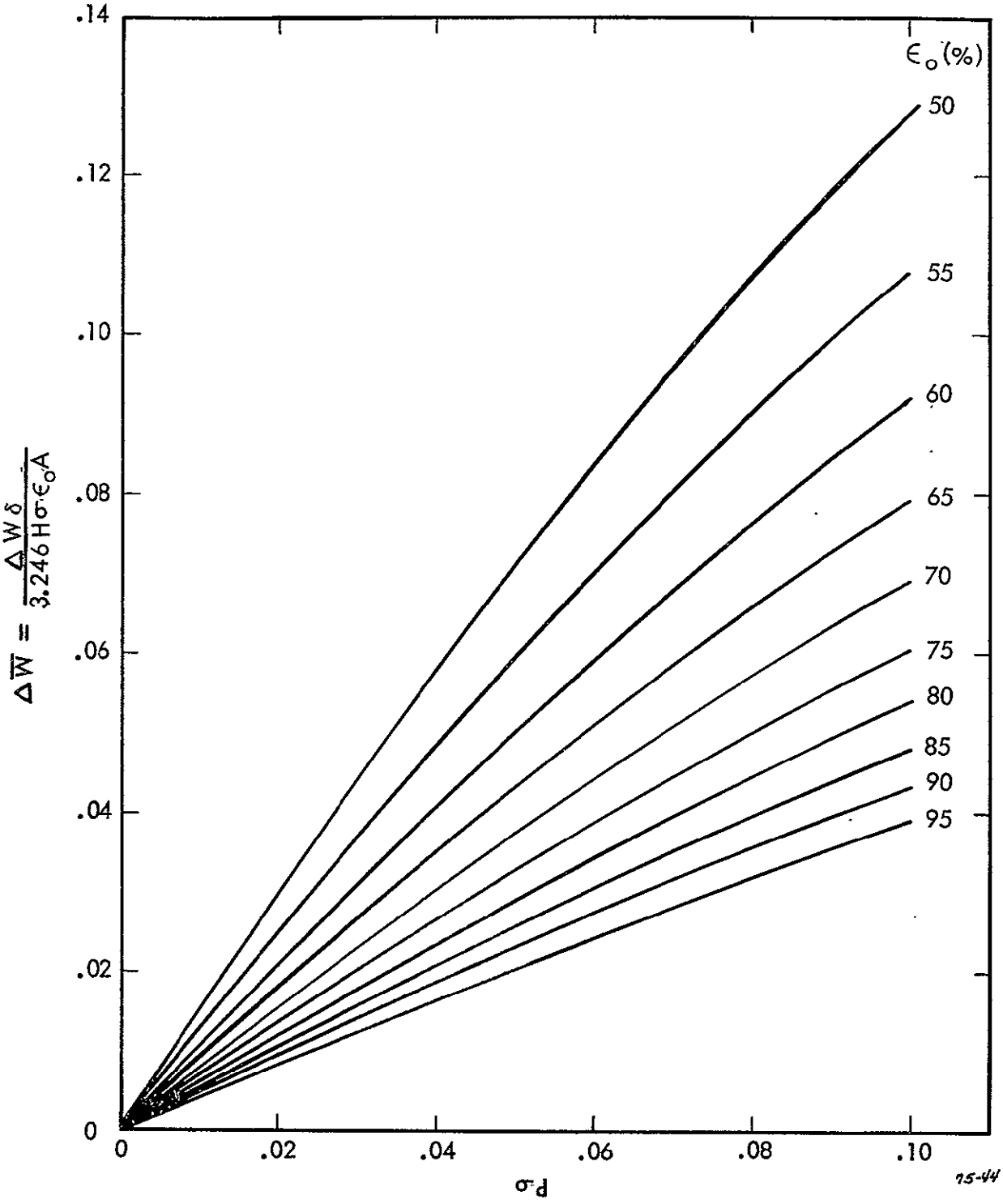

Figure 6-10. Curves for Finding the Porosity Standard Deviation σ_d from ΔW.

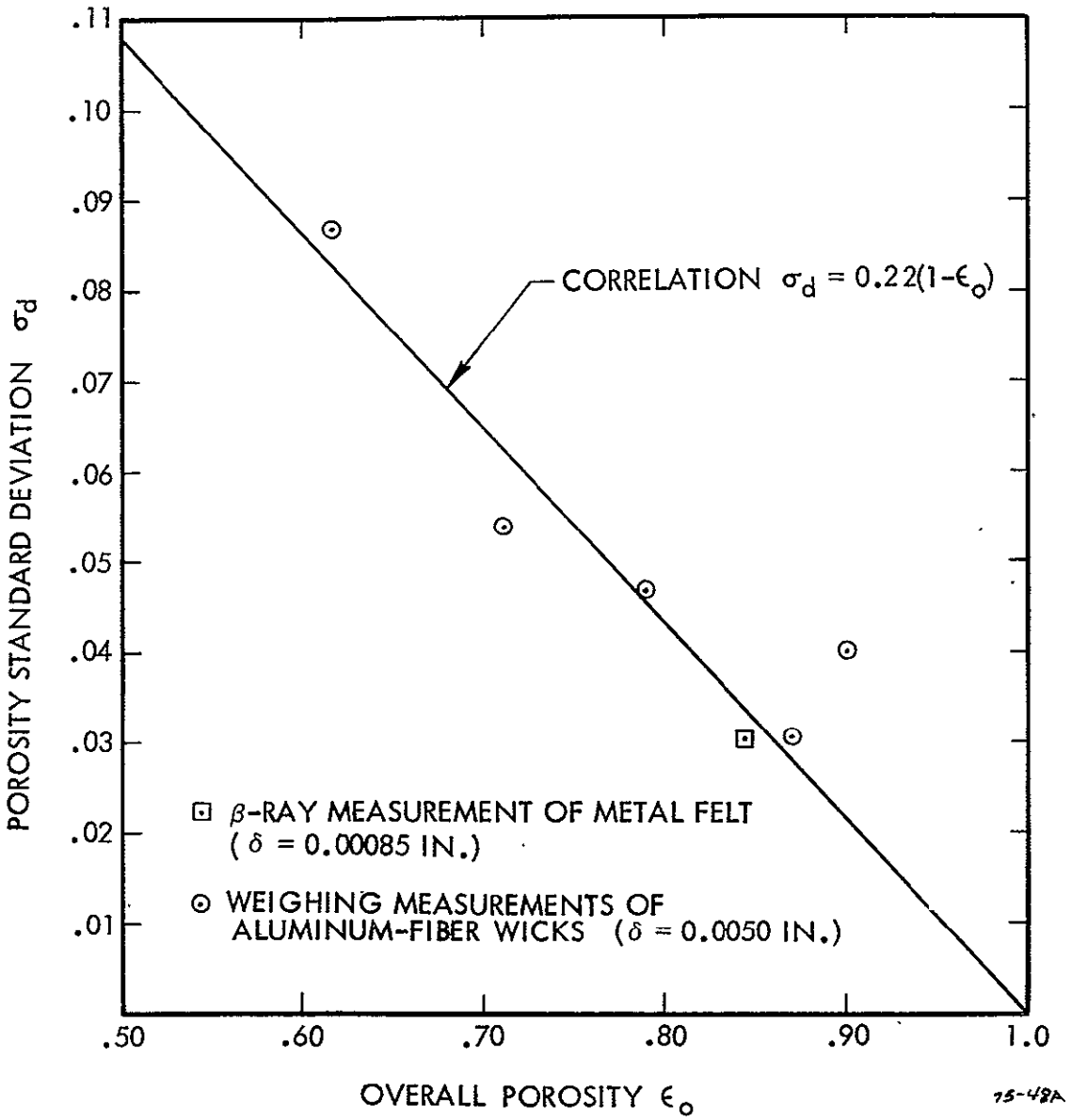

Figure 6-11. Experimental Measurements of the Porosity Standard Deviation.

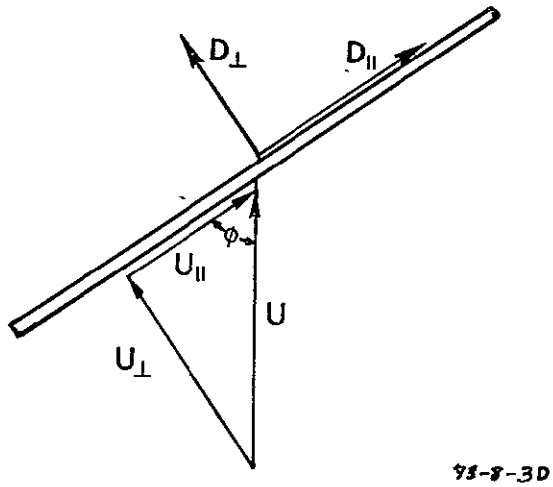

Figure 6-12. A Fiber Segment Inclined at an Angle ϕ to the Flow.

We compute the total drag as superpositions of drags due to flow components parallel and perpendicular to the fiber. In both cases, however, there are no solutions if the fiber is considered in an unbounded uniform flow. Following Happel, we require the shear to vanish on a cylindrical surface a distance b from the center of the fiber. The fractional void volume of the cylinder is taken as the porosity. For flow parallel to the fiber, in addition to the no-shear boundary condition, the total integrated volume flow rate through the annulus is required to equal the parallel component of the superficial velocity $U \cos\phi$ times the cross-sectional area of the cylinder. For flow perpendicular to the fiber, it is convenient to assume the fiber is moving perpendicular to its axis with velocity $U \sin\phi$, and the cylindrical surface on which the shear and normal velocity are required to vanish is stationary. Thus, from Happel we obtain for the drag components per unit length of fiber

$$D_\parallel = \frac{16\pi\mu U\varepsilon \cos\phi}{4(1-\varepsilon) - (1-\varepsilon)^2 - 2\ln(1-\varepsilon) - 3}$$

and

$$D_\perp = \frac{-4\pi\mu U \sin\phi}{\ln(1-\varepsilon) + \frac{1-(1-\varepsilon)^2}{1+(1-\varepsilon)^2}}$$

The total of drag components in the flow direction on all fiber segments in a unit volume with orientations between ϕ and $\phi + d\phi$ is given by

$$dD = \{D_{\parallel}\ell\cos\phi+D_{\perp}\ell\sin\phi\}\ n\ [(3-J)2/\pi + (J-2)\sin\phi]d\phi \qquad [6.22]$$

where the part of the expression in braces is the flow-direction drag component on a single fiber segment, and the remainder is the number of segments per unit volume with orientation between ϕ and $\phi + d\phi$ (see Equation 6.3). Consider a cylindrical volume of unit length and cross-sectional area that is aligned with the flow. The total drag on all segments within the volume, which is calculated by integrating Equation 6.22 from $\phi = 0$ to $\pi/2$, is balanced by the difference in pressure forces acting on the liquid at each end of the cylinder, which is $\varepsilon\frac{dP}{dx}$. The permeability K_0 is then obtained from the Darcy relation $\frac{dP}{dx} = \frac{\mu U}{K_0}$, which results in

$$K_0 = \frac{3}{8}\delta^2\frac{\varepsilon}{1-\varepsilon}\left\{\frac{2\ (5-J)}{4(1-\varepsilon)-(1-\varepsilon)^2-2\ln(1-\varepsilon)-3} - \frac{2(1+J)}{\ln(1-\varepsilon)+\frac{1-(1-\varepsilon)^2}{1+(1-\varepsilon)^2}}\right\}^{-1} \qquad [6.23]$$

The corresponding expression derived by Happel contains an additional factor ε in the second term in the braces.

For the permeability of a partially saturated wick, we apply the above expression to those local regions that have a porosity low enough to remain filled. The increased tortousity of the flow paths as regions empty is neglected. The resulting permeability expression is

$$K = \int_0^{\varepsilon^*} K_0(\delta,\varepsilon)f(\varepsilon)d\varepsilon \qquad [6.24]$$

where the porosity distribution $f(\varepsilon)$ is given by Equation 6.13 and the critical porosity ε^* is given by Equation 6.11. The integral must be evaluated numerically.

6.1.4 Permeability Experiments

The apparatus used to measure the permeability of a partially saturated wick is depicted schematically in Figure 6-13. The test wick was a 5 cm x 15 cm slab of 1.27-mm-thick metal felt with a porosity of 0.835 and an average fiber diameter of 0.0216 mm. A thin 2.29 mm layer of wick having a high capillary-pressure limit (0.61 porosity, 0.0025 fiber diameter) was sintered to the bottom of the test wick for the purpose of providing a surface that remains saturated even when the test wick is partially saturated. The liquid pressure profile along the wick is measured by eight pressure taps spaced at 1.27 cm intervals that are clamped against the saturated layer and connected to an inclined manometer bank. The wick is supported only by these taps, and unlike other permeability apparatus that contain the wick in a close-fitting conduit, a parallel leak path is impossible. Methanol is supplied to and drained from the wick by tubes connected to shallow metal reservoirs clamped against the bottom of the wick at each end. The flow rate through the wick is measured by collecting a sample of liquid for a known time duration.

The pressure distribution in the wick for various upstream and downstream conditions is displayed in Figure 6-14. For each curve the wick was initially flooded and then the stress at each end was increased to the desired level by lowering the supply reservoir and the drain tube. If the wick remained fully saturated, the pressure distribution would be linear. We see, however, that in regions of relatively high stress the curves bend down, which indicates a lowering in the value of permeability due to partial saturation. For a particular curve in Figure 6-14 the permeability at a given stress is calculated from the mass flow rate and the local pressure gradient at that stress. Results for permeability vs stress are shown in Figure 6-15 along with the theoretical curve from Equation 6.24. Although the qualitative shape of the theoretical and experimental curves are similar, the experimental permeability drops off faster with stress. One possible explanation is that we have not taken into account that liquid must flow around empty regions.

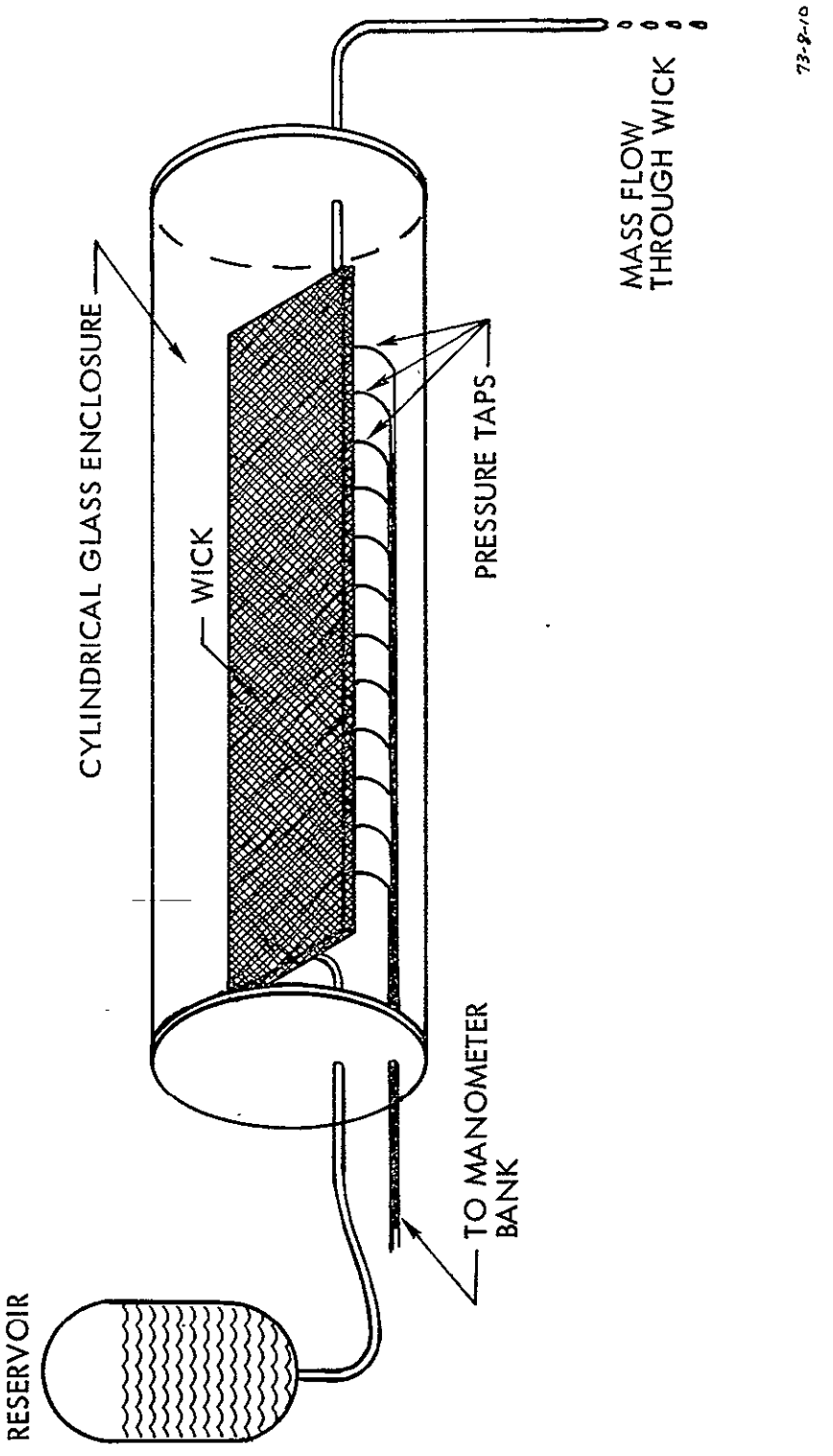

Figure 6-13. The Apparatus for Studying Permeability in a Partially Saturated Wick.

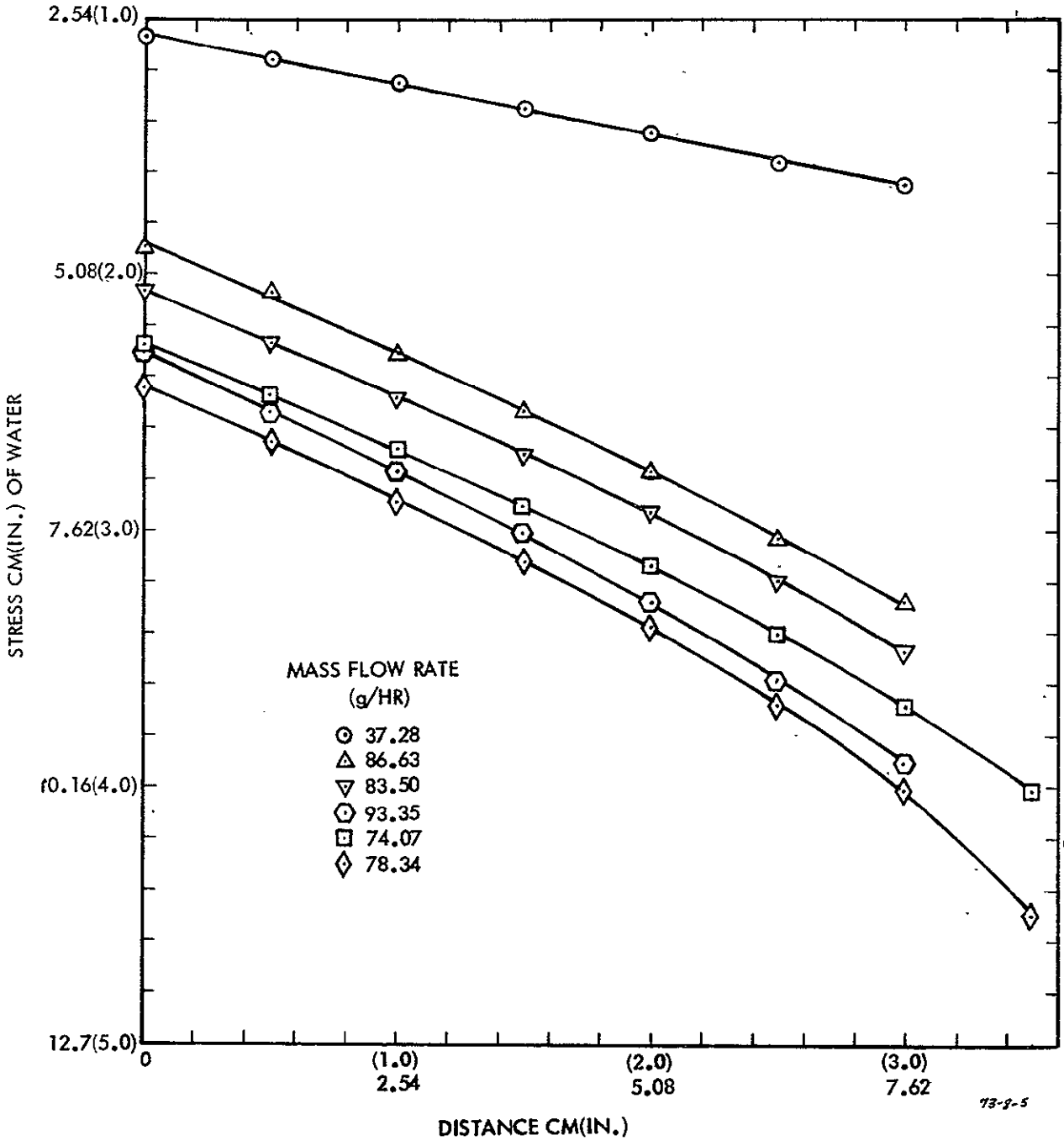

Figure 6-14. Experimental Pressure Distribution in the Wick.

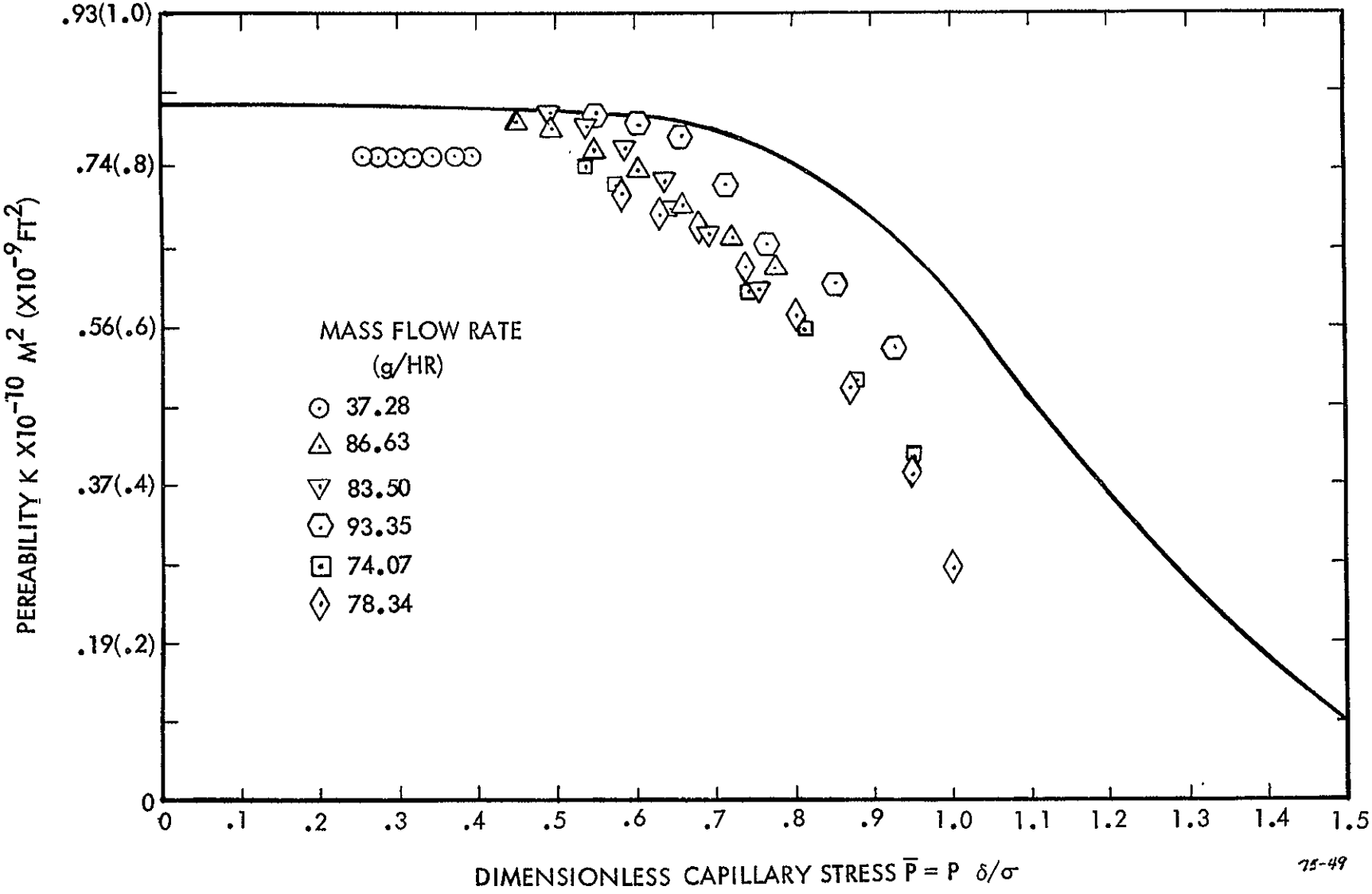

Figure 6-15. Theoretical and Experimental Results for Permeability as a Function of Capillary Stress.

A simple glass apparatus was fabricated to measure the permeability of the set of aluminum-fiber wicks in their saturated state. As in the capillary-pressure tests, the wicks have a fiber diameter of 0.005-in. and differ only in their porosities. As shown in Figure 6-16 the test portion of the wick is suspended between the ends of two U-shaped manometers. Acetone is supplied from a reservoir that maintains a constant head by means of an overflow weir and a constant inflow, and the flow rate through the wick is measured by collecting a sample of liquid from the drain tube. The pressure drop along the wick is kept sufficiently low that the wick remains saturated.

The experimental results are displayed in Figure 6-17, along with experimental results for metal felt of Corman (Reference 6.9) and Alexander (Reference 6.10), the present theoretical results, and the theoretical results of Schmidt (Reference 6.6). The permeability normalized by the square of the fiber diameter is plotted as a function of porosity. The most marked feature of Figure 6-17 is the close agreement for porosities from 0.55 to 0.80 between the theoretical permeability given by Equation 6.23 and that given by Schmidt based on the Kozeny hydraulic-diameter theory. For high porosity where flow interactions between close-spaced fibers are minimum, the present theory is valid, whereas, for low porosity where the flow passages resemble tortuous channels the Kozeny theory is valid. The agreement over an intermediate range of porosity gives credibility to both theories. In addition, Schmidt presents a large quantity of data for screen wicks that are successfully correlated by the Kozeny theory.

The experimental results for the aluminum-fiber wicks generally follow the theoretical curve, but lie above it. Corman's and Alexander's measurements with metal felt also follow the curve, but lie below it. For purposes of heat-pipe design, an empirical factor can be included in the theoretical permeability Equation 6.23 to obtain good agreement for a particular type of wick.

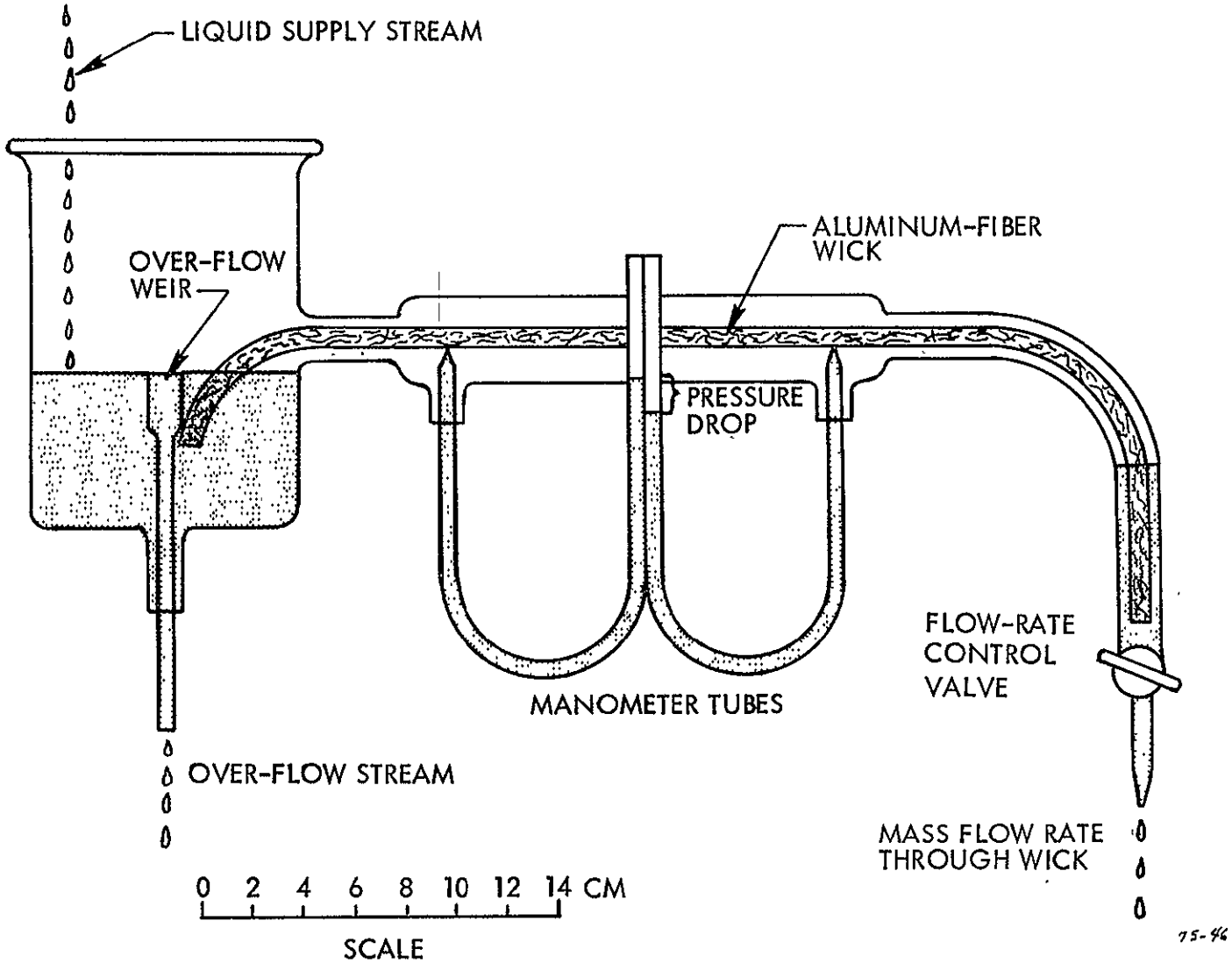

Figure 6-16. Glass Apparatus for Measuring the Permeability of Saturated Aluminum-Fiber Wicks.

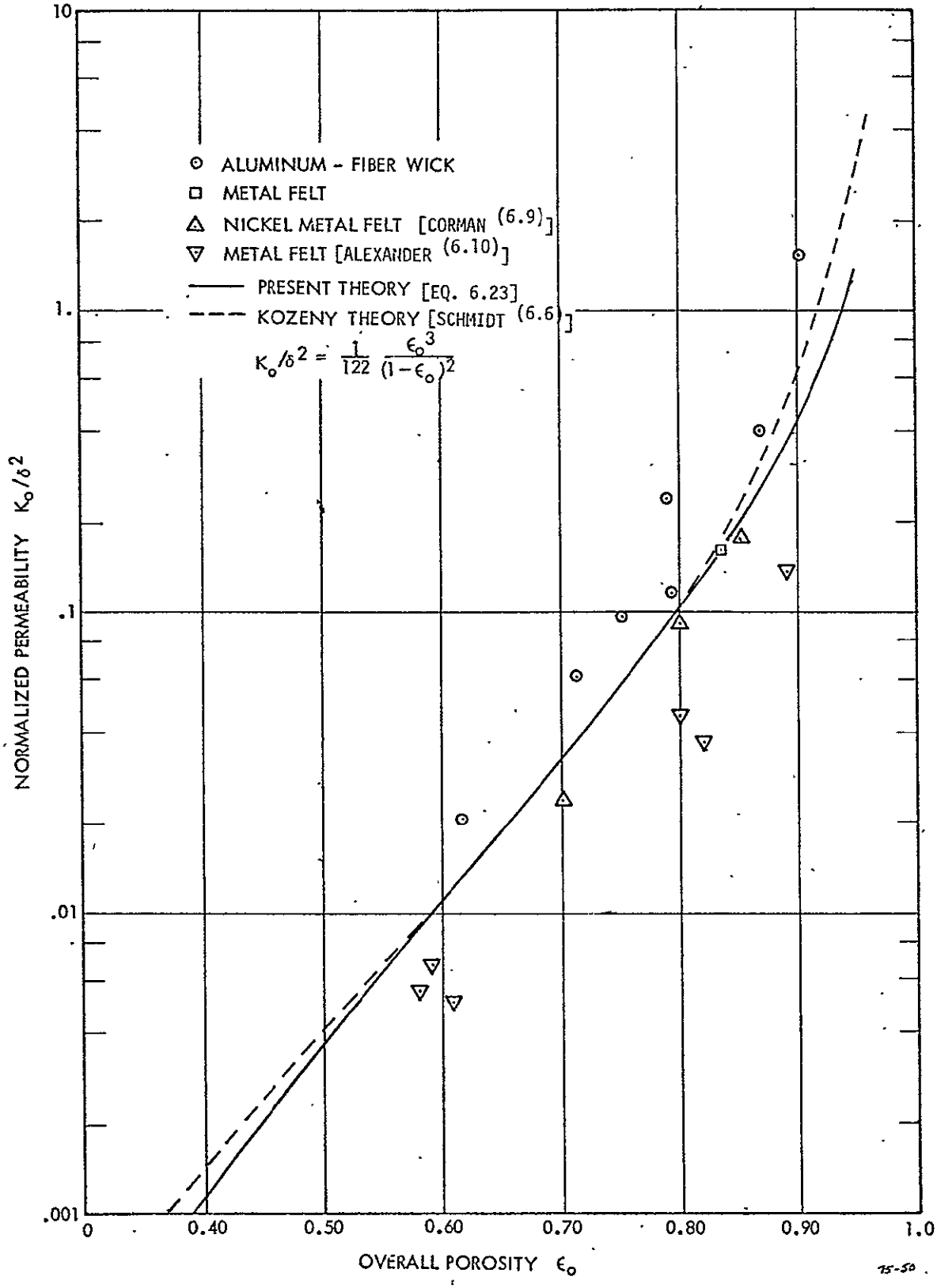

Figure 6-17. Permeability as a Function of Overall Porosity - Experiment and Theory.

6.1.5 Optimum Wick

For a simple model of a wick, full saturation is assumed, and Equation 6.10 is used for the capillary-pressure limit P_c and Equation 6.23 for the permeability K_o. Since both P_c and K_o depend on two wick parameters, ε and δ, a crucial optimization question arises - for a specified capillary-pressure limit, what values of porosity and fiber diameter provide the greatest permeability? Equation 6.10 is solved for δ in terms of P_c and ε, and the result is used to eliminate δ from Equation 6.21, which gives for the permeability

$$\overline{K}_o = K_o \Big/ \left(\frac{3.246H\sigma}{P_c}\right)^2 = \frac{3}{8}\,\frac{(1-\varepsilon)}{\varepsilon}\left\{\frac{4\varepsilon}{4(1-\varepsilon)-(1-\varepsilon)^2-2\ln(1-\varepsilon)-3} - \frac{8}{\ln(1-\varepsilon)+\dfrac{1-(1-\varepsilon)^2}{1+(1-\varepsilon)^2}}\right\}^{-1} \qquad [6.25]$$

The dimensionless permeability $\overline{K}_o$ as a function of ε is displayed in Figure 6-18, where we see that the greatest permeability occurs at a porosity of 0.79 . The corresponding fiber diameter necessary to give the capillary-pressure limit is calculated from Equation 6.10.

If one used the Kozeny expression for the permeability instead of the present theory, then one finds, as shown in Figure 6-18, that the greatest permeability is obtained in the limit $\varepsilon \to 1$ and $\delta \to 0$ such that P_c given by Equation 6.10 is the specified value. In fact, the present theory gives a zero permeability in this limit. As discussed previously, the difference is that the Kozeny theory is not valid for high porosity whereas the present theory is.

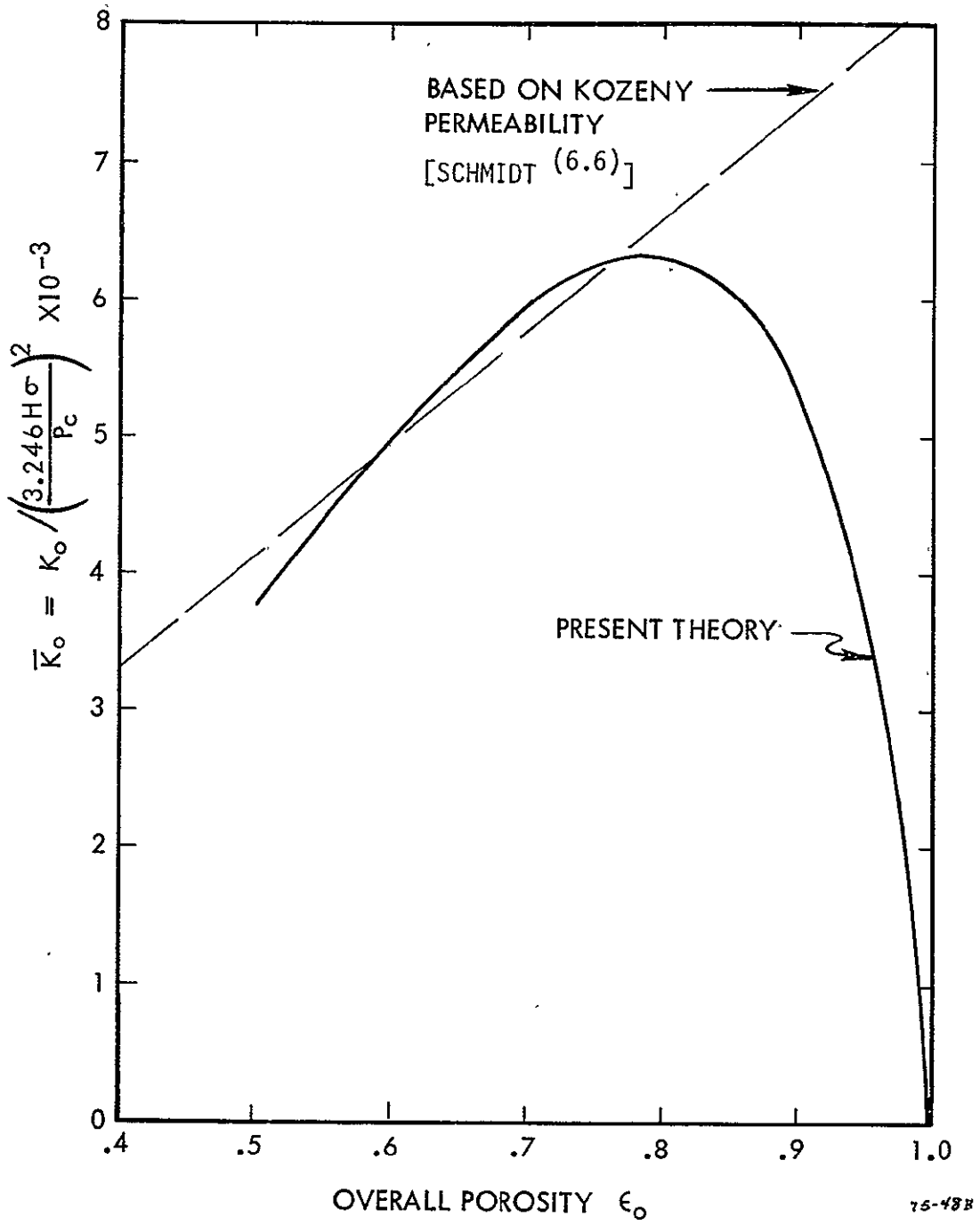

Figure 6-18. Normalized Permeability for a Specified Capillary-Pressure Limit.

6.2 DESIGN OF GRADED-POROSITY WICKS

The theoretical expressions developed in the previous section for the capillary-pressure limit and permeability of fibrous wicks are the basis of the computer program GRADE (Reference 6.2) that was written to design and predict the performance of graded-porosity wicks. Since the model for the program is being refined continuously, we will wait until the final report to present the mathematical details. Here we will describe in words its current state of development, and the reader can refer to the User's Manual for the original version.

The key variable in the program is capillary stress, which is the vapor-liquid pressure difference that must be supported by the wick. Since in earth gravity the stress varies hydrostatically across the heat pipe, to be specific we take for its value the vapor-liquid pressure difference at the top of the wick. GRADE currently does not include partial saturation, so when the stress exceeds the wick's capillary-pressure limit the wick is considered failed.

The stress at the condenser end is set so there is an incipient puddle condition at the bottom of the cross section. If this stress is so low that a liquid slug forms in the lowest vapor space, then the stress is increased to a point where the slug just vanishes. The mathematical model for vapor-space slugging is a research problem that has not yet been solved. The crude criteria currently used in GRADE is that a slug forms if 4 x (surface tension)/(hydraulic diameter) exceeds the stress at the top of the vapor space.

The program starts with the condenser-end stress as a boundary condition and with an assumed value for the heat-transport rate, it numerically integrates the first-order differential equation that describes the rate of stress increase with distance along the pipe. The stress increases due to liquid pressure drop in the wick, vapor pressure drop in the vapor space, and the hydrostatic pressure drop if the heat pipe is inclined in a gravitational field. In the wick-design mode, at each step of the numerical integration the porosity of the wick is set at the highest value that meets the following requirements:

1) The capillary-pressure limit is not exceeded by the stress

2) The wick self primes under the hydrostatic load alone.

For the second condition, the user can specify whether he desired the wick to prime at the operating inclination or level. The wick's porosity in the later case will generally be higher in some region, and hence the heat-transport capacity will be greater. In actual operation, however, the heat pipe will have to be leveled to prime the wick before it is elevated to its operating inclination.

After the integration is complete, the solution is checked at the evaporator end to see if it meets the user specified value of the stress or porosity. The user specifies a maximum value for the stress, for example, so that the pumping ability of circumferential grooves is not exceeded, or a minimum value for the porosity so that the wick does not become exceedingly dense. GRADE repeatedly integrates the equations, with values for the heat-transport rate adjusted by a binary search routine, until the conditions are met at the evaporator end.

In addition to designing graded-porosity wicks, GRADE also designs non-graded homogeneous wicks optimized for heat-transport capability in terms of the fiber diameter and/or the uniform porosity.

6.3 DESIGN AND PERFORMANCE OF ALUMINUM/AMMONIA HEAT PIPES

The computer program GRADE was used to design a graded-porosity and a homogeneous wick for two all-aluminum heat pipes for use with ammonia. The heat pipes are 180-cm long with equal evaporator, adiabatic, and condenser lengths of 60-cm. The tube for the heat pipes has an outside diameter of 1.27-cm and a wall thickness of 0.889 mm, and it is circumferentially threaded on the inside with 40 threads/cm. The wick is a 0.457-cm slab fabricated from aluminum wire with a diameter of 0.127 mm.

The porosity for the actual wicks is displayed in Figure 6-19. The measured distribution for the graded-porosity wick was found by cutting up one of six identical wicks in two-inch segments and weighing them. Nondestructive porosity measurements were also made of each wick by x-raying

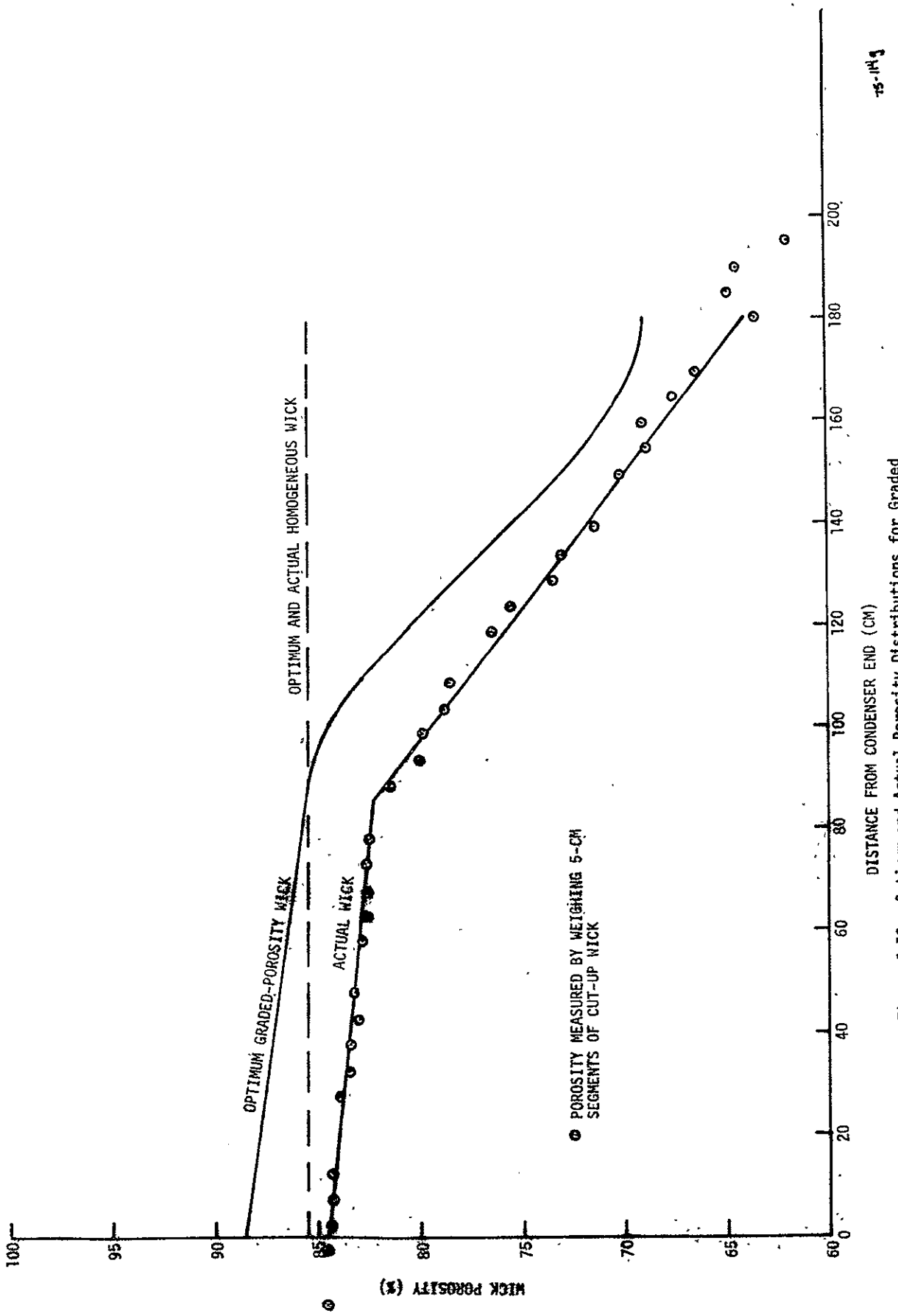

Figure 6-19. Optimum and Actual Porosity Distributions for Graded and Homogeneous-Porosity Wicks for the Aluminum/Ammonia Heat Pipes

and reading the film with a densitometer. Although the measurements indicated that all the wicks were nearly identical, the scatter in the data was too great to precisely define the porosity variations. Further development of a nondestructive test is required.

The computer-designed optimum porosity distribution differs from the actual wick primarily because the mathematical model had been updated since the wick was fabricated. The performance predictions based on the updated model for both the actual and optimum porosity distributions are displayed in Figure 6-20. The optimized wick was designed to self-prime and operate with the evaporator end elevated 0.5 cm higher than the condenser end. The same wick, when operated at higher elevations may not self-prime, but because of the hysteresis in fibrous wicks, once it is primed at 0.5 cm or lower, it can then be raised above 0.5 cm and operated. In this case, however, capillary failure of the wick is predicted at some point other than the evaporator end. For operation below 0.5 cm, on the other hand, failure is predicted at the evaporator end. This difference is the reason for the step change in slope of the Q-vs-h curve for the optimum wick.

The measured performance for the graded-porosity heat pipe, which is also displayed in Figure 6-20, is in reasonable agreement with the theoretical predictions. The wick was initially primed by leveling the pipe prior to elevating it. After a burnout occurred, the heat load was shut off to allow the wick to reprime at its operating elevation. The test was then repeated and no difference was found in the measured capacity. Thus, the graded-porosity wick had repriming capability at least up to 3 cm.

As also shown in Figure 6-20, the measured performance for the heat pipe with the homogeneous wick was better than predicted at the higher elevations. The measured wick porosity of 0.855 is exactly the optimum. Because of hysteresis, the wick did not reprime after a burnout when the evaporator elevation was 2 cm or higher, which is in accord with prediction.

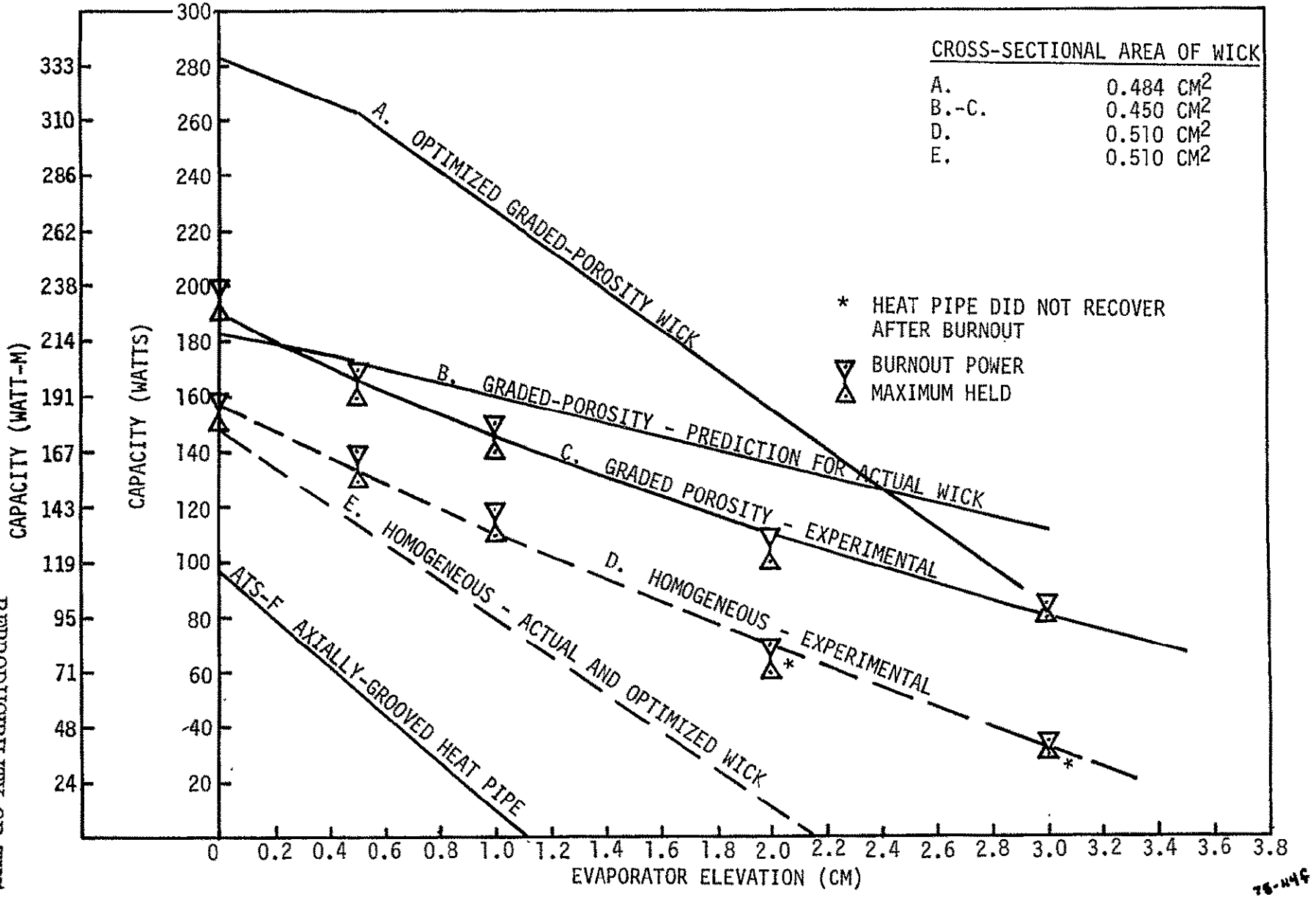

Figure 6-20. Predicted and Measured Performance of Aluminum/Ammonia Heat Pipes.

The demonstrated performance increase of the graded-porosity wick over the homogeneous wick was not as large as it potentially could be. Primarily, the homogeneous wick was optimum, while the graded-porosity wick was everywhere too dense. The measured performance increase of the graded-porosity wick was due only to increased capillary pressure and no advantage was gained by having in the condenser region a higher porosity, and, hence a lower flow resistance than the homogeneous wick. Another factor that detracted from the relative performance of the graded-porosity wick was that its cross-sectional area was 13% less than that of the homogeneous wick.

The temperature distribution along the heat pipes is shown in Figure 6-21 for a transport rate of 140 watts. The nonuniformity of temperature along the condenser is attributed to nonuniform thermal contact with the heat-sink blocks. The heat-transfer coefficients for evaporation and condensation based on an average wall temperature and the inside effective surface are respectively 25000 watts/m^2-°C and 9000 watts/m^2-°C for the graded-porosity heat pipe and 27000 watts/m^2-°C and 6500 watts/m^2-°C for the homogeneous-wick heat pipe.

The graded-porosity-wick heat pipe that was tested had high performance, for example, compared to the performance of the ATS-F axially-grooved heat pipe also displayed in Figure 6-20 (Reference 6.11). Although the goals of the development task have been achieved, the computer model predicts that much higher performance is possible with an updated porosity variation for the wick.

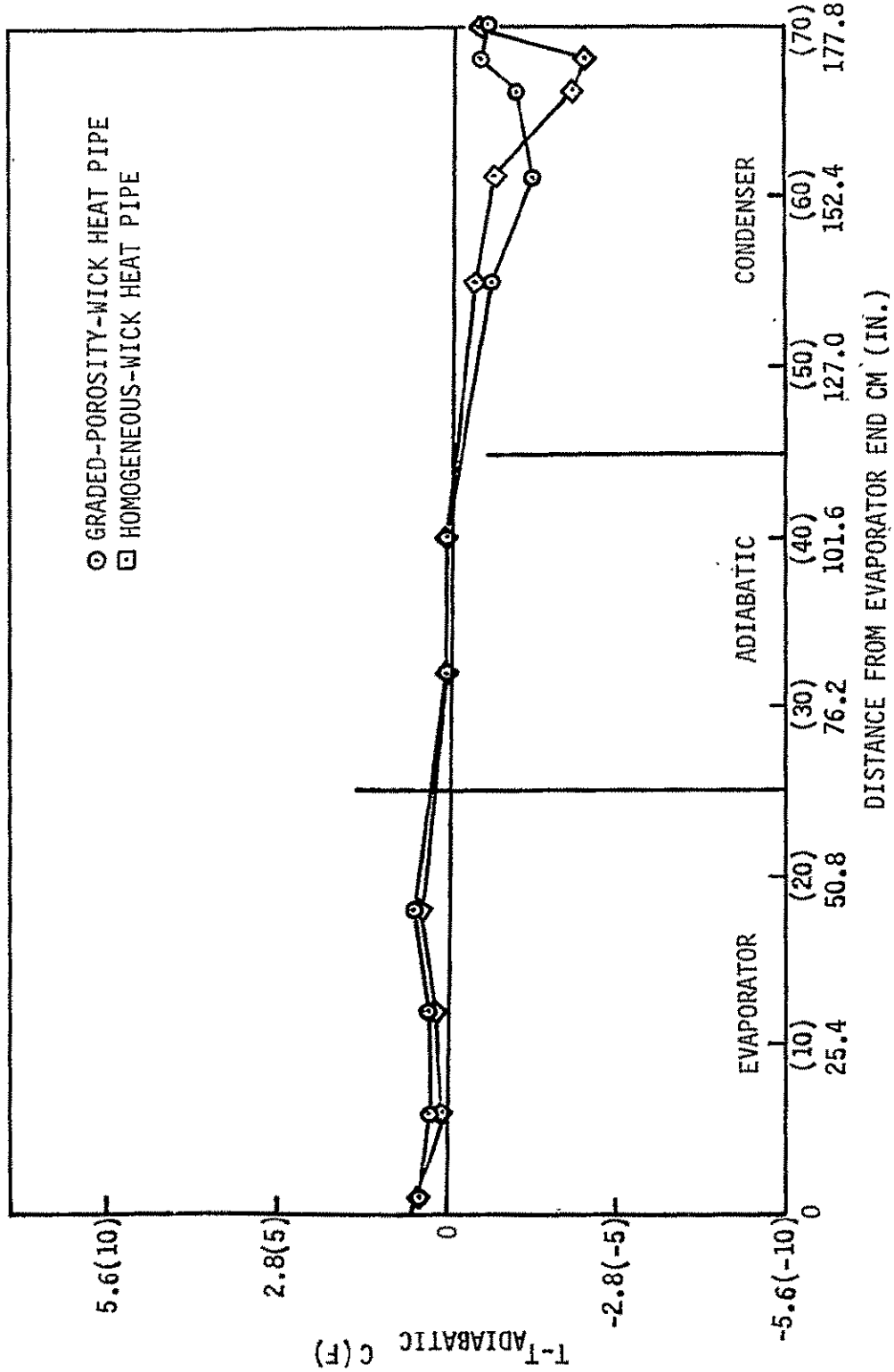

Figure 6-21. Temperature Distribution Along the Heat Pipes With a 140-Watt Load.

6.4 REFERENCES

6.1 Anderson, W.T., Edwards, D.K., Eninger, J.E., Marcus, B.D., "Variable-Conductanct Heat Pipe Technology - Final Research Report," NASA CR-114750, March 1974.

6.2 Eninger, J. E., "Computer Program GRADE For Design and Analysis of Graded-Porosity Heat-Pipe Wicks," NASA CR-137618, August 1974.

6.3 Eninger, J. E., and Marcus, B. D., "Capillary Flow Through Partially Saturated Fibrous Wicks - Final Report," TRW Report No. 21160-6005-RU-00, June 15, 1973.

6.4 Eninger, J. E., "Capillary Flow Through Heat-Pipe Wicks," AIAA Paper 75-661, May 1975.

6.5 Tien, C. L. and Sun, K. H., "Minimum Meniscus Radius of Heat Pipe Wicking Material," Int'l J. Heat and Mass Trans., 4 (1971), 1853.

6.6 Schmidt, E., "Contribution a l'Etude des Calodues," Ph.D. dissertation, Univ. of Grenoble, France, 1968.

also see

Busse, C. A., "Heat Pipe Thermionic Converter Research in Europe," Paper No. 699105, Proc. Fourth Intersociety Energy Conversion Engr. Conf., Washington D. C., 1969.

and

Marcus, B. D., "Theory and Design of Variable Conductance Heat Pipes," NASA CR-2018, 1972.

6.7 Happel, J., "Viscous Flow Relative to Arrays of Cylinders," A. I. Ch.E. Jour. 4 (1958), 197.

also see

Happel, J. and Brenner, H., Low Reynolds Number Hydrodynamics, Prentice-Hall, 1965.

6.8 Beavers, G. S. and Sparrow, E. M., "Non-Darcy Flow Through Fibrous Porus Media," J. Appl. Mech 36 (1969).

6.9 Corman, J. E., Trefethen, L. and Walmet, G. E., "Characterization of Parameters for Liquid Flow in Rigid Porus Media," ASME Paper No. 73-WA/HT-3.

6.10 Alexander, E. G., "Structure-Property Relationships in Heat Pipe Wicking Materials," Ph.D. dissertation, North Carolina State University, 1972.

6.11 "Summary Report for Qualifying Extruded 6063 Grooved Tubing for Use in ATS-F Heat Pipes," Dynatherm Corporation Report No. DTM-74-3, May 10, 1974.

APPENDIX A

APPENDIX A: DIFFUSION FLOW ANALYSIS

For transient analysis of hot-gas-reservoir heat pipes, flow of vapor and noncondensable gas between the reservoir and condenser by diffusion are important in determining performance characteristics of the system. Figure A-1 shows schematically a VCHP system.

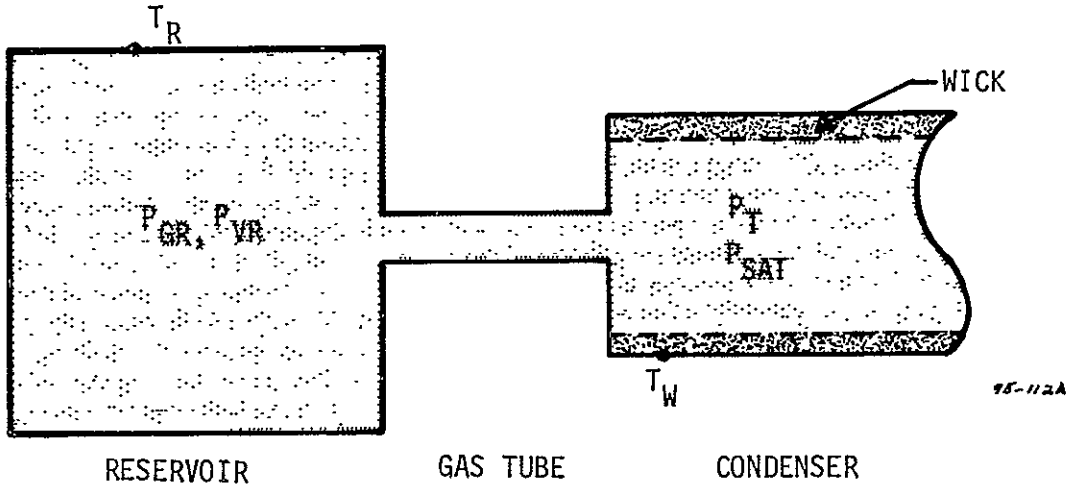

Figure A-1. Hot reservoir VCHP.

Where:

T_W = Heat-pipe wick temperature at the end of the wicked portion of the heat pipe

T_R = Reservoir temperature

P_T = Total pressure in heat pipe

P_{SAT} = Working fluid saturation pressure at temperature T_W

P_{GR} = Noncondensable gas partial pressure in reservoir

P_{VR} = Working fluid partial pressure in reservoir.

A simplified representation of the diffusion flow of vapor has been adopted to allow integration into the heat-pipe thermal model. It is assumed that the gas tube is the dominant resistance to diffusion and that partial pressures of working-fluid vapor and noncondensable gas are uniform throughout the reservoir. The further assumptions that diffusion is one-dimensional at constant temperature and pressure over a time step and that the vapor partial pressure is small compared with the total pressure give for the rate of diffusion of vapor:

$$\dot{M} = \frac{-DA}{RT}\left(P_{VR} - P_{SAT}\right)$$

Where:

M = Mass flow rate into the reservoir

D = Diffusion coefficient

R = Working fluid vapor gas constant

A = Gas tube cross-sectional area

T = The gas temperature.

In addition to diffusion, there is a flow of working fluid vapor due to changes in total pressure. If the total pressure decreases over a time step:

$$\Delta M = \frac{-M\left(P_T - P_{T\Delta\tau}\right)}{P_T}$$

Where:

ΔM = Mass flow of vapor out of reservoir

P_T = Total pressure at time τ

$P_{T\Delta\tau}$ = Total pressure at time $\tau + \Delta\tau$

M = Amount of working fluid vapor in reservoir at time τ.

If the total pressure increases over a time step:

$$\Delta M = \frac{(P_{SAT})\ (V)\ (1 - P_T/P_{T\Delta\tau})}{RT_R}$$

Where:

P_{SAT} = Working-fluid saturation pressure at the entrance to the reservoir at time $\tau + \Delta\tau$

V = Reservoir volume

R = Working fluid gas constant.

The mass of working-fluid vapor in the reservoir at time $\tau + \Delta\tau$ then becomes:

$$M_{\tau+\Delta\tau} = M + \Delta M + (\dot{M})(\Delta\tau)$$

This new value of working-fluid vapor then is used to calculate the partial pressure of vapor in the reservoir and used in the gas-front location calculations.

APPENDIX B

CONTENT OF APPENDIX B

SK	REVISIONS			
	LTR	DESCRIPTION	DATE	APPROVED

Top View

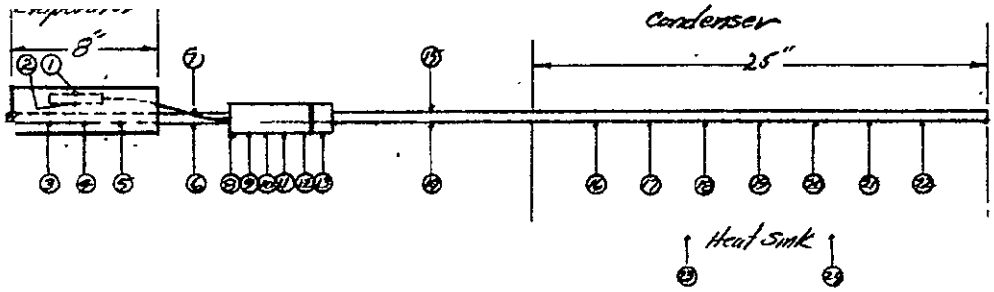

Thermocouple	Dist. from Evap. End
1	} on either side of control vol.
2	
3	2.0
4	4.0
5	6.0
6	10.0
7	10.0
8	12.0
9	13.0
10	14.0
11	15.0
12	16.0
13	17.0
14	23.0
15	23.0
16	32.0
17	35.0
18	38.0
19	41.0
20	44.0
21	47.0
22	50.0

Note: 1. High-limit Tc on control volume.

2. Heat sink TC's 8" & 16" from condenser end.

3. Use 6 mil teflon tape between evap. saddle & heat pipe

4. Use RTV between control volume & evaporator saddle and on all condenser heat-transfer interfaces.

ENGINEERING SKETCH	TRW SYSTEMS GROUP ONE SPACE PARK • REDONDO BEACH, CALIFORNIA
ORIGINATOR: Jim Ensinger — DATE: 3/24/75	Instrumentation for VMHP FIGURE 1
MJO	SIZE: A — CODE IDENT NO.: 11982 — SK 750324E
	SCALE — SHEET 1 OF

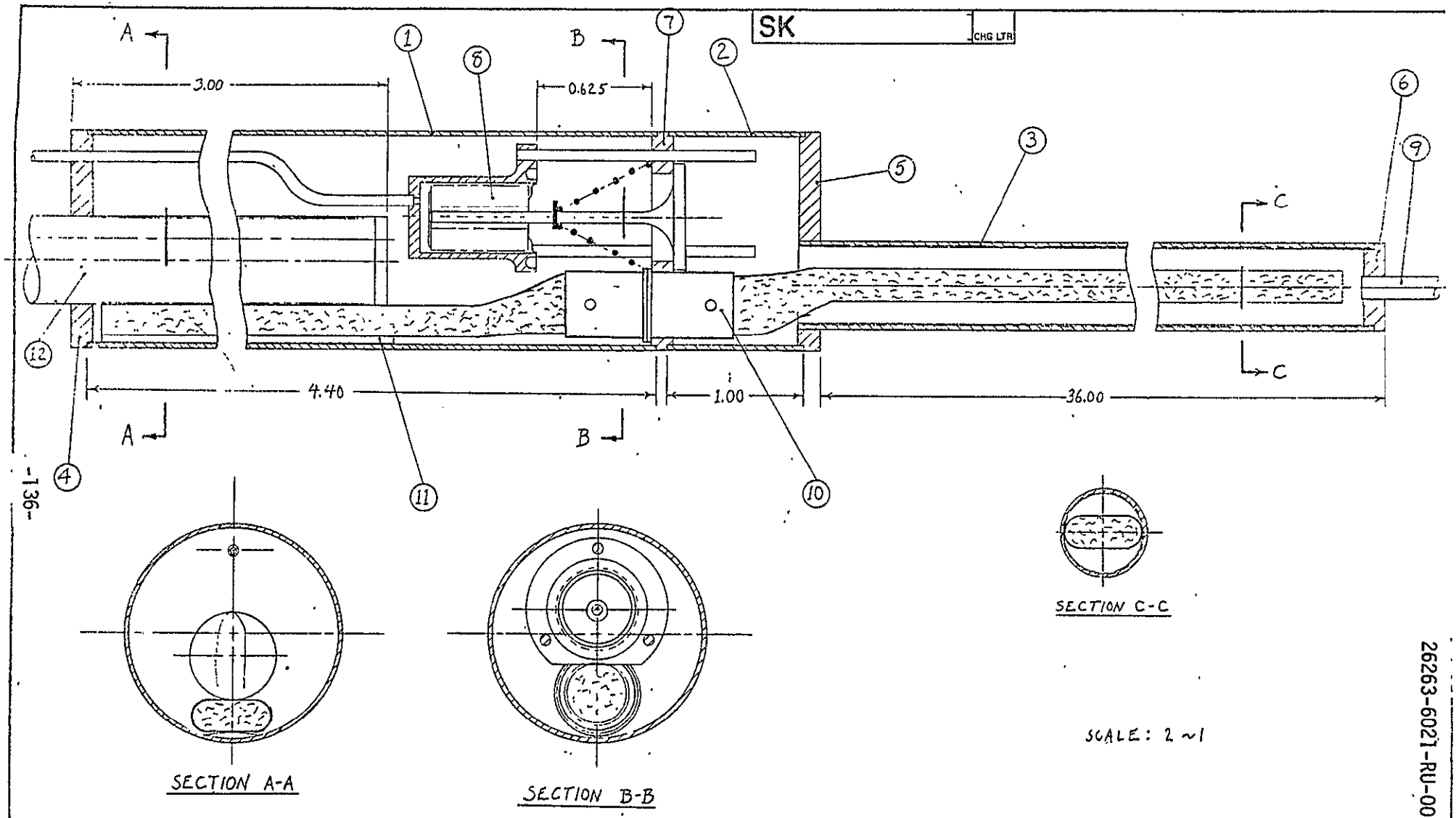

SECTION A-A

SECTION B-B

SECTION C-C

SCALE: 2 ~ 1

ORIGINATOR	DATE	TITLE	ENGINEERING SKETCH
	9/16/74	VAPOR MODULATED HEAT PIPE ASSEMBLY (VMHP)	TRW
MJO			SK 740903
			SHEET OF

SYSTEMS 5228 REV. 9-67

26263-6021-RU-00

SK

REVISIONS			
LTR	DESCRIPTION	DATE	APPROVED

ITEM	PART NO.	QTY	DESCRIPTION	MATERIAL	SPEC.
12	SK740915	1	EVAPORATOR SUB-ASSEMBLY	—	—
11	SK740914	1	FLAT SPRING 0.007 THK. SHIM STOCK	STAINLESS STEEL 302	
10	SK740910	1	WICK SUB-ASSEMBLY	—	—
9	SK740905-3	1	FILL TUBE 1/8 O.D. X 0.020 WALL X 2.00	STAINLESS STEEL 304	
8	SK740907	1	VALVE SUB-ASSEMBLY	—	—
7	SK740906	1	BULKHEAD 1-1/4" ROD STOCK	STAINLESS STEEL 304	
6	SK740905-2	1	END CAP 1/2" DIA ROD	STAINLESS STEEL 304	
5	SK740904-2	1	END CAP 1/8 THK. SHEET	STAINLESS STEEL 304	
4	SK740904-1	1	END CAP 1/8 THK. SHEET	STAINLESS STEEL 304	
3	SK741001-3	1	TUBE, THREADED 1/2 OD X 0.035 WALL	STAINLESS STEEL 304	SP-13B-02
2	—	1	TUBE 1 1/4 OD X 0.028 WALL	STAINLESS STEEL 304	
1	—	1	TUBE 1 1/4 OD X 0.028 WALL	STAINLESS STEEL 304	

PARTS LIST

ENGINEERING SKETCH

TRW SYSTEMS GROUP
ONE SPACE PARK • REDONDO BEACH, CALIFORNIA

ORIGINATOR	DATE
	9/16/74
MJO	

VAPOR MODULATED HEAT PIPE (VMHP)
PARTS LIST

SIZE	CODE IDENT NO.	
A	11982	SK 740903

SCALE		SHEET 1 OF

SYSTEMS 523 REV. 12-71

NOTES:

1. TUBE I.D. TO CONFORM TO REQUIREMENTS OF SPEC., SP-13B-02.
2. INTERNAL GROOVES ENTIRE LENGTH PER SPEC. SP-13B-02.

SK

CHG LTR

DASH NO.	L	T (STK.)
-1	35.75	0.035
-2	23.55	0.035
-3	35.85	0.035
-4	70.86	0.035
-5	38.58	0.028

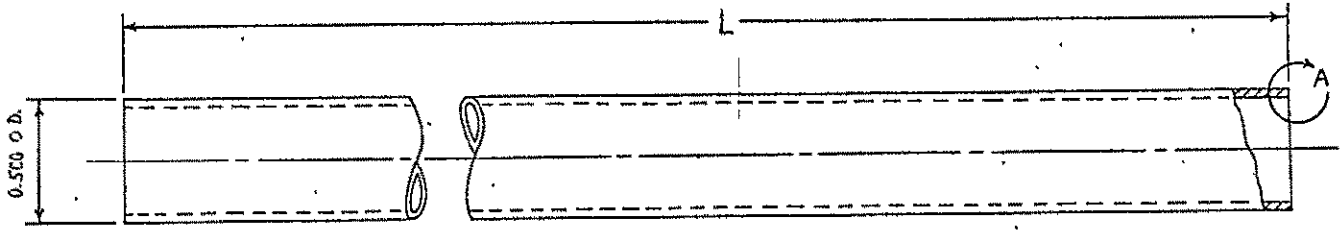

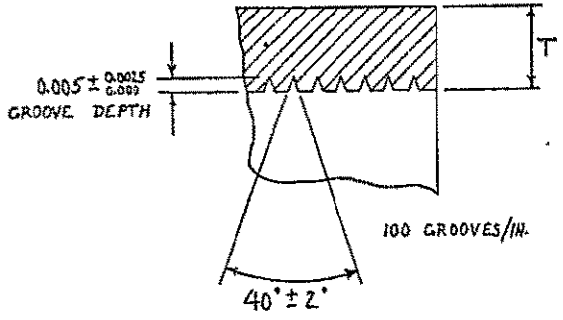

DETAIL A (20~1)

C	PH15-7 Mo s.s.
B	304 CRES
A	6061-T6 AL
LETTER	MATERIAL

ORIGINATOR	DATE	TITLE
G. FLEISCHMAN	10-1-74	TUBE, GROOVED
MJO		

ENGINEERING SKETCH

TRW

SK 741001

SHEET OF

SYSTEMS 5288 REV. 9-67

26263-6021-RU-00

SK

REVISIONS			
LTR	DESCRIPTION	DATE	APPROVED

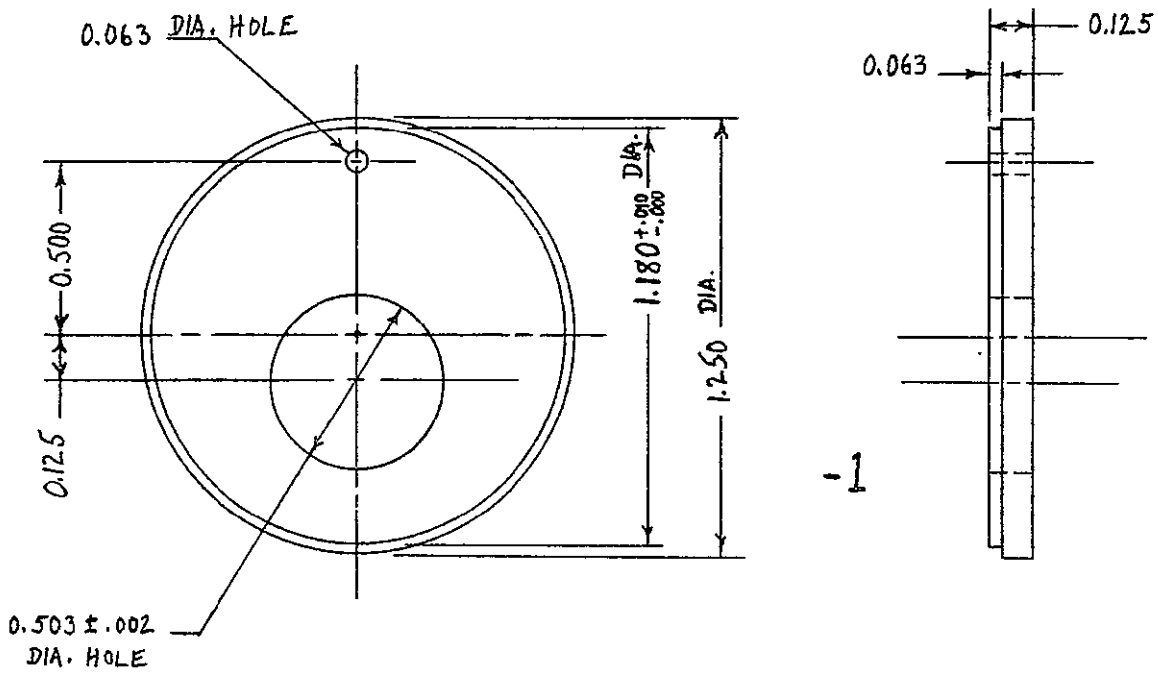

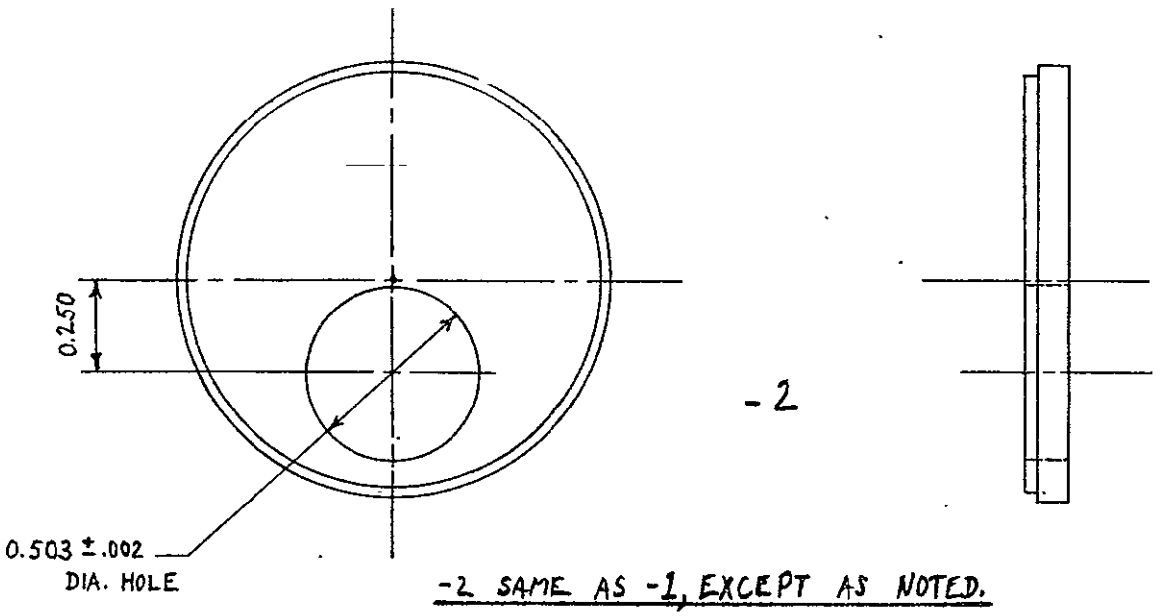

-2 SAME AS -1, EXCEPT AS NOTED.

ENGINEERING SKETCH

TRW SYSTEMS GROUP
ONE SPACE PARK • REDONDO BEACH, CALIFORNIA

ORIGINATOR	DATE
	9/16/74
MJO	

VMHP
END CAP

SIZE	CODE IDENT NO.	
A	11982	SK 740904

SCALE 2~1 | SHEET 1 OF

SK

REVISIONS			
LTR	DESCRIPTION	DATE	APPROVED

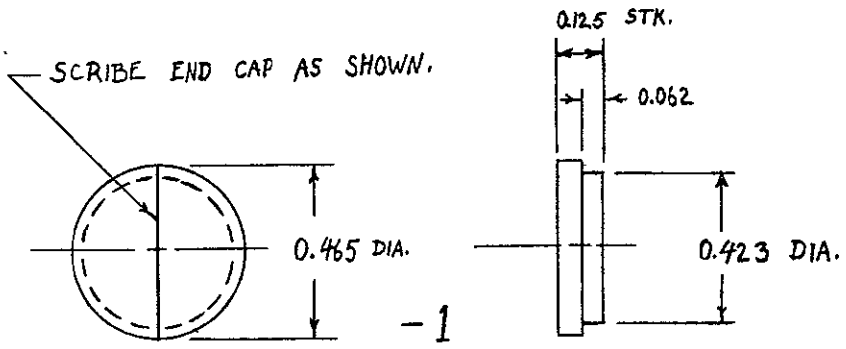

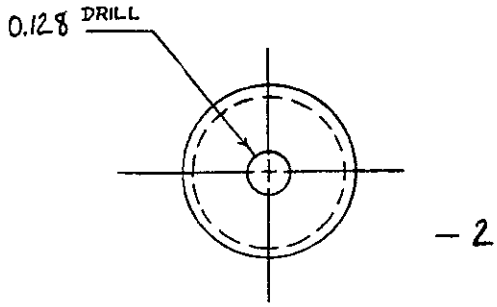

-2 SAME AS -1, EXCEPT AS NOTED.

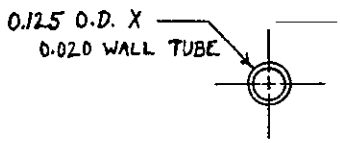

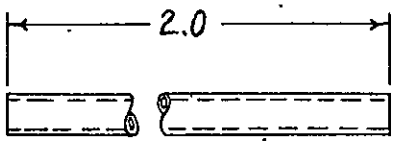

PART NO.	DESCRIPTION	MATERIAL
SK740905-3	FILL TUBE	304 CRES TUBE, 0.125 O.D. X 0.020 WALL
SK740905-2	END CAP	304 CRES ROD, ½" DIA.
SK740905-1	END CAP	304 CRES ROD, ½" DIA.

ENGINEERING SKETCH

TRW SYSTEMS GROUP
ONE SPACE PARK • REDONDO BEACH, CALIFORNIA

ORIGINATOR	DATE
G. FLEISCHMAN	10/18/74
MJO	

END CAPS AND FILL TUBE

SIZE	CODE IDENT NO.	
A	11982	SK 740905

SCALE 2 ~ 1 | SHEET 1 OF

SK | CHG LTR

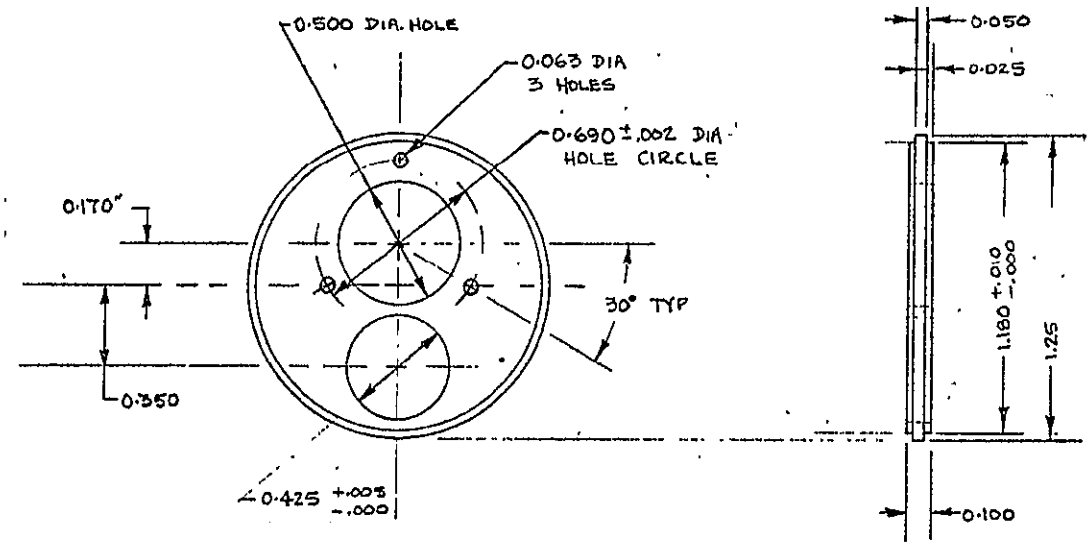

ORIGINATOR	DATE	TITLE	ENGINEERING SKETCH
	10/12/74	VMHP BULKHEAD	TRW
MJO			SK 740906
			SHEET OF

SYSTEMS 5238 REV. 9-67

26263-6021-RU-00

SK	REVISIONS			
	LTR	DESCRIPTION	DATE	APPROVED

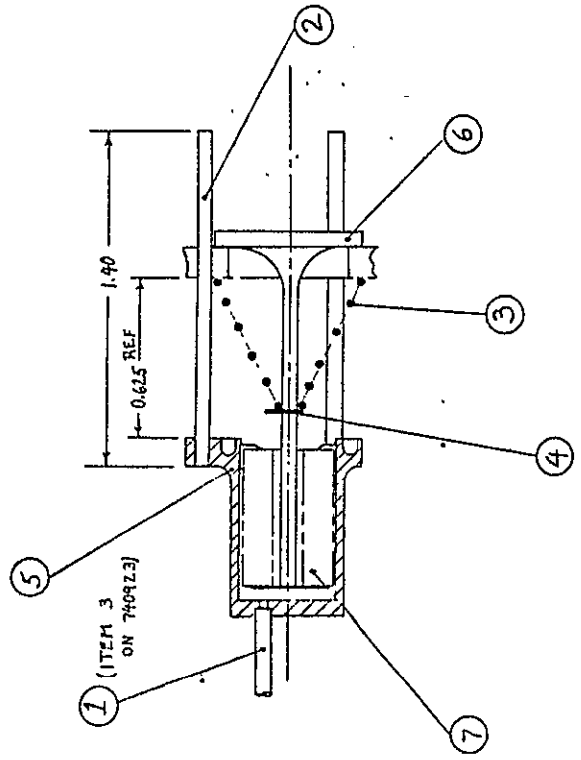

ITEM	PART NO.	QTY	DESCRIPTION	MATERIAL	SPEC.
7	—	1	BELLOWS METAL BELLOWS COMPANY	STAINLESS STEEL 347	
6	SK740909	1	VALVE 5/8 DIA. ROD	STAINLESS STEEL 304	
5	SK740908	1	BELLOWS CAN 7/8 DIA. ROD	STAINLESS STEEL 304	
4	—	1	RETAINING RING TRUARC	STAINLESS STEEL (PH 15-7 Mo)	Y5133-6H
3	—	1	CONICAL SPRING PARAGON SPRING COMPANY	STAINLESS STEEL 302	C-4447 (P/N 9974)
2	—	3	VALVE GUIDE 1/16 DIA. ROD X 1.40"	STAINLESS STEEL 304	
1	—	1	SENSOR FEEDTUBE 1/16 O.D X 0.020 WALL X 240"	STAINLESS STEEL 304	

PARTS LIST

ENGINEERING SKETCH	TRW SYSTEMS GROUP — ONE SPACE PARK • REDONDO BEACH, CALIFORNIA	
ORIGINATOR / DATE		
MJO	SIZE: A	CODE IDENT NO.: 11982
	SCALE	SHEET 1 OF
	SK	

SYSTEMS 523 REV. 12-71

SK	REVISIONS			
	LTR	DESCRIPTION	DATE	APPROVED

ENGINEERING SKETCH	TRW SYSTEMS GROUP — ONE SPACE PARK • REDONDO BEACH, CALIFORNIA	
ORIGINATOR / DATE: 9/17/74	VMHP VALVE SUB-ASSEMBLY	
MJO	SIZE: A	CODE IDENT NO.: 11982
	SCALE 2~1	SHEET 1 OF
	SK 740707	

SYSTEMS 523 REV. 12-71

26263-6021-RU-00

SK	REVISIONS			
	LTR	DESCRIPTION	DATE	APPROVED

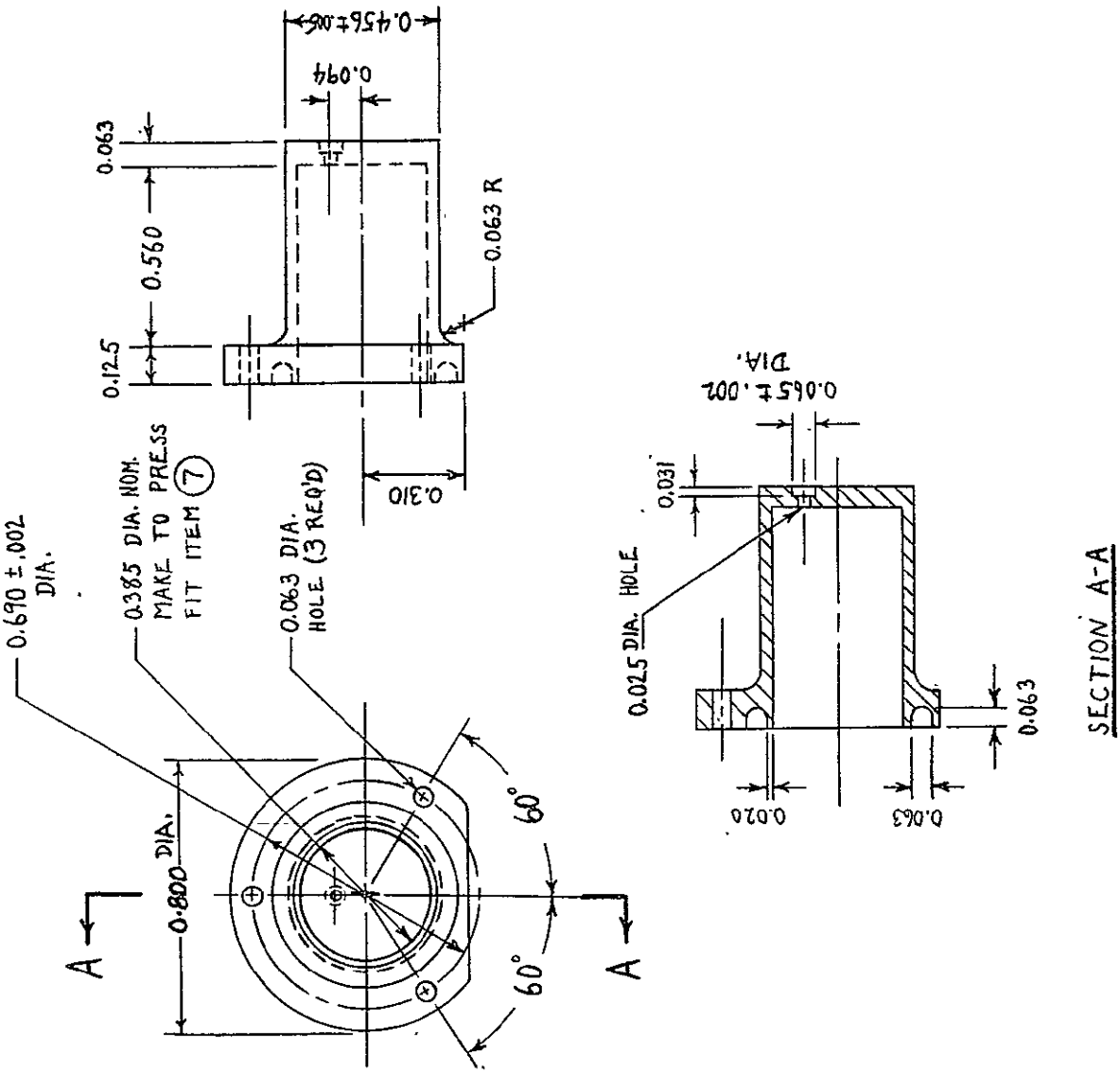

ENGINEERING SKETCH	TRW SYSTEMS GROUP ONE SPACE PARK • REDONDO BEACH, CALIFORNIA	
ORIGINATOR	DATE 9/17/74	VMHP BELLOWS CAN
		SIZE A · CODE IDENT NO. 11982 · SK 740908
MJO		SCALE 2~1 · SHEET 1 OF

SYSTEMS 523 REV. 12-71

SK	REVISIONS			26263-6021-RU-00
	LTR	DESCRIPTION	DATE	APPROVED

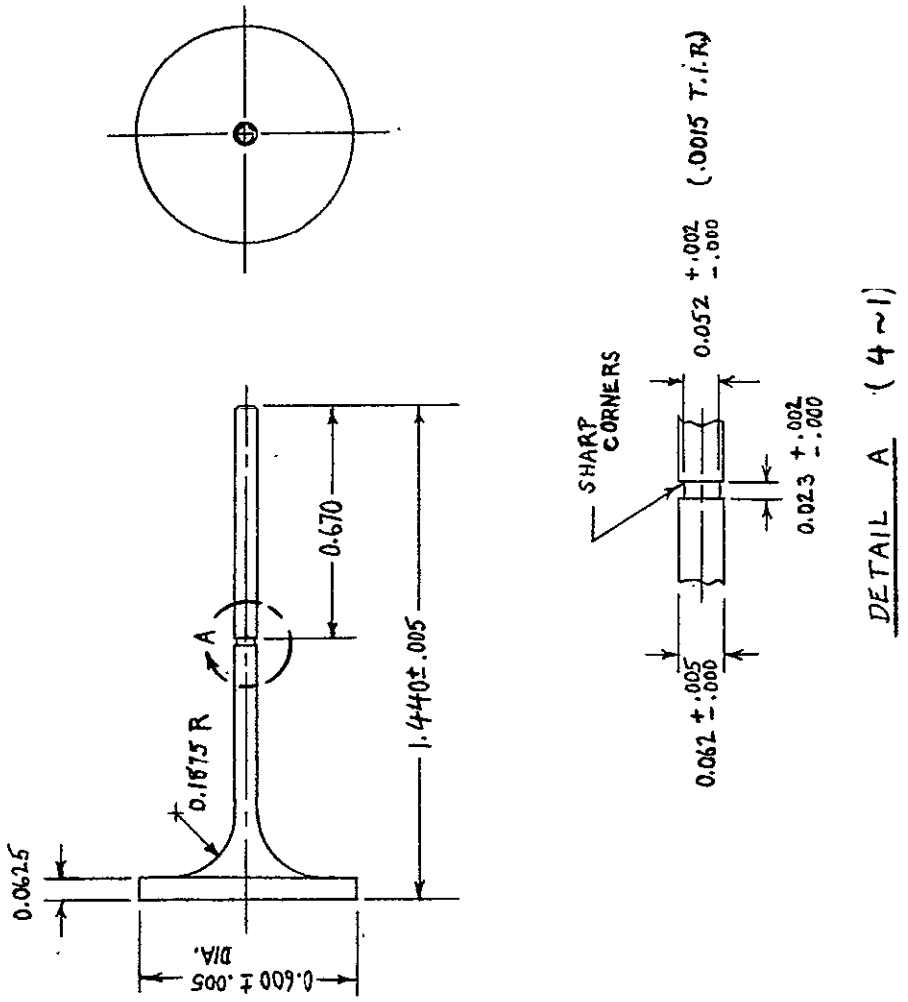

ENGINEERING SKETCH	TRW SYSTEMS GROUP ONE SPACE PARK • REDONDO BEACH, CALIFORNIA	
ORIGINATOR	DATE 9/9/74	VMHP VALVE
		SIZE A | CODE IDENT NO. 11982 | SK 740909
MJO		SCALE 2~1 | SHEET 1 OF

SK | CHG LTR

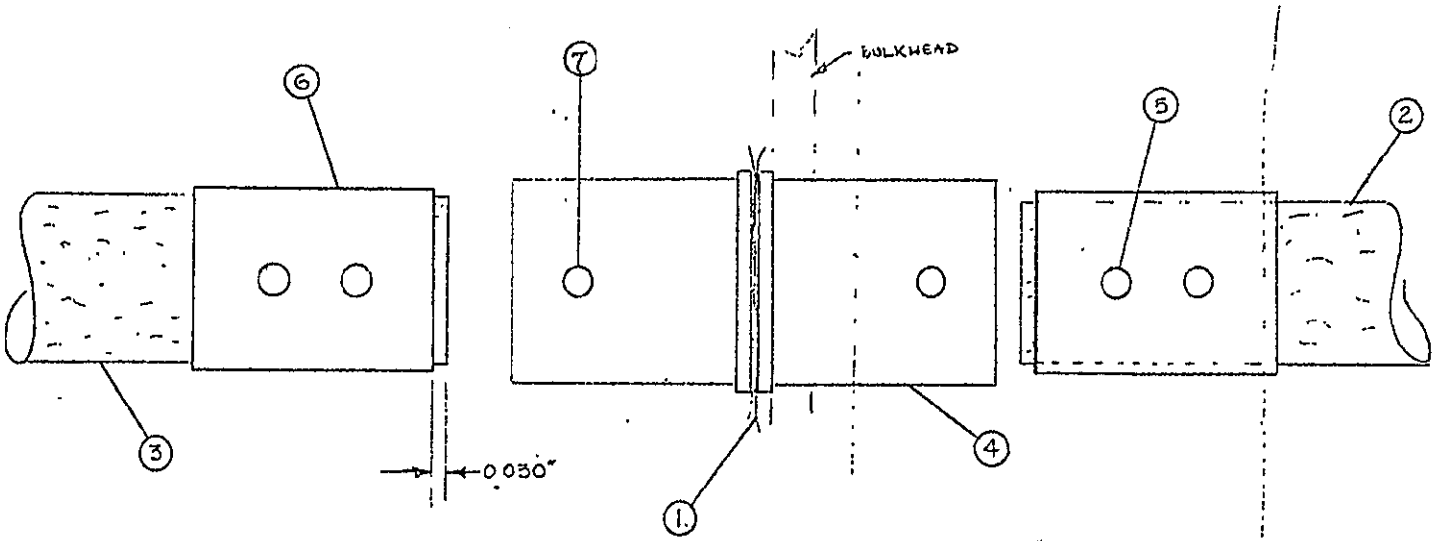

ASSEMBLY NOTES:

1. INSERT WICK ③ & ② INTO WICK CLAMP SO THAT PIN HOLES ARE PARALLEL TO WIDEST WICK DIMENSION
2. EXTEND WICK BEYOND WICK CLAMP BY ~.1", DRILL THRU & INSERT PIN ⑤
3. USE FIXTURE TO CUT WICK EXTENSION TO 0.030"
4. CLAMP WICK TUNNEL PARTS TOGETHER, ALIGN PIN HOLES, WELD AT SCREEN-WICK TUNNEL INTERFACE

ITEM	PART NO.	QTY	DESCRIPTION	MATERIAL SIZE	SPEC.
7	740913-2	2	WICK CLAMP PIN	CRES 304	
6	741113	2	WICK CLAMP	CRES 304	
5	740913-1	4	[illegible]	[illegible]	
4	740912	2	[illegible]	[illegible]	
3	740911-2	1	[illegible]	[illegible]	SK 740913-2
2	740911-1	1	[illegible]	[illegible]	SK 740913-2
1	—	2	[illegible]	[illegible]	

PARTS LIST

ORIGINATOR	DATE	TITLE	ENGINEERING SKETCH
MJO	10/18/74	VMHP WICK SUB-ASSEMBLY	TRW SK 740910 SHEET 2 OF 3

SK	REVISIONS			26263-6021-RU-00
	LTR	DESCRIPTION	DATE	APPROVED

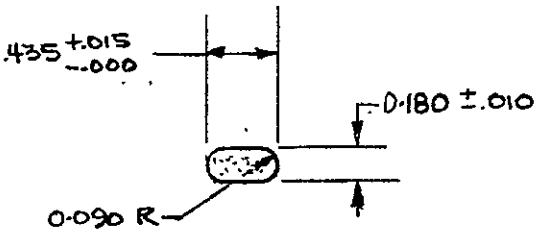

DASH NO.	A
-1	38.0
-2	5.0

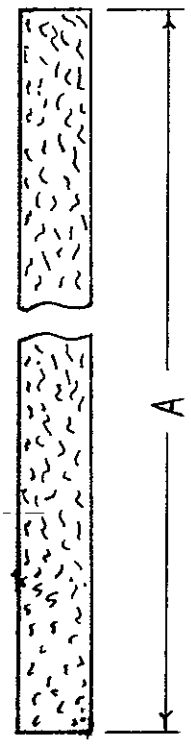

NOTE: DIMENSION 'A' INCLUDES EXCESS TO BE TRIMMED AFTER INSTALLATION.

ENGINEERING SKETCH	TRW SYSTEMS GROUP ONE SPACE PARK • REDONDO BEACH, CALIFORNIA
ORIGINATOR: MJO — DATE: 9/19/74	VMHP WICK
	SIZE: A — CODE IDENT NO.: 11982 — SK 740911
	SCALE 2~1 — SHEET 1 OF

SYSTEMS 523 REV. 12-71

SK | CHG LTR

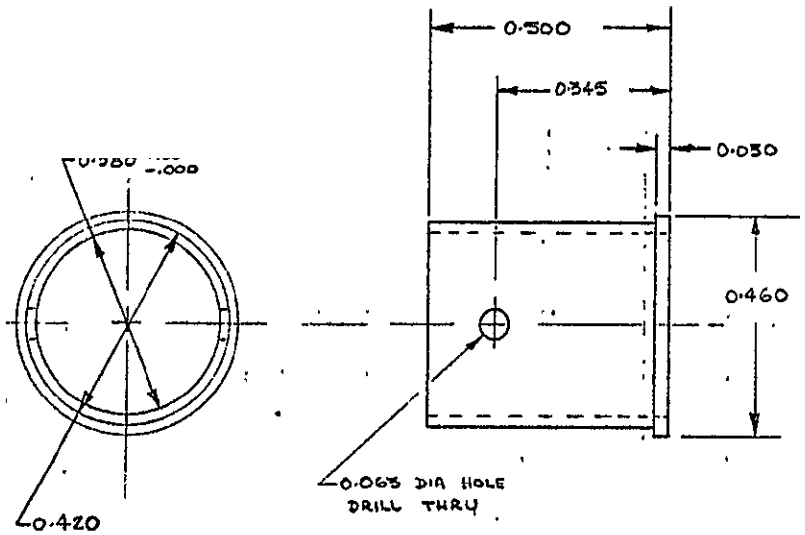

SCALE : 4~1

ORIGINATOR	DATE	TITLE	ENGINEERING SKETCH
E.E.LUEDKE	10/22/74	VMHP WICK TUNNEL	TRW
			SK 740912
MJO			SHEET OF

SYSTEMS GROUP REV. 8-67

26263-6021-RU-00

SK

REVISIONS			26263-6021-RU-00
LTR	DESCRIPTION	DATE	APPROVED

DASH NO.	LENGTH - ℓ - in.
-1	0.375
-2	0.420

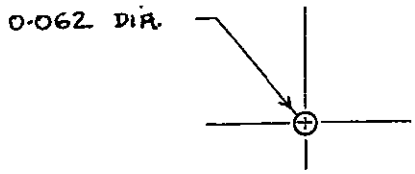

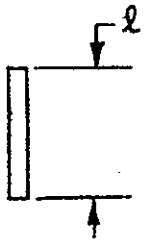

ENGINEERING SKETCH

TRW SYSTEMS GROUP
ONE SPACE PARK • REDONDO BEACH, CALIFORNIA

ORIGINATOR	DATE
MJO	9/19/74

VMHP
WICK PIN

SIZE	CODE IDENT NO.	
A	11982	SK 740913

SCALE 2~1 | SHEET 1 OF

SYSTEMS 523 REV. 12-71

SK	REVISIONS		26263-6021-RU-00	
	LTR	DESCRIPTION	DATE	APPROVED

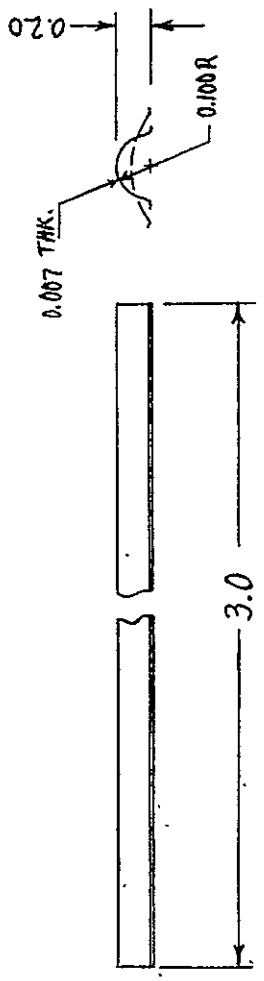

ENGINEERING SKETCH		TRW SYSTEMS GROUP ONE SPACE PARK • REDONDO BEACH, CALIFORNIA		
ORIGINATOR	DATE	VMHP FLAT SPRING		
	9/19/74			
		SIZE: A	CODE IDENT NO.: 11982	SK 740914
MJO		SCALE 2 ~ 1		SHEET 1 OF

SYSTEMS 523 REV. 12-71

SK | CHG LTR

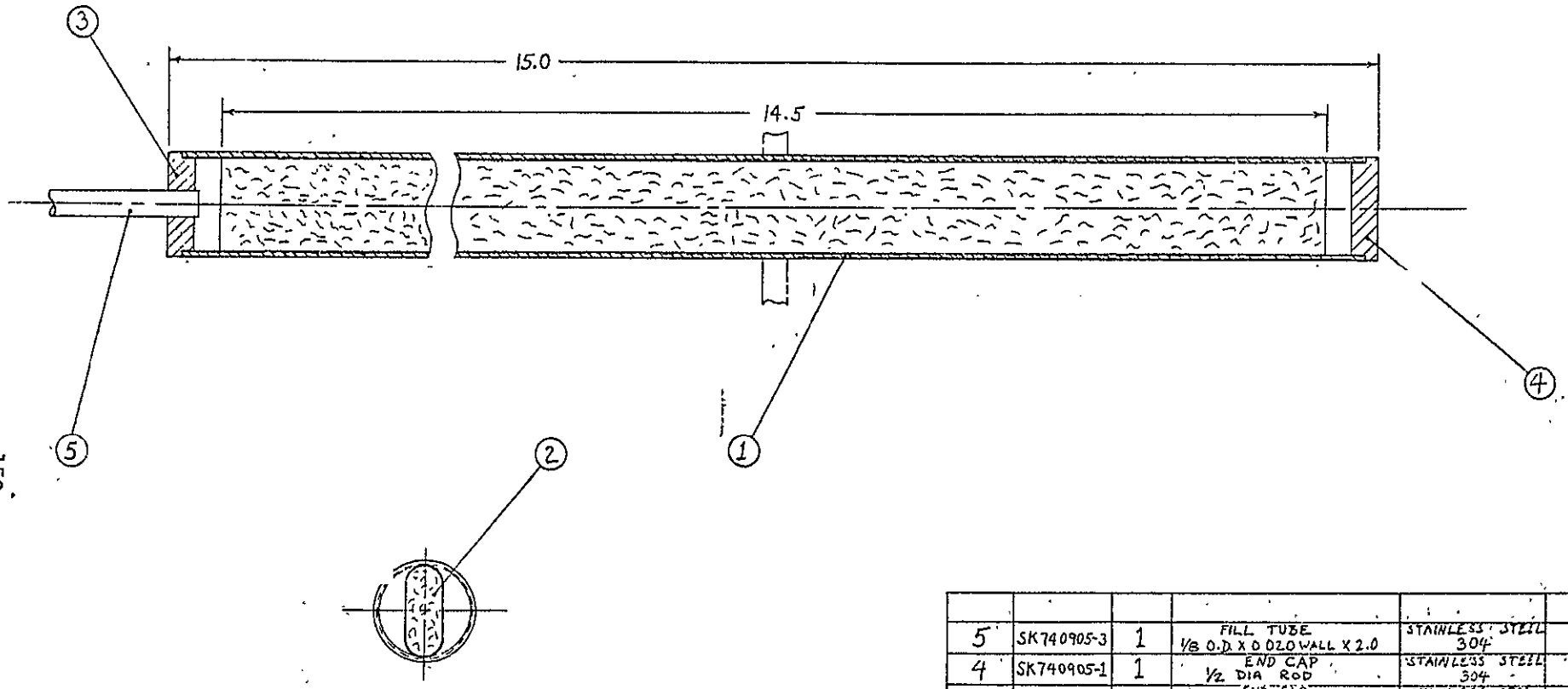

-150-

26263-6021-RU-00

ITEM	PART NO.	QTY	DESCRIPTION	MATERIAL	SPEC.
5	SK740905-3	1	FILL TUBE 1/8 O.D X 0.020 WALL X 2.0	STAINLESS STEEL 304	
4	SK740905-1	1	END CAP 1/2 DIA ROD	STAINLESS STEEL 304	
3	SK740905-2	1	END CAP 1/2 DIA ROD	STAINLESS STEEL 304	
2	SK1003-2	1	EVAPORATOR WICK (21% DENSITY, 0.005 WIRE)	STAINLESS STEEL 304	SK1003-2
1	SK740916	1	TUBE, THREADED 1/2 OD X 0.035 WALL	STAINLESS STEEL 304	SP-13B-02

PARTS LIST

SCALE : 2 ~ 1

ORIGINATOR	DATE	TITLE	ENGINEERING SKETCH
	9/20/74	VMHP	TRW
		EVAPORATOR SUB-ASSEMBLY	SK 740915
MJO			SHEET OF

SYSTEMS 8230 REV. 9-67

SK 1003	REVISIONS		26263-6021-RU-00	
	LTR	DESCRIPTION	DATE	APPROVED

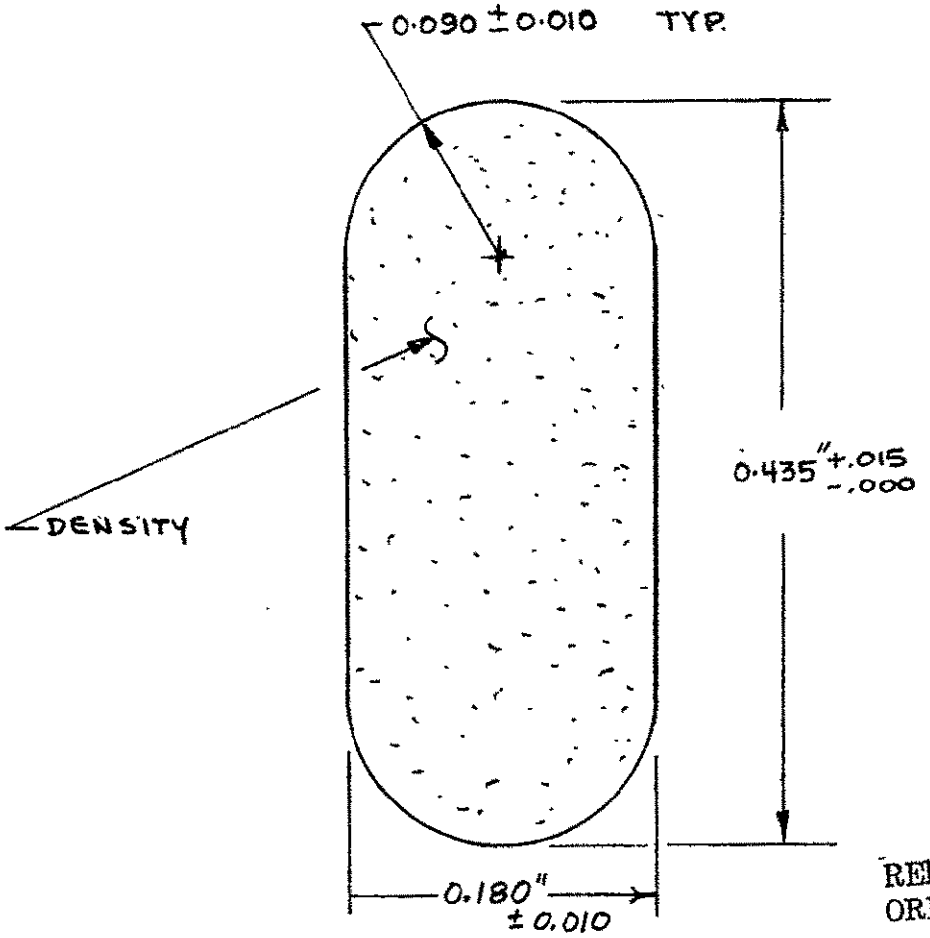

PART NO.	MATERIAL	WICK DENSITY
SK1003-3	304 CRES WIRE, 0.0036 ± 0.0002 DIA.	24 ± 1 %
SK1003-2	304 CRES WIRE, 0.0050" ± 0.0002 DIA.	21 ± 1 %
SK1003-1	5056 ALUMINUM WIRE, 0.0050" ± 0.0002 DIA.	21 ± 1 %

ENGINEERING SKETCH

TRW SYSTEMS GROUP
ONE SPACE PARK • REDONDO BEACH, CALIFORNIA

ORIGINATOR E.E. LUEDKE — DATE 10/7/74

MJO

HOMOGENEOUS WICK

SIZE A | CODE IDENT NO. 11982 | SK 1003

SCALE | SHEET 1 OF

SK | CHG LTR

NOTES:

1. INTERNAL GROOVES ENTIRE LENGTH PER SPEC. SP-13B-02.

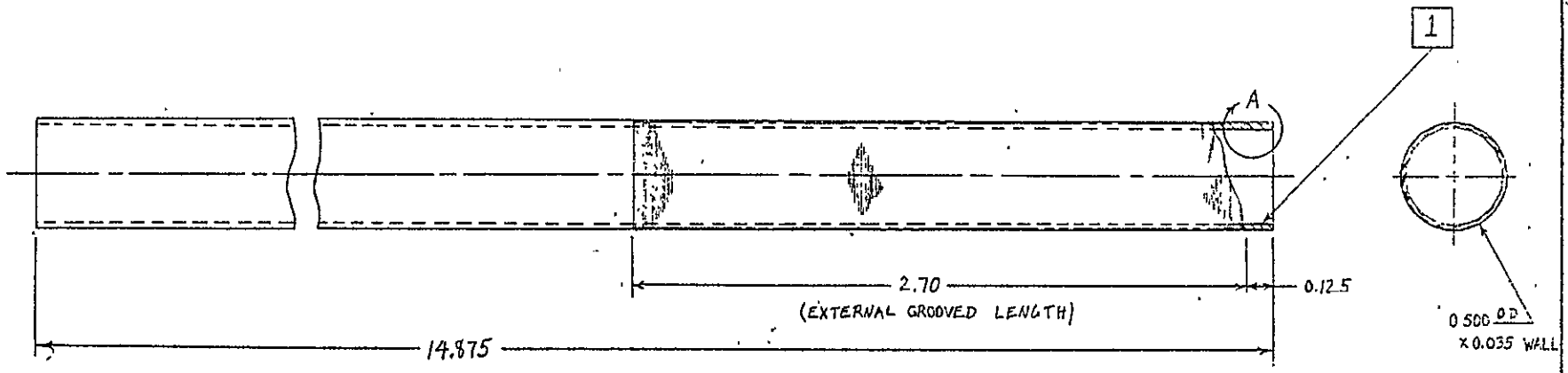

SCALE: 2~1

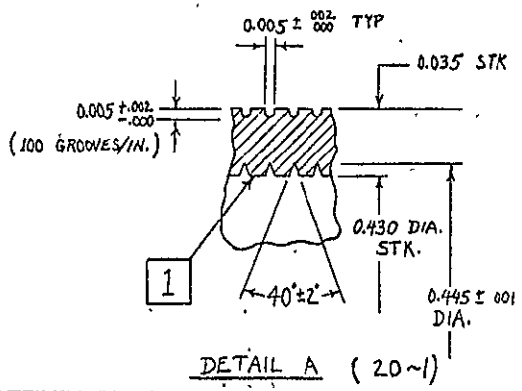

DETAIL A (20~1)

ORIGINATOR	DATE	TITLE	ENGINEERING SKETCH
	9/20/74	VMHP	TRW
		TUBE, THREADED	SK 740916
MJO			SHEET OF

SYSTEMS 6258 REV. 9-67

26263-6021-RU-00

SK	REVISIONS			26263-6021-RU-00
	LTR	DESCRIPTION	DATE	APPROVED

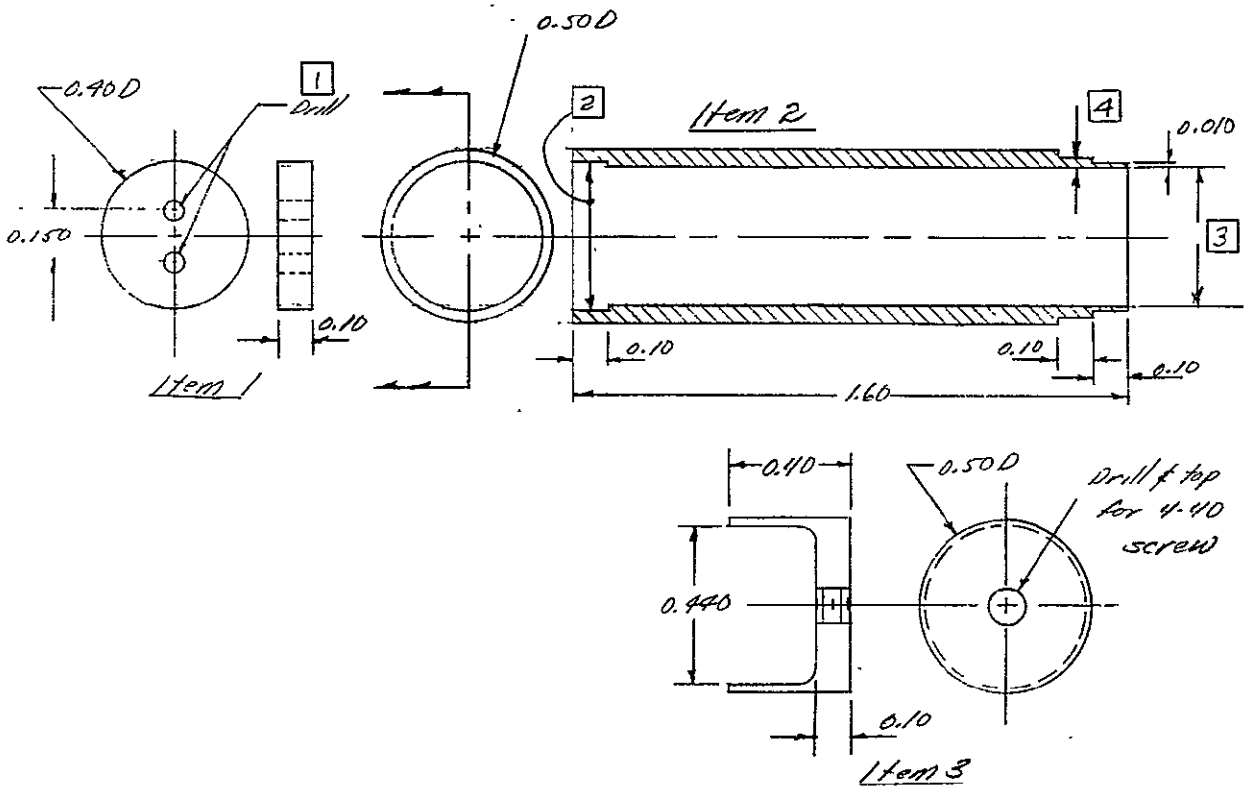

MATERIAL : 304 CRES

4 Machine so Item 3 fits over shoulder

3 Machine so flange on supplied bellows fits snugly inside.

2 Machine to fit Item 1

1 Drill for snug fit of 0.063 O.D. tubing supplied.

Notes:

ENGINEERING SKETCH		TRW SYSTEMS GROUP ONE SPACE PARK • REDONDO BEACH, CALIFORNIA		
ORIGINATOR	DATE	Control Volume parts		
Jim Emmser	3/10/74			
X 50370		SIZE: A	CODE IDENT NO.: 11982	SK 750310 E
		SCALE		SHEET 1 OF
MJO				

SYSTEMS 523 REV. 12-71

APPENDIX C

CONTENT OF APPENDIX C

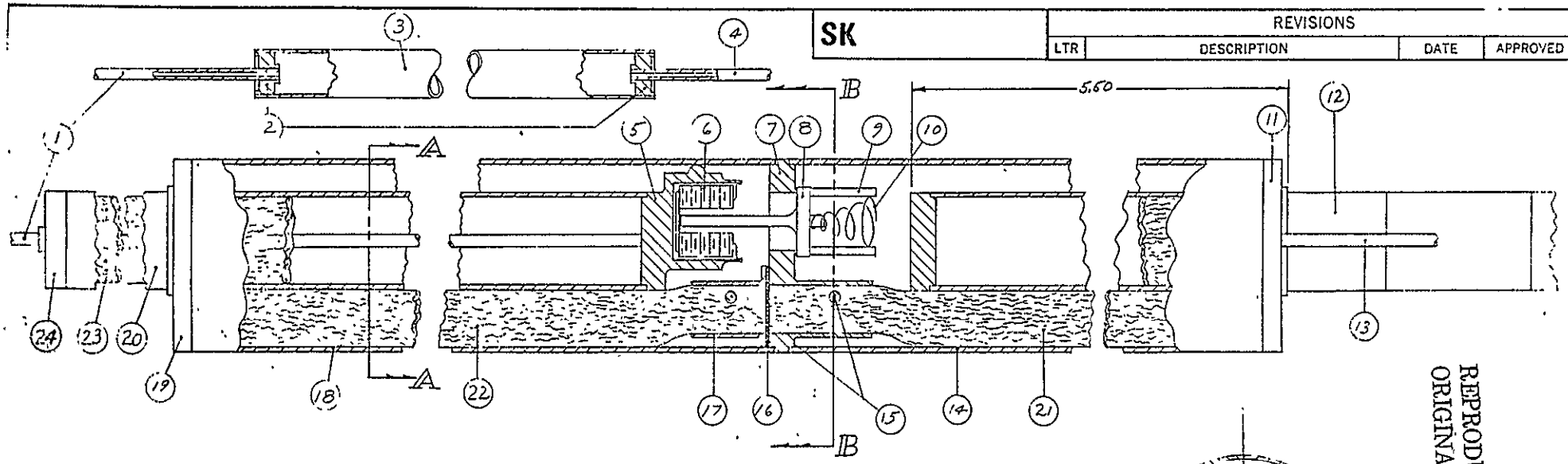

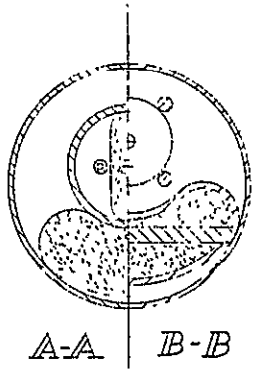

ITEM	SKETCH NO.	QTY.	DESCRIPTION	MATERIAL
24	SK75049-1	1	END CAP VMHP	304 SS
23	SK75057	1	INPUT-HEAT-PIPE WICK (HOMOGENEOUS)	304 SS
22	SK75059-2	1	HIGH-STRESS WICK	304 SS
21	SK75039-1	1	LOW-STRESS WICK	304 SS
20	SK75055	1	INPUT-HEAT-PIPE TUBE	304 SS
19	SK75023-2	1	END CAP (SHEET STOCK)	304 SS
18	———	1	TUBE (1 O.D. X 0.020 WALL X 6)	304 SS
17	SK75027	1	WICK HOLDER	304 SS
16	———	1	CAPILLARY BARRIER (2 LAYERS 250 MESH SCREEN)	304 SS
15	———	2	WICK PINS (1/16 ROD, CUT AFTER INSERTION)	304 SS
14	———	1	TUBE (1 O.D. X 0.020 WALL X 6)	304 SS
13	———	1	FEED TUBE (1/16 O.D. X 0.020 WALL X 3)	304 SS
12	SK75048	1	OUTPUT-HEAT-PIPE SUBASSEMBLY	
11	SK75023-1	1	END CAP (SHEET STOCK)	304 SS
10	———	1	RETURN SPRING	347 SS
9	———	4	VALVE GUIDE POSTS (1/16 ROD X 0.575)	304 SS
8	SK75026	1	VALVE	304 SS
7	SK75025	1	BULKHEAD	304 SS
6	———	1	BELLOWS (METAL BELLOWS P/N 61105-1)	347 SS
5	SK75024	1	BELLOWS CAN	304 SS
4	———	1	SENSOR-VOLUME FILL TUBE (1/16 O.D. X 0.020 WALL X 3)	304 SS
3	SK75045-1	1	SENSOR TUBE	304 SS
2	SK75015-2	2	SENSOR END CAP	304 SS
1	———	1	PRESSURE TUBE (1/16 O.D. X 0.020 WALL X)	304 SS

-156-

SK

REVISIONS			
LTR	DESCRIPTION	DATE	APPROVED

REPRODUCIBILITY OF THE ORIGINAL PAGE IS POOR

26263-6021-RU-00

ENGINEERING SKETCH

ORIGINATOR: J Ennis — DATE: 8/25/75

MJO

TRW SYSTEMS GROUP
ONE SPACE PARK • REDONDO BEACH CALIFORNIA

VAPOR-MODULATED HP ASSEMBLY

SIZE	CODE IDENT NO.	
B	11982	SK 75044

SCALE | SHEET 1 OF

SK	REVISIONS		26263-6021-RU-00	
	LTR	DESCRIPTION	DATE	APPROVED

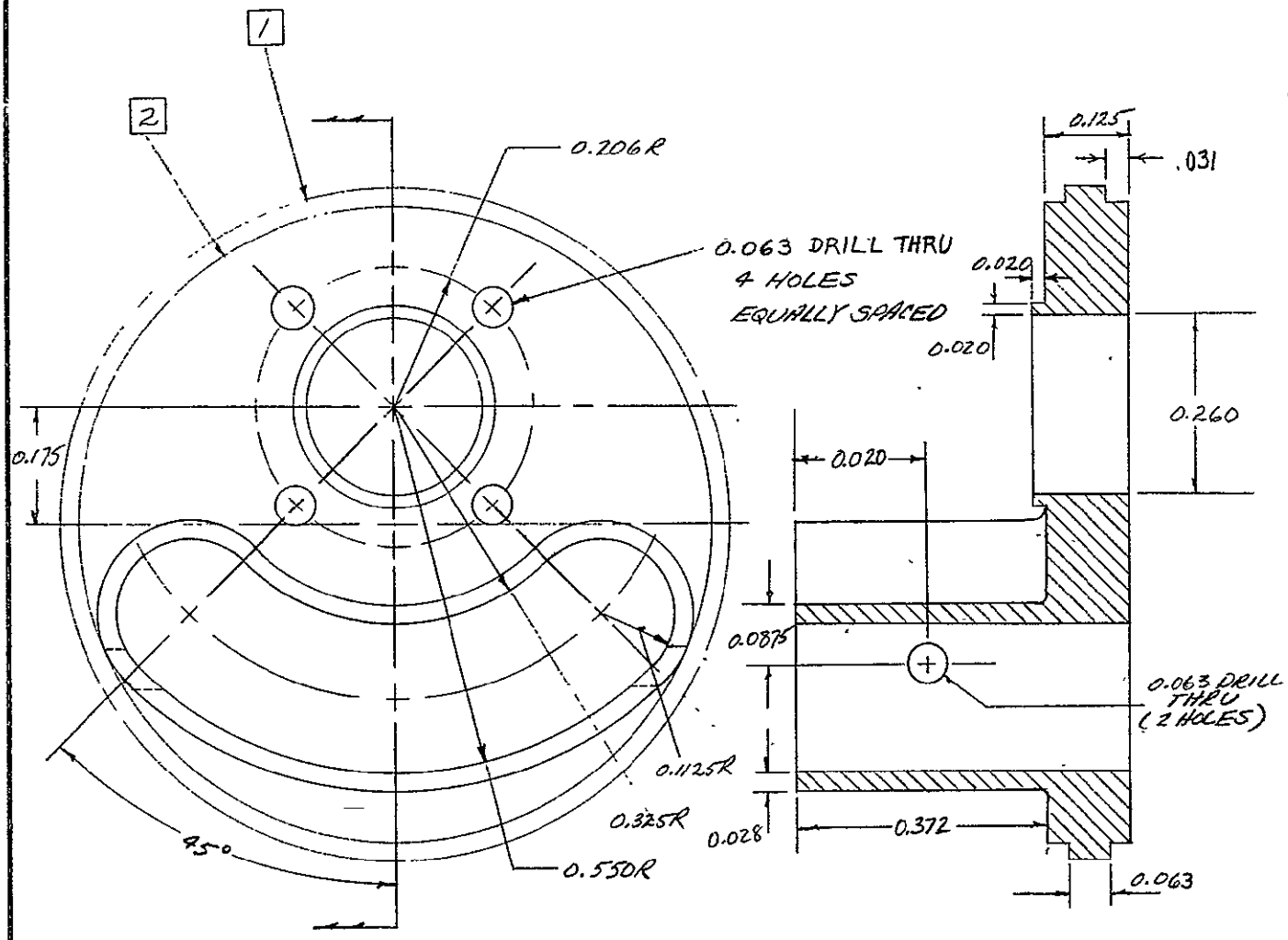

2 machine dia. to match I.D. of item 14

1 machine dia. to match O.D. of item 14

ENGINEERING SKETCH		TRW SYSTEMS GROUP ONE SPACE PARK • REDONDO BEACH, CALIFORNIA	
ORIGINATOR: A. Ennezer	DATE: 6/11/75	BULKHEAD	
SCALE 4:1		SIZE: A	CODE IDENT NO.: 11982
MJO: 251098		SCALE	SHEET 1 OF

SK 75025

SYSTEMS 523 REV. 12-71

SK

REVISIONS			26263-6021-RU-00
LTR	DESCRIPTION	DATE	APPROVED

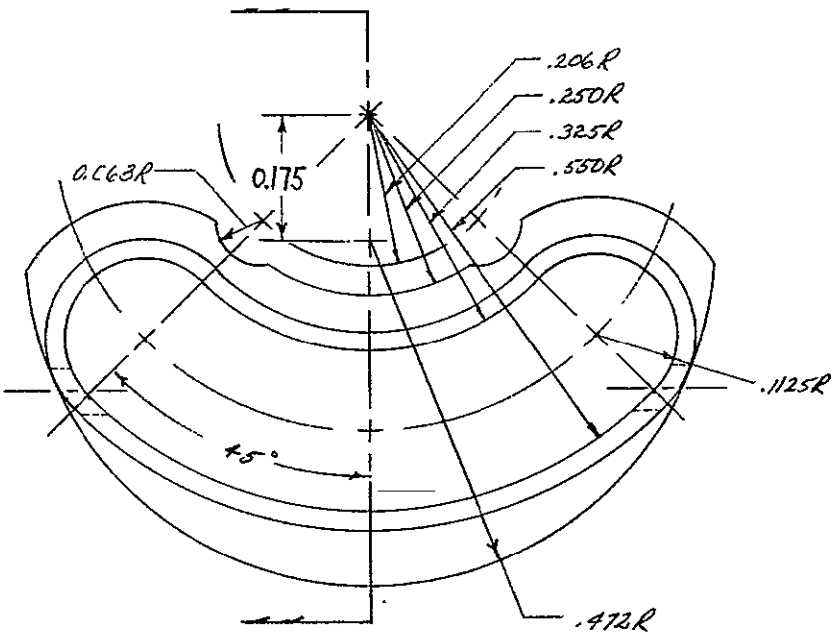

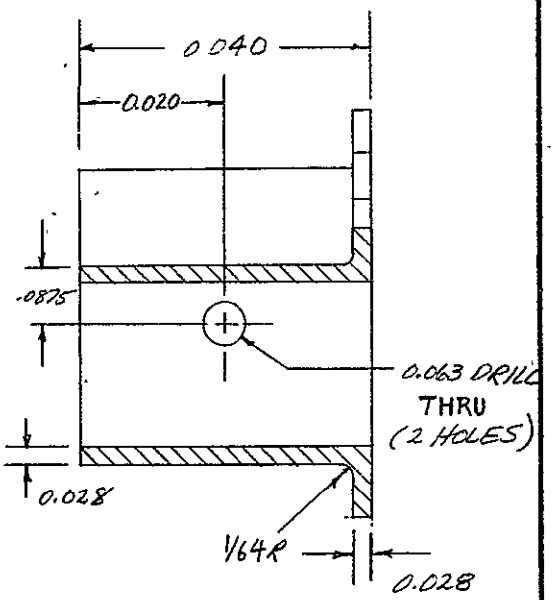

ENGINEERING SKETCH	TRW SYSTEMS GROUP ONE SPACE PARK • REDONDO BEACH, CALIFORNIA
ORIGINATOR: A Emmiger — DATE: 6/12/75	WICK HOLDER
SCALE 4:1	SIZE: A — CODE IDENT NO.: 11982 — SK 75027
MJO 251099	SCALE — SHEET 1 OF

SYSTEMS 523 REV. 12-71

SK	REVISIONS			26263-6021-RU-00
	LTR	DESCRIPTION	DATE	APPROVED

REPRODUCIBILITY OF THE ORIGINAL PAGE IS POOR

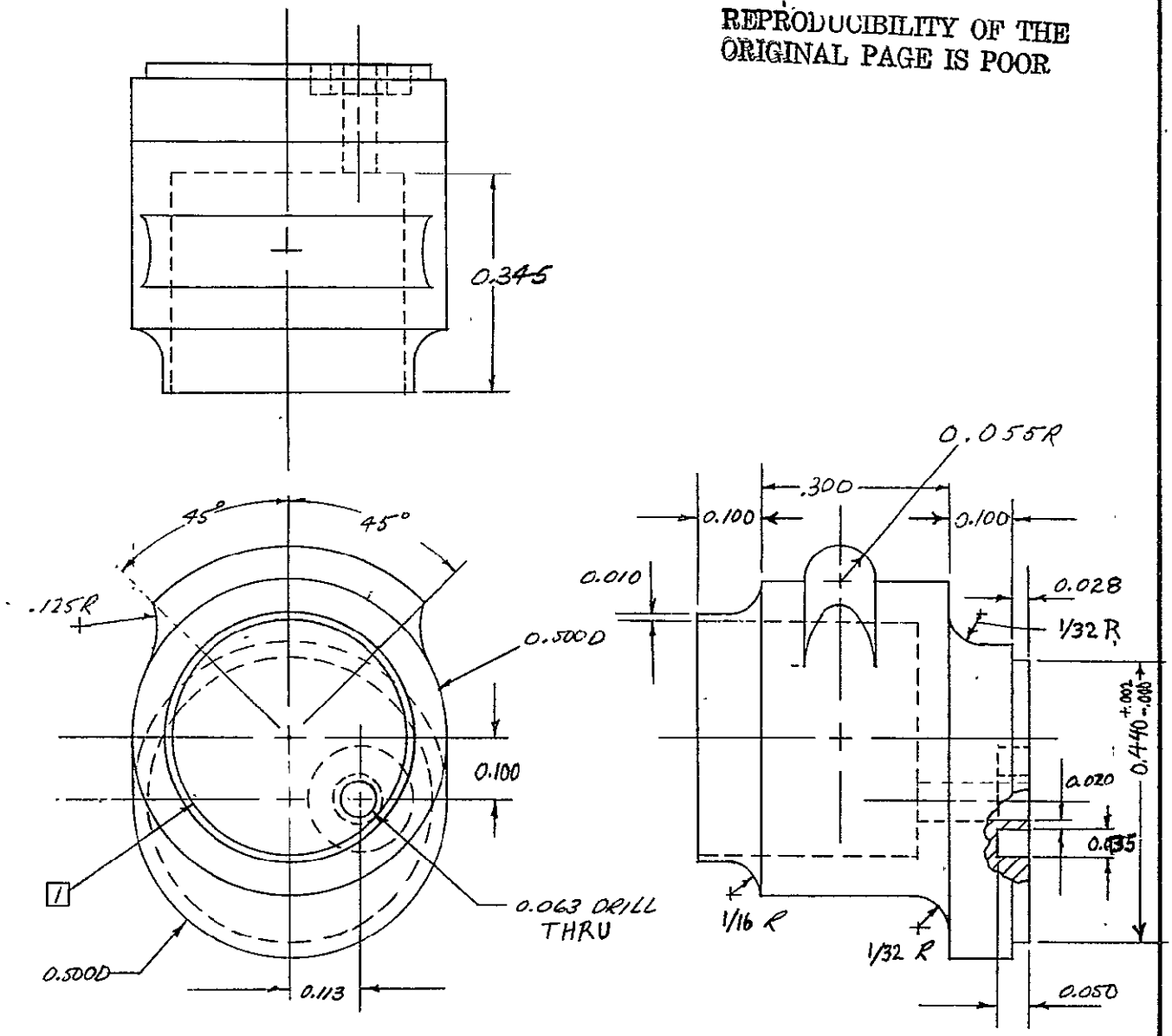

MAT'L: 304 CRES

[1] BORE TO FIT ITEM 6 (BELLOWS)

ENGINEERING SKETCH	TRW SYSTEMS GROUP ONE SPACE PARK • REDONDO BEACH, CALIFORNIA	
ORIGINATOR: J. Ennis	DATE:	BELLOWS CAN
SCALE 4:1		SIZE: A · CODE IDENT NO.: 11982 · SK 75024
MJO 251098		SCALE · SHEET 1 OF

SYSTEMS 523 REV. 12-71

SK	REVISIONS		26263-6021-RU-00	
	LTR	DESCRIPTION	DATE	APPROVED

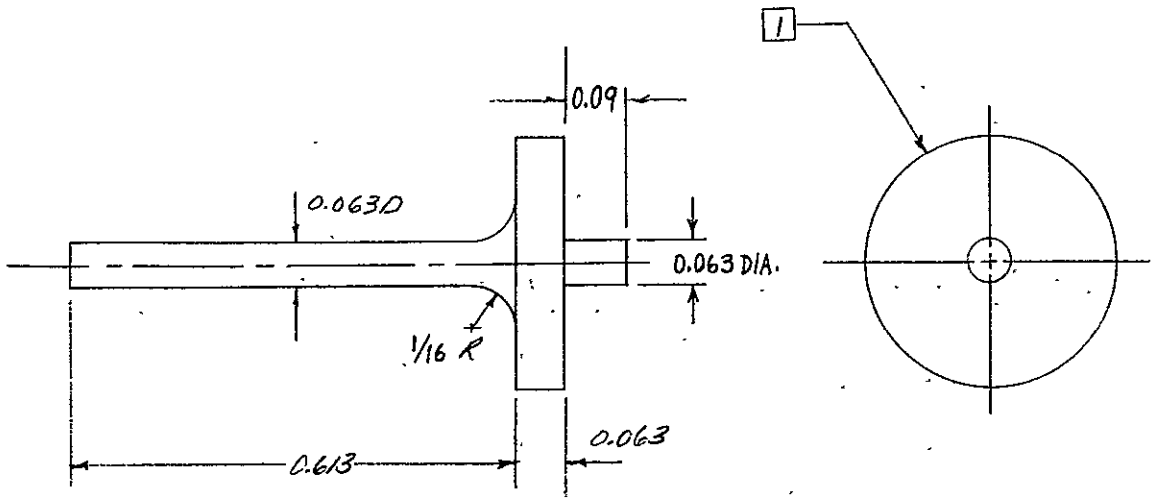

1 MACHINE DIA. FOR SLIP FIT IN VALVE-GUIDE POSTS (ITEM 9) WHEN INSERTED IN PART SK 75025 (ITEM 7 - BULKHEAD)

ENGINEERING SKETCH	TRW SYSTEMS GROUP ONE SPACE PARK • REDONDO BEACH, CALIFORNIA	
ORIGINATOR: J Ennis	DATE: 6/12/75	VALVE
SCALE 4:1		SIZE: A / CODE IDENT NO.: 11982 / SK 75026
MJO 251098		SCALE: / SHEET 1 OF

SYSTEMS 523 REV. 12-71

SK	REVISIONS		26263-6021-RU-00
	LTR	DESCRIPTION	DATE	APPROVED

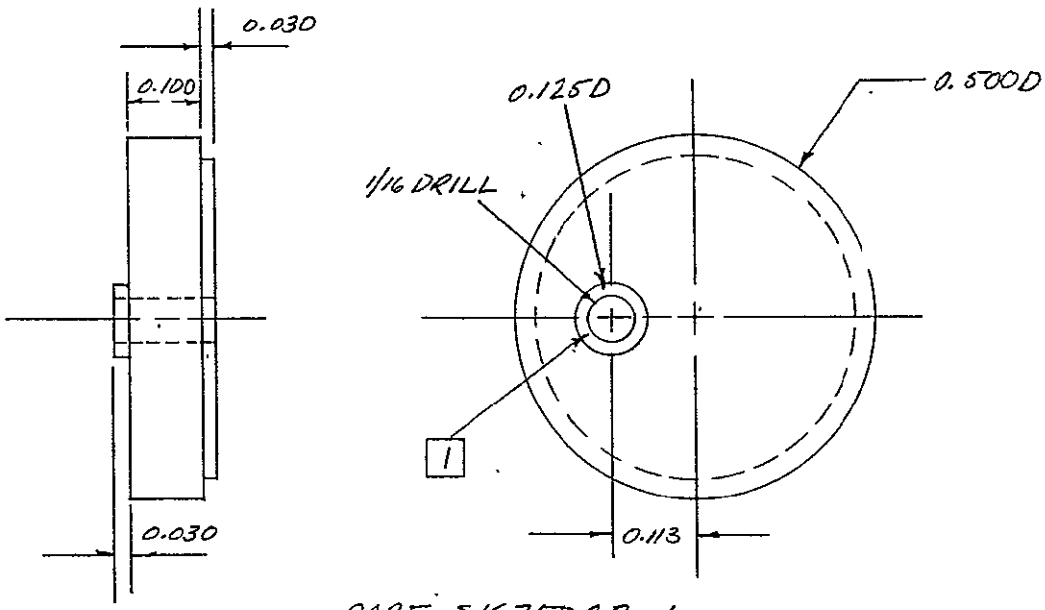

PART SK75049-1

MAT'L : 304 CRES

NOTES: [1] PART SK75049-2 IS IDENTICAL TO -1 EXCEPT OMIT HOLE AND RIDGE

ENGINEERING SKETCH	TRW SYSTEMS GROUP ONE SPACE PARK • REDONDO BEACH, CALIFORNIA	
ORIGINATOR: D. Ennis	DATE: 8/28/75	END CAP VMHP
MJO		SIZE: A; CODE IDENT NO.: 11982; SK 75049
		SCALE; SHEET 1 OF

SYSTEMS 523 REV. 12-71

SK	REVISIONS			26263-6021-RU-00.
	LTR	DESCRIPTION	DATE	APPROVED

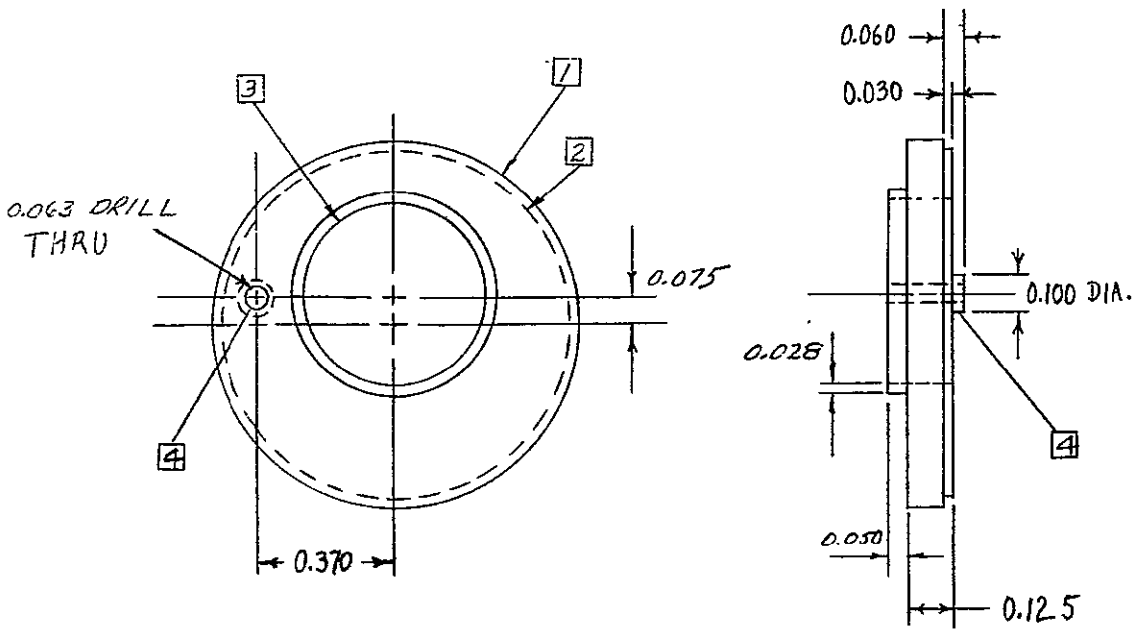

Part 75023-1

4 Part 75023-2 IDENTICAL TO -1 EXCEPT DELETE HOLE & RIDGE

3 MACHINE TO FIT O.D. OF ITEM 20

2 MACHINE TO FIT I.D. OF ITEM 18

1 MACHINE TO MATCH O.D. OF ITEM 18

ENGINEERING SKETCH	TRW SYSTEMS GROUP ONE SPACE PARK • REDONDO BEACH, CALIFORNIA	
ORIGINATOR: A. Enriga	DATE: 6/13/75	END CAP
SCALE 2:1		SIZE: A · CODE IDENT NO.: 11982 · SK 75023
MJO 257098		SCALE · SHEET 1 OF

SYSTEMS 523 REV. 12-71

SK	REVISIONS			26263-6021-RU-00
	LTR	DESCRIPTION	DATE	APPROVED

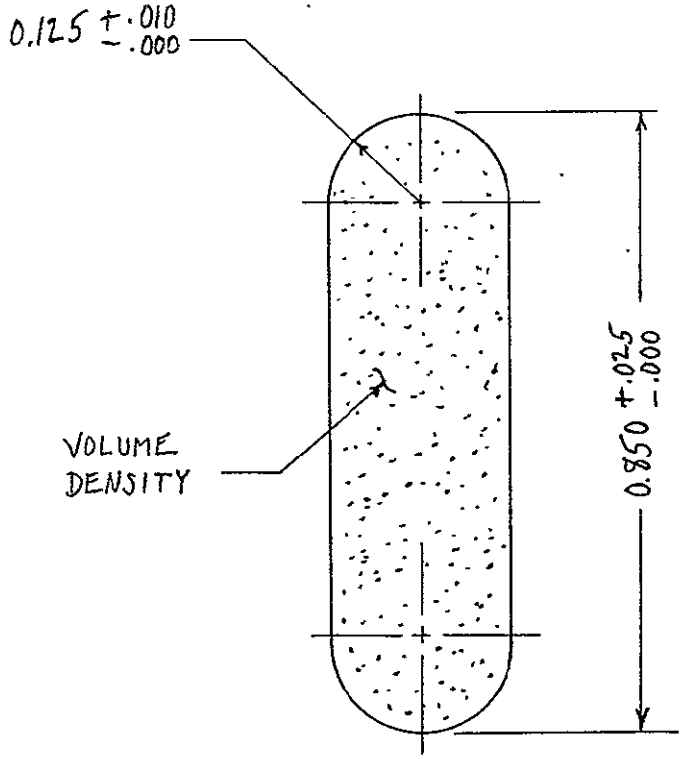

SCALE : 4~1

PART NO.	MATERIAL	VOL DENSITY
SK75039-2	304 CRES WIRE, 0.005 IN. DIA.	24 ± 2 %
SK75039-1	304 CRES WIRE, 0.005 IN. DIA.	14 ± 2 %

ENGINEERING SKETCH

TRW SYSTEMS GROUP
ONE SPACE PARK • REDONDO BEACH, CALIFORNIA

ORIGINATOR	DATE
G. FLEISCHMAN	6/24/75
MJO	

WICK, UNIFORM DENSITY

SIZE	CODE IDENT NO.	
A	11982	SK 75039

SCALE 4~1 | SHEET 1 OF

SYSTEMS 523 REV. 12-71

SK	REVISIONS		26263-6021-RU-00
	LTR DESCRIPTION	DATE	APPROVED

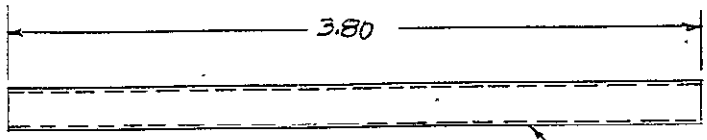

75045-1 - SENSOR TUBE

0.25 O.D. TUBE, 0.016 WALL

SCALE 1:1

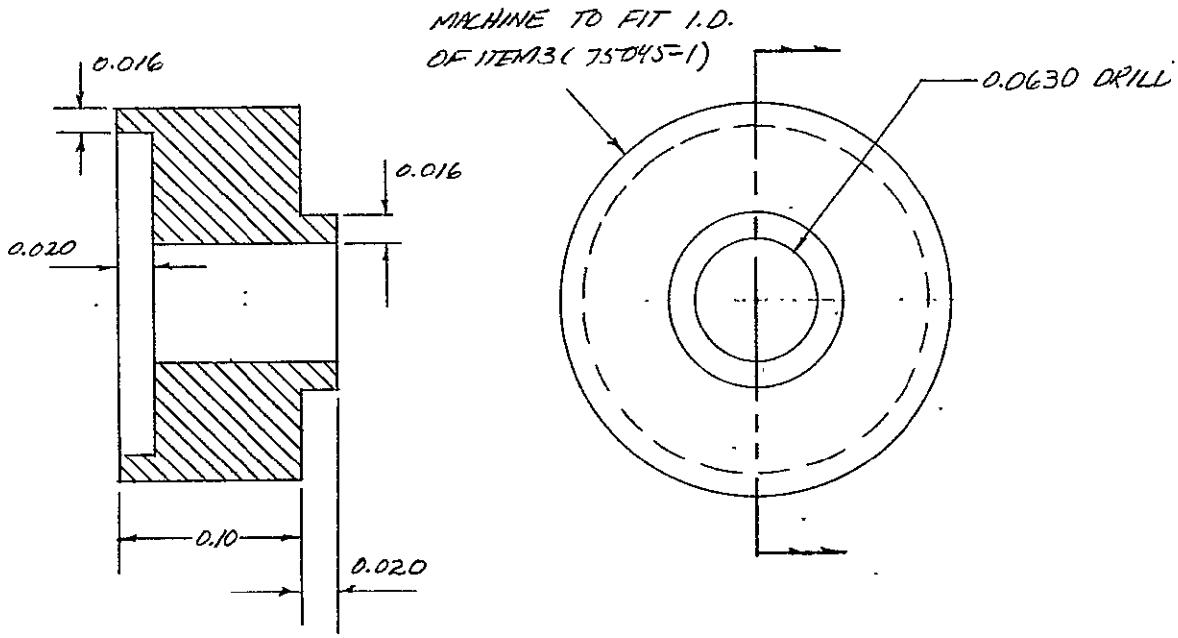

75045-2 - SENSOR END CAP

SCALE 10:1

MAT'L : 304 CRES

ENGINEERING SKETCH	TRW SYSTEMS GROUP ONE SPACE PARK • REDONDO BEACH, CALIFORNIA	
ORIGINATOR J Ennis	DATE 8/20/75	SENSOR VOLUME
MJO		SIZE A / CODE IDENT NO. 11982 / SK 75045
		SCALE / SHEET 1 OF

SYSTEMS 523 REV. 12-71

SK	REVISIONS			26263-6021-RU-00
	LTR	DESCRIPTION	DATE	APPROVED

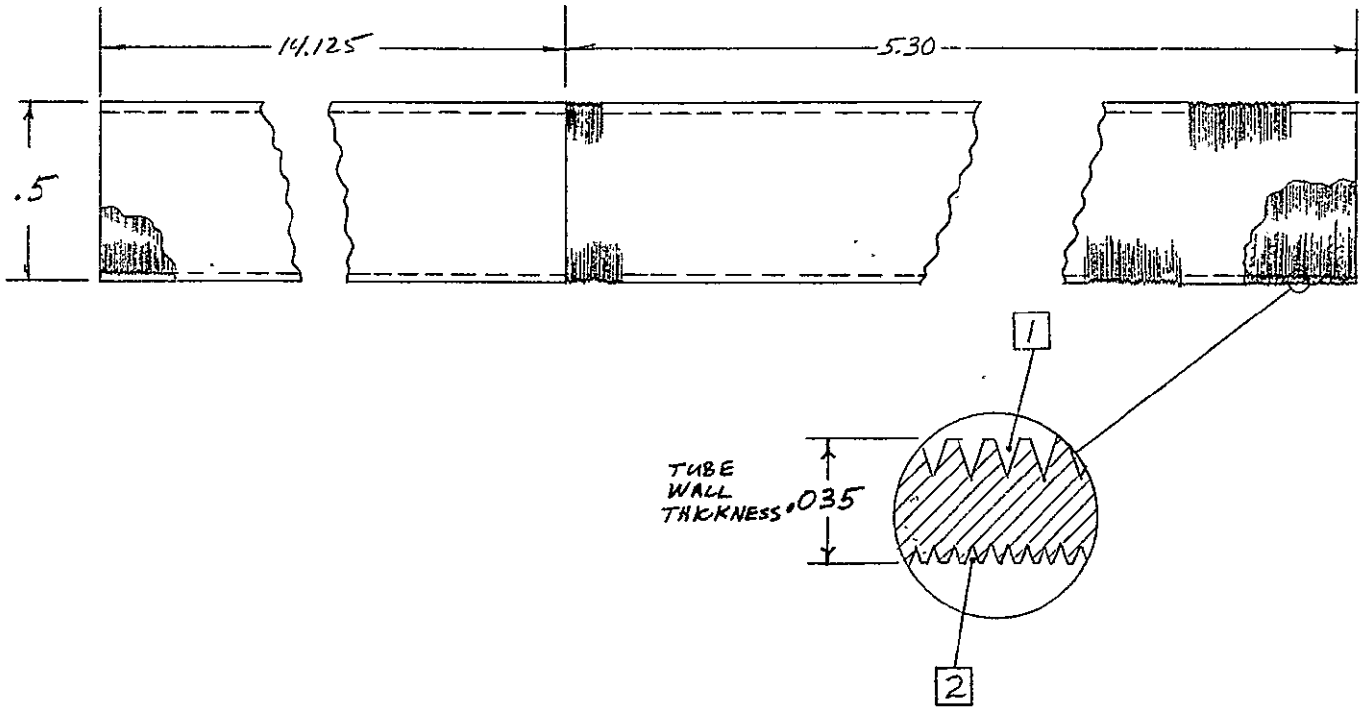

MAT'L: ½ O.D. X .035 WALL
304 CRES

[2] EXTERNAL THREADS - 200 TPI, 0.0035 OPENNING, 38° INCLUDED ANGLE.

NOTES: [1] INTERNAL THREADS - 100 TPI, 0.007 OPENNING, 38° INCLUDED ANGLE. THREAD ENTIRE LENGTH.

ENGINEERING SKETCH	TRW SYSTEMS GROUP ONE SPACE PARK • REDONDO BEACH, CALIFORNIA	
ORIGINATOR: J. ENINGER	DATE	TUBE FOR INPUT HEAT PIPE
MJO		SIZE: A · CODE IDENT NO.: 11982 · SK 75055
		SCALE · SHEET 1 OF

SYSTEMS 523 REV. 12-71

SK

REVISIONS			
LTR	DESCRIPTION	DATE	APPROVED

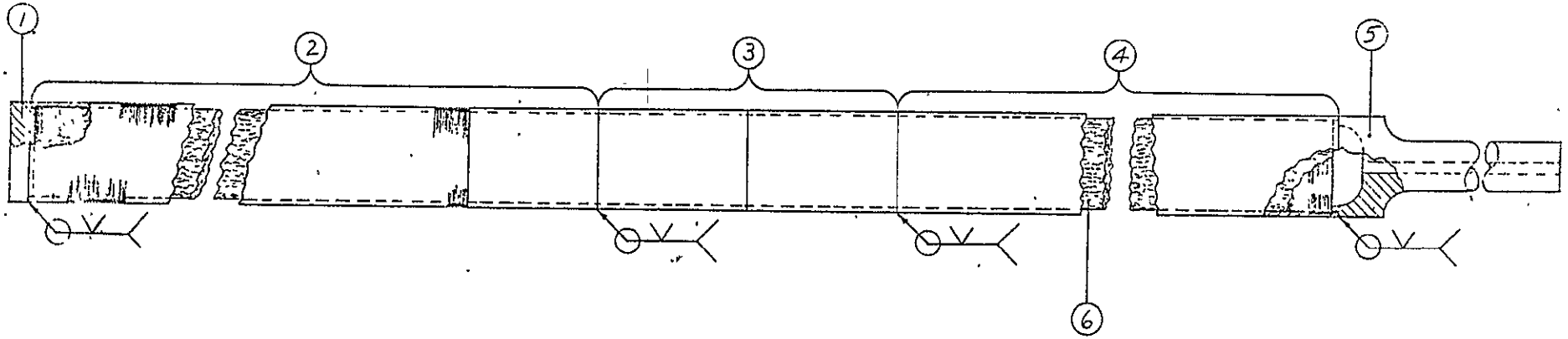

16263-6021-RU-00

ITEM	SK/PCH NO.	QTY.	DESCRIPTION	MATERIAL
6	SK75053	1	OUTPUT HP WICK (GRADED POROSITY)	6056 Al
5	SK75016-2	1	END CAP	6061-T6 Al
4	SK75052	1	OUTPUT HP CONDENSER SECTION	6061-T6 Al
3	SK75051	1	TRANSITION SECTION	304 SS / 6061-T6 Al
2	SK75050	1	OUTPUT HP INTERFACE SECTION	304 SS
1	SK75049-2	1	END CAP	304 SS

ENGINEERING SKETCH

ORIGINATOR	DATE
J Ginnings	9/28/73
MJO	

TRW SYSTEMS GROUP
ONE SPACE PARK • REDONDO BEACH, CALIFORNIA

OUTPUT-HEAT-PIPE SUBASSEMBLY

SIZE	CODE IDENT NO.	SK75048
B	11982	

SCALE | SHEET 1 OF

SK	REVISIONS			26263-6021-RU-00
	LTR	DESCRIPTION	DATE	APPROVED

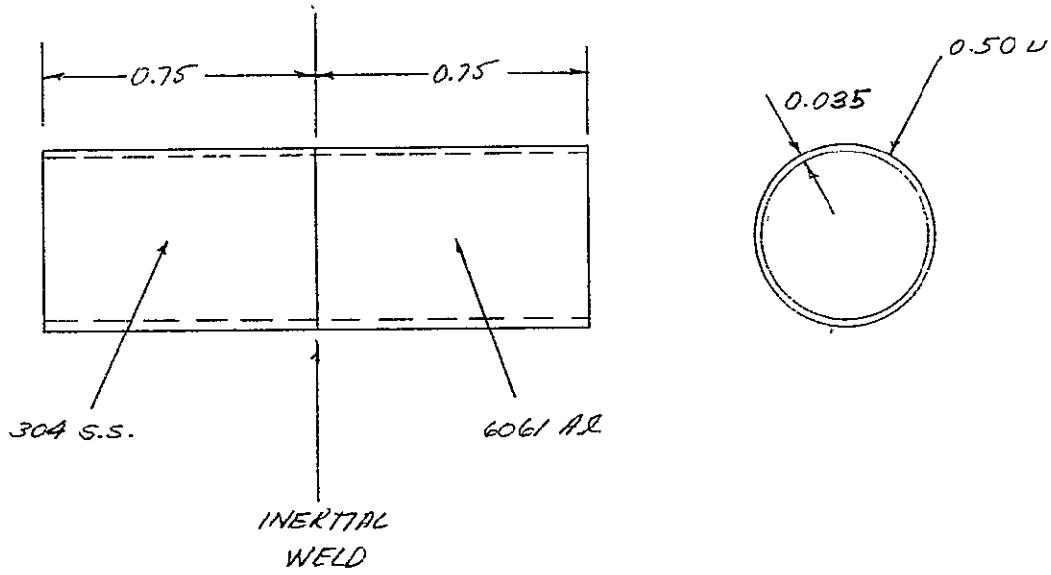

SAVE MAT'L NOT USED

ENGINEERING SKETCH	TRW SYSTEMS GROUP ONE SPACE PARK • REDONDO BEACH, CALIFORNIA	
ORIGINATOR: J Ennigh	DATE: 9/12/75	TRANSITION SECTION
MJO		SIZE: A · CODE IDENT NO.: 11982 · SK 75051
		SCALE · SHEET 1 OF

SYSTEMS 523 REV. 12-71

SK	REVISIONS			26263-6021-RU-00
	LTR	DESCRIPTION	DATE	APPROVED

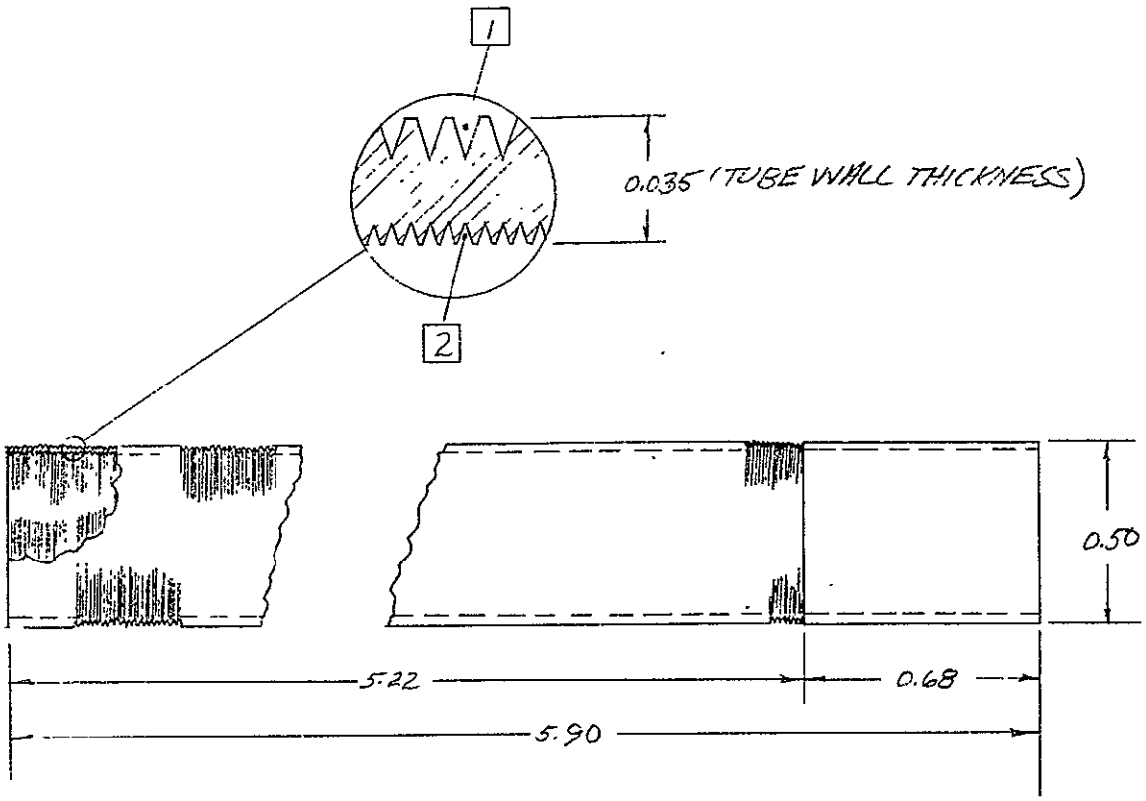

MAT'L: ½ O.D. X .035 WALL
304 CRES.

[2] INTERNAL THREADS - 200 TPI, .0035 OPENNING, 38° INCLUDED ANGLE. THREAD ENTIRE LENGTH

NOTES: [1] EXTERNAL THREADS - 100 T.P.I., 0.007 OPENNING, 38° INCLUDED ANGLE. NO EXTERNAL THREADS OVER LAST 0.68 INCHES.

ENGINEERING SKETCH		TRW SYSTEMS GROUP ONE SPACE PARK • REDONDO BEACH, CALIFORNIA		
ORIGINATOR	DATE	INTERFACE SECTION OF OUTPUT HEAT PIPE		
		SIZE: A	CODE IDENT NO.: 11982	SK 75050
MJO		SCALE		SHEET 1 OF

SK	REVISIONS		26263-6021-RU-00	
	LTR	DESCRIPTION	DATE	APPROVED

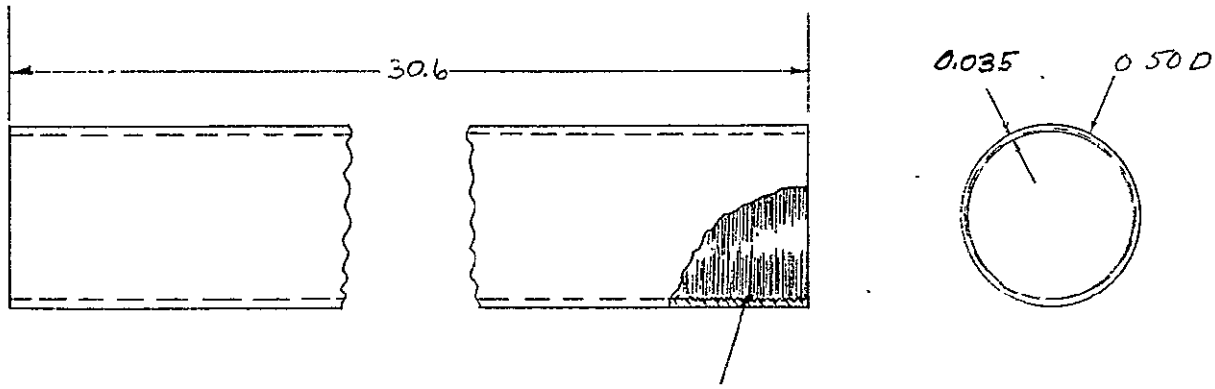

INTERNAL THREADS – 100 TPI, 0.007 OPENNING, 38° INCLUDED ANGLE THREAD ENTIRE LENGTH

MAT'L: ½ O.D. X .035 WALL
6061-T6

ENGINEERING SKETCH		TRW SYSTEMS GROUP ONE SPACE PARK • REDONDO BEACH, CALIFORNIA	
ORIGINATOR J. Ennis	DATE 9/12/75	OUTPUT HEAT PIPE CONDENSER SECTION	
		SIZE A	CODE IDENT NO. 11982
MJO		SCALE	SHEET 1 OF

SK 75052

SYSTEMS 523 REV. 12-71

SK	REVISIONS		26263-6021-RU-00
	LTR	DESCRIPTION	DATE / APPROVED

Note • Use 0.006" Teflon tape between input heat pipe and heater block.
• Use RTV or thermal grease between output heat pipe and heat sink

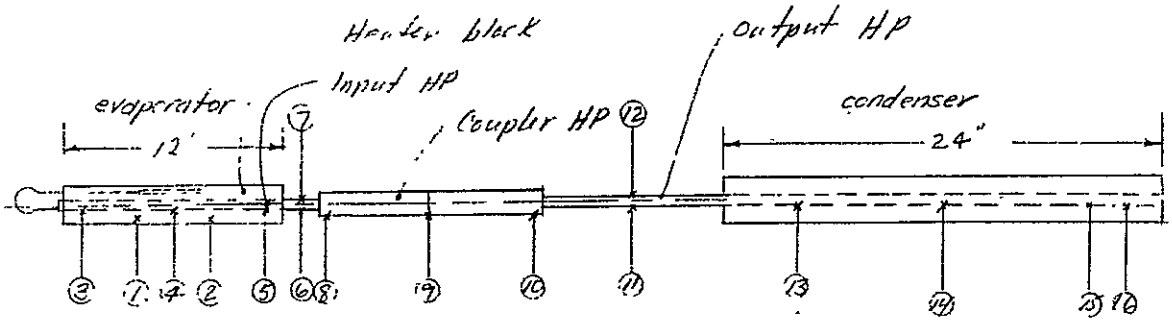

TC	Description	Location
1	Heater block	4 in. from L.H.S. of Heater block
2	" "	8 " " " " " "
3	Input HP evap.	1 in. from LHS of Input HP
4	"	6 " " " " "
5	"	11 " " " " "
6	Input HP adiab.	13 " " " " "
7	"	13 " " " " "
8	Coupler section	Left hand end cap
9	"	Bulkhead
10	"	Right hand end cap
11	Output HP	29 in. from RHS of Output HP
12	"	29 " " " " "
13	"	20 " " " " "
14	"	12 " " " " "
15	"	4 " " " " "
16	"	2 " " " " "
17	Cold plate	
18	Cold plate	

High limit - on heater block close to sensor volume

ENGINEERING SKETCH	TRW SYSTEMS GROUP ONE SPACE PARK • REDONDO BEACH, CALIFORNIA	
ORIGINATOR: J Ennis	DATE: 10/14/75	VMHP INSTRUMENTATION
MJO		SIZE: A / CODE IDENT NO.: 11982 / SK 75061
		SCALE / SHEET 1 OF

SYSTEMS 523 REV. 12-71